Late Cenozoic Stratigraphy of the Southern Terror Rift, Antarctica: Implications for Tectonic and Climatic Evolution

Dhiresh Hansaraj

January 2008

A thesis submitted in partial fulfilment towards the Degree of Master of Science in Geophysics

School of Geography, Environment and Earth Sciences

Victoria University of Wellington

Acknowledgements

I would like to gratefully acknowledge the advice and assistance provided to me throughout the writing of this thesis. First and foremost I am deeply indebted to my supervisors, Tim Naish and Stuart Henrys, for their constant and dependable guidance from day one on the ice, to the final proof.

A huge thanks to everyone at the Antarctic Research Centre (ARC) for providing me with a stimulating working environment, and for making me feel welcome and a part of the team. In particular I would like to thank Rob McKay, Lionel Carter, Peter Barrett, Tamsin Falconer, Michelle Dow and Nancy Bertler for their encouragement and helpful constructive criticism. It was greatly appreciated.

Similarly I would also like to thank everyone at GNS Science for providing me with the support and resources to complete this work, but special thanks go to Tony Harrison, Guy Maslen, Suzannah Toulmin, Chris LeBlanc and Mike Milner for their assistance with the technical aspects.

The biggest thanks I can give, is to my friends; for keeping me motivated during the harder times, as well as simply being there to keep me sane. A huge sense of gratitude to Hannu Seebeck, Andrew Cassels, Joseph Coyle, Christopher Town, Jodi Williams, Oscar Clark, Rosanne Simes, Jessica Humphrey, Hannah Bushe, James Hollway, Mark Huser, and everyone else who was there for me whether they knew it or not.

Finally I would like to thank Antarctica New Zealand, for providing logistical support, and all the good people who helped during the long days of data acquisition in Antarctica.

ABSTRACT

This thesis presents an integrated analysis of late Cenozoic (last 14 Ma) glacimarine stratigraphy within the Terror Rift in southern McMurdo Sound, Antarctica. The study area is located in the Windless Bight region of the McMurdo Ice Shelf (NW corner of the Ross Ice Shelf), which overlies a 600 to 1000 m-deep bathymetric moat surrounding Ross Island in the depocentral axis of the Victoria Land Basin (VLB). The VLB, one of a number of extensional sedimentary basins within the West Antarctic Rift System, comprises a 7-km-thick succession of syn- and post-rift glacimarine sediments that accumulated during the Oligocene and Miocene periods, respectively. Renewed rifting, known as the Terror Rift, in the centre of the VLB began between 17 to 14 Ma and has accommodated as much as one third of the entire Cenozoic basin-fill. The development of rift-related alkalic volcanoes associated with the Erebus Volcanic Province from c. 5 Ma has produced localised flexural basins/moats around Ross Island that have preserved a thick Pliocene-Pleistocene stratigraphic record.

A new stratigraphic architecture is presented for southern Terror Rift based on: (1) the acquisition, processing and interpretation of 73 kilometres of over-ice shelf multi-channel seismic reflection data; (2) correlation of seismic stratigraphy with the integrated chrono-, litho- and cyclostratigraphy of the 1285 m-deep ANDRILL McMurdo Ice Shelf (MIS) Project drill core (AND-1B) using a synthetic seismic-well tie, and time-depth data from a vertical seismic profile (VSP). Five seismic units bounded by regionally-mappable unconformities, which thicken into the centre of the basin, are identified and their relationship to the existing seismic stratigraphy of western VLB (Fielding et al. 2007) is established. In addition, a further 17 mappable seismic surfaces bounding higher-frequency depositional units are identified. The seismic units are interpreted on the basis of characteristic features, seismic facies, and correlations with the lithostratigraphy of the core.

1). Rg (light green) surface is the oldest regionally-mappable reflector. It directly overlies a redeposited volcanic unit sampled by the AND-1B core and yielded an age of ~13.8 Ma, dated using the $^{40}Ar/^{39}Ar$ method. The unconformity is undulating, dislocated by normal faults, truncates underlying strata, and is characterised by stratal onlap above. The 500 m-thick interval of Late Miocene strata between surface Rg (1260 metres below sea floor (mbsf) in the AND-1B core) and surface Rh (760 mbsf) comprises seismic Unit M1. Within Unit M1 a prominent reflector Rg_1 (1100 mbsf) separates a subjacent, c. 160 m-thick interval of diamictite-dominated glacial-interglacial sedimentary cycles deposited from a proximal, predominantly-grounded, cold polar-style ice sheet, from an overlying c. 250 m-thick interval diamictite-mudstone-dominated cycles representing a warmer, wet-based more dynamic ice sheet in the western Ross Sea. The considerable thickness of Unit M1, its association with normal faulting, and correlation with the Rg surface in western VLB implies that this unit is associated with renewed rifting and initiation of the Terror Rift. However the unit may have a polyphase origin as the erosion associated with the Rg_1 unconformity and the overlying dry-based, polar glacial deposits also correspond to a major period of global cooling and inferred Antarctic ice sheet expansion at 13.8 Ma, in marine oxygen isotope records (the Mi-4 glaciation).

2). Rh (dark green) surface is also characterised by truncation of underlying strata and onlap by overlying strata, is also dislocated by normal faulting, and marks the base of a c. 150 m-thick unit of proximal sub-marine volcanic deposits. Within the study area, Rh (~770 mbsf) is correlated with the base of White Island basaltic deposits dated at c. 7 Ma. Unit M2 comprises in its lower interval the proximal volcanic material associated with the submarine apron of White Island volcano, which is overlain at the Rh_1 seismic reflector (600 mbsf), of alternating cycles of ice proximal diamictite and open marine diatomite and terrigenous mudstone. Unit M2 represents continued rift-related subsidence and sedimentation based on its association with syn-depositional normal-faulting and volcanism. The core stratigraphy implies that a wet-based margin of a dynamic Antarctic ice sheet oscillated across the study area during the Late Miocene (13.8-7 Ma).

3). Ri (red) surface is correlated with the "b-clino" surface in western VLB and marks regional subsidence possibly associated with marine transgression. In the study area the surface is correlated with the onset of load-induced sea-floor subsidence associated with the emplacement of Mt. Bird (e.g. 4.6 Ma). It is generally characterised as a downlap surface and mildly truncates underlying strata. The lower c. 80 m of the c. 180 m-thick, overlying seismic Unit M3 is dominated by seismically-homogenous diatomite representing up to 300 ka of open-marine deposition in western Ross Sea. The upper part of Unit M3 corresponds to cycles of diatomite and diamictite interpreted as successive glacial-interglacial advances and retreats of the grounding-line. Noteworthy is the coincidence of a dynamic ice margin and periodically open Ross Sea with global warmth of the Early and middle Pliocene period.

4). Rj (turquoise) surface is scoured and undulating, and is marked by underlying stratal truncation. Overlying Unit M4 (c. 300-150 mbsf) comprises five distinct Milankovitch-scale, glacial-interglacial diatomite-diamictite cycles that can be mapped across the entire study area and are coincident with Late Pliocene cooling and expansion of ice sheets: both on the Northern hemisphere and in the Ross Embayment. The Rj surface has an age c. 3 Ma and is coincident with expansion of grounding-lines elsewhere on the Antarctic margin onto the continental shelf. This surface is also correlated with the beginning of a phase of significant cone building on Ross Island that promoted the local creation of accommodation space and preservation of strata.

5). Rk (pink) surface represents an unconformity dated at c. 2 Ma. It is expressed by pronounced truncation of underlying strata and onlap by strata above. Overlying Unit M5 (c. 145-0 mbsf) is characterised by diamictite dominated cycles and a return to a cold, polar, dry-based ice sheet with conditions similar to today.

Table of Contents

List of Figures:

1. Introduction

Antarctica plays a pivotal role in the global climate system and can be an extremely sensitive climate indicator. An understanding of ice volume variation and physical changes through time in and around Antarctica is essential to understand Antarctica's impact on other elements of the Earth system such as ocean, atmosphere, lithosphere and biosphere. Variations in the Earth's cryosphere can have very strong influences on: (a) global sea-level (b) the Earth's albedo (c) heat transport via the ocean and atmosphere and (d) the global ocean conveyor, by affecting the distribution of ice shelves and sea-ice which form the cold-bottom currents that drive the conveyor. The ocean conveyor, or more appropriately the thermohaline circulation, is the key distributor of heat in the ocean, as well as gases and nutrients.

Ice sheet and ice shelf response to Cenozoic glacial-interglacial climate variability remains poorly understood. The extent of our knowledge and understanding of continental glaciation is related to our ability to access the sedimentary record left behind by previous ice sheets that have occupied the Earth. The present geomorphic and geologic record on land provides an incomplete picture of Antarctic ice sheet history, as sedimentary products are veiled at the surface through burial, overprinting, and poor preservation. As a result, our understanding of Antarctica's climate history has had to rely heavily on inferences from low latitude climate proxy-records, such as deep-sea oxygen isotope records (Fig. 1) (Zachos et al., 2001b). However because these records are indirect and limited, due to erosion and reworking of sediments, they

do not provide physical evidence of past ice volume changes that are necessary to understand Antarctica's role in the global climate system.
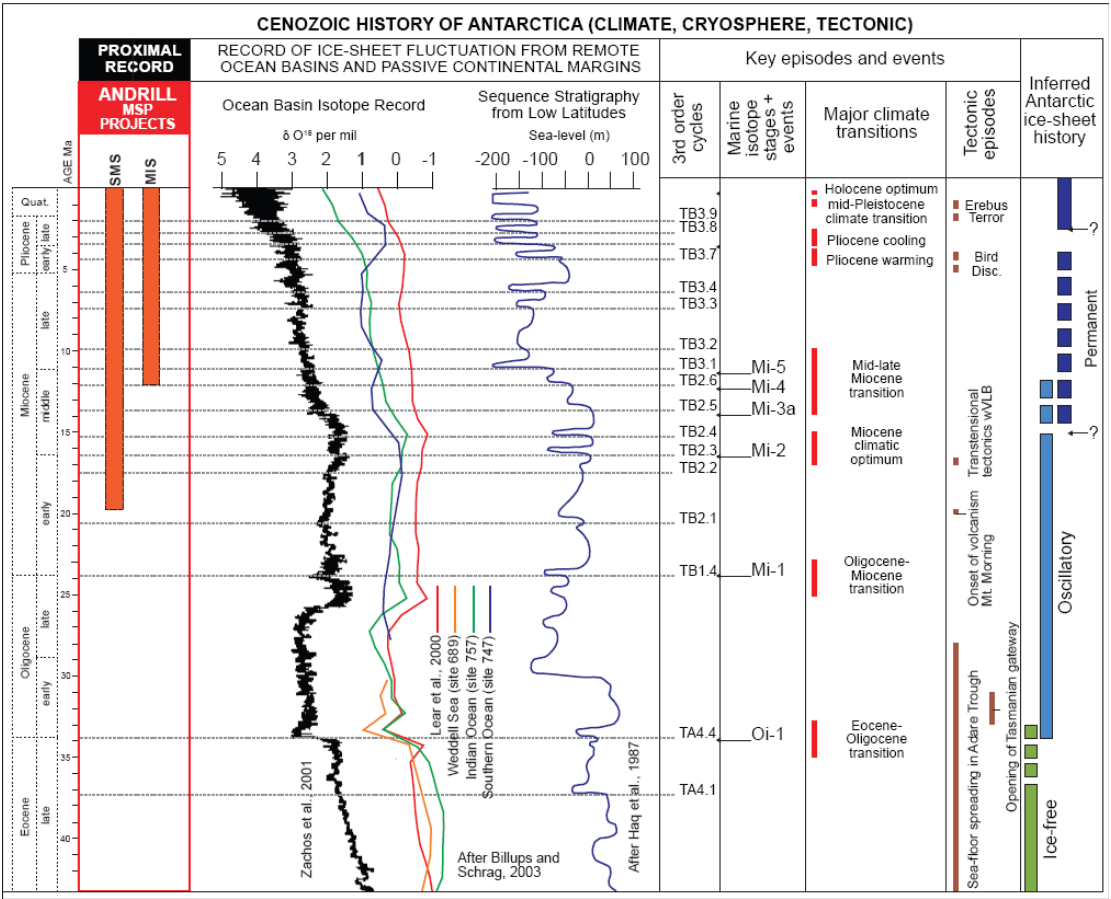
Figure 1. Antarctic Cenozoic history showing target records for the ANDRILL Program. Figure from ANDRILL Scientific Logistics Implementation Plan (Naish et al., 2006).

Increases in the level of CO_2 and other greenhouse gases from human activity are projected to increase mean global temperature, if greenhouse gas emissions are not reduced to 1990 levels (IPCC, 2001). The most recent review of projected temperature increase by the Intergovernmental Panel of Climate Change (IPCC) regards the best estimate range (the midpoint of the lowest emission scenario to the midpoint of the highest) to be between 1.8 to 4.0 degrees Celsius by the end of the century. Warming is expected to be most severe at high northern latitudes (IPCC,

2007). These predictions have brought Antarctica and its role as a sensitive climate indicator into focus and prompted significant co-ordinated studies into climate variability and its consequences.

The ice sheets of Greenland and Antarctica are the main reservoirs capable of affecting sea level; with an equivalent 7 m and 65 m rise, respectively (IPCC, 2007). Even a small change in mass balance of the ice sheets could have significant influence on future sea level, with likely climatic implications. Ice produced by continued snowfall eventually spreads under the influence of gravity towards the coast, where it melts or calves into the ocean to form icebergs. If the glaciers expand onto the seabed they may form marine-based ice-sheets. In coastal regions of Greenland and Antarctica, ice sheets are thinning (IPCC, 2007). Unfortunately, uncertainties regarding the basal conditions of the glaciers and how they interact with the surrounding ocean, limit the accuracy of the estimates for contribution to sea level (Vaughan & Arthern, 2007). In Antarctica this contribution would occur in two-stages, first from the marine-based quasi-stable West Antarctic Ice Sheet (WAIS), followed by the larger East Antarctic Ice Sheet (EAIS).

In order to predict correctly the future behaviour of the Antarctic ice sheets, knowledge of their dynamic variability during the past is required for periods when the Earth's atmospheric composition was similar to that of today. Based on warming scenarios for the Earth developed by the IPCC, a period of global warmth during the Early Pliocene (5-3 Ma) is now regarded as a window into our climate future. Thus more paleoclimatic data must be obtained from the geological record for the Pliocene and earlier in order to better constrain models of ice sheet variability in a warmer

world. An understanding of the tectonic evolution of sedimentary basins allows time-specific stratigraphic packages to be targeted, which may contain continuous geological records of climate history. The influence of tectonism is vital as a mechanism for developing accommodation space and providing a sink into which sediments can be deposited, preserved, and later examined. Understanding the role of tectonism from the stratigraphic record is critical in order to improve our existing interpretation of the climatic signature.

1.1 ANDRILL Overview and Objectives

The ANtarctic DRILLing Program (ANDRILL) is a multinational research initiative with a key aim to recover stratigraphic core records for use in interpreting Antarctica's climatic, glacial and tectonic history over the past 50 million years and at varying scales of age resolution (1 to 100 000 years) (Harwood et al., 2002).

The ANDRILL Program recognizes that efforts to understand the role of Antarctic drivers on global climate variability require a fundamental knowledge of Antarctic cryospheric evolution, not only in recent times, but also for earlier periods when global temperature and atmospheric pCO_2 were similar to levels that might be reached by the end of this century (Naish et al., 2006).

Initial focus of the ANDRILL program is on the McMurdo Sound region, and involves two drill sites; the McMurdo Ice Shelf (MIS) and Southern McMurdo Sound (SMS) projects (Fig. 2). The stratigraphic and tectonic framework here has been extensively studied through previous drilling projects; the Deep Sea Drilling Project (DSDP) (Hayes et al., 1975), Cenozoic Investigations in the Western Ross

Sea (CIROS)-1 (Barrett, 1989; Wilson et al., 1998) and the Cape Roberts Project (CRP)-1, 2/2A, 3 (Cape Roberts Science Team [CRST], 1998, 1999, 2000; Hambrey, et al., 1998; Barrett, et al., 2001). The area is also in a critical setting for sampling three significant components of the Antarctic cryospheric system: East Antarctic Ice Sheet (EAIS), Ross Ice Shelf (RIS)/West Antarctic Ice Sheet (WAIS), and Ross Embayment sea-ice. It is for this reason that McMurdo Sound has been the site of a number of other drilling projects (Fig. 2) over the past 30 years (DVDP-15, CIROS-1, MSSTS-1, CRP) attempting to provide data that can constrain the rate, magnitude and timing of ice-shelf/ice-sheet advance and retreat in the western Ross Sea.

A key objective of the ANDRILL program was to gain a fundamental understanding of RIS behaviour during the past glacial-interglacial climatic extremes, to address concerns over the future stability of the WAIS in a warming world. The Ross Ice Shelf, together with the Ronne Ice Shelf, provides a buttressing effect to the WAIS offering greater stability (Mercer, 1978). If the RIS were to diminish or recede entirely, it may affect the stability and dynamics of the WAIS (Rignot et al, 2004; Rignot, 2006). This would consequently leave the marine-based WAIS even more vulnerable to warming sea surface temperatures and probable ice sheet collapse. Results from the MIS project are contributing to our understanding of the behaviour of the RIS and WAIS as dynamic elements of the global climate system.

The ANDRILL MIS project took place between 29 October and 26 December 2006, with an aim to recover a continuous sediment core through approximately 1,200 m of late Neogene (0-3 Ma) sediment. The project successfully recovered a 1284.87 m-long succession of cyclic glacimarine sediment from beneath the McMurdo Ice Shelf.
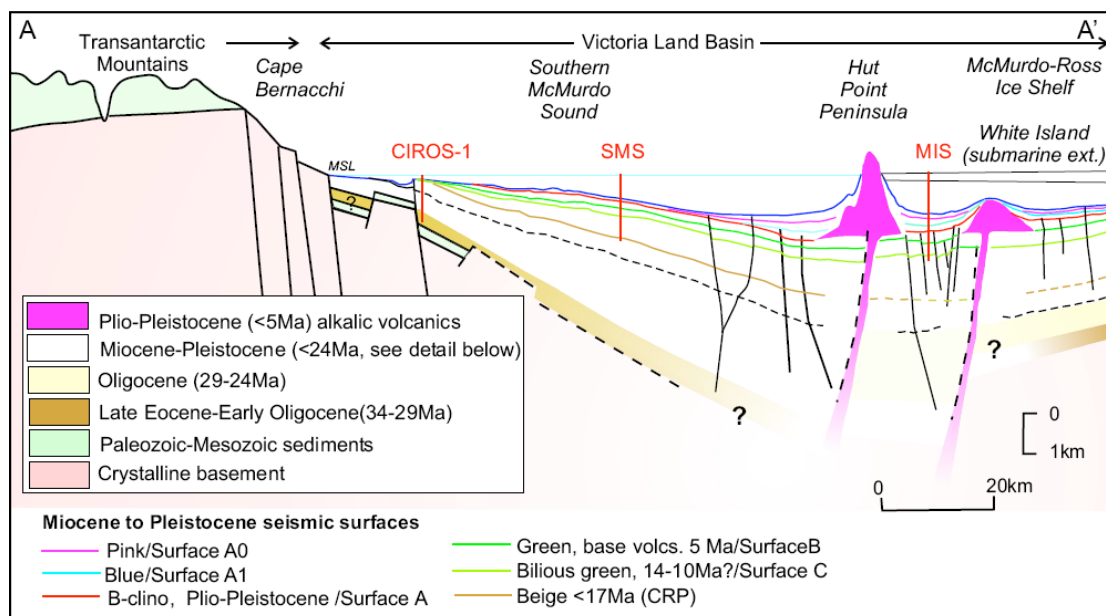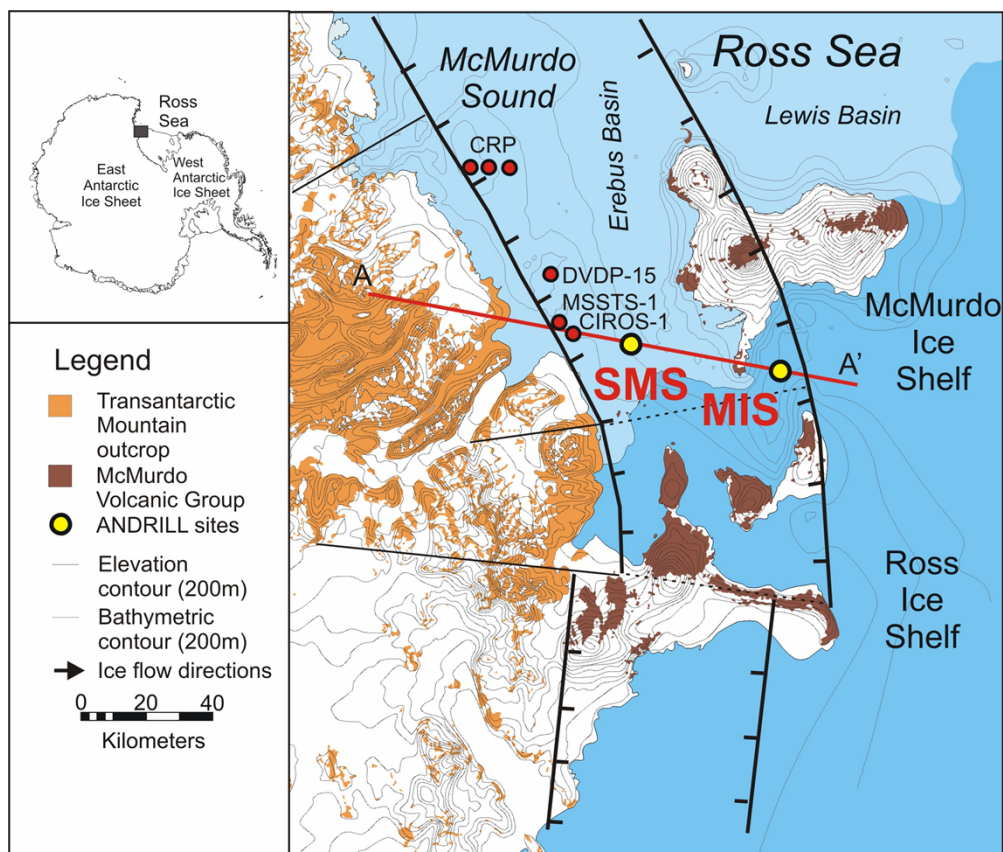
Figure 2. Location map and basin cross-section showing key geographical and tectonic features in southern McMurdo Sound, as well as previous drill sites. Figure from ANDRILL Scientific Logistics Implementation Plan (Naish et al., 2006).

Very few drill records of high resolution have been recovered due to the limitations of seasonal sea ice, and low core recovery from inadequate drilling techniques. The MIS drill core (AND-1B) however, represents the longest and most complete (98% recovery) geological record from the Antarctic continental margin to date. There are two key scientific objectives of the MIS project: (1) to provide an understanding of the behaviour and variability of the Ross Ice Shelf and the West Antarctic Ice Sheet, and their influence on global climate, sea-level and ocean circulation, and (2) to provide an understanding of Neogene tectonism in the West Antarctic Rift System (WARS), including the evolution of the Transantarctic Mountains (TAM) and the Victoria Land Basin (VLB).

1.2 Thesis Outline

This thesis covers seismic reflection acquisition, processing, and interpretation for (1) locating the ANDRILL MIS drill hole (2) establishing the basin-scale stratigraphic architecture and (3) correlation with the drill hole data to facilitate regional interpretation of the Late Cenozoic strata. Therefore the specific aims of this thesis are to:

- Acquire multi-channel seismic reflection data from beneath the McMurdo Ice Shelf.

- Develop techniques used to process and interpret 2D seismic lines and a vertical seismic profile, from an ice shelf setting.

- Map reflectors within and between six 2D seismic lines and provide a detailed correlation to the AND-1B stratigraphic hole, thus allowing a refinement of

the existing regional seismic stratigraphy for the southern Victoria Land Basin.

- Identify the architecture and geometry of the Victoria Land Basin, so as to evaluate the tectonic and climatic evolution of the basin, and its features such as the Terror Rift and the Ross Island volcanic complex.

Chapter 2 describes the regional, tectonic, and climatic setting of the southern Terror Rift. It presents results from previous work in the area in order to highlight what is known, and more importantly what isn't, so that the relevance of this thesis is made clear. Accounts are given on: (1) The timing and extent of the multi-phase extensional rift history of the Ross Sea region of the West Antarctic Rift System (WARS), specifically the evolution of the VLB and the Terror Rift. (2) Implications of this rift history for the evolution of the Ross Island volcanic complex. (3) Identification of possible local and global climate events and processes within the basin. A description of the oceanic regime beneath Windless Bight, where the AND-1B drill hole was located, is also given.

Chapter 3 outlines the acquisition and processing methodology of three multi-channel 2D seismic profiles from the McMurdo Ice Shelf (MIS), over two field seasons. It describes both the 2D seismic data acquisition and processing parameters (2005 data), as well as the vertical seismic profile (VSP) acquisition conducted through the AND-1B drill hole and the processing that was undertaken on the 2006/2007 data. The VSP data was used to provide an accurate correlation of the seismic profiles to the AND-1B drill hole, and is explained in detail in chapter 5.

Chapter 4 presents an analysis of seismic units and surfaces interpreted within the MIS seismic grid. In addition to the previously recognised, regionally mappable reflectors, a number of finer-scale surfaces were identified beneath Windless Bight from the seismic profiles. Local regional extent of these surfaces within the grid offer insight into the nature and processes of ice sheet fluctuations in McMurdo Sound during the Neogene Period.

Chapter 5 describes the process of correlating surface seismic data from ANDRILL MIS site surveys, to the AND-1B core. A description of the core lithostratigraphy is provided, followed by an account of the physical properties data, which were used to derive a synthetic seismogram. This was then compared to the seismic profile at the core location. Travel times with depth into the Earth were extracted from vertical seismic profile (VSP) data to provide an accurate well-tie. Reflections were also matched between surface seismic data and VSP data. All of these components combine to produce a successful tie.

Chapter 6 discusses the integrated chronostratigraphic, seismic-stratigraphic, and lithostratigraphic framework for the southern Terror Rift during the Late Cenozoic. It assesses the role of tectonic and climatic controls on the stratigraphic architecture of the basin, and discusses implications for the evolution of this region of the Western Ross Sea.

Chapter 7 summarises the primary results of the study and outlines future/further research that could be undertaken to further the knowledge and understanding of the processes active in this region of Antarctica.

2: Background

2.1 Climatic Setting

The Antarctic atmosphere-cryosphere-lithosphere system constantly changes, and so continuously influences the global system (e.g. Anderson, 1999). It is now widely accepted that Earth's climate over the last 65 million years has seen drastic shifts in both warming and cooling. The key components driving the climate system throughout this period were: (1) gradual trends driven by tectonic processes (10^5-10^7 years), (2) rhythmic climate cycles driven by variations in the Earth's orbital geometry (10^4-10^6 years), and (3) abrupt and extreme shifts which stand out above "normal" variations (10^3-10^5 years) (Zachos et al., 2001a). A major scientific goal of the ANDRILL program is to document the climatic evolution of Antarctica and the effect it has had on the Earth's climatic-oceanic system through to the present.

A significant factor affecting a region's climate is its latitude. It dictates how influences such as solar radiation affect the climate and ocean. The affect of latitude can be modified by one or more secondary aspects, including position relative to land and water masses, altitude, topography, prevailing winds, and ocean currents (Lamb, 1985; Herman and Goldberg, 1985). Ocean currents can have a very significant effect on climate and in Antarctica, this is clear due to the Antarctic occupying a polar position since the early Cretaceous (~120 Ma ago), but appearing not to have accumulated extensive ice until about 34 million years ago (Barrett, 1999). Following Gondwana break-up, the separation of the southern continents and influence of ocean circulation initiated the inception of the Antarctic Circumpolar Current (ACC).

Antarctica then became progressively isolated both geographically and thermally, which was one of the factors that led to the development of its ice sheets and present-day arid, polar climate (Kennett et al., 1974; Kennett, 1977).

As described by Barrett (1999), Antarctic glacial history can be divided into 4 broad time segments: (i) pre-glacial times 100-34 Ma, (ii) first phase of continental glaciation 34-15 Ma, (iii) persistent ice sheet on the Antarctic continent 15-2 Ma, and (iv) the present Antarctic glacial regime 2-0 Ma. An ice sheet is believed to have covered the entire continent for the present glacial regime, although some parts of it may have expanded and contracted periodically. Our ability to reconstruct a glacial history for Antarctica comes from: (i) information inferred from climate proxy records, namely deep-sea oxygen isotope records, and (ii) proximal evidence from cores along the continental margin. Both however also have their drawbacks.

Foraminiferal $\delta^{18}O$ records from deep-sea marine sediments contain both global (ice volume) and local (temperature, salinity) components and so can be used as a proxy to understand past climate changes. Atmospheric oxygen isotopes exchange with marine oxygen isotopes through global photosynthesis and evaporation/precipitation processes. When ice sheets form on land, the lighter isotope ^{16}O is preferentially incorporated into continental ice sheets. As a result, the heavier ^{18}O isotopes remain in the ocean and, through enrichment or depletion in the ratio of ^{18}O to ^{16}O, indicate when the Earth experienced warm and cold periods. Enrichment in $\delta^{18}O$ reflects glacial periods where a positive shift towards cooler conditions and increased ice volume is visible in the ocean oxygen isotope ratio, whilst enrichment in ^{16}O during interglacial periods causes the ratio to become less positive (i.e. warmer conditions).

The long term $\delta^{18}O$ record exhibits a number of steps and peaks that imply episodes of cooling and warming and ice sheet growth and decay (Fig. 3). It is important to note that proxy evidence is indirect and model dependent. Accurate interpretation of the oceanic $\delta^{18}O$ record is complicated due to the additional influences of ocean temperature/salinity and vital effects on oxygen isotopic fractionation (Shackleton, 2000). Notwithstanding these issues, *estimates* of ice volume variations can still be made. However they cannot determine where these variations took place, e.g. Arctic or Antarctic (Barrett, 1999). Thus these inferences are ambiguous, and often in disagreement.

Onshore, the geological record of glaciation is sparsely distributed and inaccessible due to the long-term existence of the EAIS and WAIS. The ability to date the record is also difficult due to the erosional processes of the ice sheets over time. Offshore, particularly along the continental margin, the sedimentary record is thick, extensive and significantly more accessible. Erosional processes of the ice sheets provide a mechanism for offshore sedimentation. However, if a stable depocentre isn't available for preservation of the record, the effects of erosion, variations in sedimentation rates, and mixing of materials can lead to difficulties in determining accurate ages for sediments recovered from drill cores.

During the Cenozoic era, the most prominent trend in warming is visible from the mid-Paleocene (ca. 60 Ma) to the early Eocene (52 Ma). This trend terminates at the Eocene Climatic Optimum (ECO) between 51-50 Ma. The Early Eocene was ice-free and has been referred to as the "greenhouse world" (Miller et al., 1991), but it is unclear if ice sheets existed following the ECO, between 50 and 33 Ma, when a drift

to cooler temperatures occurred. This period is referred to as the "doubt house world" (Miller et al., 1991). The long-term post-ECO decline is believed to have promoted the expansion of the Antarctic ice sheet during the earliest Oligocene.

The initiation of Antarctic glacial history occurred at the Eocene/Oligocene boundary approximately 34 Ma (Zachos et al., 2001a; Barrett, 1996; DeConto & Pollard, 2003; etc.) where there is evidence of major cooling and the growth of an EAIS. This accumulation of extensive ice is referred to as the Oi-1 glaciation, for which evidence is available from both oxygen isotope information in marine records (e.g. Zachos et al., 1996; Shackleton & Kennett, 1975), as well as from direct evidence provided by glacial sedimentary records in the southern ocean, and along the East Antarctic margin (e.g. Barrett, 1989; Ehrmann & Mackensen, 1992; Zachos et al., 1992; Wilson et al., 1998). Oxygen isotope records reveal a <1.0‰ rise in benthic $\delta^{18}O$ that reflects gradual cooling from an Eocene "greenhouse" world to an Oligocene "ice house world" (Miller et al., 1991). Fossil assemblages containing Antarctic vegetation reported by Francis (1999) also support this transition. Evidence of ice sheets comes from unconformities seen in seismic profiles (Eittreim et al., 1995) as well as glacial-marine sediment recovered from the CIROS-1 drilling project (Barrett, 1989; Wilson et al., 1998), Ocean Drilling Program from Prydz Bay (Hambrey et al., 1991), and Cape Roberts drilling project (Cape Roberts Science Team, 1999, 2000).

A coupled climate/ice-sheet model by DeConto and Pollard (2003) offers an alternative explanation to the Kennett et al. (1974) theory for rapid ice sheet formation in Antarctica, at the Eocene/Oligocene boundary. The model suggests that the commencement of Antarctic glaciation was due to a combination of long term changes in tectonic boundary conditions and the opening of ocean gateways, but

primarily the role of atmospheric CO_2, orbital forcing, and feedbacks from ice-climate interactions.

A considerable decrease in $\delta^{18}O$ values in the Late Oligocene has been widely observed in composite deep-sea records (e.g. Miller et al., 1987; Zachos et al., 2001a) and has been attributed to warming of the deep-sea and an associated decrease in Antarctic ice volume (Zachos et al., 2001a). On the contrary, results from the CIROS-1 and CRP drilling projects show a steady cooling in Antarctica during the Oligocene culminating in a peak cold period by the Early Miocene (e.g. Raine, 1998; Raine and Askin, 2001; Thorn, 2001; Roberts et al., 2003; Prebble et al., 2006). Indications from this proximal evidence are that Antarctica was sufficiently cold to support the existence of ice sheet calving at sea level (e.g. Barrett, 1989; Cape Roberts Science Team, 1998, 1999, 2000; Naish et al., 2001). Ice sheet grounding lines near Prydz Bay (Cooper et al., 1991; Bartek et al., 1997), as well as evidence for repeated sea-level lowering (Kominz and Pekar, 2001) during the late Oligocene further support this observation. Pekar et al. (2006) have put forth an explanation to this contradiction of low $\delta^{18}O$ values in deep-sea records, coeval with proximal Antarctic records suggesting persistent cold temperatures and large-scale ice sheets on East Antarctica. They propose the existence of at least two deep-water masses; one near Antarctica to sustain glaciation, and a warmer second deepwater mass which possibly expanded into the world's ocean basins and created the large temperature gradient among deep-sea sites. Pekar and DeConto (2006) also proposed that, though ice volume may have fluctuated, Antarctica could have been mostly glaciated, by ~50% to 125% of the present-day EAIS, during most of the Early Miocene.
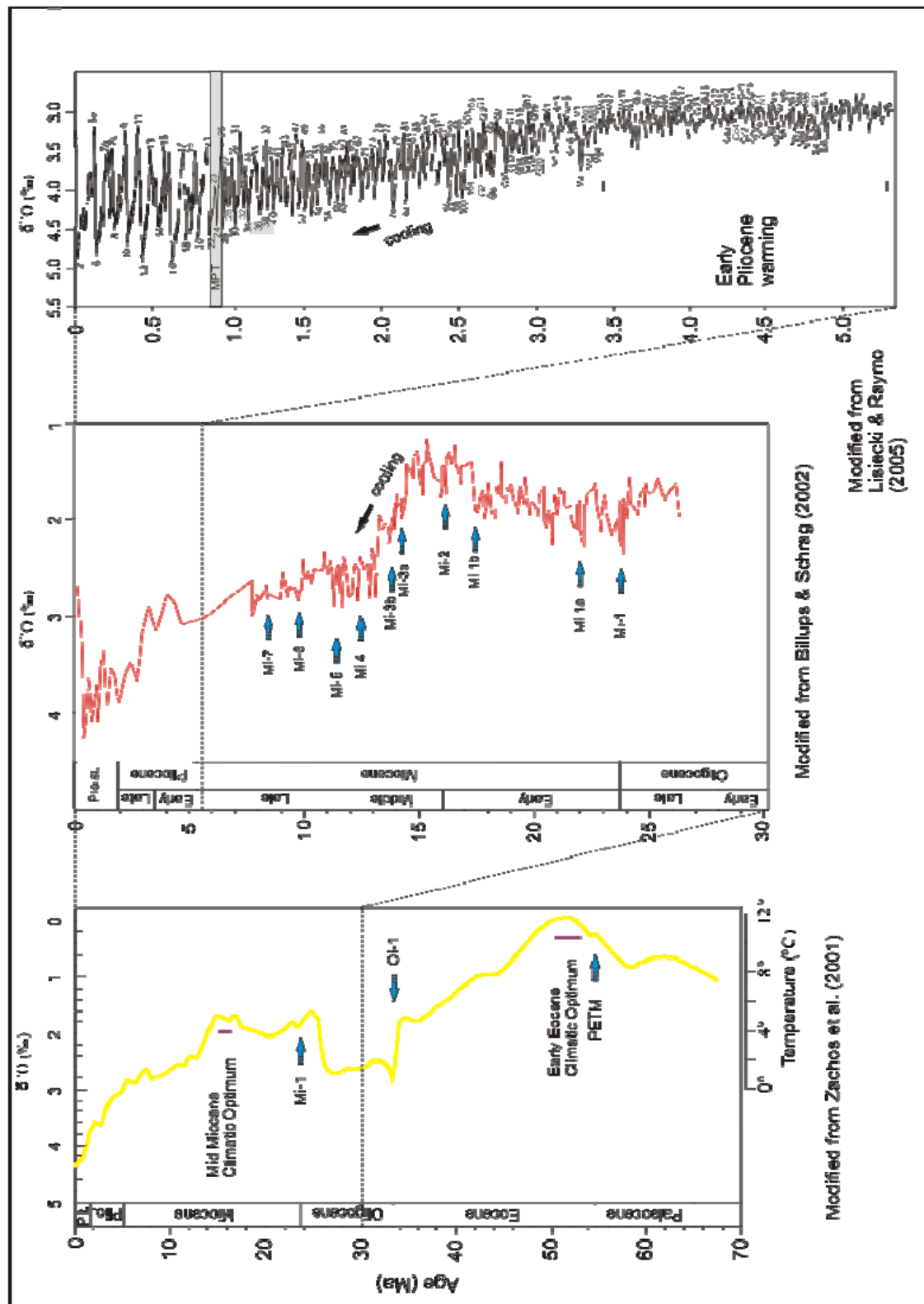
Figure 3. Global deep-sea oxygen isotope records for the Cenozoic.

The only exception to the pattern of low $\delta^{18}O$ values from the late Oligocene to the middle Miocene (~15 Ma), are the Mi glaciations (Wright et al., 1992; Miller et al., 1991) (Fig. 3) of which Mi-1 at the Oligocene-Miocene boundary displayed the most significant cooling (Miller et al., 1991; Zachos et al., 1997). The Mi glaciations relate to waxing and waning of a dynamic Antarctic ice sheet during this period, which is believed to have led into the modern "ice house world" (Miller et al., 1991). The cooling marked by the Mi-1 glaciation has been shown by Naish et al. (2001) and Zachos et al. (2001b) to correspond to sensitivity in the Earth's orbital oscillations.

A major unconformity in the CIROS-1 core, representing a 9 Myr gap, has been detected in regional seismic stratigraphy and extends out into the Ross Sea (Roberts et al., 2003). The presence of this unconformity has also been suggested as reflecting expansion of Antarctic ice during the Mi-1 glaciation. Evidence for warmer conditions between the Mi glaciations is offered through the presence of *Nothofagus* leaves and pollen in the early Miocene part of the CIROS-1 (Mildenhall, 1989). It implies that the present climatic regime in southern Victoria Land was not reached until after the Mi-1 glaciation.

The middle-Late Miocene marks one of the most important events in the global development of the cryosphere during the Cenozoic. At this time, a warm phase occurred which culminated with a climatic optimum between 17-15 Ma. This was followed by a gradual cooling that may have initiated the re-establishment of Antarctic ice sheets between 15 and 10 Ma (Flower and Kennett, 1995). The transition from relatively warm climates during the early Miocene to colder climates

in the late Miocene involved rapid cooling, significant growth of the EAIS, a drop in global sea level, and critical changes in ocean circulation (Flower and Kennett, 1995). The build up of ice from this cooling was accompanied by cooling of the deep ocean by as much as 3°C, inferred from benthic foraminiferal $\delta^{18}O$ values in conjunction with Mg/Ca ratios from benthic foraminifera (Billups and Schrag, 2002). Changes in deepwater circulation have been attributed to variations in the EAIS (Flower and Kennett, 1995). $\delta^{18}O$ values and vertical gradients in $\delta^{13}C$ on benthic foraminifera from Deep Sea Drilling Program (DSDP) sites in the southwest Pacific allowed detailed examination of deepwater circulation from ~17.5 Ma to 12 Ma. The data indicate that circulation strength was at a maximum at this time, and was critical to major EAIS growth (Flower & Kennett, 1995).

Seismic stratigraphic analysis of the Ross Sea continental shelf by Chow and Bart (2003) suggests that there were at least five shelf-wide grounding events of the West Antarctic Ice Sheet (WAIS) during the middle Miocene. These events are consistent with $\delta^{18}O$ enrichments and eustatic lowstands, and illustrate that the WAIS also comprised significant ice volume during the middle Miocene, at least in the Ross Sea area.

A dynamic Antarctic ice sheet may have existed during the Late Miocene. Grützner et al. (2005) use iron mass-accumulation rates as a proxy for sediment accumulation rates. Based on changes in these rates, as well as episodic patterns in ice-rafted debris which indicate deglaciations, they propose a dynamic and likely wet-based Late Miocene EAIS. This dynamic behaviour for the EAIS implies that a significant

proportion of the variability seen in oxygen isotope records of the late Miocene reflects Antarctic ice-volume changes (Grützner et al., 2005).

The Early Pliocene (5-3 Ma) is widely regarded as a period of global warmth (e.g. Dowsett et al., 1994; Crowley, 1996; Ravelo and Andreasen, 2000; Whitehead et al., 2001). The foraminiferal $\delta^{18}O$ record supports this and exhibits a warming trend from the start of the Pliocene, which terminates in the mid-Pliocene Climatic Optimum (MPCO) ~3 Ma (Raymo et al., 2006). Proximal evidence from Antarctica for a warm early Pliocene is also available from diatoms in sediments within the Sørsdal Formation, Prydz Bay (Harwood et al., 2000; Whitehead et al., 2001). Comparisons between modern day diatoms in the region and those in the Sørsdal Formation indicate early Pliocene sea surface temperature (SST) of between 1.6°C and 3°C warmer than today (Whitehead et al., 2001). Further proximal evidence for warming is available from a study by Webb et al. (1984) examining sediments from the Transantarctic Mountains, displaying Pliocene aged marine microfossils that provide evidence for an ice-volume decrease. Despite such evidence for a period of global warmth in the Early Pliocene, data also exists to suggest that the Antarctic cryosphere remained stable during this warming, making this a highly debated topic.

Kennett and Hodell (1993) outlined evidence for stability which included: significant ice rafted debris (IRD) throughout the Pliocene indicating presence of ice sheets and, a lack of biocalcareous sediments with a dominance of biosiliceous sediments, which suggest conditions similar to present. They also proposed, based on oxygen isotopic values from Ocean Drilling Program (ODP) sites, that the marine transgression in the early Pliocene was marked by sea levels no higher than 25 m above present.

Sea surface temperature estimates inferred from the observed low oxygen isotopic values constrain the degree of warming for Antarctic surface waters to a maximum of 3°C (Hodell and Venz, 1992; Kennett and Hodell, 1993; Shackleton et al., 1995). This is believed to be too small to cause major deglaciation and therefore so supports the theory of relative EAIS stability. A warm Earth climate during the Early Pliocene that supports a relatively stable Antarctic cryosphere is of particular relevance to our climate future and requires further examination.

Analyses of marine and terrestrial records from the Early Pliocene have also been used as a basis for constraining palaeoclimate modelling. These simulations incorporate atmospheric general circulation models (GCM) to reconstruct parameters such as sea level, vegetation, land-ice distribution, sea-ice distribution, and sea surface temperature (SST). Results indicate that during the Early Pliocene: sea level was ~20-40 m higher (Dowsett and Cronin, 1990; Dowsett et al., 1994), SSTs were very similar to modern temperatures in tropical regions but were ~1.4 - 5°C warmer at higher latitudes (Chandler et al., 1994; Haywood et al., 2000), sea ice was reduced (Dowsett et al., 1994), wind-driven gyral circulation was enhanced, and variations in orbital parameters had an influence on seasonality (Haywood et al., 2002).

It is clear that the nature and magnitude of climatic variability witnessed during the Early Pliocene is not fully understood. Possible mechanisms to explain the warming include enhanced thermohaline circulation, and greater concentrations of atmospheric CO_2 (Haywood et al., 2000). The Early Pliocene represents the last sustained interval where a climate warmer than today's existed and spans the transition into the cooler climate of the Pleistocene. Stratigraphy from DSDP-ODP drilling, and correlation

with seismic stratigraphic information has been used by Rebesco et al. (2006) to discern changes to the Antarctic continental margin during the late Pliocene. The changes they observed agree with the global cooling trend from foraminiferal records leading into the Pleistocene and the onset of Northern Hemisphere glaciations between 2.8 and 2.5 Ma (Shackleton et al., 1984; Maslin et al., 1998).

Antarctica encountered a major event during the Neogene – a change from warm-based glaciations to cold-based glaciations. However debate continues as to when the warm, dynamic ice sheet was replaced by a cold, stable ice sheet. One view, the stabilist view, suggests that the switch occurred during the middle-late Miocene at 13.8 Ma, while the dynamicist view claims the warm inter-glacial regime lasted until the Late Pliocene. Valid arguments are presented for both scenarios; however there are inconsistencies (see Miller and Mabin, 1998 for review; Wilson, 1995; Sugden et al., 1993). The contention lies in analysis of glacial sediments in the Transantarctic Mountains known as the Sirius Group. The dynamicist view argues that the presence of reworked marine diatoms, of Pliocene age in the tills, provides evidence for a major deglaciation in Antarctica at this time (Webb and Harwood, 1991; Barrett et al., 1992).

The stabilist view argues that the EAIS remained relatively constant, experiencing only minor ice volume fluctuations including during the period of Pliocene warmth (Shackleton and Kennett, 1975; Kennett, 1977; Clapperton and Sugden, 1990; Rebesco et al., 2006). Due to convincing evidence for recycling of marine diatoms by wind (Burckle and Potter, 1996; Kellogg and Kellogg, 1996; Stroeven et al., 1996), the concept of large scale fluctuations and reworking by the EAIS is further in question. The fact that the Sirius Group deposits are of varying ages does not help the

controversy. Passchier (2001) used mineralogy to suggest that the reason for discrepancies in age is that the Sirius Group was deposited over a long time frame and was influenced by tectonic processes in the Transantarctic Mountains.

Suffice to say, a definitive resolution to this debate has not yet been found. The extreme stabilist view (e.g. Sugden et al., 1993) claims a cold polar ice sheet since 14 Ma: The extreme dynamicist view (e.g. Webb and Harwood, 1991) claims a large mid-Pliocene deglaciation of the EAIS based on diatom data. A consensus view is perhaps for a relatively stable ice sheet since 14 Ma exhibiting minor fluctuations, but with a dynamic Greenland and WAIS combining with a dynamic EAIS margin, to produce the sea level change of ~20 m evident during the Early Pliocene (Naish et al., 2007b).

The Earth's orbital geometry is one of the major factors driving the climate system. It is controlled by eccentricity, obliquity and precession, all of which are regarded as Milankovitch parameters. Because the changes to the Earth's orbital position relative to the sun are so periodic, these parameters provide a predictable model of long term climate variability. Differences in Milankovitch parameters have a considerable affect on proxy climate records from deep-sea sediments, as they control the distribution and amount of incident solar energy on the Earth (insolation). Eccentricity takes place over 400 kyr and 100 kyr year cycles and impacts on the seasonal solar energy budget, though also alters the amplitude of precession, which occurs over 19 kyr and 23 kyr year cycles. Obliquity affects the latitudinal distribution of insolation and takes place over 41 kyr cycles (Zachos et al., 2001a).

The cooling trend from Late Pliocene to present contains two periods of unexpected climate variation; the onset of Northern Hemisphere glaciation between 2.8 and 2.5 Ma (Shackleton et al., 1984; Maslin et al., 1998), and the mid-Pleistocene transition (MPT). Northern Hemisphere glaciation began in the Late Miocene with the accumulation of ice on Southern Greenland, but the Northern Hemisphere did not become fully glaciated until 3.0-2.5 Ma (Maslin et al., 1998) when much of northern Europe, Asia, North America and Northern Greenland were periodically ice-covered. A possible explanation for the beginning of this glaciation was offered by Maslin et al. (1998). They proposed that tectonic changes, such as uplift of the Himalayan and Tibetan Plateau, and opening of the Panama Seaway, brought the Earth to a critical threshold where orbital parameters subsequently drove glaciation.

The mid-Pleistocene transition describes a period in Earth history where a shift occurred from 41 kyr obliquity cycles, to 100 kyr eccentricity cycles. This variation in orbital parameters can be seen from a 1.0-1.5‰ change in benthic $\delta^{18}O$ records between Marine Isotope Stages (MIS) 25-22 (Mudelsee and Schulz, 1997), which had a profound effect in the response of the Earth's climate system. Prior to the MPT, the growth and decay of polar ice sheets can be resolved as responding to 41 kyr obliquity cycles (Raymo et al., 1989; Zachos et al., 2001a). From the MPT to the present, however, a clear influence by the 100 kyr eccentricity cycles is evident much like the earlier Cenozoic periods of increased sensitivity to eccentricity which correspond closely to periods of extensive ice sheet development at the poles (Pälike et al., 2006; Holbourn et al., 2005; Zachos et al., 2001a; Naish et al., 2001; Mudelsee and Schulz, 1997). Positive feedback effects are needed to explain the large climatic responses to relatively weak eccentricity forcing (e.g. Imbrie et al., 1993).

These effects may have included the ocean-atmosphere circulation (Broecker and Denton, 1989), the carbon cycle (Shackleton, 2000; Medina-Elizalde and Lea, 2005), internal dynamics of ice sheets (Clark and Pollard, 1998), and obliquity pacing during the Late Pleistocene, when only every second or third obliquity cycle produced a glacial termination (Huybers and Wunsch, 2005). A large work effort continues in order to understand the previous climate responses to orbital forcing in Antarctica during the Plio-Pleistocene (Paillard and Parrenin, 2004; Huybers and Wunsch, 2005; Huybers, 2006, 2007; Raymo, 2006; Lisiecki and Raymo, 2007).

Shifts in climatic conditions can influence the advance and retreat of glaciers in Antarctica. In addition to this, variations in climate play a pivotal role in the production, transport and accumulation of sediments. This is particularly prevalent along the continental margin where the lasting effects of glacier variability are well preserved. Examination of seismic stratigraphy within the southern Terror Rift, together with core data from AND-1B, provides evidence for climatic variability. Core chronology constrains the timing of these events and can link them to the proximal stratigraphic record from Antarctica. Antarctica's climate history during the Neogene is poorly constrained however, the refinement to the existing stratigraphic framework, which this study aims to produce, will help our understanding of the climate evolution, at least for the VLB.

2.2 Geological and Tectonic Setting

Antarctica consists of two major regions: East Antarctica, a stable, Precambrian, Palaeozoic craton, and West Antarctica, a mountainous archipelago consisting of several smaller microplates that have moved relative to each other and to East Antarctica (Dalziel & Elliott, 1982; Cande & Stock, 2000). Running across the interior of the continent are the Transantarctic Mountains (TAM). At ~3000 km long, and with elevations up to 4500 m, they have a commanding presence on the Antarctic landscape. The TAM formed as an uplifted rift-flank in an extensional environment, during the Cenozoic (Fitzgerald et al., 1986; Stern & Ten Brink, 1989) and were strongly influenced by the interplay between tectonic and climatic changes during this time. In the past, the EAIS has grown to an extent larger than the TAM, significantly modifying the mountain front landscape (Huerta, 2006). Today the TAM serve as a barrier between East and West Antarctica and as a drainage passage for the EAIS.

Tectonic processes within Antarctica are complex. This is evinced no more aptly than by the active West Antarctic Rift System (WARS), a low-lying region which separates the East and West Antarctic domains (Behrendt, 1999; Huerta & Harry, 2007). The WARS represents one of the largest areas of crustal extension in the world (Rocchi et al., 2002). It is an asymmetrical rift-system bounded on its western side by the Transantarctic Mountains and on its eastern side by Marie Byrd Land (Behrendt, 1999). The WARS extends from the continental shelf of the Ross Sea, beneath the Ross Ice Shelf and the West Antarctic Ice Sheet (WAIS) (Fig. 4). The WARS is characterized by sparse exposures of alkaline volcanic rocks extending from northern Victoria Land throughout Marie Byrd Land. An alkaline pluton in northern Victoria

Land has been reported as having an age of 48 Ma (Tonarini et al., 1997). However, it is considered anomalous and most exposures range in age from 15 Ma to the present.
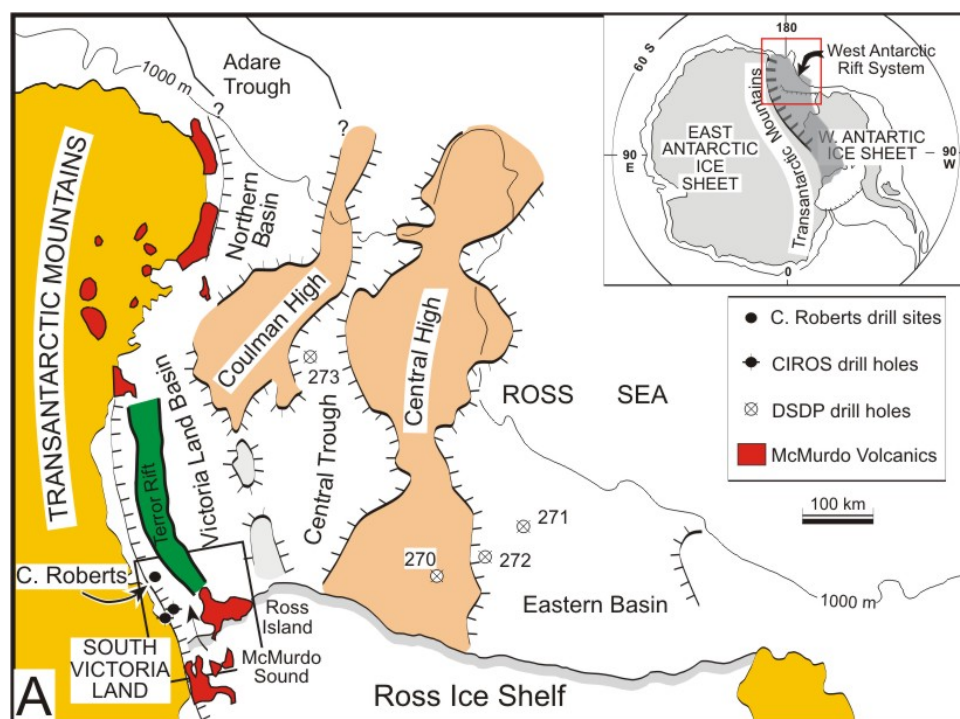
Figure 4. Map of Ross Sea region of WARS delineating major basins and geology of adjacent East Antarctica and Transantarctic Mountains (TAM). Inset shows Antarctic location map and West Antarctic Rift System. Figure from Henrys et al. (2007).

Aeromagnetic surveys indicate the presence of a large volume ($> 10^6$ km^3) of these volcanic rocks, which were likely to have been removed through glacial processes (Behrendt, 1999; Behrendt and Cooper, 1991). Volcanism within the WARS has previously been attributed to a mantle plume source (Behrendt et al., 1991). However, new evidence suggests that decompression melting of the mantle, related to transtension during Cretaceous amagmatic extensional rifting, (Rocchi et al., 2002, 2003, 2005), is the more likely explanation (Cooper et al., 2007).

This is enigmatic however, as most of the dated volcanics within the WARS are Late Cenozoic in age (e.g. LeMasurier and Thomson, 1990; Marchant et al., 1993, 1996; Behrendt, 1999). Following the progressive fragmentation of Gondwana, completed by ~85 Ma, intraplate rifting and volcanism within the WARS continued in Cenozoic

time (Cooper and Davey, 1985; Behrendt et al., 1991; Davey and Brancolini, 1995), leaving the Antarctic continent presently surrounded by oceanic spreading centers. Strata within the rift system have inadequate chronological constraints and this limits an understanding of rifting patterns. Nevertheless, tectonic investigations combining geophysical, geochemical, and core data have extended our understanding of the timing and nature of processes that shaped the WARS. The total amount of extension is difficult to determine, but estimates suggest several hundred kilometers of relative motion (e.g. Behrendt et al., 1991; Behrendt, 1999; Fitzgerald. 2002).

This amount of extension in the WARS is believed to have occurred essentially in two phases: (1) an early stage of broad extension during the Late Cretaceous, and (2) a later stage of more focused extension in the Ross Sea and Victoria Land Basin (VLB) during the Paleogene (Cooper and Davey, 1985; Behrendt et al., 1991; Davey and Brancolini, 1995; Wilson, 1995b; Cande et al., 2000, Hamilton et al., 2001; Karner et al., 2005). This proposed extensional history for the WARS is unusual compared to other continental rifts, such as the East African Rift, Rhine Graben, or Rio Grande Rift (Huerta and Harry, 2007). Initial regional deformation in a rift system occurs over relatively short periods, followed by progressive focused extension with time (Ruppel, 1995). The WARS, however, experienced broadly distributed extension for a prolonged period, before the transition to more focused extension (Huerta and Harry, 2007). Also unusual is the size of the area affected by extension (750 to 1000 km wide), which is much larger than in other rift systems such as the East African Rift or Baikal Rift where areas narrower than 150 km are affected (Huerta and Harry, 2007).

The WARS includes the Ross Sea region, a 1200-km-wide embayment where N–S striking sedimentary basins (Eastern Basin, Central Trough, and Victoria Land Basin) and basement highs (Coulman High and Central High) (Fig. 4) provide a record of extension and crustal thinning during the early Late Cretaceous and Paleogene Periods (Huerta & Harry, 2007). The crustal structure here has been explored through geophysical data collected from both marine and airborne surveys (Behrendt, 1999; Trey et al., 1999; Hamilton et al., 2001; Luyendyk et al., 2001; Studinger et al., 2002; Davey et al., 2006). These data indicate varying crustal thickness across the southern Ross Sea, with the thinnest crust located beneath the sedimentary basins and the thickest crust under the adjacent basement highs.

Lawrence et al. (2006) used seismic receiver functions, surface wave phase velocities, and airborne gravity measurements to investigate the structure of the TAM and adjacent regions of the Ross Sea and East Antarctica. Their results indicated a crustal thickness increase from 20 ± 2 km in the Ross Sea to a maximum of 40 ± 2 km beneath the crest of the TAM, at a distance of 110 ± 10 km inland. Differences in crustal thickness suggested that between 200 km and 500 km of extension is accommodated in the Ross Sea sector of the WARS, initiating during the late Mesozoic (Trey et al., 1999; Fitzgerald et al., 1986).

In general, sedimentary basins are characterized by negative free-air and Bouguer gravity anomalies. However, the extensional basins of the Ross Sea are paradoxical in that positive gravity anomalies overlay the Northern Basin, Central Trough, Northern Central Trough, and northern extent of the VLB, while basement highs are associated with negative gravity anomalies (Karner et al., 2005).

Basement densities from DSDP cores indicate a normal density relationship between basement and sediment infill therefore another explanation is needed. Karner et al. (2005) demonstrated that this inconsistency to standard gravity observations within sedimentary basins is the consequence of a relatively low flexural strength of the lithosphere during rifting which is contrasted by higher flexural strengths later during sedimentation. Gravity values slowly become more positive over time as the difference between the rigidity of rifted lithosphere and the lithosphere undergoing sedimentation increases. It is for this reason that the southern extent of the VLB contains a negative gravity anomaly, as it is the zone of most recent extension and thus thinner crust. The timing of sedimentation following episodes of rifting appears to have a considerable effect on the presence of these abnormal gravity relations, and have also been observed elsewhere such as the western platform of New Zealand (Liu et al., 1982; Holt and Stern, 1991).

By ~65 Ma the majority of the extending WARS regions had become more rigid and extension was focused near the East Antarctic/West Antarctic boundary (Huerta & Harry, 2007), which allowed the formation of the VLB. The VLB is 140 km-wide and is broadly extended in a north-northwest direction. This is defined by major bounding faults and horsts. The western side of the basin has an east-northeast depositional dip direction, and an opposite sense towards the eastern side (Fielding et al., 2006).

Within the VLB is a sedimentary succession 12-14 km thick that was previously believed to be Cretaceous-Paleogene in age (Cooper & Davey, 1985; Fitzgerald et al., 1986; Trey et al., 1999, Davey et al., 2006). However, cores recovered from the CIROS-1 and CRP projects on the western margin of the VLB, have established that the sedimentary succession ranges in age from Latest Eocene (ca. 34 Ma) to late Early

Miocene (ca. 17 Ma) on its western margin. Latest Eocene sediments overlie Mesozoic Beacon Supergroup metasediments and fine upwards. This is interpreted to record the initial rifting of the VLB at 34 Ma and its subsequent subsidence (Davey et al., 2006). At Cape Roberts, the late Early Miocene sediments are unconformably overlain by a thin Plio-Pleistocene section.

A number of subsurface seismic reflectors were detected in the Cape Roberts area. These surfaces have been resolved in the CRP sedimentary section, and have been traced using marine seismic data from McMurdo Sound, into the VLB where a more complete sedimentary section is available (Fielding et al., 2006). The reflectors define boundaries between seismic stratigraphic units and have been used to develop a new model for the evolution of the VLB describing five phases of rift history (Wilson et al., unpublished). Phase 1 (pre-latest Eocene) involved a substantial degree of erosion and regional uplift of the TAM. CRP cores reveal that at the floor of the VLB, earliest Oligocene strata directly overlie Devonian sandstones, and that the boundary between the TAM and the VLB, known as the TAM Front, is a large-offset normal fault system (Wilson et al., unpublished). In order for this to have occurred, ~2000m of post-Devonian Beacon Supergroup and Jurassic dolerite intrusions and basaltic lavas were eroded away. Apatite fission track data from the TAM are interpreted to indicate uplift and denudation beginning at ~55-50 Ma (Fitzgerald, 1992), and it is probable that the erosion recorded in the CRP core began at this time.

Phase 2 (latest Eocene to Early Oligocene) was an early rift phase when deposition occurred in distributed grabens commencing around ~34 Ma. This rift phase lasted 5 Myr until ~29 Ma (Wilson et al., unpublished). Phase 3 (Early Oligocene to Early

Miocene) consisted of a reorganization of the VLB rift during which sediment accumulation was no longer confined to grabens in the west, but rather formed an eastward-thickening wedge into the centre of the basin. This was the main rift phase. During Phase 4 (Early Miocene) broad thermal subsidence occurred over the entire basin. Sedimentation was substantial during this phase and widened the VLB. Phase 5 (post-Early Miocene) is associated with extensional fault reactivation in the western Ross Sea which resulted in the formation of the narrow linear basin, the Terror Rift, in the central VLB.

The Terror Rift is a 70 km wide axial rift zone (Cooper et al., 1987) which extends from Cape Washington at its northern extent, to beneath Ross Island ~4 km south south-east (Fig. 5). It is a zone of intraplate deformation within the Antarctic plate. Regional seismic lines, including the USGS 403/404 line (Cooper et al., 1987), demonstrate stratal thickening from both west and east towards a central depocentre, where deformation is most prevalent and thus attenuates reflector amplitudes.

The Terror Rift comprises the down-faulted Discovery graben, and the adjacent Lee arch. The graben and arch deform some 50-70 km of the VLB, with intensity of deformation increasing southward along the rift (Cooper et al. 1987). Data from marine seismic surveys taken across the western Ross Sea reveal details of neotectonic rift geometry (Henrys et al., 2006b). The presence of fault scarps on the seafloor, and young volcanism (Esser et al., 2004) at both the northern and southern extents of the Terror Rift indicate recent activity and suggest that it has experienced the most recent extension in the VLB. This superimposed transtensional faulting is thought to have formed the Terror Rift (Wilson et al., unpublished). Syn-extensional

weakening caused by mantle necking (where the ductile mantle deforms under tension forming a thin *neck*) has also been suggested as the catalyst to narrow-rift extension in the central VLB and thus the formation of the Terror Rift ~26 Ma (Huerta and Harry, 2007).
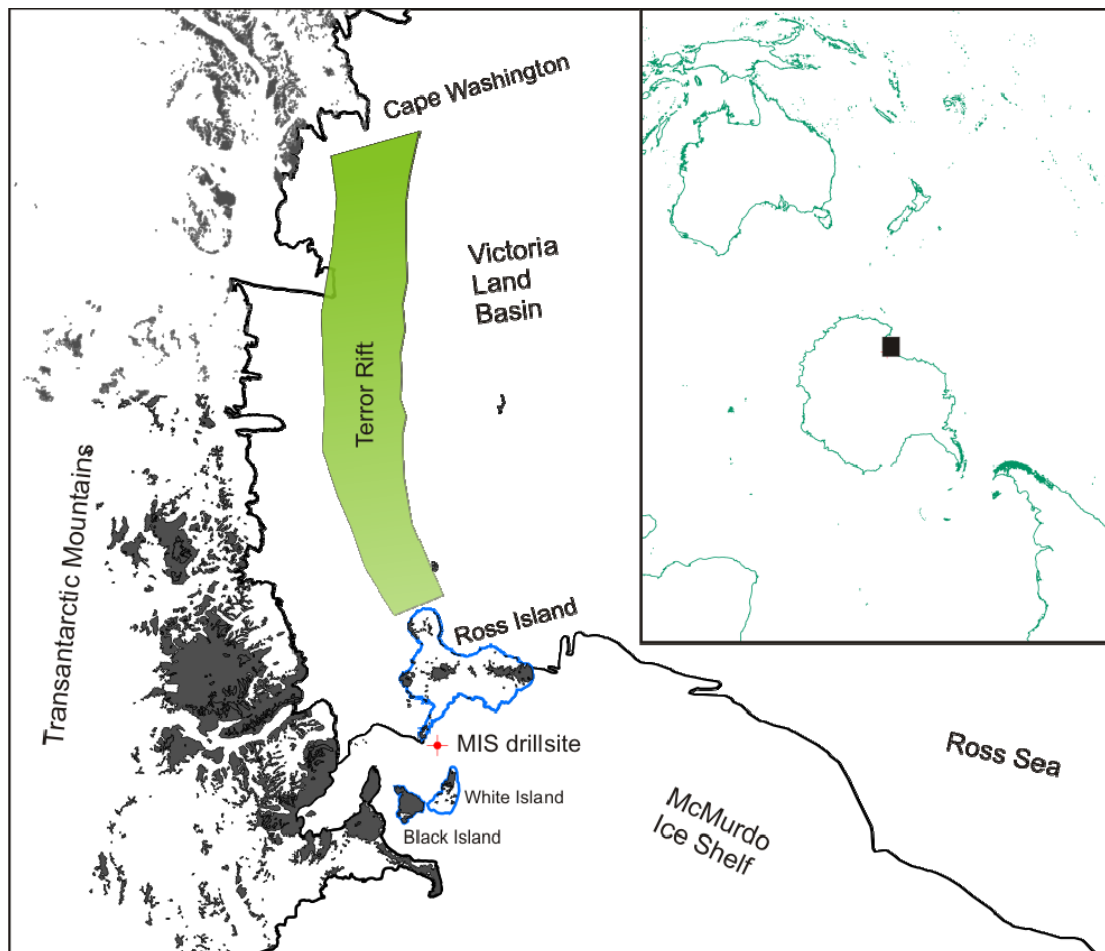
Figure 5. Location map outlining Terror Rift, which extends beneath Ross Island and MIS drill site.

The Neogene tectonic history of the VLB, Terror Rift, and thus the western margin of the WARS, is not fully understood. The ANDRILL MIS project offers a step forward as it samples the southern edge of the Terror Rift; the youngest episode of rifting in the WARS. This is significant because it can provide constraints on extension in the VLB, which is linked to extension in the Northern Basin, and is associated with

seafloor spreading at the Adare spreading axis (Davey et al., 2006). This is of particular importance because spreading in the Adare Trough has been used to constrain motion between East and West Antarctica (Cande et al., 2000). Uncertainties in this motion make it one of the least constrained components of the global plate circuit (Steinberger et al., 2004).

A regional seismic unconformity detected across the VLB, Eastern Basin and Central Trough, was used to date the onset of the Terror Rift episode of rifting. Previous works (Busetti, 1994; Salvini et al., 1997; Brancolini et al., 1995a) suggested that the age of this unconformity is older than 26 Ma, with a tentative age of 30 Ma. Results from CRP-1 and CRP-2/2A, however, reveal that within the VLB this unconformity is significantly younger (< 17 Ma). The miscorrelation of this event across basement highs between Eastern Basin and the Northern and Victoria Land Basins, can be attributed to the difficulties presented by extensive erosion of sedimentary sections, as well as the influence of extensive tectonism present around the perimeter of the VLB (Brancolini et al., 1995a, 1995b; Salvini et al., 1997). Results from the ANDRILL MIS project and this study further constrains the age of this unconformity.

In contrast to the larger Ross Sea basins, the narrow width of the relatively young Terror Rift associates it with negative free air and Bouguer gravity anomalies (Karner et al., 2005). Cooper et al. (1987) proposed a "magmatically intruded Lee Arch" along the eastern margin of the Terror Rift. Seismic lines from the Drygalski Ice Tongue, in the north, to south of Ross Island show that the 'arch' is a structural feature not associated with magmatic intrusion or doming (Henrys et al., in press; Fielding et al., 2006; Wilson et al., unpublished data; Hall et al., 2007).

The structural geometry of the arch is obscured by extensive intrusion of Late Cenozoic volcanic rocks both north and south of Ross Island. Moving southward down the rift, the arch forms an eastern uplifted margin of a half graben that has accommodated approximately 3.5 km of Neogene sediment beneath Windless Bight (Henrys et al., in press).

Progressive loading of the lithosphere occurs at the southern end of the Terror Rift due to the Ross Island volcanic complex, which is comprised of the basinite shield volcanoes Mt. Bird (4.6-3.8 Ma) and Mt. Terror (1.7-1.3 Ma), and the composite phonolitic volcano Mt. Erebus (1.0-0.0 Ma) (Moore and Kyle, 1990; Wright and Kyle, 1990a, 1990b). Volcanic activity in the Erebus Volcanic Province initiated at ~18-14 Ma, south west of Ross Island (Kyle, 1990a, 1990b; Rocchi et al., 2002). Around ~4 Ma, activity became more widespread and extended north eastwards towards Ross Island and into the Ross Sea (Kyle, 1990a, 1990b). This loading of Ross Island has depressed the crust by up to 1800 m centred on Mt. Erebus, forming a sub-circular flexural moat around the periphery of the south-eastern side of the island (Horgan et al., 2005). Subsidence such as this increases the preservation potential of ice-proximal records produced during glacial/interglacial cycles by protecting them from erosive events. Coupled with a high sediment supply rate from the TAM, this moat accommodates a well-stratified, regionally extensive sedimentary succession of at least 1.2 km below the seafloor in the deepest part of the depression between ca. 4.6 and 1.3 Ma (Horgan et al., 2005).

The sedimentary record under the deepest part of the depression contains sediments that record the advance and retreat history of the RIS-WAIS as well as phases of volcanism through time (Naish et al., 2007b).

Hence, the AND-1B drill hole was ideally situated within the depocentral and bathymetric axis of the moat region (Fig. 5) for recording and dating ice sheet oscillations, associated oceanic and climatic variations, and major tectonic episodes (Harwood et al., 2002).

The evolution of Antarctica has been heavily influenced by the interaction between climate and tectonism. Crustal spreading followed by initiation of the ACC, together with changes in atmospheric CO_2 and orbital forcing, effectively instigated Antarctic glaciation (Kennett et al., 1974; Barrett, 1989, 1999; Ehrmann & Mackensen, 1992; DeConto & Pollard, 2003 etc.). Rifting between East and West Antarctica, within the WARS, not only initiated the formation of the TAM, but also the Ross Sea and its associated basins and highs. These basins provide a sink for sediments being eroded off the TAM through glaciation. Rifting at a later stage, also promoted volcanism and the emplacement of the Ross Island volcanic complex. This provides a pinning point for the Ross Ice Shelf, and helped create further accommodation space for sediments delivered by outlet glaciers in the TAM, and ice streams from the WAIS (Harwood et al., 2002; Naish et al., 2007c). This sedimentary record has been preserved and can now be accessed to help unravel the history of Antarctica.

2.3 Local Setting

AND-1B was located in the Windless Bight region of the MIS, adjacent to Ross Island. The present-day MIS forms the northwest part of the RIS, where it has been pinned by Ross Island for the last ~10 ka (McKay et al., 2008).

The MIS is nourished by ice sourced from both the WAIS, and the EAIS via several large outlet glaciers which flow through the southern TAM. Ocean current directions and ice flow directions strongly influence the sediment input to the MIS and in particular to Windless Bight. Current velocity, as measured using an Acoustic Doppler Current Profiler (ADCP), is affected by diurnal tidal cycles, with higher current speeds occurring on flood tides. During data collection in January 2006 (Carter et al., 2007) as part of the final phase of ANDRILL MIS site surveying, ice conditions caused flood tides to flow in an anti-clockwise direction around Hut Point Peninsula and into Windless Bight, whilst ebb tides flowed in the opposite direction at slower speeds. The resulting net flow was from McMurdo Sound into Windless Bight. This observation is consistent with the seafloor sediment composition which contains many diatom fragments, presumably advected under the ice shelf from the open water and seasonal sea ice cover in McMurdo Sound (Barrett et al., 2005).

3: Data Acquisition and Seismic Processing

Seismic reflection surveys measure the travel times of reflected arrivals from subsurface interfaces, between media of differing acoustic impedance. Differences in travel times are dependent on elastic physical properties and so provide detail of geological structures. Multi-channel reflection surveys, such as those carried out in this study, aim to record reflected pulses at many offset distances, from individual shot points. Seven reflection profiles were conducted on the McMurdo Ice Shelf (MIS) as part of ongoing site surveying for the ANDRILL MIS drill site location, three of which were towards this thesis.

Processing of the acquired data aimed to suppress intra-ice and intra-water multiples, and increase the signal to noise ratio of the dataset. To complete the processing steps, GLOBE Claritas™ (Ravens, 1999), a seismic processing suite developed by GNS Science, New Zealand was used. Seismic data enable the drill core stratigraphy to be interpreted away from the well (see chapters 4 and 5). To aid in this task, it is necessary to obtain the best possible seismic image. In areas of ice cover, this involves paying careful attention to velocity analysis.

3.1 2005 Data Acquisition

The acquisition of the MIS-3, MIS-4, and MIS-5 seismic lines (Event K001S) took place during the austral summer of 2005 (refer to Henrys et al., 2006a for details). In total thirty-three kilometres of data were collected, which represent the fourth phase

of ANDRILL MIS site surveying. Compared to a refraction survey, reflection was a preferred option as it requires shorter line lengths, provides higher lateral resolution, and proves robust in the presence of low velocity zones and velocity inversions. Explosive sources in the form of primers (a tube containing a small amount of explosive ordinarily used to detonate a main explosive charge) were used for all of the surveys. Reflection surveying proved a better choice in this respect as it required smaller amounts of explosives than refraction surveying. The lines were specifically positioned to broaden the coverage of all earlier seismic reflection profiles: HPP-1 (Bannister, 1993; Melhuish et al., 1995), MIS-1 (Balfour, 2002; Bannister and Naish, 2002), HPP-2 and MIS-2 (Horgan et al., 2003) (Fig. 6) in order to investigate lateral continuity of key stratigraphic horizons.
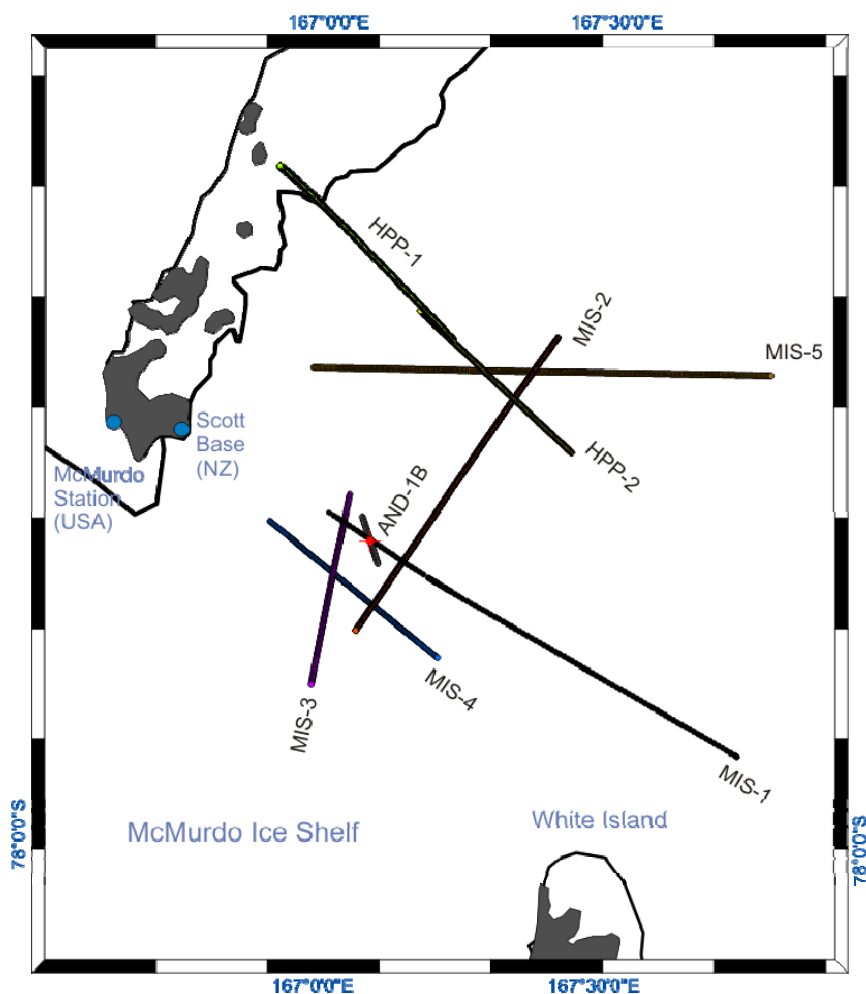
Figure 6. Location basemap showing MIS on-ice seismic surveys.

Peg and shot hole locations defined the MIS-3, 4, and 5 surveys and were all surveyed using Global Positioning System (GPS) receivers, followed by processing in the field using the Post Processed Kinematic (PPK) method. A GPS base station at Scott Base was used as the reference receiver for surveying with the furthest receiver <25 km away from Scott Base. GPS-determined shot point and geophone locations are considered accurate to ±10 cm (Clifford, 2006). Geophone locations were offset 2 m from the shots to prevent the generation of surface 'noise' in the event of disruption of cables during shooting. Shot holes were drilled and tamped using compressed snow and drill shavings, which significantly enhanced the quality of the seismic signal. 40-cm spikes replaced the standard geophone spikes to improve coupling in the poorly compacted surface snow. All survey positions were later integrated into the SEG-Y seismic trace headers.

Table 1. Summary of seismic lines recorded during the 2005/06 ANDRILL field season.

LINE	FIRST Shot Point	LAST Shot Point	Number of shots	FIRST CDP	LAST CDP	Length (km)	Direction
Mis3	102	164	62	100	386	6.89	North
Mis4	102	178	77	100	426	7.85	Southeast
Mis5	102	279	175	104	832	18.23	East

CDP – Common Depth Point

In order to image the targeted 1200 m thick body of accumulated sediment, the offset for the survey needed to be within the same range. Thus a 96 m shot spacing and 48 m receiver spacing was chosen for the 48 active channels of the survey. A split-spread survey geometry, which is commonly used for land seismic acquisition, was selected over a single-ended geometry as it provides important information regarding the dip of subsurface strata. Each of the three profile lines were designed specifically to extend the existing on-ice reflection database and provide continuity for correlating interpreted horizons into the area of more extensive marine seismic lines.

Table 2. Seismic Acquisition Parameters.

Source Type	Pentex primers 3.2-kg explosive with Redcord detonation cord. Electric, 30-m lead seismic detonators formed the primary explosive.
Shot interval	96 m
Shot depth	17-18 m
Shot-receiver near offset	24 m
Shot-receiver far offset	1128 m
Geophone interval	48 m
Geophone offset	2 m
Geophone type	single string 40-Hz vertical component with 40-cm spikes
Survey geometry	symmetrical split-spread (24:24), except for roll off at western end of each line
Number of live channels	48
Roll capability	96 channels
CDP coverage	12 fold
Recording system	Seistronix RAS-24 Exploration Seismograph
File format	SEG2
Record length	6 s
Sampling rate	1 ms
Low-cut acquisition filter	None
High-cut acquisition filter	None

3.2 2005 Seismic Data Processing

During acquisition, the seismograph was housed in the rear compartment of a Hägglund all terrain vehicle all terrain vehicle where a customised workbench and auxiliary equipment were installed. Heating inside the Hägglund ensured that all equipment remained within their respective operating temperature ranges. Data were recorded directly onto a laptop running the Linux operating system and were also recorded onto CD in the original SEG-2 format as a backup. The data were converted in the field from SEG-2 to SEG-Y format and preliminary pre-stack (Fig. 7) and post-stack (Fig. 8) processing was performed using GLOBE Claritas™ (Ravens, 1999; Henrys et al., 2006a). For each of the profiles, strong sea-floor multiples within the dataset compromise the quality. These multiples are caused by seismic reflections reverberating between the seafloor and ice shelf and proved to be a processing challenge.
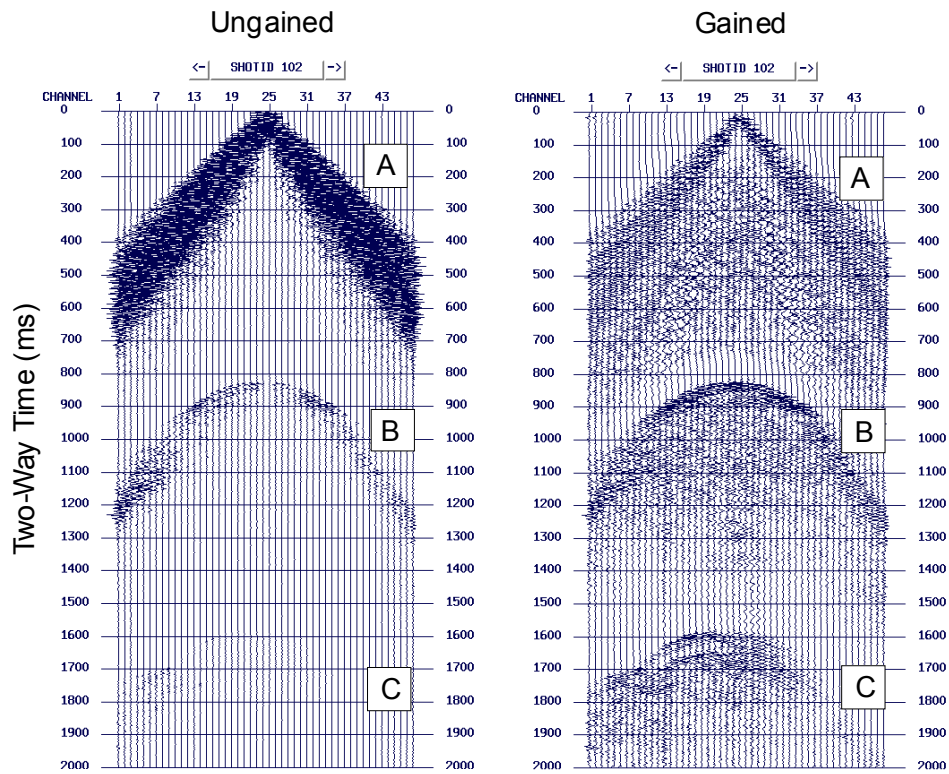
Figure 7. Shot record from MIS-5 line showing surface generated linear noise (A), seabed and sub-seabed reflections (B-C), and early long path multiple (C). Figure from Henrys et al., 2006a.
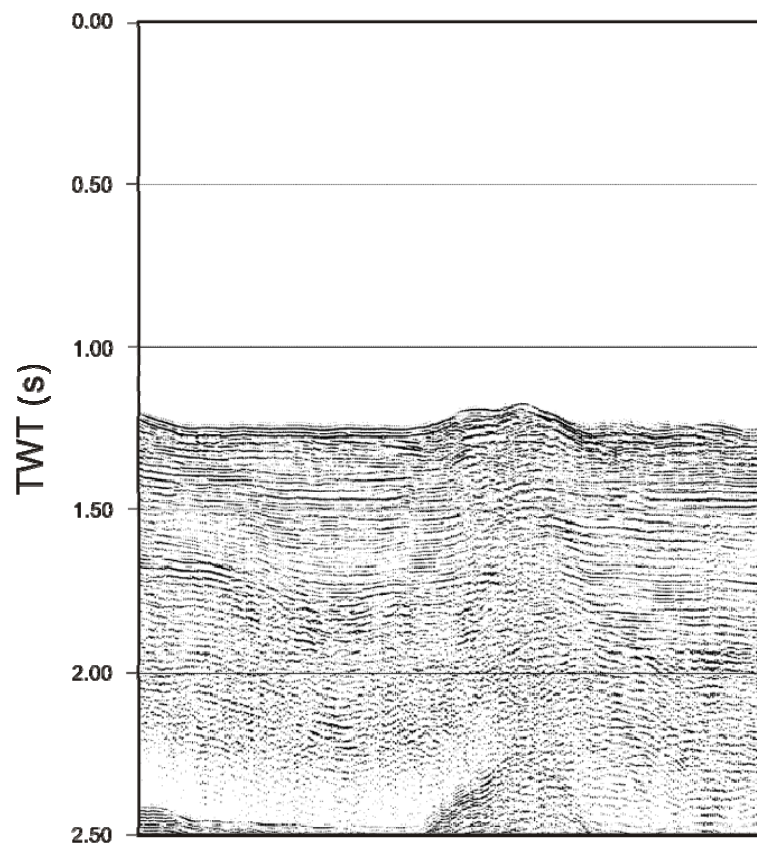
Figure 8. On-ice post-stack processing of line MIS-3. Figure from Henrys et al., 2006a.

Upon returning to New Zealand, further processing of the three seismic lines was required in order to achieve the most detailed sub-surface image possible. Off-ice processing was undertaken at GNS Science, Avalon, Lower Hutt, using GLOBE Claritas™ on a Sun Microsystems™ machine. Each of the lines underwent essentially the same processing sequence, with the MIS-5 line serving as the test line. The processing sequence was divided into "jobs" with the same modules being applied to each line at each stage of processing. A basic outline of the jobs is shown in Table 3 and a more comprehensive description of processing stages and parameters can be found in Appendix A.

Table 3. Processing steps applied to MIS seismic lines.

Job	Description
01	Read in SEGY data Resample
02	Apply trace edit Add geometry Apply spherical divergence correction Apply a band-pass filter
03	Gather shots into CDP's Apply static correction Apply surgical mute Re-order CDP's Apply normal moveout (NMO) correction Stack data Apply a band-pass filter Apply a deconvolution filter
04	Migrate data
05	Apply band-pass filter to remove low frequency noise introduced by deconvolution Apply surgical mute to remove ice and water above seafloor

The processing sequence used was designed to improve the quality of the field processed sections. Therefore, a great deal of time was spent on velocity analysis and testing different parameters in order to produce the best possible image. Velocity analysis was performed iteratively throughout the processing sequence to develop the

velocity field that enhanced reflector continuity. Accurate velocities are essential in order to develop accurate depth estimates, which are needed to determine sedimentary processes such as accumulation rates. Velocities were examined a number of times using a combination of Semblance spectra and the Claritas Velocity Analysis (CVA) tool. Semblance is a quantitative measure of the coherence of seismic data from multiple channels. The CVA tool allows velocities to be picked based on constant velocity stacks (CVS) and constant velocity gathers (CVG). All three velocity tools (Semblance, CVS, CVG) should be run simultaneously to achieve the best result. After each pass of velocity picking, the velocity field was examined for consistency. A normal move-out (NMO) correction was also applied to the data as part of the velocity analysis. Normal move-out is the amount by which seismic reflection time deviates from what it would be if the signal were reflected normally (i.e. at zero source-receiver offset). The normal move-out correction, as well as deconvolution filtering and stacking, proved to be the most efficient means to deal with sea floor multiples.

Parameter testing included frequency values, gap lengths and window lengths. The XVIEW module within Claritas allows multiple display of the seismic section side-by-side for comparison. The ability to switch between sections allows even minor differences to be detected. Each panel represents the different testing parameters and allows the processor to choose the best set for the needs of the processing. Additional processing modules including depth migration and a static correction were also applied in order to reposition reflections to their correct surface location and at a corrected reflection time, and to account for time differences introduced by near surface irregularities.

Further processing on the datasets did not significantly improve the overall quality of the seismic section though improvements are noticed in certain areas (refer to Appendix B).

3.3 2006/2007 Data Acquisition

During the austral summer of 2006, further seismic acquisition was conducted in the form of two vertical seismic profiles (VSP) at the location of the MIS drill site (Fig. 9); a standard VSP (Fig. 10) as well as a walk-away VSP (Fig. 11). The purpose of the VSP was to allow a direct correlation between two-way reflection time (from surface seismic data) and actual sub-surface geology (as seen from the AND-1B core).

A VSP typically consists of recording a surface generated seismic signal at a uniformly spaced set of depths. Seismic receivers are lowered down the bore hole using a wire-line and allow the recording of both downgoing and upgoing seismic waves. This can potentially provide a higher resolution image than can be obtained from surface receivers which record only upgoing waves. The observed waveforms are functions of time which are subsequently plotted against depth to produce a time/depth curve. This is extremely valuable during drilling as it allows prediction of depths to target reflectors. A VSP ideally should complement surface seismic surveys, but can also offer further information on the locations of reflectors as well as *in-situ* properties such as wave speed and attenuation. Shot hole and peg locations for the walk-away VSP were surveyed using a Trimble 5700 GPS system. Each record comprised of a single stack. The triggering was a simple breaking of an electrical circuit performed at the shot box.

Figure 9. Overview map of Williams Field and ANDRILL MIS drill site. Figure courtesy of Jessica Walker of Raytheon Polar Services Company, United States Antarctic Program.

Table 4. VSP recording parameters

Source Type	Anzomex P boosters (395 g each). 8 boosters (walk-away), 1 to 4 boosters (standard)
Shot interval (walk-away)	30 m
Shot depth	17-18 m
Shot-receiver near offset (walk-away)	90 m
Shot-receiver far offset (walk-away)	1020 m
Source offset (standard)	75 m
Geophone type	Z-Seis 5-channel hydrophone (30 m length). Each channel (6 m apart) comprised of 8 individual hydrophones. The entire string comprised of: hydrophones, an automatic 22-dB pre-amplifier, a selectable post-amplifier, a temperature compensator for internal pressure, and a 9 kg sinker bar
Recording system	BISON 9048 Seismograph
File format	SEG2
Record length	5 s
Sampling rate	1 ms
Pre-amplification gain	0 dB (walk-away), 20 dB (standard)
Post-amplification gain	20 dB (walk-away), 40 dB (standard)
Real-time low-cut frequency filter	4 Hz
Real-time high-cut frequency filter	2000 Hz

The standard VSP was undertaken in two phases. In Phase I, at the end of AND-1B NQ pipe coring, a VSP was successfully completed from 1930 to 920 metres below rig floor (mbrf) (29 to 30 Dec 2006). The open-hole section ranged from the base of the HQ pipe (1612 mbrf) down to the maximum depth attainable with the wireline (1934 mbrf). Part of the VSP run in casing was found to be contaminated with noise and wave trains dominated by arrivals having velocity of the steel casing (~4000 m/s). During Phase II (8 Jan 2007), the VSP was repeated over the interval 1370 to 920 mbrf. By allowing the hydrophone cable to stand for approximately 15 minutes between steps, the amount of cable noise was reduced (Morin et al, 2007). The open hole available for Phase II was from 1270 to about 1164 mbrf (about 106 m).

Data from the walk-away VSP is not included in this study but will be the focus of future work.
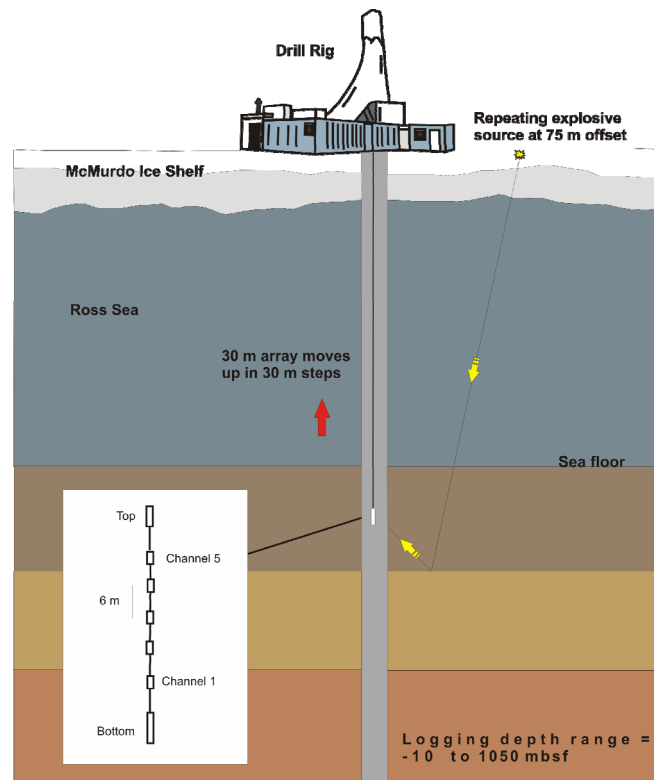
Figure 10. Standard VSP stepping up the well at 30 m intervals with a 5-channel Z-Seis 30 m hydrophone array and one explosive source (75 m from the well head) recorded at each depth.
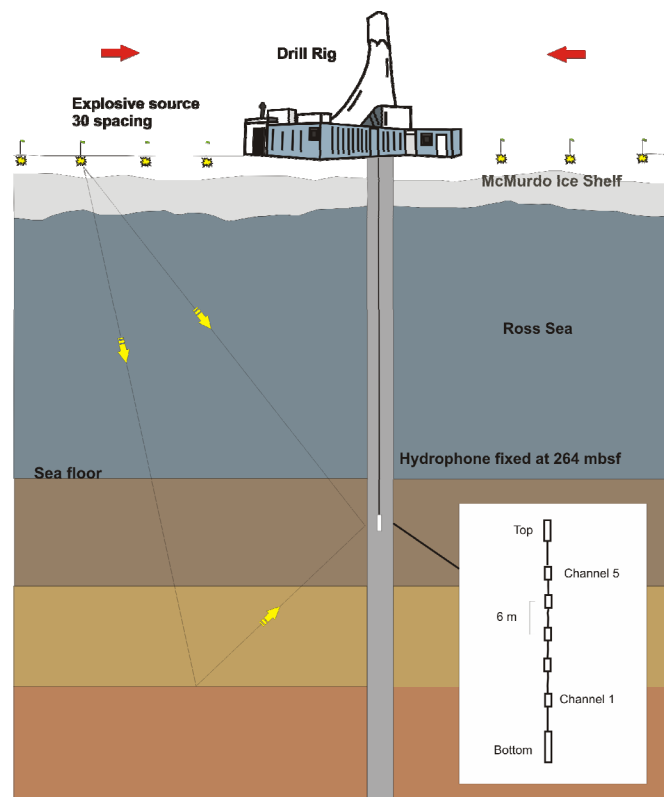
Figure 11. Walk-away VSP stepping towards the well (30 m steps) with shots recorded in a fixed receiver array, located approximately 1192 m below the rig floor (mbrf), or 264 m below sea floor (mbsf).

3.4 2006/2007 Seismic Data Processing

VSP data processing presents a number of challenges. The dominant downgoing wavefield obscures the upgoing primary reflections and makes any interpretation very difficult. In addition to this, both random and coherent noises cause contamination, and multiples can be quite common in the dataset. Even though both a standard and a walk-away VSP were conducted, only the standard VSP data has been used for this study.

During processing, upgoing and downgoing waves need to be distinguished from one another. By analysing the difference between direct wave arrivals (downgoing) and reflections (upgoing), a separation between them can be achieved (Schmitt et al., 2007; Henrys et al., 2000; Burton & Lines, 1996). Adding direct arrival times together emphasizes upward-travelling waves, while subtracting direct arrival times aligns the travel times of the downgoing waves horizontally making them easier to interpret (Hardage, 2000). The separation is aided by reflections having a slope opposite to the first breaks on the seismic record (Fig. 12). One of the most effective means of achieving this separation is through *f-k* filtering. In the time-depth domain, the upgoing and downgoing events obstruct one another; however in the frequency-wavenumber (*f-k*) domain the two wavefields will ideally be clearly separate. This allows either the upgoing or the downgoing waves to easily be removed (Hardage, 2000). Processing of the VSP data within GLOBE Claritas™ was non-standard and required specific tailoring of processing modules, with a primary focus on separation of the wavefields. The total number of seismic traces represented in the VSP was considered as a single shot gather for the purposes of seismic processing.

Once the raw SEG-Y data was loaded, the auxiliary traces were removed before the survey geometry was added. The data were then sorted by offset, which corresponded to depth down the hole. The GLOBE Claritas™ seismic quality control (SQC) application was used to pick first breaks on the shot gather. In order to develop the most accurate time/depth curve possible, picks were refined and tested a number of times before being added to the trace headers of the data.
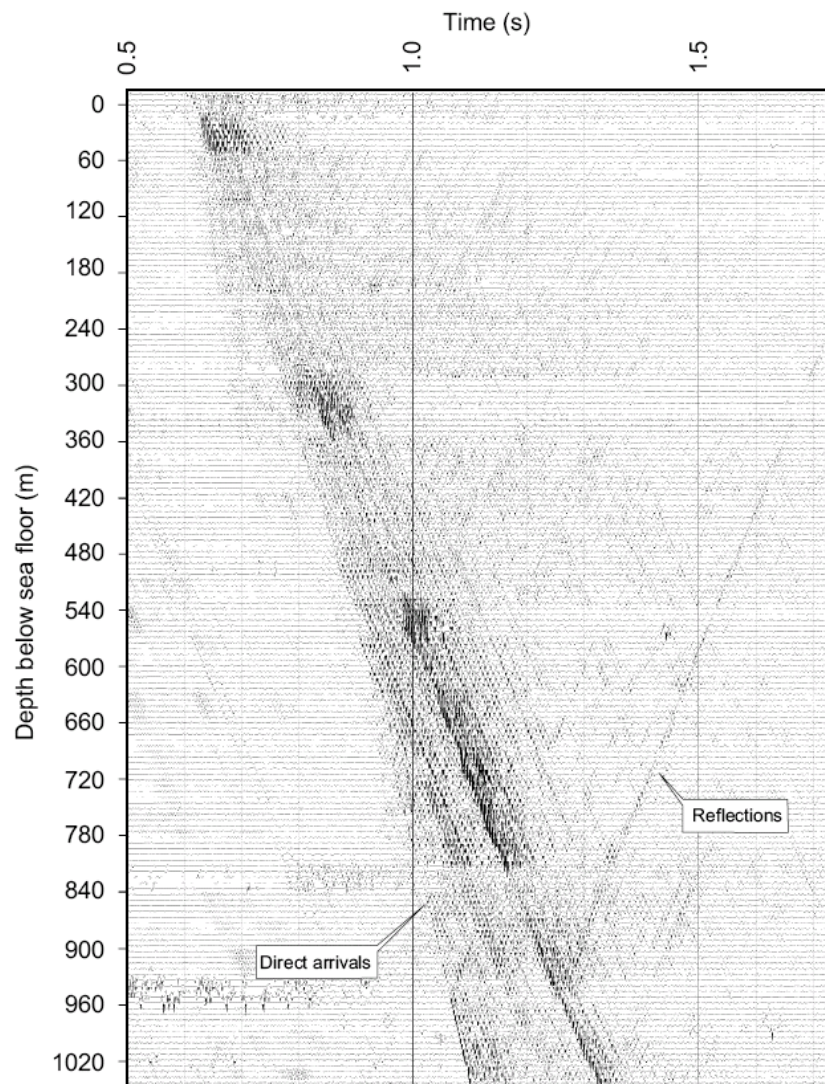
Figure 12. Raw seismogram from the Standard VSP experiment completed during Phase 2 of the downhole logging programme. Clear direct arrivals and reflections are observed in the raw data.

Unwanted signal (or noise) can cause degradation to the primary-reflection section of VSP datasets. One such source of noise, which is prevalent on VSP data, is the multimode energy. It refers to any energy that has been converted from P-wave energy to S-wave energy *on transmission* through an interface (Stewart, 1998). S-wave conversions travel down the array with a slower wave speed than P-waves. As a result this energy is aliased. Aliasing refers to a distortion of the frequency and when this occurs, signals on adjacent traces are exactly anti-phase, making the dip polarity of the event impossible to determine.

Because the dip is frequency dependent, spatially aliased components were seen to clearly "wrap around" from positive to negative dip on *f-k* spectra, making *f-k* filtering impossible. As *f-k* filtering is the means by which the upgoing and downgoing waves are separated, the presence of P to S conversions and the aliasing it introduced posed a problem. To help this and aid in the identification of reflectors, a suite of synthetic VSP's were developed (refer to chapter 5) to help design an appropriate *f-k* filter which was then applied to the observed data (Fig. 13) (Fig. 13). Lastly, a high-pass filter was applied to the data to remove low frequency bursts/spikes of noise before a static shift was applied, whereby the data was time-shifted down by values outlined in the first arrival picks, in order to 'flatten' the reflections.
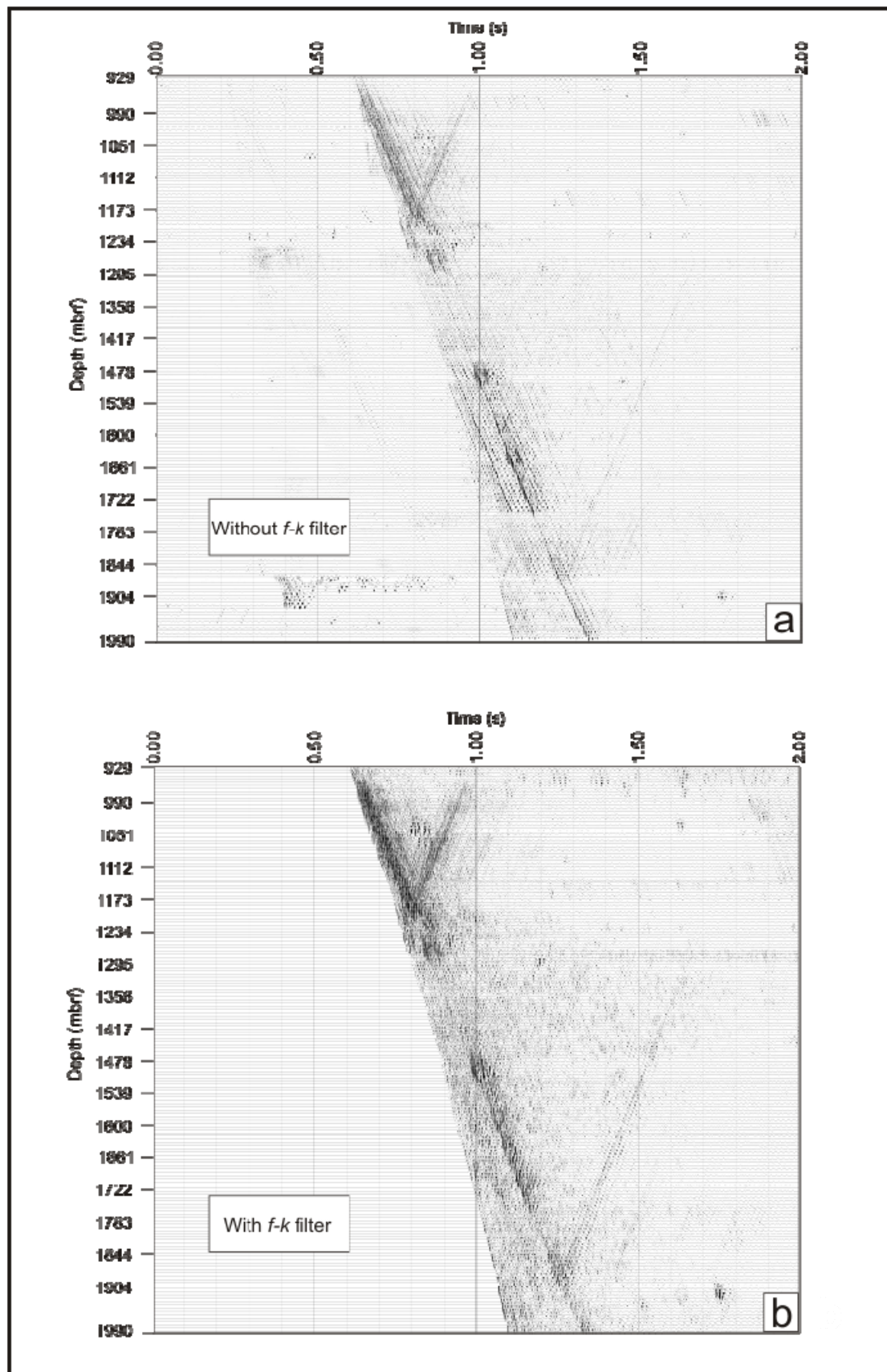
Figure 13. Processed observed VSP section showing effect of *f-k* filtering. (a) non *f-k* filtered (b) *f-k* filtered**.**

3.5 Results

Horizontal sampling is equal to half the detector spacing, thus based on the shot-receiver near offset (Table. 2), the horizontal resolution for the data is ~12.5 m. The vertical resolution is a measure of the ability to recognise individual reflectors at depth. Based on the dominant frequency of the data (~70 Hz), and the velocity at which seismic waves penetrate the subsurface strata (~2000 ms^{-1}), the vertical resolution is likely to be between 7-10 m (1/4λ – Keary et al., 2002).

An analysis of the processed datasets provides useful geological and geophysical information. For example, the shot record from the MIS-5 line (Fig. 7) indicates that the depth to the seafloor is ~0.82 s (two-way travel time), which corresponds to approximately 600 m. Two-way travel time can be used to calculate depth (z) using the formula z = v t/2, where (v) equals 1500 ms^{-1} (wave velocity in water) and (t) equals 0.82/2. The affect of ocean temperature and salinity on wave travel times were considered negligible. The tail end of the first surface waves that are detected comprise of direct arrivals, at approximately ice velocity (typically 3500 ms^{-1}), water velocity (typically 1500 ms^{-1}), and slow surface waves (typically 440 ms^{-1}). Imaging of sub-seafloor reflections occurs within a window of roughly 800 ms, before the arrival of long-path seafloor multiples. Despite presenting difficulty during processing, the apparent early arrival of long-path multiples can indicate the thickness of the ice shelf. The difference between the expected arrival time (twice the seafloor arrival time = 1.63 s) and the actual arrival time (1.58 s), provides an estimate of the thickness of the ice shelf in two-way-travel-time (0.05 s or ~90 m) using the aforementioned formula with (v) being the wave velocity in ice.

The stacked section of MIS-3 (Fig. 14) shows the seabed at ~1.25 s (~900 m) along most of the profile and rising to ~1.20 s (~850 m) near the middle. Prominent high amplitude events are observed along the whole section to depths greater than 2.0 s (>1000 m of strata). The small topographic high observed on the sea floor may be a thin, seismically high-velocity, volcanic flow that has not disrupted the sedimentary section.
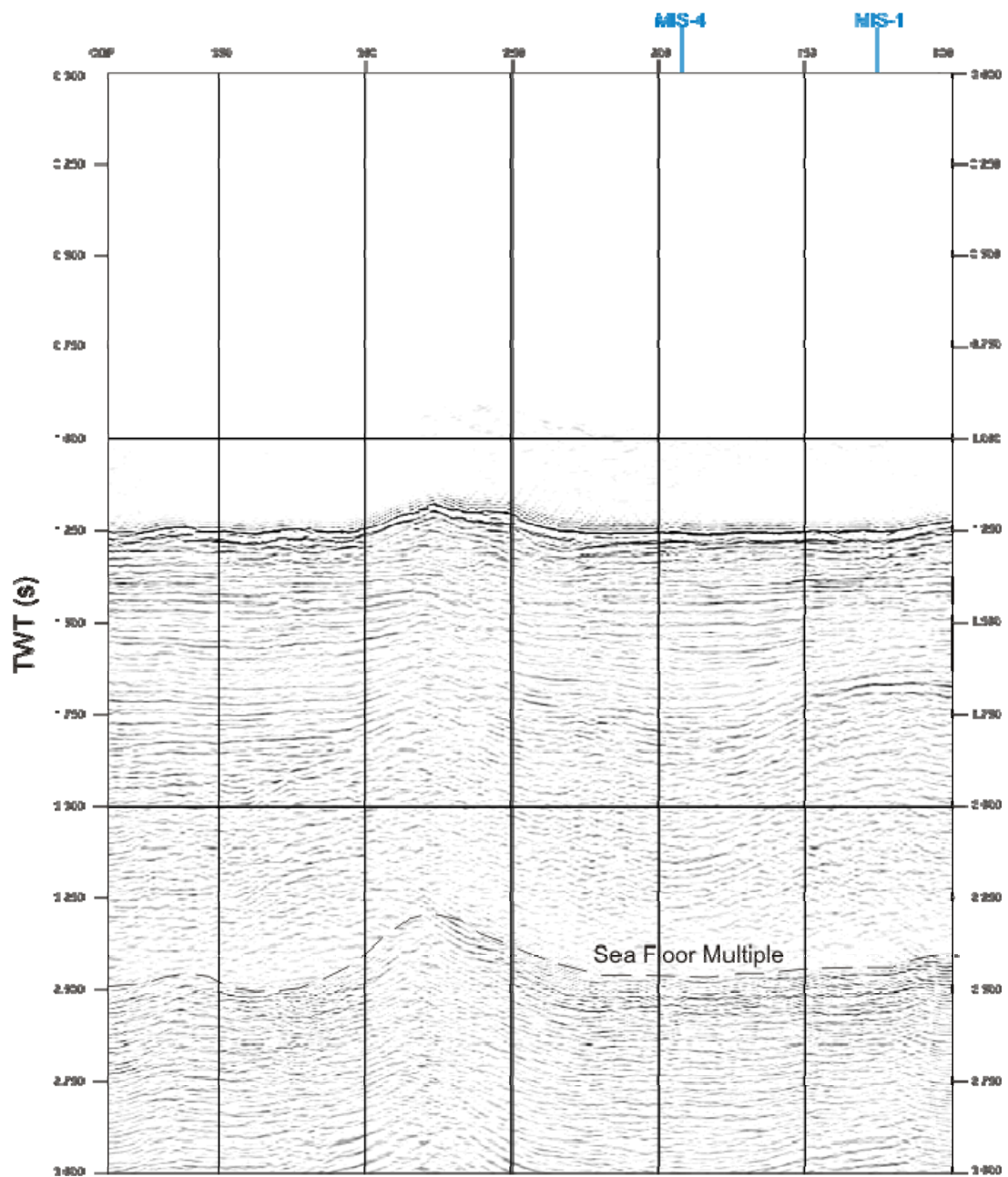
Figure 14. Processed MIS-3 line displaying points of intersection with MIS-1 and MIS-4 seismic lines.

MIS-4 (Fig. 15) crosses MIS-3 and also displays seabed at ~1.25 s (~900 m) along most of the profile. High amplitude events are again observed along the section, almost to the seafloor multiple (2.50 s), and correspond to at least 1500 m of sub seafloor strata. A major unconformity, between 1.60 s and 1.80 s, is observed on both profiles and separates more coherent horizons above from discontinuous strata below.
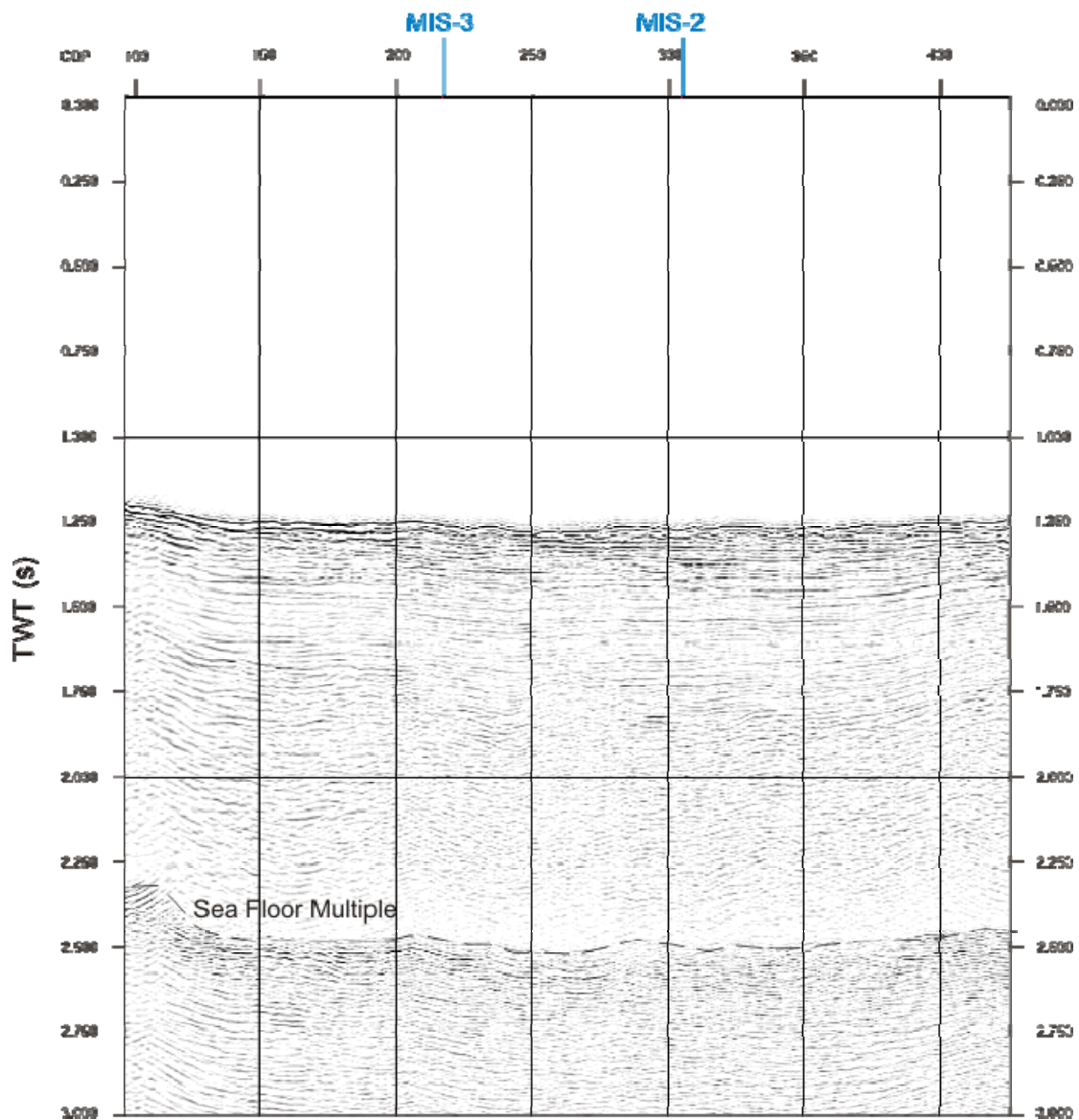
Figure 15. Processed MIS-4 line displaying points of intersection with MIS-2 and MIS-3 seismic lines.

MIS-5 (Fig. 16) runs east-west across the southern edge of the Terror Rift, and places the drill-hole stratigraphy into the wider basin structure. Previous marine seismic reflection data (Fielding et al., 2006; Whittaker, 2005; Wilson et al., 2004)
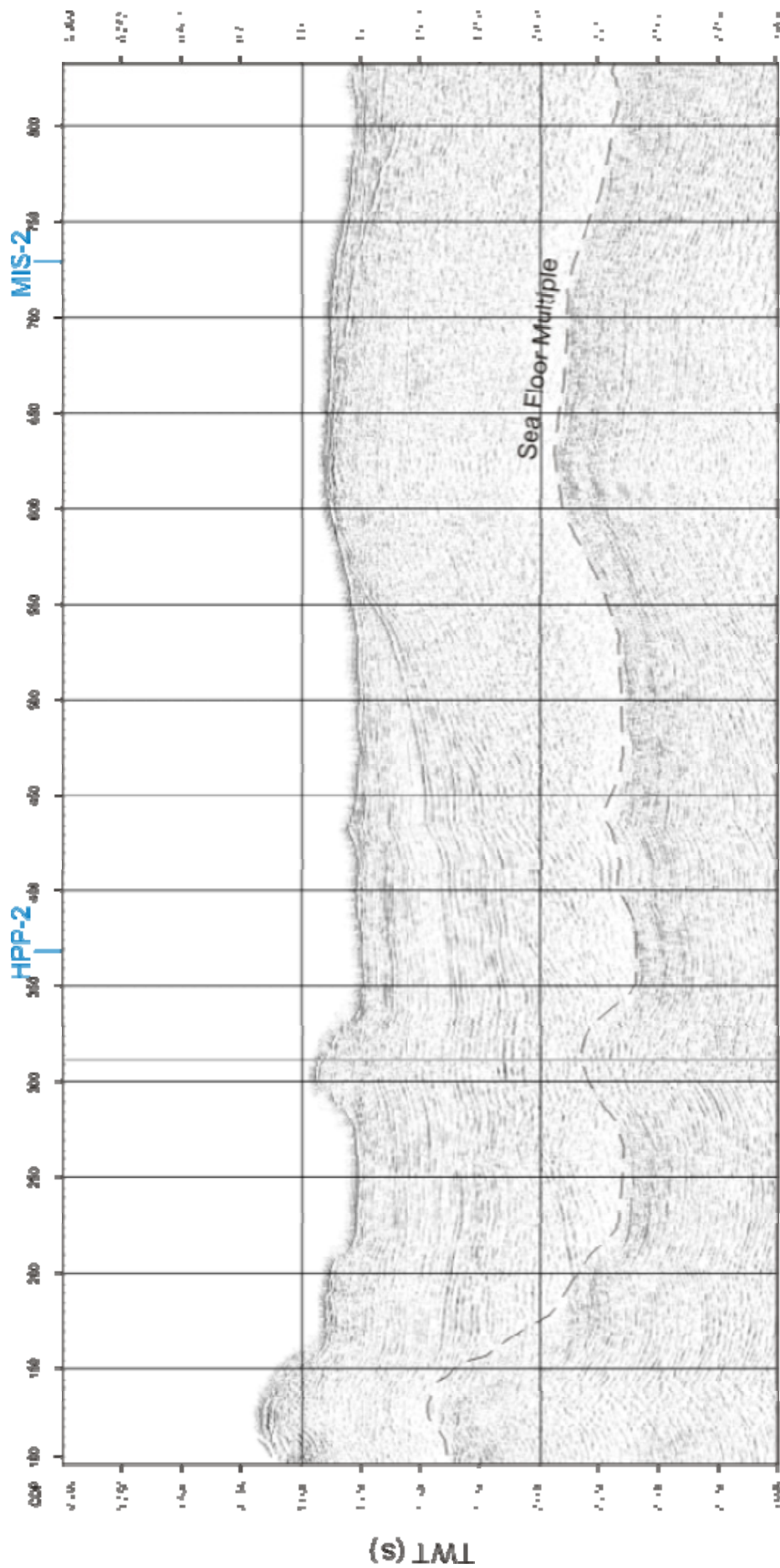
Figure 16. Processed MIS-5 line displaying points of intersection with MIS-2 and HPP-2 seismic lines

in the vicinity, reveals normal faults that offset young (<17 Ma) strata and extend in some places to the seafloor. MIS-5 displays an irregular seabed from ~1200 ms (~860 m) in the east to ~800 ms (~575 m). A 200 ms (140 m) mound is present towards the western side of the line that is likely the flank of a volcanic cone which is visible on aeromagnetic data (Wilson et al., 2007). Below the seafloor, strata are observed to dip in a westerly direction. Reflectors are clearly visible at the western half of the line within the Erebus Moat, and appear to on-lap the extension of the White Island volcanic massif on the east side of the line.

Between the western reflectors and the seafloor multiple at ~2.30 s, approximately 1400 m of sub-seafloor strata have accumulated in the Erebus Moat. The seismic image in the eastern half of the line is less clear and marked by discontinuous westerly dipping reflectors. The stratigraphic succession in the western half of the line is similar to that seen in MIS-1 (refer to chapter 4), while the structural high on the eastern half is also similar as both lines encounter the White Island volcanic massif.

3.5.1 Vertical Seismic Profile Results

The main advantage of the VSP data to this study, and the ANDRILL MIS project, was the accurate time/depth information that it provided. This allowed prediction of depths to target reflectors, and also provided an estimate of velocities downhole that were independent of whole-core measurements (refer to chapter 5).
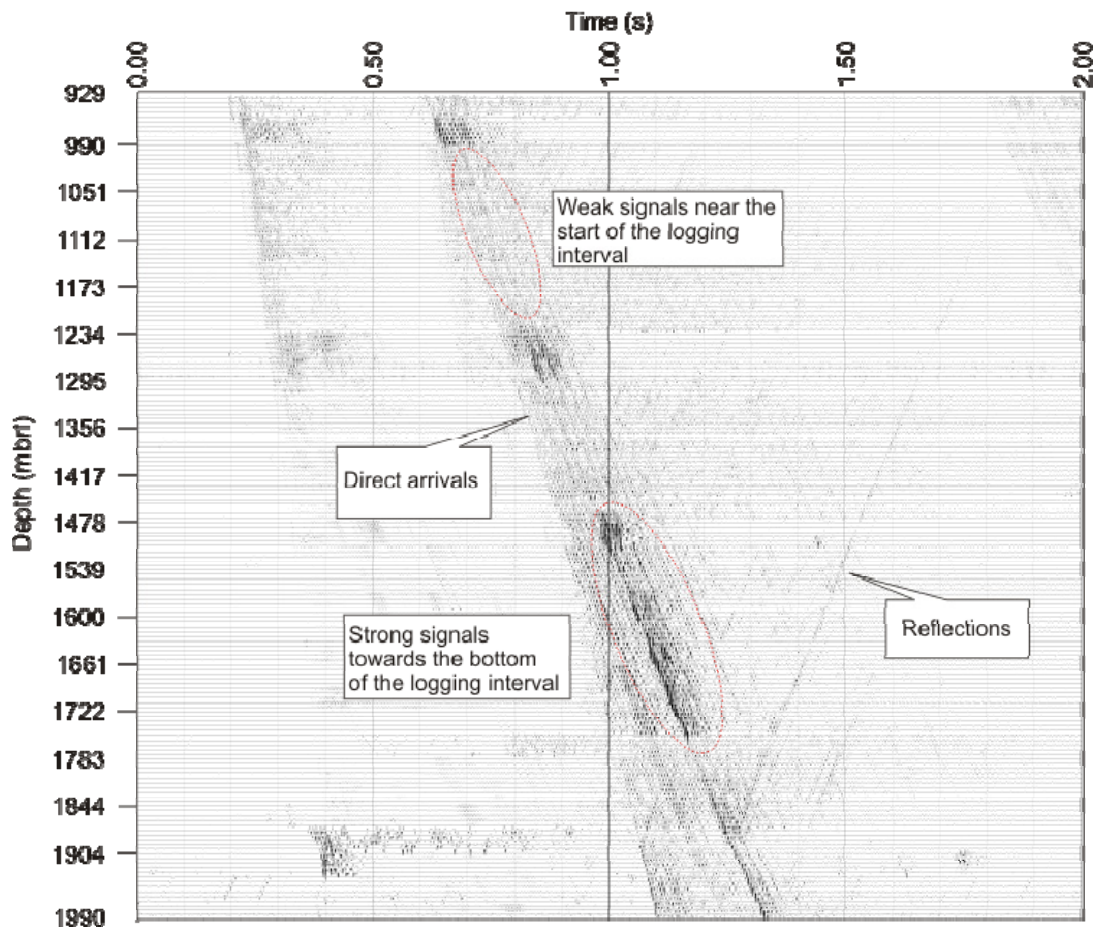
Figure 17. VSP from Phase I highlighting problems experienced during acquisition.

Figures 17 and 18 illustrate the significant improvement in data quality achieved by allowing time between shots for the hydrophone receiver to settle. Direct arrivals from Phase I are clearly visible between 0.60 s and 1.10 s TWT over the depth range. A strong reflection occurs at ~1874 m depth (1.30 s TWT).

Phase II displays direct arrivals between 0.60 s and 1.00 s TWT over a shorter depth range than Phase I (929-1370 m). A clear reflection is visible in the upper section at ~1170 m depth (0.80 s TWT). In order to produce a suitable and complete vertical seismic profile, Phase I and II were merged together (Fig. 18).

This essentially resolved the upper section of the depth range sampled by downhole logging where weak low quality data was recorded. Seismic processing was carried out on the merged VSP data in order to produce the final section.
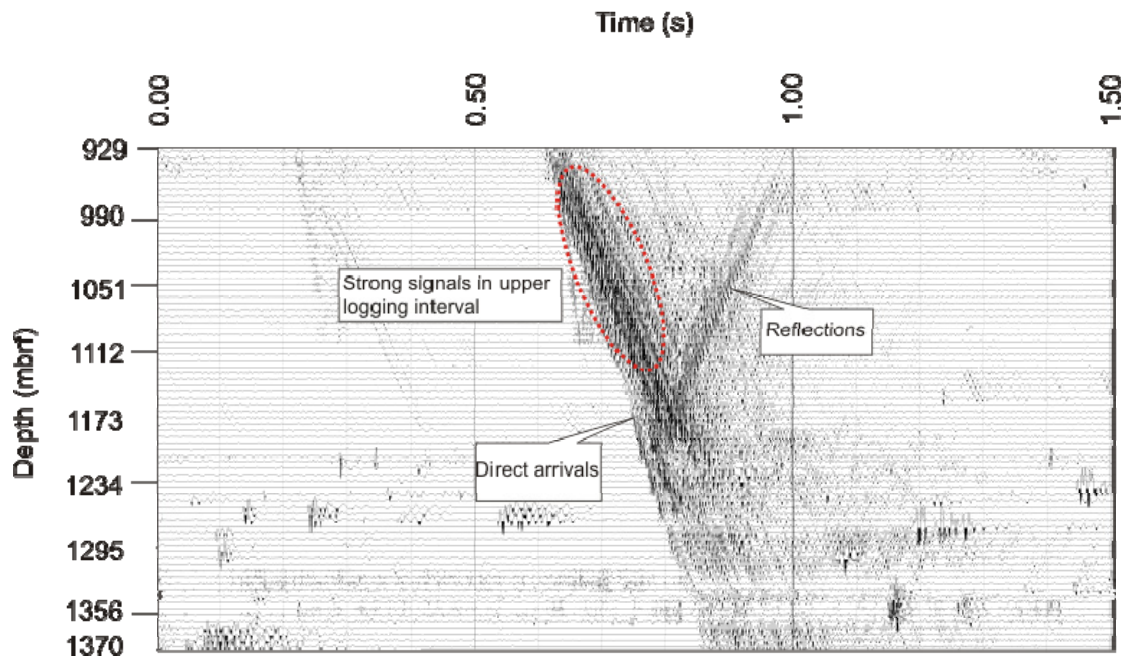
Figure 18. VSP from the shorter Phase II acquisition which re-sampled the upper logging interval.

The presence of dominant P to S conversions (Fig. 20) and coherent noise within the VSP dataset prohibits any direct correlations to be made with the borehole stratigraphy, without further comprehensive data processing. For the purpose of this study, the aim of all data acquisition and processing was to develop detailed images to facilitate accurate seismic interpretation of the stratigraphy in the vicinity of the drill site.

Figure 20 identifies P-S conversions, which correspond to the clear reflections evident from both Phase I and Phase II. A narrow window of P-wave energy lies between 0.60 s and 1.30 s TWT, between the P- and S-wave arrivals. Only S-wave energy is present at times greater than the S-wave arrival. Overall the VSP data was of most use for time/depth information. Reflections provided minimal knowledge due to the overwhelming presence of P-S conversions.
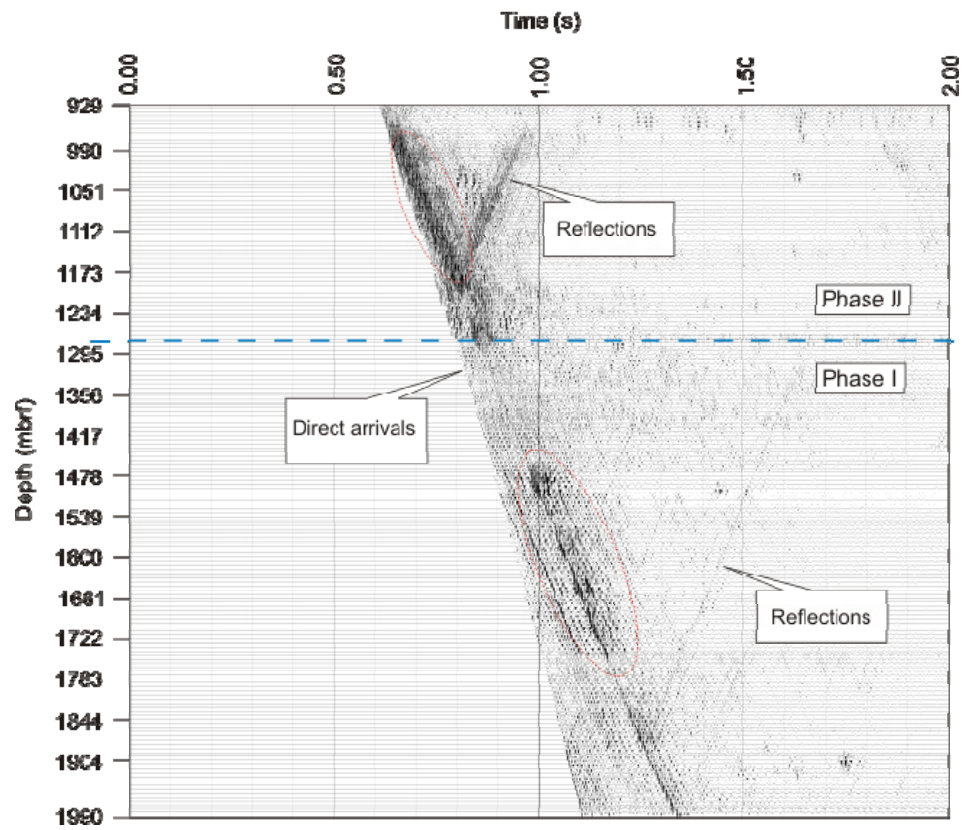
Figure 19. Merged VSP highlighting the contributions of both phases of data.
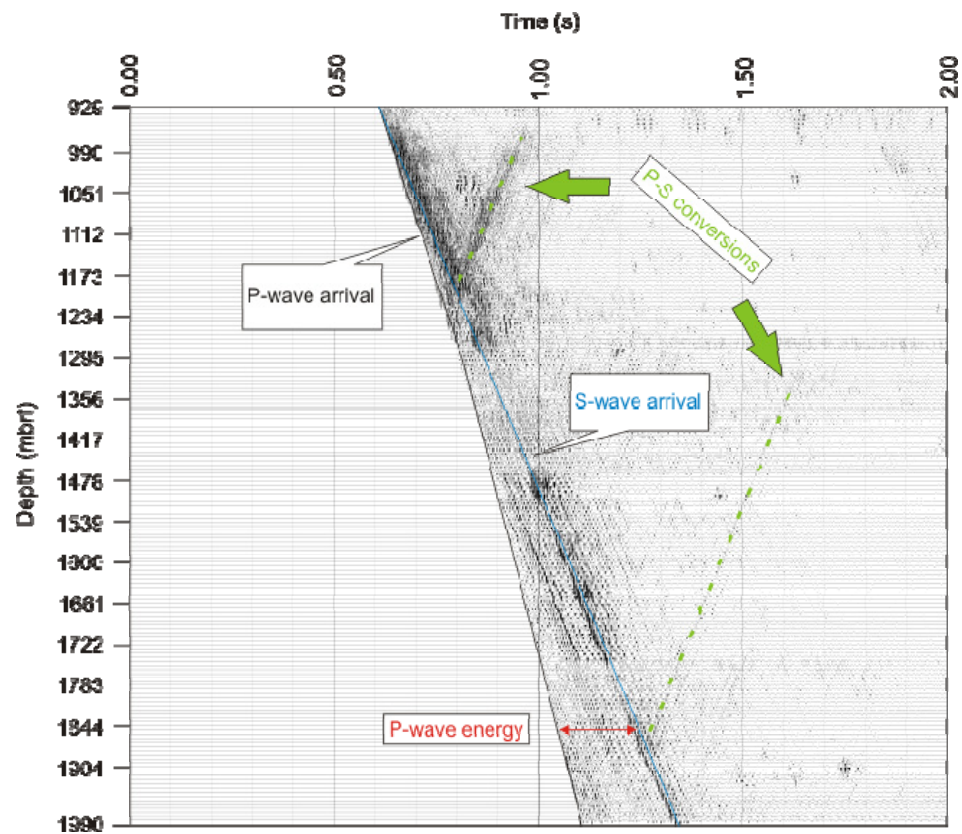
Figure 20. P-wave and S-wave reflection wavefields, and P to S conversions.

4: Seismic Stratigraphic Interpretation

An extensive network of seismic data now exists in the southern VLB, from which the most comprehensive review of the stratigraphic framework has been presented by Fielding et al. (20078). It incorporates all available seismic reflection data from the McMurdo Sound region, and includes drill-hole data from MSSTS-1 and CIROS-1.

This thesis presents a significant contribution to the seismic stratigraphy of the VLB (Table. 5) through analyses of the on-ice MIS seismic grid that broadens the stratigraphic architecture to the east and centre of the basin. Correlation with the AND-1B drill hole (refer to chapter 5) allows regional sequence and lithostratigraphic interpretation, with a chronostratigraphic framework. Twenty-two sub-seafloor horizons have been interpreted across the entire grid of seismic lines. Five can be correlated into the scheme of Fielding et al. (20078) using a seismic well-tie, and seventeen horizons are new to the stratigraphic network. These new horizons are located within seismic units and bound thinner packages of sediment. Five seismic facies have been interpreted (Table. 6) and are described in this chapter.

The correlation with the AND-1B record allows the 3-D architecture of the VLB, and its development, to be evaluated in terms of known climatic and tectonic influences during the Late Cenozoic (refer to chapter 6).

Cooper et al., 1987	Anderson & Bartek, 1992	Brancolini et al., 1995	Bartek et al., 1996	Horgan et al., 2005	Fielding et al., 2006		Rift Phase	This Study	Unit
V1		A-B	A-B	Unit IA	Rk			Rk₁ / Rk₂ / Rk₃	M5
	3/2?	RSU 1?	C-D?	Surface A2	Rj			Rk₄	
			A-H	Unit IB				Rk	
	5/6	RSU 2	E-F	Surface A1	Rv	Ri	5b	Rj₁ / Rj₂ / Rj₃ / Rj₄	M4
		RSS 5-8 (MIDDLE MIOCENE IN DSDP273) RSU4 (LOWER MIOCENE IN DSDP 273) RSS4	G-H	Unit II				Rj	
V2	9/10	RSU 4a		Surface B	Rh		5a	Ri₁ / Ri₂ / Ri₃ / Ri₄	M3
		RSS 3		Unit III				Ri	
V3	10/11	RSU 5	L-M	Surface C	Rg		4	Rh₁ / Rh₂ / Rh₃	M2
		RSS 2							
		-RSU 6	P-Q		Rf			Rh	
V4			R-S		Re			Rg₁	M1
					Rd		3	Rg	
V5		RSS 1	T		Rc				
					Rb		2		
					Ra				
V6 / V7			("Volcanics") ("Basement")				1		

An analysis of seismic facies and their boundary surfaces aims to define the differences between sedimentary units based solely on their seismic characteristics. These characteristics include: reflector amplitude, vertical reflector frequency, reflector polarity, interval velocity, lateral continuity of reflectors, abundance of reflectors, and facies geometry (Roksandic, 1978). Seismic facies can be used to infer geological parameters of units, such as lithology, but also allow preliminary (pre-drilling) interpretations of the depositional processes and environments that may be represented by the units. This interpretation was critical to the siting of the AND-1B drill hole.

Key criteria for this were to find a location with: (1) the thickest late Cenozoic record (2) limited structural complications such as faults (3) no primary volcanic features (4) the least unconformities and (5) the most distal marine deposits from the ice margin.

Lithologic facies allow a stratigraphic unit to be divided up and made distinguishable from other parts of a sequence, based on characteristics such as: mineralogy, sedimentary source, fossil content, sedimentary structures and texture. In a similar way, seismic facies divide units based on the seismic parameters specific to that unit. The more geological verification there is, the better the interpretation. If a determination of facies is to be carried out on a seismic section (i.e. a seismic facies analysis), it is essential that the acquisition and processing methodology, and all limitations that result from it, be accounted for. These limitations can include migration effects, the presence of multiples, as well as gain and filtering effects. It is important to remember that the resolution provided from seismic data will limit the resolution of facies subdivision and data collected from floating ice is additionally affected by the presence of intra-ice and intra-water multiples.

Notwithstanding this, the information seismic data provide can only offer a very cursory indication of actual geological units and facies (Roksandic, 1978). Secondary processes, such as the presence of gas, compaction, and diagenesis, for example, may also affect seismic parameters. It is for these reasons that seismic facies do not always correspond to lithologic facies.

Table 6. Characteristics used to distinguish seismic facies in Windless Bight.

	Facies Name	Occurrence	Vertical Reflector Frequency	Lateral Reflector Continuity	Reflector Geometry	Amplitude	Inferred lithology
	MSF-1	Most common	High	High	Flat-lying, Parallel	High	Coarse-grained glacigenic and fine-grained marine sediments
	MSF-2	Common	Moderate to low	Moderate	N/A	Low	Fine-grained homogenous sandstone/ mudstone
	MSF-3	Rare	Moderate	Moderate	Chaotic	Moderate	Volcanic sandstone
	MSF-4	Common	Moderate to high	Moderate to high	Clinoformic, Semi-parallel	Moderate to high	Coarse-grained sandstone
	MSF-5	Common	Low	Low	Semi-chaotic	Moderate	Coarse-grained glacigenic sediments

4.1 Seismic Surfaces and Units

The six seismic lines that comprise the MIS seismic grid (Fig. 222 to Fig. 277) provide a stratigraphic architecture for Windless Bight, and the succession of sediments accumulated beneath it. Five continuous unconformity-bounded sequences, or seismic units, were mapped across the MIS seismic grid. The units are labelled M5 to M1 (top to bottom) and are separated by five seismic surfaces labelled Rk to Rg (top to bottom), as per the naming scheme established by Fielding et al. (20078). These previously recognised, regionally-extensive, unconformities are marked by either stratal truncation below and/or onlap above. Onlap of strata onto the seismic surfaces possibly indicates transgression and thus a receding shoreline, but could also represent the effect of differential subsidence due to loading of the lithosphere caused

by sediments, volcanoes, or faulting. This study identifies 17 additional reflectors throughout the seismic grid, labelled Rk_5 to Rg_1 (top to bottom) (Fig. 211). These surfaces bound higher frequency sedimentary packages interpreted as glacimarine cycles (refer to chapter 5). Prior to drilling, these high resolution units were speculated to be cycles of glacial advance and retreat of possible Milankovitch duration.

All six seismic lines that comprise the MIS seismic grid were imported into Schlumberger's GeoFrame™ interpretation software. The lines were first interpreted individually, and then viewed as both a composite path and vertical foldout at tie-points (i.e. where one line intersected another). Interpretation began with MIS-1 so as to trace reflectors away from the bore hole. Paper prints of individual lines were also interpreted independently to serve as a quality control mechanism. For each line, the interpretation was carried out from the seafloor down. Particular attention was given to matching the lines at the tie points in order to develop the most accurate and coherent grid of data possible. The presence of seafloor multiples, due to seismic waves ringing between the ice shelf and the seafloor, limited the range of data in which to interpret. Amplitude data were not normalised across all the surveys. Nevertheless, the data retain information on the relative reflection geometry.

It is important to note that the lines were not processed in exactly the same way or by the same processor. MIS-1 was processed by Balfour (2002); HPP-2 and MIS-2 were processed by Horgan (2005) with MIS-3, MIS-4 and MIS-5 processed in this study. Due to the strong influence of magmatism in the area, some sections of the seismic profiles are partially obscured by volcanic intrusions. Reflectivity across MIS-1 (Fig.

22) and MIS-5 (Fig. 26) is significantly reduced towards the eastern edge of the profiles where the White Island submarine volcanic ridge is encountered. Geometric and acoustic relationships were used to aid interpretation of sequence boundaries across these disrupted areas.

Rg surface (*light green*) and Unit M1

Rg is the deepest and least discernible reflector within the MIS seismic grid. Along MIS-1, the surface is disturbed by normal faulting which has caused dislocation and tilting. Rg is not easily identifiable along MIS-2 (Fig. 23) due to diminished seismic reflectivity. This is attributed by Horgan et al., (2005) to N-S trending normal faults that intersect the line at an acute angle. Rg is however quite well imaged along MIS-5, but is again disrupted by normal faulting. It is least visible along the MIS-3 (Fig. 24) and MIS-4 (Fig. 25) lines.

The M1 unit is bounded at its base by Rg and above by Rh. It is characterized by regional onlap of moderate to high amplitude reflections, onto Rg. M1 is dominated by facies MSF-5 and has low reflector continuity. The dip of the facies is attributed to the faulting. Time/depth information from the seismic profiles suggests that the unit is approximately 200 m to 500 m thick throughout the grid. Along the MIS-1 line through the well-site it is ~500 m thick but moving north along MIS-2 the unit thins to ~200 m thick, although interpretation is limited by poor reflectivity at depth along MIS-2. One reflector, Rg_1, has been identified within unit M1. It is a smooth, broadly undulating surface but is not laterally continuous throughout the grid and is only weakly visible along MIS-1 and MIS-2.
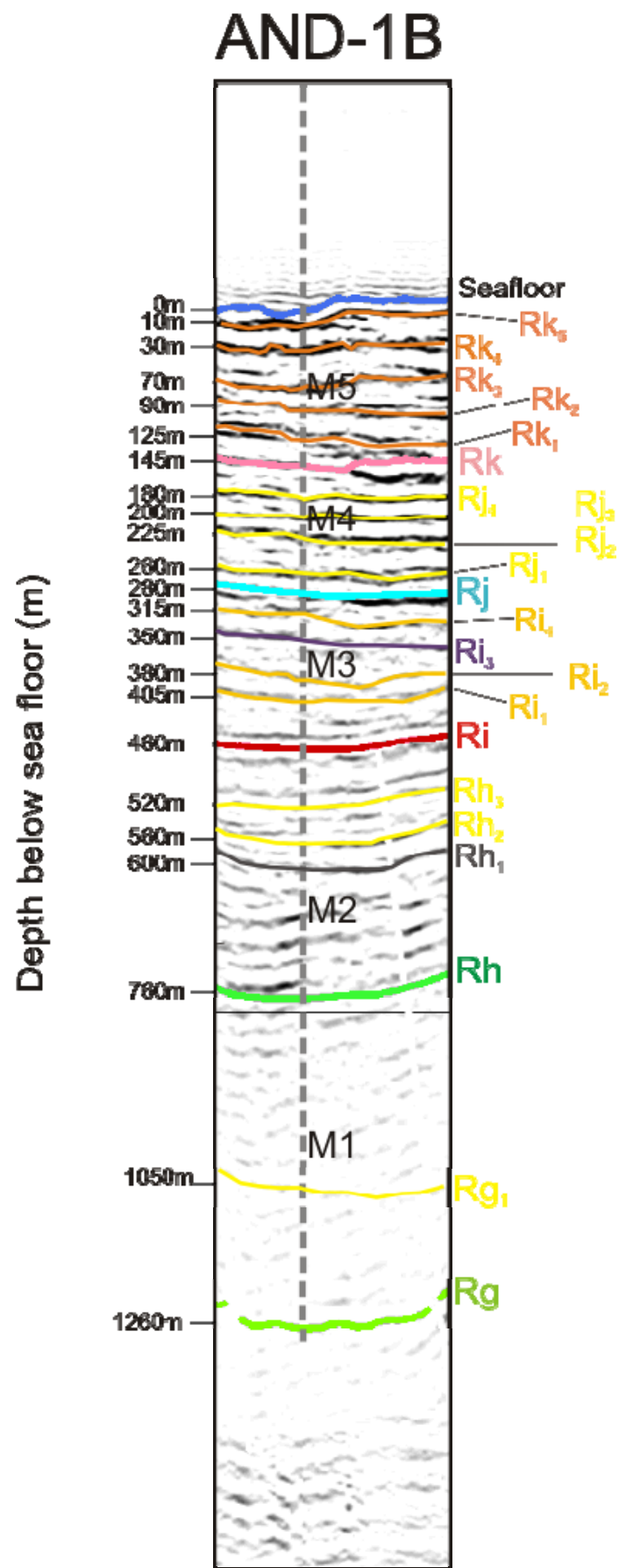
Figure 21. Identification and depth to seismic surfaces through AND-1B.
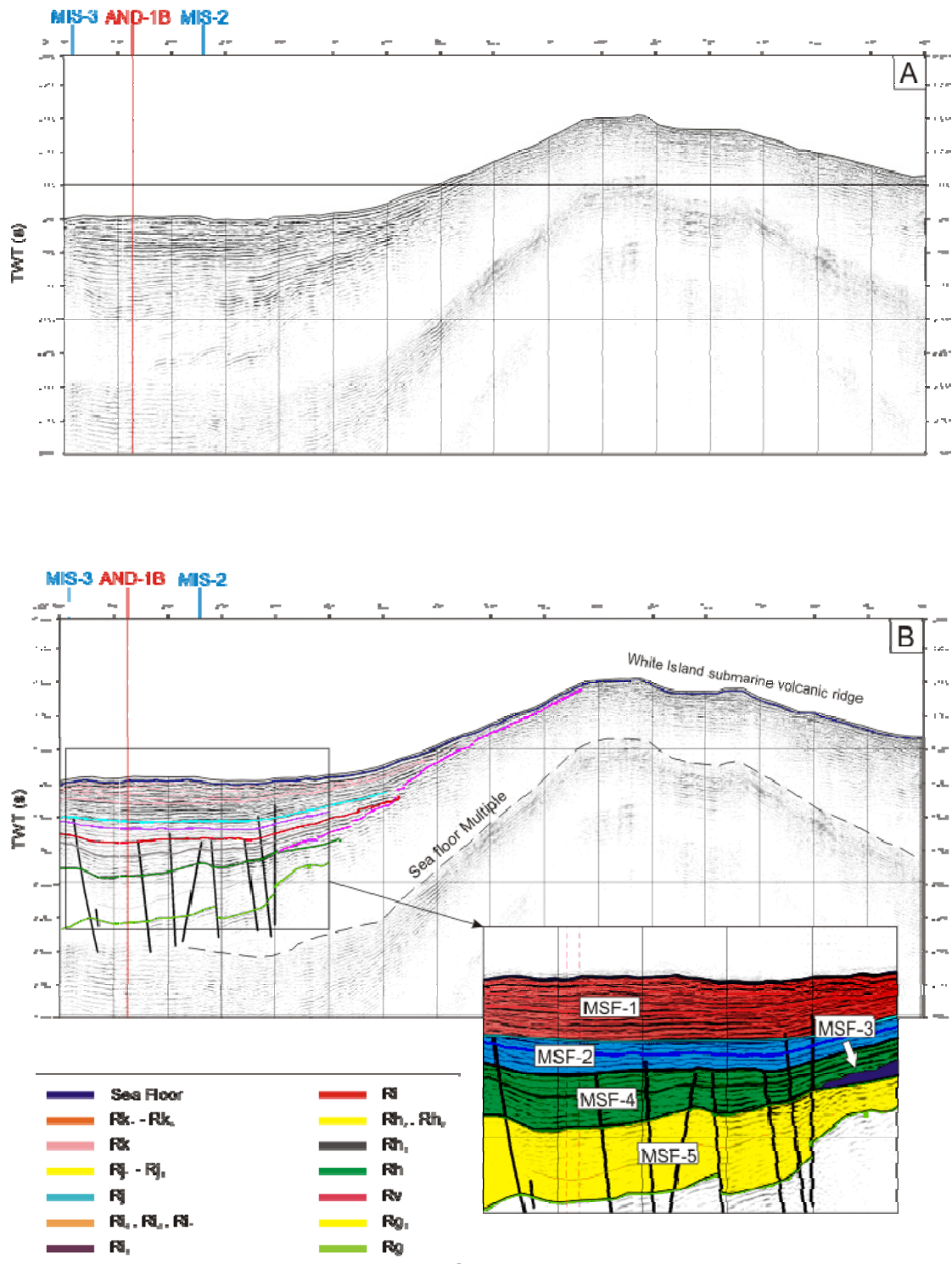
Figure 22. MIS-1 seismic line both non-interpreted (A) and interpreted (B). Inset of B identifies seismic facies. Larger figure can be found in Appendix F.

<u>Interpretation</u>

The Rg reflector is one of many well-defined unconformities across the MIS seismic grid marked by truncation of underlying strata and onlap of overlying strata. The M1 unit is interpreted as alterations of alterations of coarse-grained glacigenic and fine-grained marine sediments, as they produce moderate amplitude alternating reflectors. The presence of faulting above the Rg surface is one reason to suggest that it marks the onset of an episode of rifting; the Terror Rift rifting phase (Cooper et al., 1987; Wilson, 1995; Salvini et al., 1997; Fielding et al., 2007; Henrys et al., in press).

Seismically, the M1 unit thickens toward the Erebus moat region. The similarity in geometry between the marine seismic profiles from the McMurdo Sound (e.g. Henrys et al., in press) and the sequences within the MIS seismic grid, suggests that M1 represents a continuation of the Early Miocene sedimentation above the 17 Ma unconformity in the CRP cores. This further supports that the Rg surface is associated with renewed rifting. It is likely, based on the amount that has accumulated that the section records sediments of Middle Late Miocene age and has had substantial influence by glacial advance and retreat (Fielding et al., 2007). Cross-sections across the Victoria Land Basin reveal that the sediments deposited above Rg thicken for several hundred metres towards the centre, and taper at both the eastern and western margins; creating a steers head rifting geometry. Furthermore in chapter 5 an age of 13.8 Ma is established for the Rg reflector which also corresponds to a period of widespread cooling and Antarctic ice sheet expansion.

Rh surface (*dark green*) and Unit M2

Rh is characterized by truncation of the underlying discontinuous to continuous, moderate-amplitude reflections of unit M1, and regional onlap of high amplitude reflections (unit M2) above. It occurs at a depth of ~760 mbsf along MIS-1. Rh is also influenced by N-S trending normal faults, but not to the same degree as Rg. Regionally, Rh is moderately smooth and undulating, and correlates with the base of volcanic bodies (Rv) in the VLB (Fielding et al., 2007) (e.g. White Island).

Unit M2 ranges in thickness from ~230 m to ~450 m. It has a greater thickness along the southern profiles (MIS-1, MIS-2, MIS-3), but thins significantly moving northward along MIS-2, and on MIS-5. Unit M2 is bound at its lower limit by Rh and at its upper limit by Ri, and is dominated by seismic facies MSF-4. Within the upper part of M2 are three reflectors, namely Rh_1, Rh_2, and Rh_3. These horizons are moderately smooth and parallel throughout the area. Towards the eastern end of MIS-1, and along the northern half of MIS-2, the Rh_3 reflector is truncated over a small section by the Ri surface.

Interpretation

Volcanic rocks that comprise a submarine volcanic ridge extending from beneath White Island have been mapped above Rh, along MIS-1 and MIS-5. An age of 7.65 ± 0.69 Ma for White Island has been presented by Cooper et al. (2007) therefore allowing a reasonable inference of the same age for Rh. The relationship between Rh, volcanic deposits, and significant thickening of the section above, strongly suggests that the formation of Rh and the overlying M2 unit was to some extent due to tectonic processes and is associated with a phase of volcanism. This association with normal

faulting and volcanism is interpreted by Fielding et al. (2007) as the onset of renewed rifting in the VLB linked to the initiation of the Terror Rift.

Ri surface (*red*) and Unit M3

Ri is marked above by onlap of low-amplitude reflections, onto the high-amplitude reflections in unit M2. The presence of this low-amplitude, seismically opaque interval (unit M3) superjacent to Ri, makes it the most easily detectable unconformity across the region. The surface displays minimal truncation of subjacent strata, is smooth, and is considered a conformable boundary. Ri is located at a depth of ~460 mbsf. It is marked above by clinoform downlap and near volcanoes by onlap.

Unit M3 as a whole has a thickness of between ~180 m and ~270 m, however in the immediate vicinity of the drill site, it is comprised chiefly of the ~110 m-thick seismically opaque unit in its upper section. Despite this, four horizons (Ri_1 to Ri_4) can be mapped, albeit weakly, through the unit. These horizons are mainly parallel and moderately smooth, with minor irregularities seen along MIS-2. M3 maintains a consistent thickness across all profile lines except MIS-3 and MIS-4 where it thickens. M3 corresponds well to facies MSF-2.

<u>Interpretation</u>

Based on its low amplitude seismically opaque character, unit M3 is likely to be a homogenous interval of sandstone/mudstone. Fielding et al. (2007) correlate Ri to the base of prograding clinoforms north of Ross Island, and associate the surface with the beginning of flexural subsidence linked to the onset of volcanic loading on Ross Island. Clinoform geometries indicate progradation broadly eastward from the TAM into the VLB, north of Ross Island (Fielding et al., 2007). In cross-section across the

VLB, as seen best on MIS-5 and HPP-2 (Fig. 27), M3 is observed as an eastward thickening wedge of sediments. Ri has been attributed an age of 4.6-4.0 Ma based on its correlation to the litho- and biostratigraphy of the MSSTS-1 core (Fielding et al., 2006), where Ri is located in close proximity to a sample of microfossils of Pliocene age.

Rj surface (*turquoise*) and Unit M4

Rj constitutes a young broadly undulating unconformity separated by alternating high and low-amplitude reflections above (M4), and moderate-amplitude reflections below (M3). It is laterally continuous across the entire grid of seismic data.

Unit M4 is ~70 m to 170 m thick and contains within it strongly alternating high- and low-amplitude reflections (Rj_1 to Rj_4). At the location of the drill site, M4 is ~135 m thick. It retains a uniform thickness throughout most of the lines, only thinning at the northern end of MIS-2, and thickening slightly along MIS-3. Along MIS-4, unit M4 is thickest, at the western end, and thins considerably towards the east.

Interpretation

The high- and low-amplitude reflections in unit M4 (Rj_1 to Rj_4) are interpreted to represent cyclicity between coarse and fine-grained lithologies, caused by repetitive advances and retreats of the ice terminus in Western Ross Sea. High-amplitude reflectors are interpreted as conglomerates or diamictites associated with grounding line proximal environments. Low amplitude reflectors are interpreted to represent intervening periods of open marine sedimentation. Assuming Rj was influenced by flexural loading of the Ross Island volcanic edifices, a reasonable age estimate prior to drilling is 2 Ma, as this was when the main phase of Mt. Terror and Mt. Erebus

cone building began producing ~2000 km^3 (Kyle, 1990b; Esser et al., 2004) of sediment. With this assumption, Rj can be correlated into the Erebus Moat region where it represents the oldest stratigraphic horizon influenced by flexural loading.

Rk surface (*pink*) and Unit M5

The Rk seismic surface represents the youngest unconformity visible in the dataset. It is a smooth, mainly uniform surface with only minor irregularities. A significant proportion of Rk is truncated along the MIS-2 line, by a lens-like structure likely to comprise of overlying volcanic rocks and sediments.

Unit M5 overlies Rk and is the youngest part of the sedimentary succession. It is characterised by alternating high- and low-amplitude reflectors similar to those in unit M4. Unit M5 is flat-lying and parallel, and consists of four horizons (Rk$_1$ to Rk$_4$), all of which are clearly distinguishable throughout the grid. As the youngest unit, M5 is directly subjacent to the, quite variable, seafloor. Nevertheless, it has a thickness of ~140 m and is relatively uniform along all profiles except MIS-2 where the influence of the volcanic lens causes it to thin significantly, obscuring Rk$_1$ to Rk$_3$ for ~6.0 km of the ~14 km long line. M5 is dominated by the MSF-1 seismic facies.

Interpretation

Along a profile further north of Ross Island which has a very similar orientation to MIS-5, the sedimentary section above Rk (equivalent to M5) has been attributed to a large-scale clinoform set which downlaps in an eastward direction onto Rk (Fielding et al., 2007). It is possible that this same set extends down to the Windless Bight area. The stratal characteristics of M5 suggest that it is comprised of glacimarine

sediments, possibly diamictite/mud cycles produced as a result of recent glaciation. There is also evidence for erosion within the unit.

Seafloor

Exploratory measurements carried out in January 2003 recovered sediments down to 60 cm beneath the seafloor (Barrett et al., 2005). The recovered cores consist of a diamicton (a sandy terrigenous mud with scattered pebbles) which grades up into sandy mud with a large amount of biogenic silica and diatom assemblages (Barrett et al., 2005). A high amplitude seafloor reflection is visible on all profiles, and is taken to represent the velocity and density contrast between seawater and this diamicton layer (Horgan et al., 2005).

Summary of Interpretations

The interpretation of seismic surfaces and units described in this chapter are based on the reflectivity, lateral continuity, and internal geometry of the strata, within the context of the environment in which they were deposited. A seismic facies interpretation, coupled with the existing knowledge of the region, provides an indication of the types of lithologies within the seismic units (Table. 5). In general, units of low seismic amplitude have been interpreted as fine-grained marine sediments, such as hemipelagic mudstone and/or diatomite. The effect of rapid subsidence and bathymetric deepening, as a result of rift extension and volcanic crustal loading, are interpreted to be responsible for providing accommodation space for the accumulation and preservation of the sequences.

Sequences displaying high amplitudes have been interpreted as more coarse-grained, sediments such as sandstones, conglomerates, diamictites or volcanic deposits. The geometry of the seismic units M1 to M5 is described in terms of sediment deposition into accommodation space created by both extensional subsidence and progressive loading of the lithosphere by volcanoes. Based on the eruptive history of Ross Island, Kyle (1990b) proposed that there have been three phases of volcanism and so three phases of load induced subsidence, which has produced the flexural moat. Mt. Bird loading occurred between 4.6 and 3.8 Ma (Wright and Kyle, 1990a), Mt. Terror loading occurred between 1.7 and 1.3 Ma (Wright and Kyle, 1990b), and Mt. Erebus loading occurred between 1 Ma and today (Moore and Kyle, 1990). Despite the clear influence of glaciation in southern VLB, analysis of individual sequences and seismic facies reveal that tectonics, specifically subsidence patterns, are the primary factor characterizing the stratigraphy.

The connection between unconformities (seismic surfaces) and evidence for a widespread change in the environment however, strongly suggest that a combination of both tectonic and climatic factors control the stratigraphy.

Now that seismic stratigraphic interpretations have been made on the existing network of on-ice seismic reflection data, a correlation to the AND-1B well can be made and this can be used to test the validity of the interpretations (refer to chapter 5). The interpretations can then be used to evaluate the relative roles of both tectonic and glacial/climatic variations on the evolution of this part of the Western Ross Sea (refer to chapter 6).
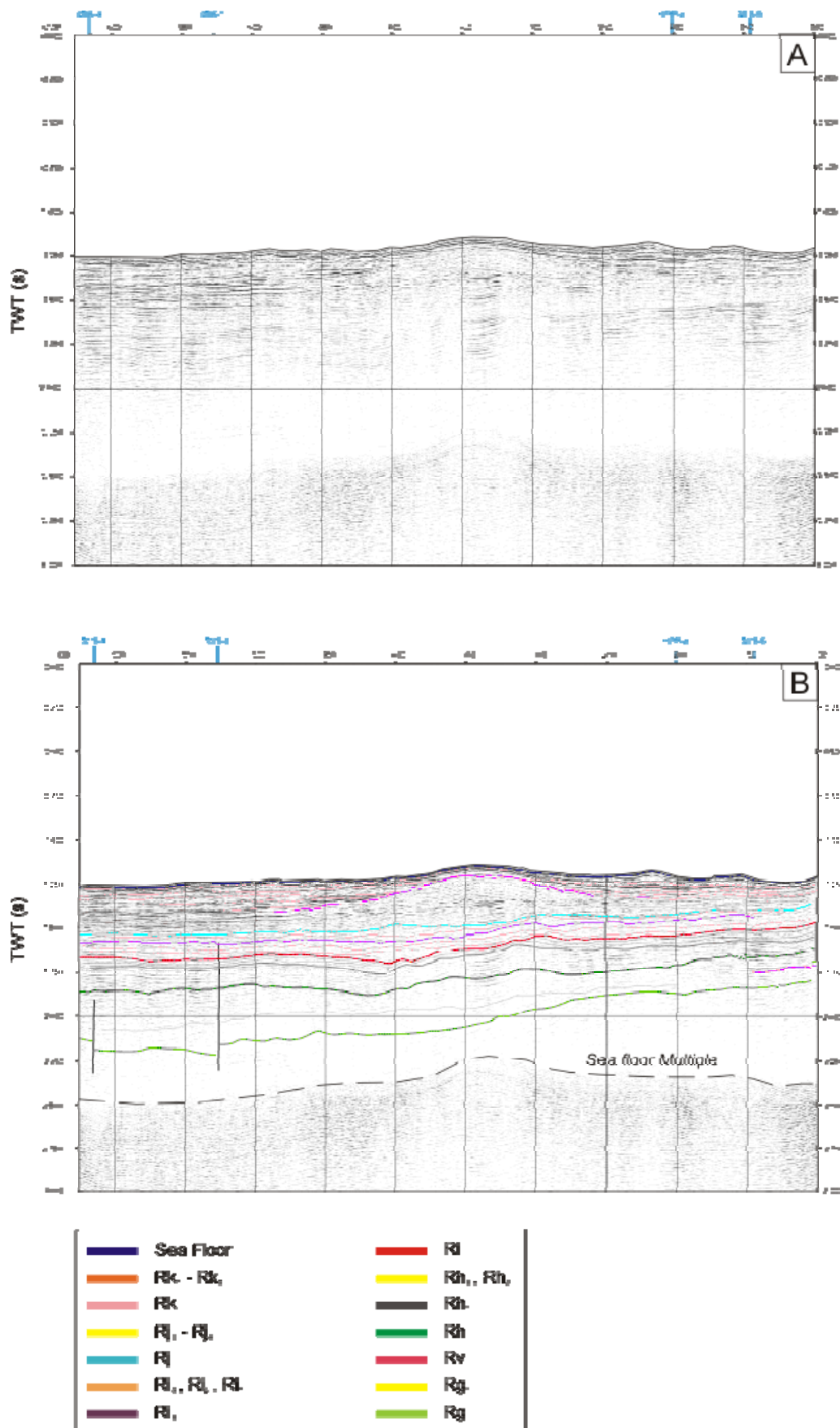
Figure 23. MIS-2 seismic line both non-interpreted (A) and interpreted (B). Larger figure can be found in Appendix F.
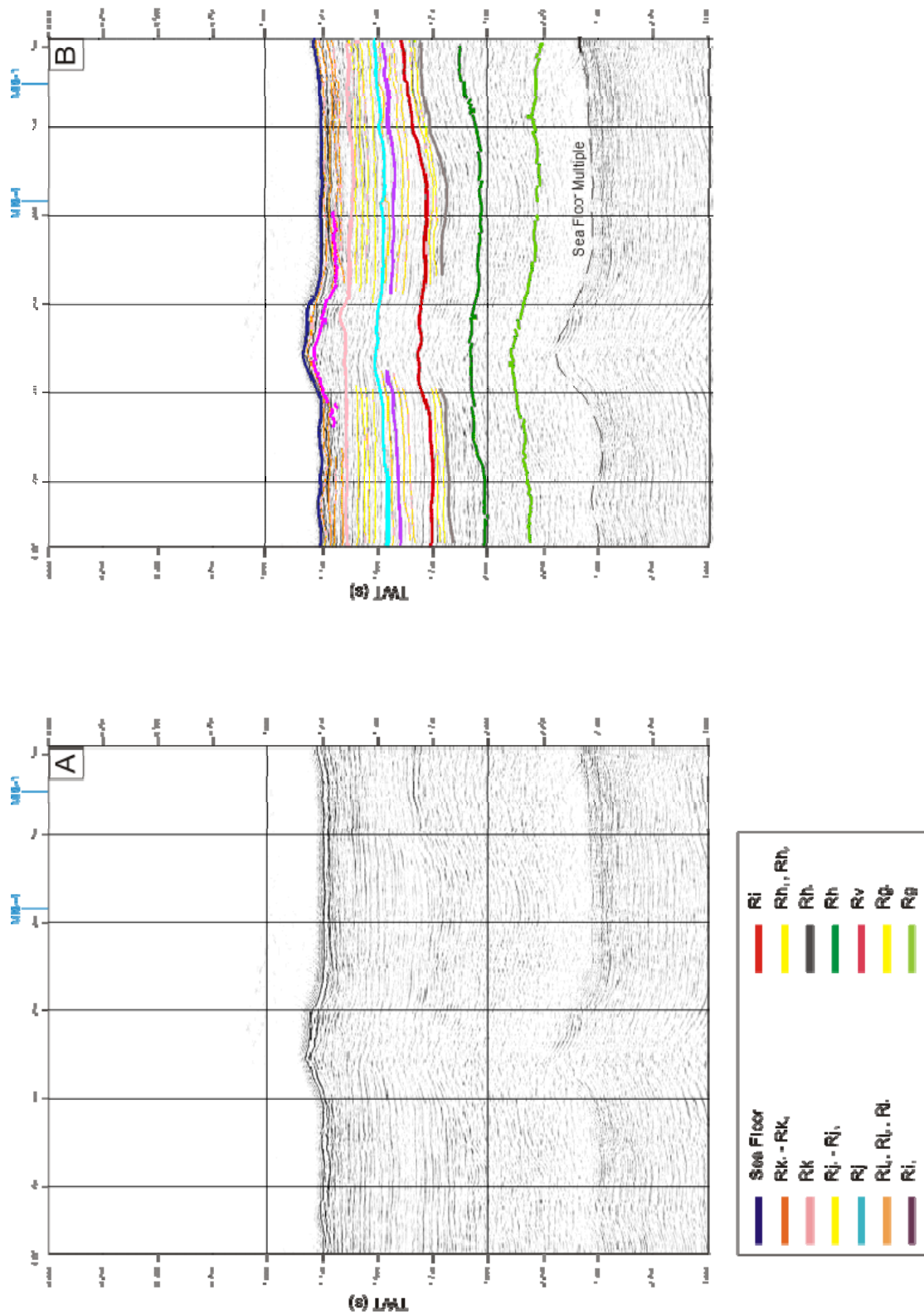
Figure 24. MIS-3 seismic line both non-interpreted (A) and interpreted (B). Larger figure can be found in Appendix F.
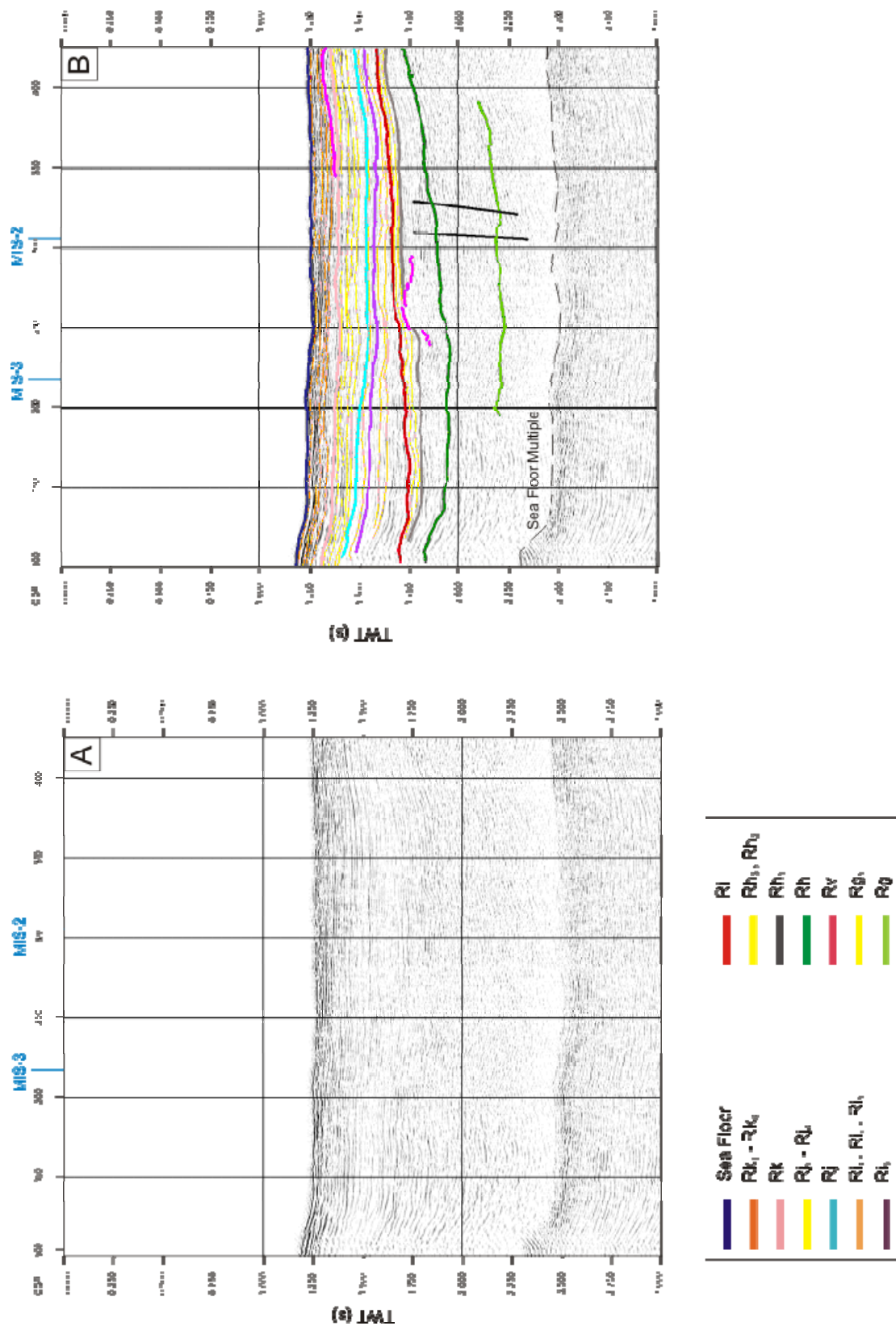
Figure 25. MIS-4 seismic line both non-interpreted (A) and interpreted (B). Larger figure can be found in Appendix F.
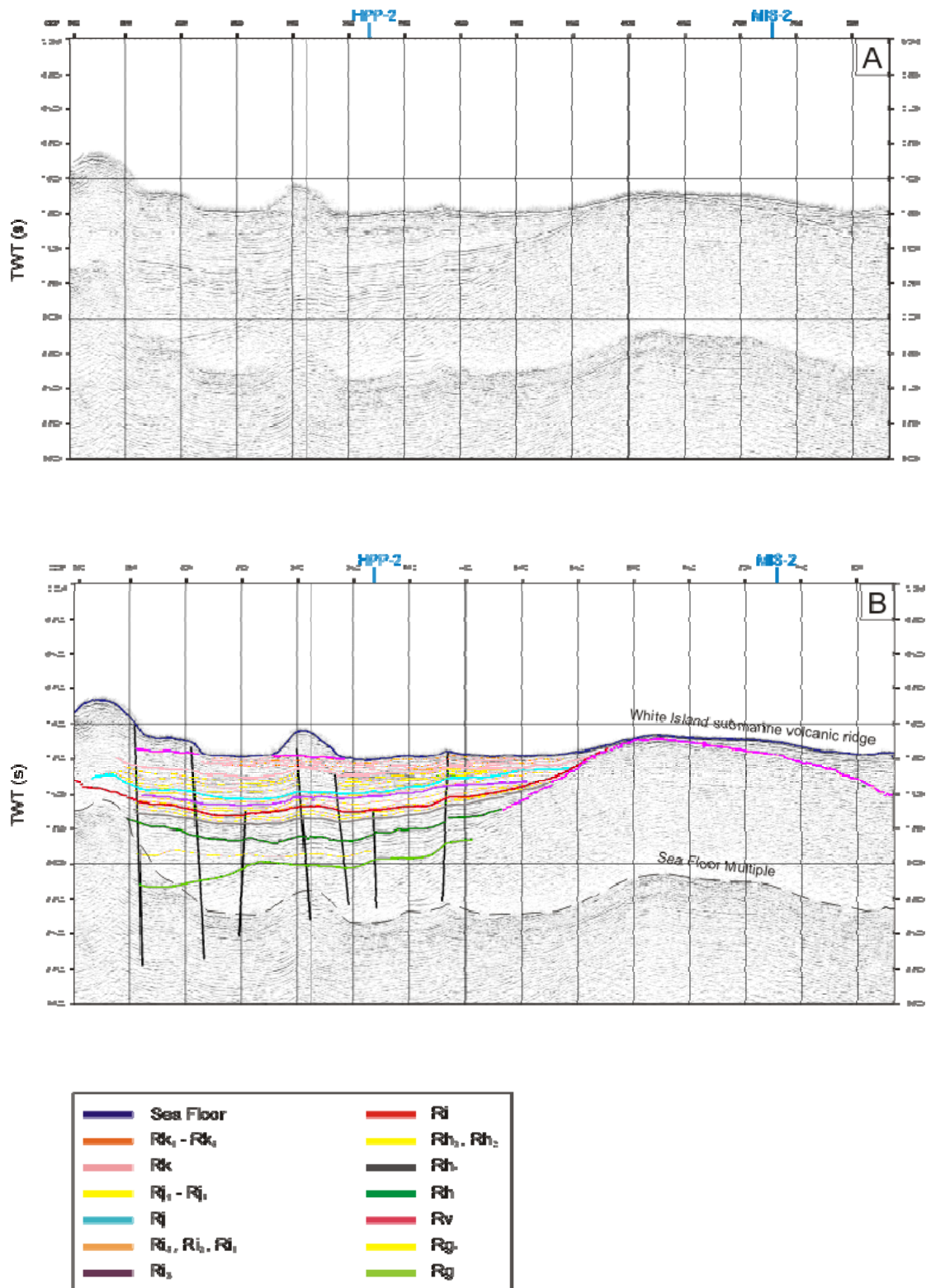
Figure 26. MIS-5 seismic line both non-interpreted (A) and interpreted (B). Larger figure can be found in Appendix F.
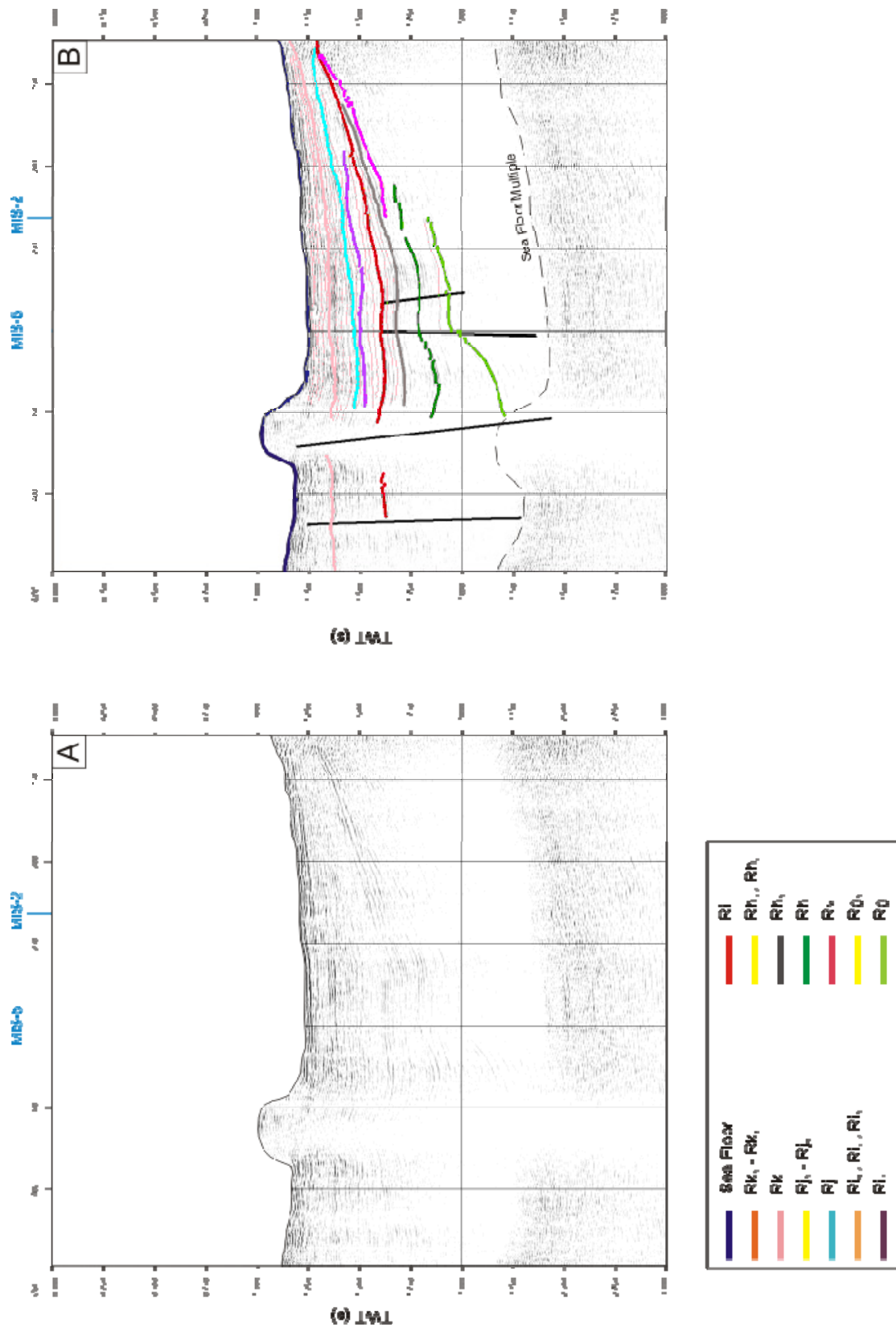
Figure 27. HPP-2 seismic line both non-interpreted (A) and interpreted (B). Larger figure can be found in Appendix F.
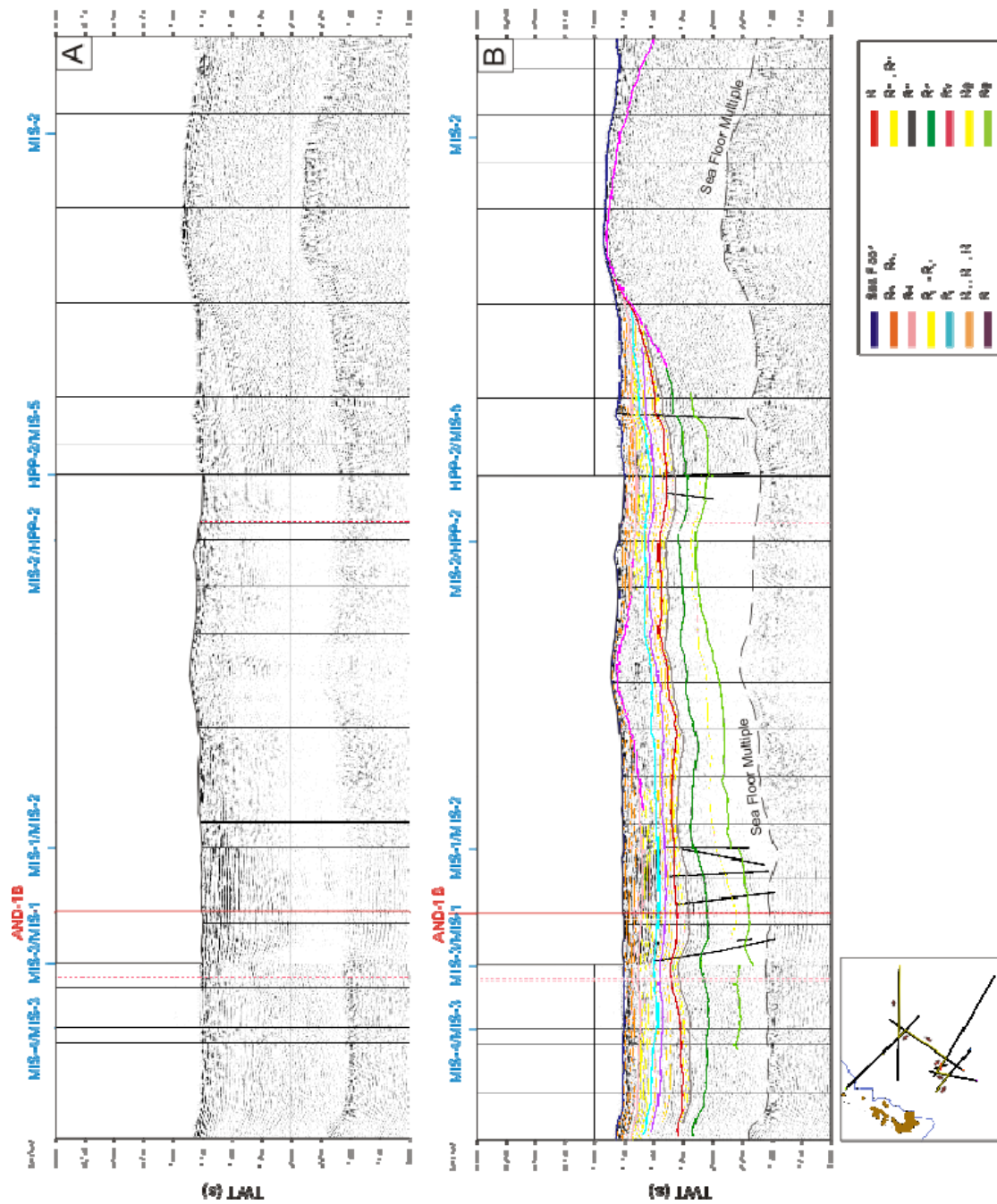
Figure 28. Non-interpreted (A) and interpreted (B) composite path across entire MIS seismic grid.

Inset shows path direction. Larger figure can be found in Appendix F.

Chapter 5: AND-1B Seismic-Well-Correlation

In the previous chapter, seismic sequence stratigraphic interpretations of the MIS seismic grid are presented independently of the AND-1B core and borehole data. In this chapter, a seismic-well correlation is established between the MIS seismic sections and the AND-1B core and borehole data, so that the stratigraphy can be extended away from the borehole. This is to provide a regional understanding of the depositional processes and controls interpreted for the borehole and core data (e.g. Naish et al., 2007aa). To achieve this, lithologic and physical properties data for the core and seismic data are integrated so that a correlation can be made between stratigraphic data (in depth) and seismic data (in two-way travel time).

For a conventional well-to-seismic tie all that is required is the development of a synthetic seismogram using borehole data, which can then be compared with surface seismic data. In order to develop a synthetic seismogram, sonic and density log data are required. Sonic data are a measure of travel times of seismic waves over a unit distance, and so are the reciprocal of P-wave velocity. These data can be acquired directly using a downhole sonic tool, but are also obtained from a check-shot survey. Check-shot surveys are a type of borehole survey designed to measure the seismic travel time from the surface to a known depth, and are used as a means to calibrate the sonic log data. Another way to do this is by conducting a vertical seismic profile (VSP), which is in essence a densely sampled check-shot survey. Using the best possible travel time data and downhole density measurements will produce a high-quality synthetic seismogram.

The well-correlation carried out for this study however was somewhat unconventional. Due to unstable borehole conditions, a density log was not run and due to a failure of the data acquisition system used to run the sonic tool, a sonic log was not run either (Morin et al., 2007). As a result, the synthetic seismogram was developed using whole-core physical properties measurements of P-wave velocity and wet bulk density. As the measurements were made on the recovered core, they are not an *in-situ* indication of density and velocity. Nevertheless they produced a very reasonable synthetic seismogram (Fig. 322) when compared to surface seismic data (i.e. the MIS-1 line) which provided the well correlation.

Due to the failure in acquiring a sonic log, the VSP was not used to calibrate sonic data. The travel time data it provided did however allow for the development of a time/depth curve. Further to this a suite of synthetic VSP's were also developed using whole-core density and velocity values. These VSP models served as a means to test for deviation in the well, and also aided in processing of the observed VSP dataset.

5.1 Lithostratigraphy

The AND-1B core represents a 1285 m-long succession of cyclic glacimarine sediment from the continental margin of Antarctica. It contains a range of lithologies, including both siliciclastic and volcanic diamictites, sandstones and mudstones; diatomites and biosiliceous bearing mudstones; and volcanic ash/tuff, with one phonolitic lava flow (Krissek et al., 2007). The primary lithologies within the core are diamictites, diatomites, and volcanic sediments and rocks. A lithostratigraphic description was developed based on differences in characteristics such as: abundance,

mineral content, biosiliceous content, colour, and texture/grain size. Accordingly, the cored sequence was subdivided into 8 lithostratigraphic units and 25 subunits to highlight these features (Fig. 299). Subunits were outlined based on smaller-scale lithologic differences observed during core description (Krissek et al., 2007) (Krissek et al., 2007).

Lithostratigraphic Unit (LSU) 1 is dominated by diamictites. LSU 2 is dominated by siliciclastic facies but contains a variety of lithologies, including volcanic sandstones and mudstones, volcanic ash/tuff, and mudstone-rich diatomaceous ooze. For this reason, LSU 2 is subdivided into three subunits. LSU 3 is a ~230 m thick unit dominated by alternating diatomites and diamictites. It is subdivided into six subunits. LSU 4 comprises a variety of lithologies, including diatomite, diamictite, mudstone, and volcanic diamictite; it is subdivided into four subunits. LSU 4 contains a ~80 m thick diatomite layer which records an extended period of open water marine conditions with little or no influence of glacial ice alternating with ice-proximal and sub-glacial deposits. LSU 5 is dominated by volcanic sediments (volcanic diamictite, volcanic sandstone, and volcanic mudstone), and includes a phonolitic lava flow ~2.8 m thick; this LSU is subdivided into four subunits. LSU 6 is dominated by siliciclastic diamictites and mudstones, which are separated into three subunits. LSU 7 is composed of volcanic sandstones and volcanic mudstones, whereas siliciclastic diamictite forms LSU 8 (For detailed description, see Krissek et al., 2007).

Figure 29. Composite log of core age, lithology/lithostratigraphic units, velocity and density profiles. Data sourced from ANDRILL-MIS Science Team (Krissek et al., 2007; Niessen et al., 2007).

5.1.1 Lithofacies

Lithofacies describe rock units in order to differentiate one from another, but also indicate the type of environment in which the unit was likely to have originated. AND-1B contains eleven lithofacies that range from open marine diatomites and mudstones, to turbidites, to ice-proximal massive and stratified diamictites (Krissek et al., 2007). Bed contacts, sedimentary structures and bed thickness, are also examined to distinguish lithofacies. The facies assemblage as a whole illustrates a progression from marine to sub-glacial environments of deposition. Facies 1 records the most distal (least influenced by ice) environment, ascending through to Facies 10 which records the most proximal (most ice influenced) environment. Facies 11 covers the range of volcanic rocks that are within the core and offers little information regarding glacial proximity (Krissek et al., 2007).

Facies 1 is a diatomite that is interpreted to record sedimentation in an open marine environment. Facies 2 is primarily a massive mudstone that is interpreted to record hemipelagic environments where suspension settling of sediments plays a significant role. Ice rafting is inferred from the poorly sorted sands and lonestone clasts. Facies 3 is an interstratified mudstone and sandstone, similar to Facies 2. However it contains inter-bedding that is interpreted to record hemipelagic sedimentation and distal to proximal sediment gravity flows, which could be due to grounding line processes or volcanic/tectonic activity. Facies 4 is a mudstone with dispersed clasts. It is interpreted to record an environment much like that of Facies 2, but with increased clasts sourced from floating ice. Facies 5 is interpreted to record a quiet-water setting. It is an interlaminated mudstone/siltstone/sandstone, with a distinct rhythmic nature

that may reflect interactions with tidal currents. Facies 6 is a sandstone but contains a clear volcanic influence and includes well-stratified sandstones and inter-bedded siltstones. Based on sedimentary structures and fining upwards beds, it is interpreted to be the deposits of turbidity currents. Facies 7 is a conglomerate and is unusual in the core. It is interpreted to be the product of submarine sediment re-deposition. Deformation of mudstone intraclasts within facies 7 suggests an interaction with grounded ice.

Facies 8 is a breccia also interpreted to have resulted from sediment re-deposition. The prominence of volcanic clasts and/or mudstone intraclasts in Facies 8, suggests a volcanic source. Facies 9 is a stratified diamictite and hence is interpreted to record a range of depositional environments including: ice rafting or debris flow deposition, rainout of basal glacial debris, or deposition beneath grounded ice. Facies 10 is a massive diamictite thought to have originated through sub-glacial deposition, though rainout from floating ice and deposition by mass flow are also possibilities. Facies 11 considers the volcanic rocks and sediments and includes volcanic diamictites, lapilli tuffs, and the singular phonolitic lava flow.

Sixty unconformity-bounded glacimarine sedimentary cycles have been identified, representing repeated advances and retreats of an ice sheet across the drill site during the Late Neogene (Krissek et al., 2007). Glacial surfaces of erosion (GSE's) mark disruptions between facies. Those facies immediately below a GSE display a range of deformation features, including physical mixing of lithologies, clastic intrusions, and faulting. Facies above these surfaces are typically diamictites and conglomerates, and are interpreted as subglacial tillites or near grounding-line glacimarine deposits. In

many cycles, the facies succession reflects retreat of the grounding line through ice shelf into open-ocean environments, followed by ice re-advance characterized by progressively more glacially-influenced facies in the upper parts culminating in a glacial surface of erosion (GSE) at the glacial maximum (Naish et al., 2007a).

On the basis of facies characteristics, three types of vertical facies successions or "sequence-motifs" have been identified (McKay, 2008). Each motif represents a distinct style of glacial-interglacial cycle which are being linked to major changes in ice sheet thermal regimes and climate (McKay, 2008; Naish et al., 2009).

(1) Sequence Motif 1 is dominated by massive, matrix-supported diamictite of sub-glacial origin which passes upwards into a thin, non-fossiliferous mudstone deposited under an ice shelf. The sequence contains no evidence of significant sub-glacial melt-water or erosion. They do however provide a stratigraphic signature of WAIS advance and retreat under cold, polar conditions.

(2) Sequence Motif 2 is characterized by a basal interval of sub-glacial to glacimarine diamictite that passes upwards through a relatively thin pro-glacial-marine interval into a diatom-bearing mudstone or diatomite deposited under open-marine conditions with little to no terrigenous input. The dynamic fluctuations between ice-grounded and open-marine environments offer a stratigraphic signature of ice advance and retreat under conditions warmer than present perhaps similar to west Greenland today.

(3) Sequence Motif 3 displays a retreat succession from sub-glacial diamictite upwards into a 5 to 10m-thick pro-glacial succession of stratified diamictite, graded-conglomerate and sandstone, turbidite, and/or rhythmically-stratified mudstone. These facies imply increased subglacial melt-water and terrigenous sediment supply by the WAIS, and/or the EAIS margin. Motif 3 is characteristic of higher melt-water

production during grounding line retreat, and from nearby terrestrial sources during interglacial times, than occurred during deposition of Motif 2.

A chronostratigraphic framework for the AND-1B core has been developed through sub-division into nine chronostratigraphic intervals; on the basis of the facies cycles (refer to Wilson et al., 2007 and Naish et al., 2007b). Interval 1 is a Late Miocene volcanic sandstone (1275.24-1220.15 mbsf), part of LSU 7. Interval 2 comprises Late Miocene diamictite-dominated sedimentary cycles (1220.15-1069.2 mbsf) which are part of LSU 6.4. Late Miocene, diamictite/mudstone and sandstone sedimentary cycles (1069.2-759.32 mbsf) define Interval 3. These cycles are part of LSU 6.1-6.3. Interval 4 contains a Late Miocene-Early Pliocene lapilli tuff, lava flow, and volcanic sandstone and mudstone (759.32-586.45 mbsf) that are also in LSU 5. Interval 5 contains Early Pliocene diamictite/diatomite sedimentary cycles (586.45-459.24 mbsf) also contained in LSU 4.2-4.4. Interval 6 is an Early Pliocene diatomite (459.24-382.98mbsf) also in LSU 4.1. Interval 7 comprises Late Pliocene diamictite/diatomite sedimentary cycles (586.45-146.79 mbsf), contained in LSU 3. Interval 8 is similar to Interval 7 and contains Late Pliocene-Early Pleistocene diamictite/volcanic mudstone and sandstone cycles (146.79-82.72 mbsf) that are in LSU 2. Finally, Interval 9 represents Middle-Late Pleistocene, diamictite-dominated sedimentary cycles (82.72-0mbsf) that are a part of LSU 1.

A preliminary age model derived from chronostratigraphic data is presently only available for the upper 700 m of the core. The data used for the model include diatom biostratigraphy, magnetostratigraphy, ^{40}Ar/^{39}Ar ages on volcanic material, ^{87}Sr/^{86}Sr ages on calcareous fossil material, and surfaces of erosion identified from physical

appearance and facies relationships (Wilson et al., 2007). As demonstrated above, a substantial degree of variability in lithologies is evident from the core. This is reflected in the broad range of values presented by physical properties data.

5.2 Physical Properties

The physical properties of rocks penetrated by a borehole provide important information for a geological understanding of reflectors in seismic sections and their patterns and variations (McQuillin et al., 1984). Whole-core physical properties including wet bulk density (WBD), P-wave velocity (Vp), and magnetic susceptibility (MS), were determined on-site during the drilling of AND-1B using a GEOTEK MSCL (Multi-Sensor-Core-Logger). On-site determination was necessary to characterize the core and correlate it with seismic modelling in order to predict target-reflector depths. The effects of cementation and the general down-core gradients as a result of sediment compaction can be identified from physical properties data. WBD and in particular Vp identify these effects, while magnetic susceptibility can be used to identify evidence of volcanism (Niessen et al., 2007).

P-wave velocities range from $1460ms^{-1}$ in unconsolidated mud at the top of the core to more than $7000ms^{-1}$ in large single clasts (Niessen et al., 2007). The distribution of Vp is bimodal and to some extent, biased towards higher values based on measurements made on individual clasts. This is due to anomalously high P-wave velocities, measured in clasts of core size or larger. Some high velocities may also be related to cementation and diagenetic alteration. The source of bimodality in the core relates to the cyclic behavior of the core, between lower velocity mudstones and

diatomites, and higher velocities diamictites and the rest of the core. There is an overall linear down-core gradient in Vp from $1791ms^{-1}$ at the top to $3188ms^{-1}$ at the bottom of the core. WBD ranges from $1.4gcm^{-3}$ and less in mudstones, diatomites and pumice, to up to about $3.7gcm^{-3}$ in large clasts. The distribution is bimodal for similar reasons to bimodality in Vp.

At the boundaries of the major stratigraphic units, a corresponding change in the physical properties can also be observed (Fig. 30). In general, the lower velocity/density characteristics of the diatomite layers, and higher velocity characteristics of the diamictite and volcanic layers are clearly represented. Significant changes in the physical properties are visible between LSU 2 and 3, from the diatomite/diamictite alternations within LSU 3, between LSU 4 and LSU 5, and within the thick volcanic sediments of LSU 5. For the diatomite/diamictite couplets within LSU 3, the increase in velocity and density is visible at the top of the diatomite/base of the diamictite layer. Variability within and between LSU's 6, 7 and 8 is less discernable.
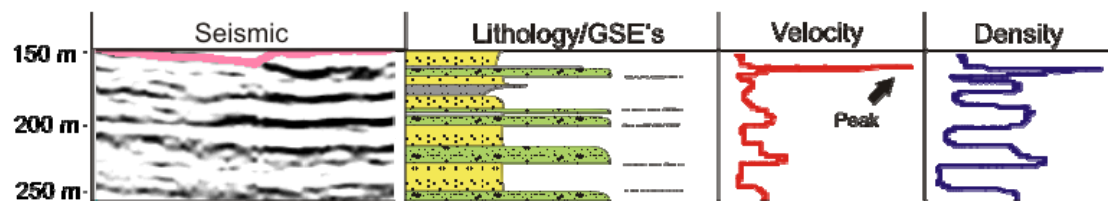
Figure 30. Upper section of LSU 2 displaying cyclicity between diamictite (green)/diatomite (yellow) versus depth in core and seismic. Seismic velocity and density variations occur synchronously with lithological changes. Peaks in both curves are seen at the base of the diamictite layers, which correspond to high-amplitude reflections in the seismic data. Diatomite sections correspond to troughs, and transitions to peak values in the curves.

For the purposes of the well-to-seismic correlation, the most significant physical properties were P-wave velocities and wet bulk density. Vp were converted to vertical acoustic travel times and used with wet bulk density data to produce the synthetic seismogram. Travel times were calculated by dividing the thickness (i.e. depth) of sections of core by the measured corresponding velocity measurement, and then multiplied by two. The accumulated travel times from core velocity measurements were also plotted against core depth to produce a time/depth curve (Fig. 31). Used in conjunction with the MIS seismic profile, the time/depth curves provide depth estimates to reflectors. The physical properties data proved essential in achieving a well-tie. They provided firm constraints on the interpretation of stratigraphic patterns, and allowed the construction of synthetic seismograms and validation of arrivals observed in vertical seismic profiles.

5.3 Synthetic Seismogram

A synthetic seismogram is an artificial reflection profile generated by passing a source wave through an assumed model of reflection points. Bulk density is mass per unit volume and is governed by the amount of water (porosity) in the *in situ* sediment. Velocity (m/s) is the speed a sound wave travels through the sediment. Core and downhole logging measurements such as magnetic susceptibility broadly agree with one another. This instilled some confidence in using core velocity and density measurements to develop the synthetic seismogram.
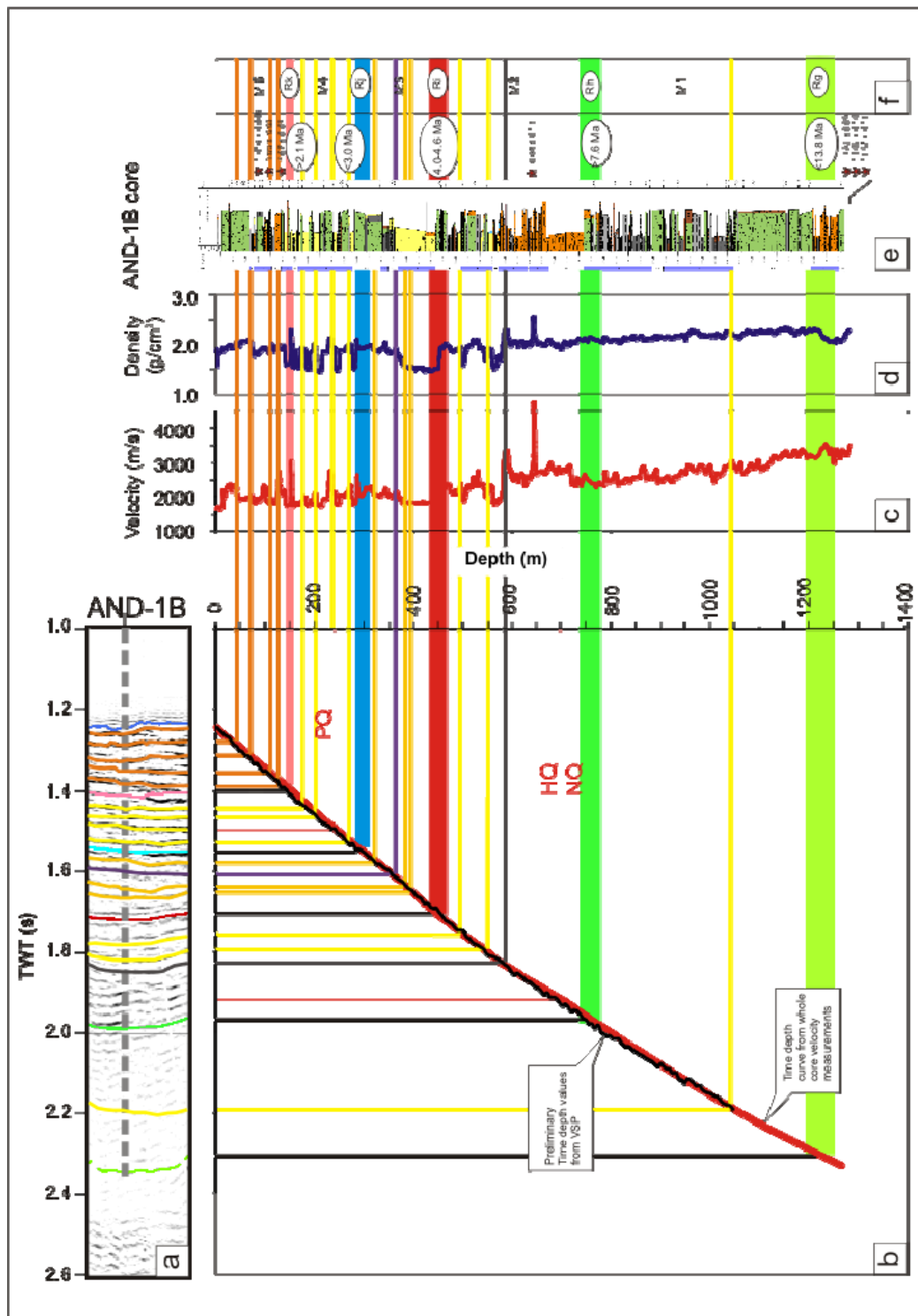
Figure 31. Integrated well-correlation diagram. Whole-core velocity (c) used to derive a time-depth conversion curve (b) to map the seismic reflection section (a) to depth. Core density data (d), lithological logs (e), and identified seismic stratigraphic units (f) are also shown.

Density and velocity data were imported into Schlumberger's GeoFrame™ software, which was used to create the synthetic seismogram (Fig. 32). An impedance profile (I) was calculated by multiplying P-wave velocity (υ) by density (ρ) → I = υρ. By comparing impedance values downcore, the reflection coefficient (R.C.) was computed. This was subsequently convolved with a source wavelet taken from the seismic data to derive a synthetic seismogram.

A number of different wavelets with different parameters were developed and tested, before choosing the optimal wavelet. A 30 Hz zero-phase normal polarity Ricker wavelet was originally used however this was unsuitable due to the frequency content of the data being much higher. The source wavelet was changed from being statistically derived to being deterministically derived as this extracts a wavelet using both the reflection coefficients and the source seismic data. The calculated synthetic seismogram was superimposed onto the MIS-1 seismic section at the location of the borehole where horizons were matched to seismic reflections. The amplitude of the synthetic seismogram corresponded closely with the variations in amplitude of the seismic reflection data. The reflection amplitudes were observed at the unconformity boundaries (or seismic surfaces) between sequences. The synthetic seismogram has only been calculated to a depth of ~850 mbsf, and not for the entire core.
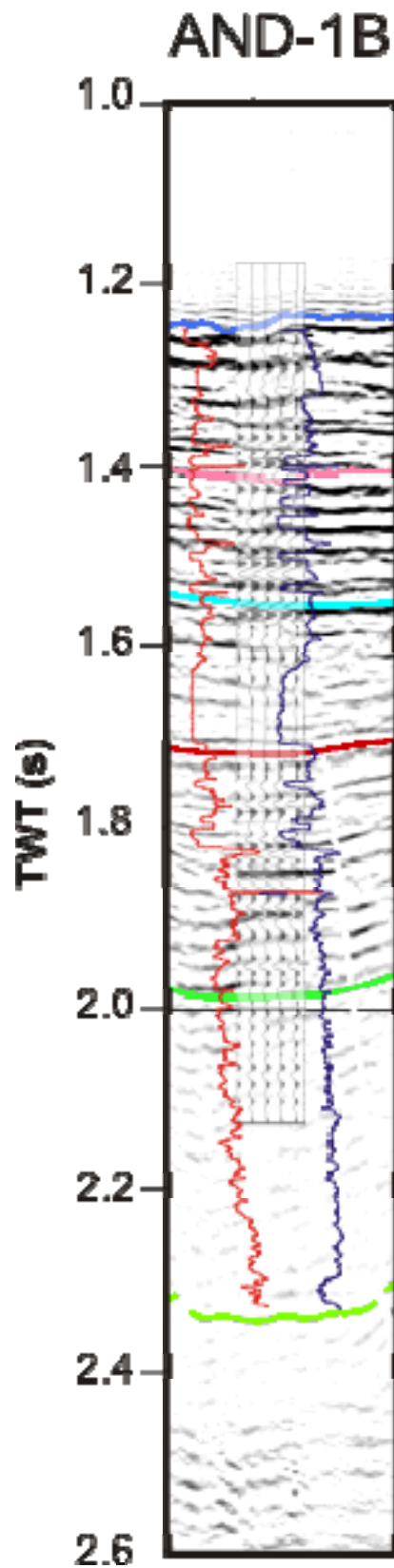
Figure 32. Synthetic seismogram, developed from physical properties measurements, and overlaid on MIS-1 at location of borehole. The red curve denotes velocity and is in time (s); the blue curve denotes density and is in g/cm^3.

5.4 Vertical Seismic Profile (VSP)

A VSP provides a level of resolution that lies between surface seismic data and well logging tools. It allows a direct correlation between two-way travel time and core depth. Vertical seismic profiles are useful because they provide an alternative travel time dataset compared to core velocity data, and can be used to validate the seismic tie with the well. This is important for comparisons with surface seismic data because of the need to correlate the borehole stratigraphy regionally. For this study, travel times from the VSP data were compared to the whole-core derived travel times and synthetic VSP's were calculated and are compared to observed data.

Picked first arrivals from the VSP provide an *in-situ* measurement of travel time with depth into the earth (Lizarralde and Swift, 1999). Because the core comprises of rocks that have been brought up from depth to the surface, the properties they exhibit are not strictly a representation of the true properties. Expansion of material due to differences in pressure and temperature can affect physical properties such as rock porosity, which influences velocity. A VSP time to depth estimate based on direct arrival observations has the significant benefit of being *in-situ,* looking at whole-rock volume from top to bottom, thus offering in some respects a more accurate velocity profile through the sub-surface. Due to the failure in acquiring a sonic log, for this study it was decided not to compute a velocity derived from VSP data but instead compare the time/depth curve from the whole-core samples, directly with the first arrival times. For a fair comparison to be made, the core data was tested for any bias towards higher velocities. Since the velocity data from the core were created from actual measurements, there was the possibility that the velocities were biased towards

higher values based on measurements made on clasts (refer to section 5.2). To account for this, the core data was re-sampled and median filtered at 5 m increments, before comparison with the VSP picks time/depth curve. The two curves match very closely (Fig. 333) apart from two areas (sections A and B) which are explored by comparing the observed data with a synthetic VSP. First arrival picks have an error estimate of ±10 ms and an RMS error value of 0.02547.
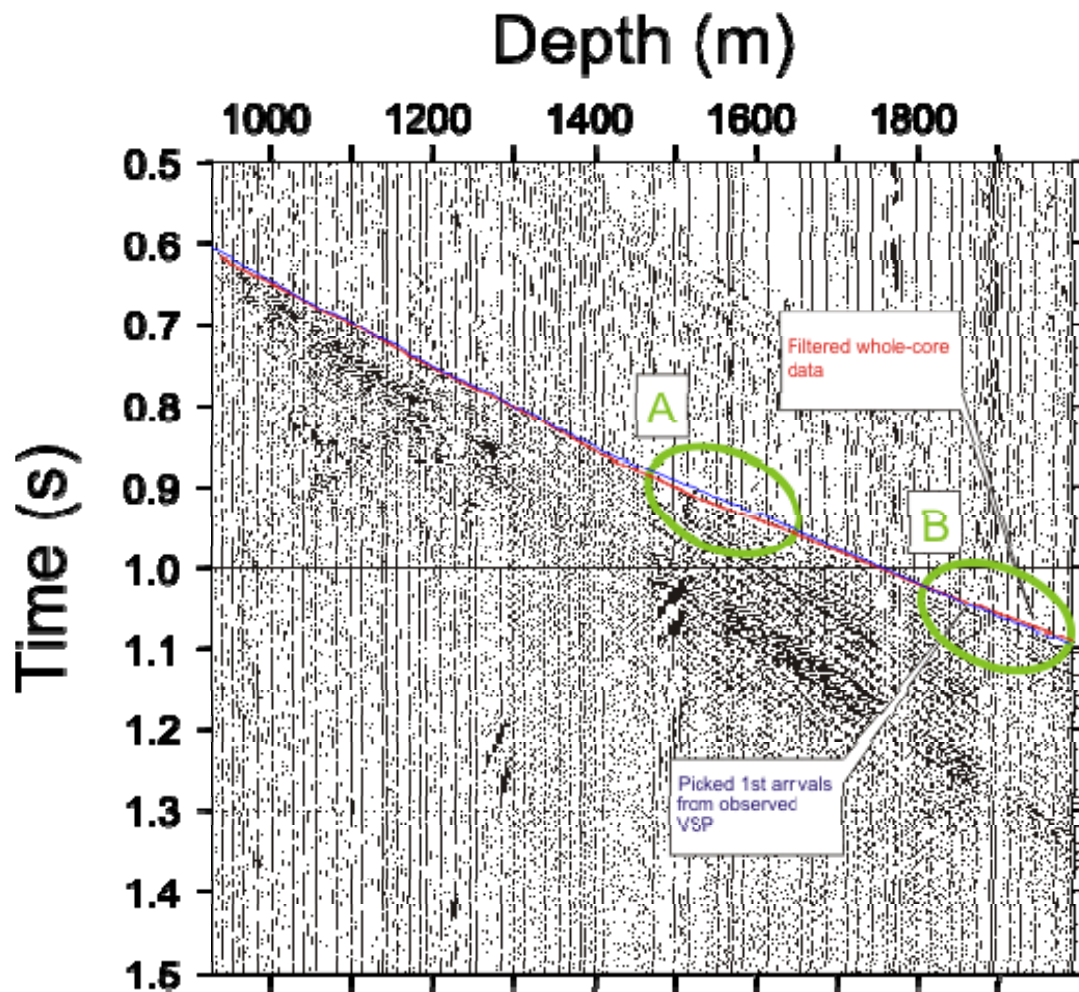
Figure 33. Comparison of time/depth curves between filtered whole-core velocities and observed picked first arrivals. A and B identify areas of mismatch between the curves.

To identify the source of events in the observed VSP section (refer to chapter 3), a suit of synthetic VSP's were employed.

5.4.1 Synthetic Vertical Seismic Profile

The main advantage of a synthetic profile is its ability to allow comparison of observed data and help to identify the source of arrivals in observed coda. This study has employed Fortran code based on a finite difference representation of the acoustic wave equation (Levander, 1989). The wave equation is a second-order linear partial differential equation that describes the propagation of waves with speed. A finite-difference approach based on the elastic wave equation takes into account the relative amplitudes of the different arrivals, and also includes the effects of converted waves, Rayleigh waves, diffractions and head waves. For this study however, the finite-difference approach was based on the much simpler acoustic wave equation; that is, only the P-wave and density values. Calculation of the synthetic seismograms required a velocity/density grid created as plane layers using whole-core P-wave velocities and averaged layers with a 1 m thickness. The extent of the model was 2 km long and 2.5 km deep. An ice layer 80 m thick and a 900 m deep water layer were introduced into the top of this subsurface model. The grid spacing adopted was 1 m, in order to avoid "grid dispersion". If the grid is too coarse, "grid-dispersion" occurs whereby the signals computed by the finite-difference method become strongly dispersed (Alford et al., 1974).

In addition, the synthetic VSP's helped in designing further processing steps (e.g. *f-k* filtering) for applying to the observed data. Thirteen models (Table. 7) were developed and these were designed to test the effect of well deviation, layer dips and for the presence of converted waves. Although the code was acoustic, we could simulate the presence of direct S-waves by assuming Poisson's ratio ($Vs = \sqrt[3]{Vp}$).
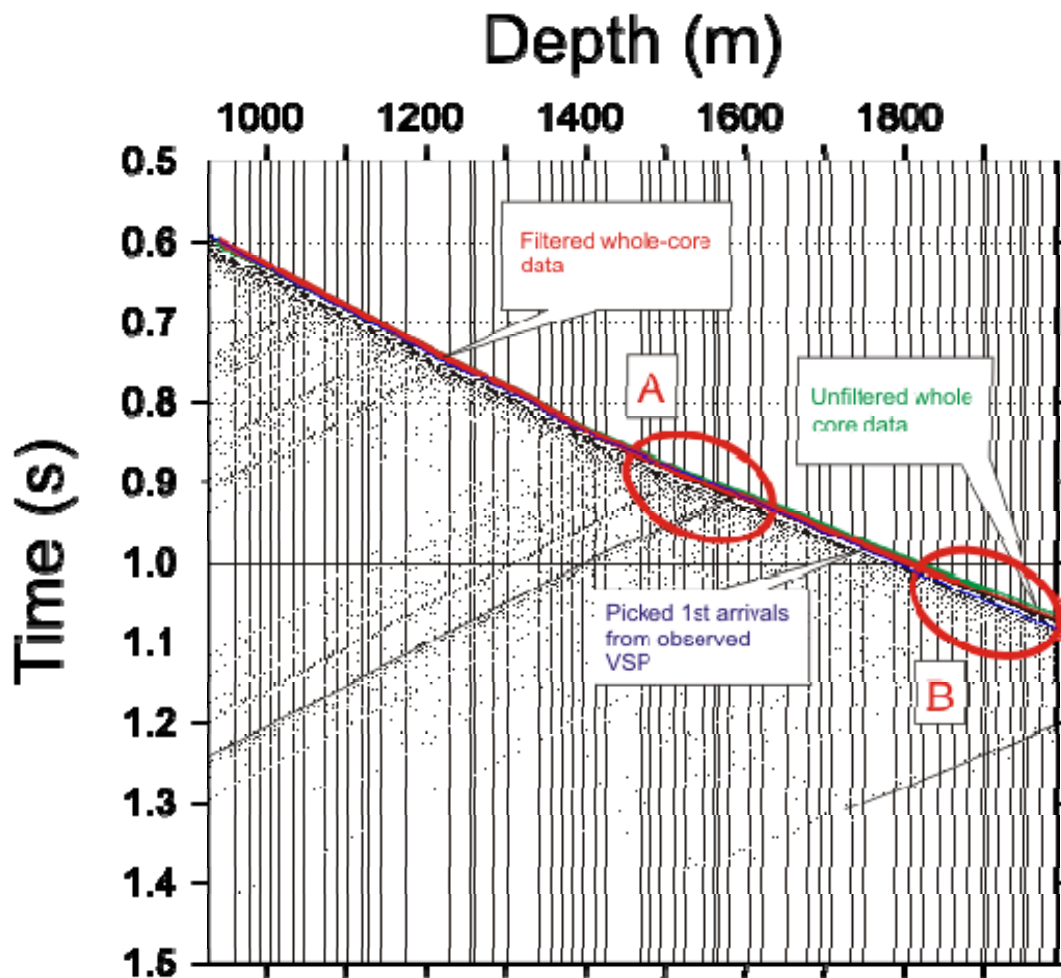
Figure 34. Comparison of time/depth curves from whole-core velocities (both filtered and unfiltered), and observed picked first arrivals. A and B identify areas of mismatch between the curves.

Figure 34 shows the standard P-wave synthetic superimposed with whole-core values (both filtered and unfiltered) and picked first arrivals from the observed data. A reasonable match exists between the observed and synthetic data but two areas of mismatch are identified (refer to Fig. 33). It is important to note that direct comparison of whole-core velocities to those measured from the VSP data is difficult due to frequency dependent dispersion resulting from both scale and rock property dependent effects (Sams et al., 1997). The first mismatch (A) is due to poor data quality over the depth range ca. 600 mbsf and thus poor quality picks of the first arrivals, while the second mismatch area (B) towards the bottom of the well suggests that it may be deviated.

Table 7. Summary of parameters used to develop modelled synthetic VSPs.

Model	Parameters	Comments
Standard P-wave	No well deviation, P-wave only, no dipping layers at depth, non-tilted strata, ~80 m offset	Original data, no alteration of or additional parameters
Zero-offset	No well deviation, P-wave only, no dipping layers at depth, non-tilted strata, zero-offset	Source simulated directly over borehole
Dip 1	No well deviation, P-wave only, bottom layer dipping, zero-offset	One layer at 1283 mbsf dipping west at 18°
Dip 2	No well deviation, P-wave only, bottom layer dipping, zero-offset	One layer at 1283 mbsf dipping east at 18°
Deviation 1	5° well deviation, P-wave only, no dipping layers at depth, non-tilted strata, ~80 m offset	Entire well deviated by 5° from surface
Deviation 2	15° well deviation, P-wave only, no dipping layers at depth, non-tilted strata, ~80 m offset	Entire well deviated by 15° from surface
Tilt 1	5° well deviation, P-wave only, no dipping layers at depth, tilted strata, ~80 m offset	Strata tilted west at 10°
Tilt 2	5° well deviation, P-wave only, no dipping layers at depth, tilted strata, ~80 m offset	Strata tilted east at 10°
Tilt 3	No well deviation, P-wave only, no dipping layers at depth, tilted strata, ~80 m offset	Strata tilted west at 10°
Tilt 4	No well deviation, P-wave only, no dipping layers at depth, tilted strata, ~80 m offset	Strata tilted east at 10°
Tilt 5	No well deviation, P-wave only, no dipping layers at depth, tilted strata, zero offset	Strata tilted west at 10°
Standard S-wave	No well deviation, S-wave only, no dipping layers at depth, non-tilted strata, ~80 m offset	P-wave velocities converted to S-wave velocities
Standard P- and S-wave	Combined standard P-wave model and standard S-wave model	Displays area of P- to S-wave conversion

Down-hole logging over the depth range from 692 to 1018 mbsf indeed documented a deviation in the well of ~2.2° in a west-northwest direction (Morin et al., 2007). Synthetic modelling of a 5° deviation improves the match between the observed and synthetic time/depth curves (Fig. 355) and broadly agrees with the deviation from logging data. Other models, using larger values of deviation (up to 15°), were tested but did not improve the fit to the observed data. The effect of tilted strata (not shown) was also found to be insignificant.

Figure 35 fold-out
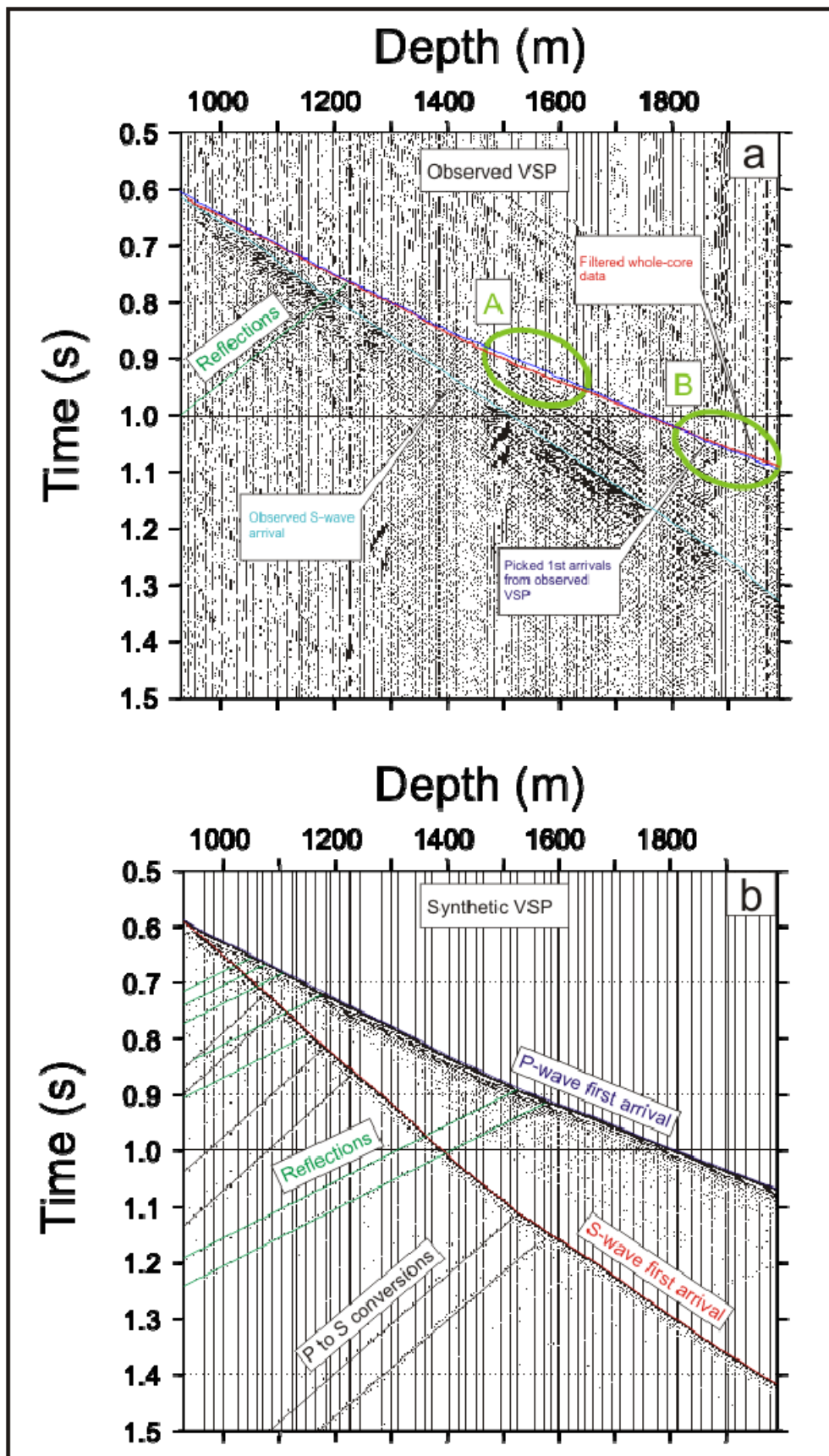
Figure 36. (a) Observed VSP outlining P- and S-wave first arrivals, and reflections. Travel time curves for whole-core and P-wave first arrival picks are also shown (b) synthetic P-wave time/depth curve overlaid on synthetic S-wave time/depth curve.

A final synthetic VSP was made using S-wave velocities instead of P-wave velocities. The time/depth curve for this model, overlaid on the curve for the P-wave model, clearly highlighted the P- to S-wave conversions that are dominant in the data (Fig. 36). Figure 36 shows both the observed and synthetic VSP's. It outlines the time/depth curves derived from P-wave first arrivals, but also indicates the S-wave arrival. Reflections from P-wave data are shown as well as the area of P- to S-wave conversions below the S-wave arrival. A high amplitude wavetrain can be observed following the direct arrival; these are the P-S conversions.

5.5 Well-correlation

A successful correlation of the AND-1B stratigraphy to the MIS-1 seismic line allows a 3-D regional understanding of the stratal geometries within the broader Ross Sea region to be established. This will help refine the stratigraphic framework for the VLB, especially via the ability to calibrate seismic data with actual lithological and age information. This correlation can also serve as a critical link to both previous and future sedimentary record investigations in Antarctica.

The Rg surface is correlated with the top of m thick interval of Late Miocene volcanic sandstone, and the base of a thick diamictite interval (Fig. 31). This surface was the deepest distinguishable on the seismic sections, and was used as a final depth target during the drilling of AND-1B. $^{40}Ar/^{39}Ar$ ages on the volcanic interval indicate an age of between 13.5 Ma and 13.8 Ma for the Rg surface (Wilson et al., 2007b). Rg_1, despite only being traceable through MIS-1 and a section of MIS-2, can be correlated to the top of a ~150 m thick diamictite layer which marks cooler conditions

and polar style glaciation at the base of the core. This corresponds to LSU 6.4. Rh is correlated with the base of a ~180 m thick interval of pyrite-cemented, volcanic sandstone and mudstone. The Rh_1 horizon, located above Rh and within seismic unit M2, corresponds to the top of this volcanic interval. As Rh_1 can be traced through the entire MIS seismic grid, it represents a localised regional 'volcanic apron' perhaps associated with White Island volcanic eruptions. The Ri surface correlates in the core to the base of the ~90 m thick diatomite unit within LSU 4. The purple Ri_3 horizon within seismic unit M3 indicates the top of this diatomite section. Both surfaces can be clearly distinguished throughout the seismic grid. Based on the opaque homogenous character of this seismic interval (between Ri and Ri_3), it is interpreted that the diatomite interval is regionally extensive in the study area.

Rj correlates to the base of seismic unit M4, within which four high amplitude reflectors are visible (Rj_1 to Rj_4). These reflectors correlate closely to regular alternations between diatomite and diamictite in the AND-1B core. Variations in density and velocity measurements (Fig. 30) complement the observed diatomite/diamictite couplets. The Rk seismic surface marks the top of the diatomite-diamictite cycles of LSU 3, but also correlates to the base of seismic unit M5, within which four high amplitude reflectors have been interpreted (Rk_1 to Rk_4). Correlating these to the core, the layers relate to the diamictites of LSU 1 and the variety of lithologies, including volcanic sandstones and mudstones that comprise LSU 2.

With the confirmation of reasonable seismic stratigraphic interpretations provided by the well-correlation, a discussion can now be made of the implications this has on the tectonic and climatic evolution of the southern Terror Rift.

6: Discussion and Conclusions

An interpretation of seismic stratigraphic architecture within the southern Terror Rift requires an understanding of fundamental aspects of both the tectonic and climatic influences on their deposition. Firstly, tectonism in the form of active rifting in the WARS has led to the formation of the VLB. This is the first order control on subsidence and the production of accommodation for sediment accumulation. Over time the architecture of the accumulating sediments is influenced by higher-order tectonic processes such as volcanism and intra--basinal faulting, together with climatic processes such as the advance and retreat of grounded ice sheets across the seabed and changing global sea level. As a result, the sediments contain a complex signature of both tectonism and climate.

In this chapter, seismic stratigraphy is reassessed within the context of temporal and geological control provided by the AND-1B core. This allows an evaluation of the spatial extent and geometry of the strata within a robust temporal framework provided by an integrated chronostratigraphy (e.g. Wilson et al., 2007). In doing so this chapter provides a synthesis that contributes to the evolving tectonic model of the Terror Rift (e.g. Fielding et al., 2008), and also identifies climatic events related to the Late Cenozoic evolution of the Antarctic ice sheets. Figure 37 summarises the controls on the Late Cenozoic stratigraphy described in this thesis.

6.1 Tectonic Implications

The entire Late Cenozoic section (< 13.8 Ma) overlying the Rg reflector tapers to the eastern and western margins of the VLB, but thickens into a central depocentre where it is intruded by magmatic rocks related to the McMurdo Volcanic Group (Fig. 2). Based on this geometry, as well as the presence of young faults offsetting strata within the overlying succession, Rg has been interpreted to represent the onset of renewed rifting in the VLB (Fig. 37); the Terror Rift phase (Cooper and Davey, 1985). Dating of volcanic clasts at the depth of the Rg reflector in the core, indicates a maximum age of between 13.5 Ma and 13.8 Ma (Wilson et al., 2007b). This provides the first robust constraint for the reflector and dates the onset of Late Cenozoic rifting in VLB following a period of thermal subsidence. Based on correlations of VLB seismic horizons with the dated Cape Roberts Project core, previous age estimates of the Rg reflector have been 'less than 17 Ma', but older than about 5 Ma (Fielding et al., 2008 and Naish et al., 2006).

In the core, Rh is correlated with the base of a ~180 m thick interval of pyrite-cemented, volcanic sandstone and mudstone. It is locally associated with products of the White Island volcanic massif and is overlain by a thick accumulation of Plio-Pleistocene glacimarine and volcanic sediments. This strongly suggests its formation was in some part due to the initiation of the Terror Rift. Rh has an estimated age of 7.65 Ma, based on the age of White Island (Cooper et al., 2007). In regional seismic data, substantial changes in both cross-sectional geometry and internal seismic facies are evident at the Rh surface and in the overlying M2 seismic unit.

Regionally it records relative uplift along the western margin of the VLB and possibly represents a major rift-related subsidence event. This interpretation is based on similarities with a study presented by Japsen et al. (2006). Rift flank uplift and subsequent erosion often result in higher volumes of sediment being deposited in adjacent basins. These sediments can be recognised in seismic facies as prograding sequences, with well-developed off-lapping clinoform geometry. Given the evidence of uplift on the western margin of the VLB (Wrenn and Webb, 1982), substantial sediment input from erosion at the TAM Front, and the resulting prograding sequence between the Rh and Ri reflectors observed in the cross-sectional geometry of the central VLB, the process described by Japsen et al. (2006) is considered plausible. Tied to this explanation is the knowledge that warmer conditions existed post-Rh, which suggests that the higher volumes of sediment were also due to climatic influences.

The Ri reflector marks a major basin-wide disconformity and is interpreted to be a regional deepening event (Fielding et al., 2008; Henrys et al., in press). Locally, it is coincident with the onset of loading of the crust by Mt. Bird as part of the Ross Island volcanic pile (Fig. 37) (Horgan et al., 2005). Ri has an attributed age of 4.63131 Ma (Wilson et al., 2007b). The Ri to Rj interval (unit M3) is regionally interpreted by Fielding et al. (2008) to reflect further clastic sediment input to the basin, especially north of Ross Island in the McKay Glacier region. Sediment packages are observed to thicken eastward across the basin, which is consistent with a western basin margin sediment source. This accumulation formed a broad, flat shelf which extends ~25 km eastward across the western slope of the basin (Fielding et al., 2008).

In the vicinity of the drill site, the region was once dominated by the accumulation of a thick pelagic diatomite. This is incongruous when compared to the northern Terror Rift where the diatomite is not present, but may simply be a reflection of the position of the drill site east of the Dry Valleys. Sugden and Denton (2004) have shown that little change occurred to the landscape in the Convoy Range to Mackay Glacier area of the TAM since 13.6 Ma. This suggests that sediment was not actively being produced and thus deposited into the western Ross Sea, which could explain how the drill site location in the southern Terror Rift was able to accumulate such a thick diatomite interval, while coeval terrigenous sediments prograded eastwards into the basin to the north.

Following substantial depression of the crust over ~1 million years, the Rj reflector represents the horizon most influenced by Ross Island flexural loading. Dating from the AND-1B core, constrained by biostratigraphy, places the age of this reflector at approximately 3.0 Ma. This supports the age for the Kaena paleomagnetic Subchron (Wilson et al., 2007b). The results from dating core samples greatly improve the age estimates for seismic units inferred by Horgan et al. (2005) prior to drilling. Above the Rj surface there is a distinct lack of tectonic signatures, and the progradational geometries from the west are no longer present. Any hint of progradation above Rj, appears to be from the south (basin axial). Furthermore, a reduction in sedimentation is also evident above Rj.

6.2 Climatic Implications

Unconformity bound stratigraphic sequences identified from previous drilling projects in the McMurdo Sound region, offer evidence for continental scale glacial advance and retreat during the late Paleogene and early Neogene (Barrett, 1989; Cape Roberts Project, 1998, 1999, 2000; Naish et al., 2001). The AND-1B core reveals these fluctuations at high resolution with more than 60 glacial-interglacial cycles visible within the14-0 Ma record (Naish et al., 2007a). These are interpreted as the result of fluctuations in the marine-based grounding lines of the Antarctic ice sheets, particularly the WAIS, and imply a dynamic nature in the western Ross Sea during the Late Cenozoic.

Every cycle consists of a Glacial Surface of Erosion (GSE) at its base caused by erosion of the sea-bed by the advancing ice sheet, and many cycles display a succession whereby the GSE is overlain by coarse, ice proximal sediments which fine upwards into deposits reflecting warmer, and often open-water marine conditions when the grounding line had retreated from the Ross Sea. In some cycles the facies succession continues by passing into deposits that reflect pro-glacial grounding-line environments during ice re-advance. However, these pro-glacial deposits are often removed by the ice sheet leaving another GSE. This description of the cycles indicates a retreat of the groundling line and is based on vertical stacking patterns of facies observed in the core (Krissek et al., 2007).

For intervals in AND-1B where diamictite is interpreted as sub-glacial till, grounded ice occupied the MIS drill site location. Although clast provenance indicates that this

ice is sourced from the EAIS (Pompilio et al., 2007) via outlet glaciers to the south of Minna Bluff, glaciological reconstructions (Denton and Hughes, 2000) require an expanded WAIS to act as a buttress in order to divert EAIS ice to the drill site location. For this reason the drill site location, and thus the AND-1B core, is believed to record fluctuations in the WAIS.

While the resolution of seismic data is low compared to core observations, our core/borehole to seismic correlations (refer to chapter 5) allow correlation of a number of surfaces distinguished within the core into the seismic data and their local 3-D architecture to be evaluated. While we have invoked a tectonic origin for a number of the horizons, all of the seismic surfaces identified by this study (Rg_1 to Rk_5) correlate with known global and local climatic events (Fig. 37) during the past ~14 Ma, except for the Rh_1 surface which simply marks the top of a volcanic section within the core.

The AND-1B core has been divided into essentially five climatically distinctive sections, with each section representing a unique interval of paleoenvironments. These paleoenvironments characterise the condition and behaviour of the WAIS in the western Ross Embayment (Naish et al., 2007a). The sections chronologically correspond to: (i) a Late Miocene interval (14-9 Ma); (ii) a latest Late Miocene interval (9-5 Ma); (iii) an Early Pliocene (5-3.6 Ma) interval; (iv) a Late Pliocene interval (3.6-1.8 Ma) and (v) a Middle-Late Pleistocene interval. Glacimarine cycles dominated by diamictite in the Late Miocene and Pleistocene sections of the core are similar in appearance and in the conditions that they represent namely, a cold polar,

grounded ice sheet whose glacial phases are interrupted by interglacial periods that produce proximal grounding lines and ice shelf conditions.

The association of cold-based glaciation and ice sheet expansion with cycles in the stratigraphic interval directly overlying the Rg reflector suggests a glacial/climatic influence in addition to subsidence associated with renewed rifting. Glacial erosion of the sea-bed at this time (~14 Ma) is also consistent with evidence for scour, incision and truncation of underlying strata. This interval corresponds to a major positive shift in the oceanic $\delta^{18}O$ records inferred as significant Antarctic cooling and expansion of the EAIS (Flower and Kennett, 1995; Billups & Schrag, 2002). Moreover it marks the transition from wet-based to dry-based tills in the Dry Valleys (e.g. Marchant et al., 1993).

The Late Miocene and Early Pliocene intervals have glacimarine cycles with dramatic oscillations between sub-glacial and open marine environments with significant quantities of terrigenous sediment interpreted as a dynamic and wet-based grounding line in the western Ross Sea. The inference of a warm, wet-based ice sheet during the latest Miocene is consistent with observations of age-equivalent sediment cores from the Prydz Bay region by Grützner et al. (2003), which provides evidence for a dynamic and likely wet-based late Miocene EAIS margin that underwent size variations at orbital time scales. The seismic data from this study do not show a major surface that is mappable through the entire grid separating cold-based glacial cycles from warm-based glacial cycles, however the Rg_1 seismic surface which is only weakly visible along MIS-1 does coincide with the separation between a thick diamictite layer and the onset of the warm wet-based Late Miocene glacial cycles.

The Ri surface has been tectonically interpreted as a regional subsidence event. From a climatic perspective it represents a transition to an extended period of open-water in western Ross Sea that spanned up to 300 000 years implying reduced ice on West Antarctica and a local terrestrial ice margin along the Victoria Land coast. Evidence for this comes from the thick diatomite deposit that directly overlies Ri, which represents a regional retreat of the ice sheet grounding line at the location of the drill site, warmer ocean conditions, and increased planktonic production. The deposition of such a thick unit requires a sustained period of open-water conditions which span at least six obliquity cycles (~250 kyr).

The Late Pliocene glacial-interglacial cycles identified in this study (Rj_1 to Rk_4) offer dramatic evidence relating to the climatic and ice sheet variability of the region around the drill site. Chronology and core stratigraphy indicate that these surfaces are Milankovitch cycles representing retreat and advance of the WAIS in the western Ross Embayment. A reduced terrigenous sediment input at the transition into pelagic interglacial units supports a cooling thermal regime of the ice sheet, coincident with the onset of major Northern Hemisphere continental glaciation. The Rj seismic surface (~3.0 Ma) may also represent this major cooling and the transition from a polythermal, cyclic ice sheet to the modern polar ice sheet. A lower sedimentation rate above Rj as well as the loss of the distinctive westerly progradation patterns (clinoforms) observed pre- Rj, support a cooling and stabilisation of the ice sheets as they expanded onto the continental shelf (Rebesco et al., 2006).

Lastly, those surfaces above the Rk surface (Rk_1 to Rk_4) are indicative of an established stabilized ice sheet through the high-amplitude reflections from seismic

data, and their correlation to polar diamictite dominated sequences within the AND-1B core. The expression of these lithological cycles in density and velocity data as well as seismic data, and their lateral continuity is consistent with a continuous advancing and retreating ice margin.

6.3 Further Work

The full dataset used for this study can provide insights to further investigations such as the intricate relationship between tectonism and climate and its influence on the geological and glaciological evolution of the western Ross Sea, Antarctica. This includes determining the origins of discontinuities and their relationship to Ross Island volcanism and subsidence in the vicinity of the drill site. These data can also be used to help understand the Neogene rifting in the VLB and the implications this has for East-West Antarctic plate motion.

References

Alford, R.M., Kelly, K.R., Boore, D.M., 1974. Accuracy of finite-difference modelling of the acoustic wave equation. *Geophysics*, v.39, 6: 834-842.

Anderson, J.B., 1999. *Antarctic Marine Geology*. Cambridge University Press, London, 289 pp.

Balfour, N., 2002. Seismic Reflection and Interpretation on the McMurdo Ice Shelf, Antarctica. BSc Honours thesis, Victoria University of Wellington, Wellington, 50 p.

Bannister, S., 1993. Seismic investigation of the Victoria Land Basin under Ross Island: New Zealand Antarctic Programme 1992/93, Event 101: Institute of Geological & Nuclear Sciences science report, v. 93/14, p. 16 p.

Bannister, S.C., Naish, T.R., 2002. ANDRILL site investigations, New Harbour and McMurdo Ice Shelf, southern McMurdo Sound, Antarctica: Institute of Geological & Nuclear Sciences science report, v. 2002/01, p. 24 p.

Barrett, P.J., 1989. Antarctic Cenozoic History from the CIROS-1 drillhole, McMurdo Sound, Antarctica. *DSIR Bulletin*, v.245, pp 251.

Barrett, P.J., Adams, C.J., McIntosh, W.C., Swisher, C.C., Wilson G.S., 1992. Radiometric ages support Antarctic deglaciation around three million years ago, *Nature*, 259: 816-818.

Barrett, P. J., 1996. Antarctic paleoenvironment through Cenozoic times - a review. *Terra Antartica*, 3: 103–119.

Barrett, P., 1999. Antarctic Climate History over the Last 100 Million Years. *Terra Antarctica Reports*, 3: 53-72.

Barrett, P.J., Davey F.J., Ehrmann, W.U., Hambrey, M.J., Jarrard, R., der Meer, J.J.M. van, Raine, J., Roberts, A.P., Talarico, F. and Watkins, D.K., 2001. Studies from the Cape Roberts Project, Ross Sea, Antarctica, Scientific Results of CRP-2/2A, Parts I and II. *Terra Antartica*, 7 (4/5), (665 pp.).

Barrett, P.J., Carter, L., Damiani, D., Dunbar, G.B., Dunker, E., Giogetti, G., Harper, M.A., McKay, R.M., Niessen, F., Nixdorf, U., Pyne, A.R., Riesselmann, C., Robinson, N., Hollis, C., 2005. Oceanography and sedimentation beneath the McMurdo Ice Shelf in Windless Bight, Antarctica. *Antarctic Data Series No. 25* A Publication of the Antarctic Research Centre: Victoria University of Wellington PO Box 600, Wellington, New Zealand.

Bartek, L.R., Andersen, J.L.R., Oneacre, T.A., 1997. Substrate control on distribution of subglacial and galciomarine seismic facies based on stochastic models of glacial seismic facies deposition on the Ross Sea continental margin, Antarctica. *Marine Geology*, 143: 223-262.

Behrendt, J., Cooper, A., 1991. Evidence of rapid Cenozoic uplift of the shoulder escarpment of the Cenozoic West Antarctic Rift System and a speculation on possible climate forcing. *Geology*, 19: 315-319.

Behrendt, J.C., LeMasurier, W.E., Cooper, A.K., Tessensohn, F., Trehu, A., Damaske, D., 1991. Geophysical studies of the West Antarctic Rift System: *Tectonics*, 10: 1257-1273.

Behrendt, J.C., 1999. Crustal and lithospheric structure of the West Antarctic Rift System from geophysical investigations - a review. *Global and Planetary Change*, 23: 25-44.

Billups, K., Schrag, D.P., 2002. Paleotemperatures and ice volume of the past 27 Myr revisited with paired Mg/Ca and $^{18}O/^{16}O$ measurements on benthic foraminifera. *Paleoceanography*, v. 17, no.1, 1003.

Brancolini G., Cooper, A.K., Coren, F. 1995a. Seismic facies and glacial history in the Western Ross Sea (Antarctica). In: Cooper, A.K., Barker, P.F., Brancolini, G. (Eds.), *Geology and Seismic Stratigraphy of the Antarctic Margin*. Antarctic Research Series, vol. 68. American Geophysical Union, Washington, D.C., pp. 209-233.

Brancolini G., Busetti, M., Marchetti, A., De Santis, L., Zanolla, C., Cooper, A.K., Cochrane, G.R., Zayatz, I., Belyaev, V., Knyazev, M., Vinnikovskaya, O., Davey, F.J., Hinz, K., 1995b. Descriptive text for the seismic stratigraphic atlas of the Ross Sea, Antarctica. In: Cooper, A.K., Barker, P.F., Brancolini, G. (Eds.), *Geology and Seismic Stratigraphy of the Antarctic Margin*. Antarctic Research Series, vol. 68. American Geophysical Union, Washington, D.C., pp. A271-A286.

Broecker, W.S., Denton, G.H., 1989. The role of ocean-atmosphere reorganizations in glacial cycles. *Geochimica et Cosmochimica Acta*, 53: 2465-2501.

Burckle, L.H., Potter, N., Jr., 1996. Pliocene-Pleistocene diatoms in Paleozoic and Mesozoic sedimentary and igneous rocks from Antarctica: A Sirius problem solved. *Geology*, 24: 235-238.

Burton, A., Lines, L., 1996. VSP detection of interbed multiples using inside-outside corridor stacking, *Canadian Journal of Exploration Geophysics*, 32 (2): 113-120.

Busetti, M., 1994. A new constraint for the age of unconformity U6 in the Ross Sea, *Terra Antartica*, 1: 523-526.

Cande, S.C., Stock, J.M., Muller, R.D., Ishihara, T., 2000. Cenozoic motion between East and West Antarctica. *Nature*, 404:145-150.

Cape Roberts Science Team, 1998. Initial Report on CRP-1, Cape Roberts Project, Antarctica. *Terra Antartica*, 5 (187 pp.).

Cape Roberts Science Team, 1999. Studies from the Cape Roberts Project, Ross Sea, Antarctica, Initial Report on CRP-2/2A. *Terra Antartica*, 6 (187 pp.).

Cape Roberts Science Team, 2000. Studies from the Cape Roberts Project, Ross Sea, Antarctica, Initial Report on CRP-3. *Terra Antartica*, 7 (209 pp.).

Carter, L., Dunbar, G., McKay, R., 2007. Sedimentation and Oceanography beneath the McMurdo Ice Shelf at Windless Bight, 2006. *Antarctic Data Series No. 32* A Publication of the Antarctic Research Centre: Victoria University of Wellington PO Box 600, Wellington, New Zealand.

Chandler, M., Rind, D., Thompson, R., 1994. Joint investigations of the Middle Pliocene climata.II. GISS GCM Northern hemisphere results. *Global and Planetary Change*, 9: 197-219.

Chow, J.M., Bart, P.J., 2003. West Antarctic Ice Sheet grounding events on the Ross Sea outer continental shelf during the middle Miocene. *Palaeogeography, Palaeoclimatology, Palaeoecology*, 198: 169-186.

Clapperton, C.M., Sugden, D.E., 1990. Late Cenozoic glacial history of the Ross Embayment, Antarctica. *Quaternary Science Reviews*, 9: 252-272.

Clark, P.U., Pollard, D., 1998. Origin of the middle Pleistocene transition by ice sheet erosion of regolith. *Paleoceanography*, 13: 1-9.

Cooper, A.K., and Davey, F.J., 1985. Episodic rifting of Phanerozoic rocks in the Victoria Land Basin, western Ross Sea. *Antarctica: Science*, 229: 1085-1087.

Cooper, A.K., Davey, F.J., Behrendt, J.C. 1987. Seismic Stratigraphy and Structure of the Victoria Land Basin, Western Ross Sea, Antarctica. *The Antarctic Continental Margin: Geology and Geophysics of the Western Ross Sea*, Earth Science Series 5B, ed. A.K.Cooper and F.J.Davey, Houston, Texas, Circum-Pacific Council for Energy and Natural Resources, pp. 27-76.

Cooper, A.K., Barrett, P.J., Hinz, K., Traube, V., Leitchenkov, G., Stagg, H.M.J., 1991. Cenozoic prograding sequences of the Antarctic continental margin: a record of glacio-eustatic and tectonic events. *Marine Geology*, 102: 175–213.

Cooper, A.F., Adam, L.J., Coulter, R.F., Nelson Eby, G., McIntosh, W.C., 2007. Geology, geochronology and geochemistry of a basanitic volcano, White Island, Ross Sea, Antarctica. *Journal of Volcanology and Geothermal Research*, 165: 189-216.

Clifford, A.E., 2006. GPS Surveying for Event K001S (ANDRILL): McMurdo Ice Shelf, Antarctica 2005: Dunedin, University of Otago.

Crowley, T.J., 1996. Pliocene climates: the nature of the problem. *Marine Micropaleontology*, 27: 3-12.

Dalziel, I. W. D., Elliot, D. H., 1982. West Antarctica: problem child of Gondwanaland. *Tectonics*, 1: 3-19.

Davey, F.J., Brancolini, G., 1995. The late Mesozoic and Cenozoic structural setting of the Ross Sea Region, *in* Cooper, A.K., Barker, P.F., and Brancolini, G., eds., *Geology and Seismic Stratigraphy of the Antarctic Margin,* Volume 68: Washington, D.C., American Geophysical Union, p. 167-182.

Davey, F.J., Brancolini, G., Hamilton, R.J., Henrys, S.A., Sorlien, C.C., Bartek, L.R., 2000. A Revised Correlation of the Seismic Stratigraphy at the Cape Roberts drill sites with the Seismic Stratigraphy of the Victoria Land Basin, Antarctica. *Terra Antartica*, 7(3): 215-220.

Davey, F. J., De Santis, L., 2005. A multi-phase rifting Model for the Victoria Land basin, Western Ross Sea. In Antarctica: Contributions to Global Earth Sciences, edited by D. K. Futterer et al., chap. 6.3, pp. 301–306, Springer, New York.

Davey, F.J., Cande, S.C., Stock, J.M., 2006. Extension in the western Ross Sea region-links between Adare Basin and Victoria Land Basin. *Geophysical Research Letters*, 33: L20315.

DeConto, R.M., Pollard, D., 2003. Rapid Cenozoic glaciation of Antarctica induced by declining atmospheric CO_2. *Nature*, 421: 245-249.

Denton, G.H., Prentice, M.L., Burckle, L.H., 1991. Cenozoic history of the Antarctic Ice Sheet, In: *The Geology of Antarctica*, R.J. Tingey, ed., pp. 365-433, Oxford University Press.

Denton, G.H., Hughes, T.J., 2000. Reconstruction of the Ross Ice Drainage System, Antarctica, at the Last Glacial Maximum. *Geografiska Annaler*, Series A: Physical Geography, 82: 143-166.

Dowsett, H.J., Cronin, T.M., 1990. High eustatic sea level during the middle Pliocene; evidence from the southeastern U.S. Atlantic coastal plain. *Geology*, 18: 435-438.

Dowsett, H.J., Thompson, R.S., Barron, J.A., Cronin, T.M., Ishman, S.E., Poore, R.Z., Willard, D.A., Holtz, T.R., Jr., 1994. Joint investigations of the Middle Pliocene climate I: PRISM paleoenvironmental reconstructions. *Global and Planetary Change*, 9: 169-195.

Ehrmann,W. U., Mackensen, A., 1992. Sedimentologic evidence for the formation of an East Antarctic ice sheet in Eocene/Oligocene time. *Palaeogeography, Palaeoclimatology, Palaeoecology*, 93: 85–112.

Eittreim, S.L., Cooper A.K., Wannesson, J., 1995. Seismic stratigraphic evidence of ice-sheet advances on the Wilkes Land margin of Antarctica. *Sedimentary Geology*, 96: 131-156.

Esser, R.P., Kyle, P.R., McIntosh, W.C., 2004. ^{40}Ar/ ^{39}Ar dating of the eruptive history of Mount Erebus, Antarctica: volcano evolution. *Bulletin of Volcanology*, 66: 671-686.

Fielding, C.R., Henrys, S.A., Wilson, T.J., 2006. Rift History of the Western Victoria Land Basin: A new Perspective Based on Integration of Cores with Seismic Reflection Data. *in* Futterer, D.K., Damaske, D., Kleinschmidt, G., H., M., and F., T., (Eds), Antarctica: Contributions to Global Earth Sciences: Berlin Heidelberg New York, Springer-Verlag, p. 307-316.

Fielding, C.R., Whittaker, J., Henrys, S.A., Wilson, T.J., Naish, T.R., 2008. Seismic facies and stratigraphy of the Cenozoic succession in McMurdo Sound, Antarctica: implications for tectonic, climatic and glacial history. *Palaeogeography, Palaeoclimatology, Palaeoecology*, 260(1-2): 8-29.

Fitzgerald, P.G., Sandiford, M., Barrett, P.J., Gleadow, A.J.W., 1986. Asymmetric extension associated with uplift and subsidence in the Transantarctic Mountains and Ross Embayment. *Earth and Planetary Science Letters*, 81, (1): 67-78.

Fitzgerald, P.G., 1992. The Transantarctic Mountains of southern Victoria Land; the application of apatite fission track analysis to a rift shoulder uplift. *Tectonics*, 11: 634-662.

Fitzgerald, P., 2002. Tectonic and landscape evolution of the Antarctic Plate since the breakup of Gondwana, with an emphasis on the West Antarctic Rift system and the Transantarctic Mountains. In: J.A. Gamble, N.B. David, S.A. Henrys (Eds.), *Antarctica at the close of a millennium*; proceeding of the 8th International Symposium on Antarctic earth sciences, v. 35, Bulletin-Royal Society of New Zealand, Wellington, New Zealand, pp. 453–469.

Flower, B.P. and Kennett, J.P., 1995. Middle Miocene deepwater paleoceanography in the Southwest Pacific: relations with East Antarctic Ice Sheet development: *Paleoceanography*, 10: 1095-1112.

Francis, J. E., 1999. Evidence from fossil plants for Antarctic Paleoclimates over the past 100 million years: *Terra Antartica Reports*, 3: 43-52.

Grützner, J. Rebesco, M.A., Cooper, A.K., Forsberg, C.F., Kryc, K.A., Wefer, G., 2005. Evidence for orbitally controlled size variations of the East Antarctic Ice Sheet during the late Miocene. *Geology*, v.31, 9: 777-780.

Hall, J.M.,Wilson, T.J., Henrys, S.A., 2007. Structure of Central Terror Rift, Western Ross Sea, Antarctica. In: *Antarctica: A Keystone in a Changing World – Online Proceedings of the 10th ISAES*, edited by A. K. Cooper and Raymond C.R. et al., pp, USGS Open-File Report 2007-xxx.

Hambrey, M.J., Ehrmann, W.U., Larsen, B., 1991. Cenozoic glacial record of the Prydz Bay continental shelf, East Antarctica. *Proceedings of the Ocean Drilling Program, Scientific Results*, ODP, Texas A&M University, College Station, TX., 119: 77-132.

Hambrey, M.J., Wise, Jr., S.W., Barrett, P.J., Davey, F.J., Ehrmann, W.U., Smellie, J.L., Villa, G., Woolfe, K.J., 1998. Scientific Report on CRP–1, Cape Roberts Project, Antarctica: *Terra Antartica*, 5 (713 pp.).

Hamilton, R.J., Luyendyk, B.P., Sorlien, C.C., Bartek, L.R., 2001. Cenozoic tectonics of the Cape Roberts rift basin and Transantarctic Mountains front, southwestern Ross Sea, Antarctica. *Tectonics*, 20 (3): 325–342.

Hardage, B. A., 2000. Vertical seismic profiling: principles: third updated and revised edition: New York, Pergamon, Seismic Exploration, v. 14.

Harwood, D.M., Lacy, L.L., Levy, R.H. (editors), 2002. *Future Antarctic Margin Drilling: developing a science plan for McMurdo Sound.* ANDRILL SMO Contribution 1. University of Nebraska-Lincoln, Lincoln, NE., 301pp.

Harwood, D.M., Florindo, F., Levy, R.H., Fielding, C.R., Pekar, S.F., Speece, M.A., & SMS Science Team, 2006. ANDRILL Southern McMurdo Sound Project Scientific Prospectus, pp 32.

Hayes, D. E., Frakes, L. A., 1975. General Synthesis: Deep Sea Drilling Project 28. *In*: D.E. Hayes and L.A. Frakes (eds.), *Initial Reports of the Deep Sea Drilling Project, Leg 28*: U.S. Government Printing Office, Washington, D.C., p. 919–942.

Haywood, A.M., Sellwood, B.W., Valdes, P.J., 2000. Regional warming: Pliocene (3 Ma) paleoclimate of Europe and the Mediterranean. *Geology*, 28: 1063-1066.

Haywood, A.M., Valdes, P.J., Selwood, B.W., 2002. Magnitude of climate variability during middle Pliocene warmth: a palaeoclimate modelling study. *Palaeogeography, Palaeoclimatology, Palaeoecology*, 188: 1-24.

Henrys, S., Naish, T., Wilson, G., Gorman, A., Clifford, A., Johnston. L. and Blakemore, H., 2006a. ANDRILL 2005 Site Investigations/Seismic Surveys, McMurdo and Southern McMurdo Ice Shelf, McMurdo Sound, Antartctica, The Institute of Geological and Nuclear Sciences (GNS Science) science report 2006/13 42 p.

Henrys, S., Hall, J.M., Wilson, T.J., 2006b. Fault Architecture within the Eastern Terror Rift, Western Ross Sea, Antarctica. *Geophysical Research Abstracts*, Vol. 8, 02428.

Henrys, S. A., Wilson, T.J., Whittaker, J.M., Fielding, C.R., Hall, J.M., Naish, T., 2007. Tectonic history of mid-Miocene to present southern Victoria Land Basin, inferred from seismic stratigraphy in McMurdo Sound, Antarctica, In: Antarctica: A Keystone in a Changing World – Online Proceedings of the 10th ISAES, edited by A. K. Cooper and Raymond C.R. et al.,, USGS Open-File Report 2007-1047, Short Research Paper 049, 4 pp.

Henrys, S.A, Wilson, T.J., Paulsen, T., McIntosh, W.C., Naish, T.R., Powell, R.D., Fielding, C.R., Whittaker, J., Wilson, G.S., Helling, D., Hansaraj, D., & the ANDRILL MIS Science Team, in prep. Neogene rifting in the Victoria Land Basin: Implications for East-West Antarctica Plate Motion. *Geology*, in press.

Herman, J.R., Goldberg, R.A., (1985). *Sun, weather, and climate.* Grand River Books.

Hodell, D. A., Venz, K., 1992. Towards a high resolution stable isotopic record of the Southern Ocean during the Pliocene-Pleistocene (4.8-0.8 Ma), In: The Antarctic Paleoenvironment: A Perspective on Global Change, Antarctic Research Series, v.56, edited by J. P. Kennett and D. A. Warnke, pp. 265– 310, AGU, Washington, D.C.

Holbourn, A., Kuhnt, W., Schulz, M., Erlenkeuser, H., 2005. Impacts of orbital forcing and atmospheric carbon dioxide on Miocene Ice Sheet expansion. *Nature*, 438: 483-487.

Holt, W.E., Stern, T.A., 1991. Sediment loading on the western platform of the New Zealand continent: implications for the strength of a continental margin. *Earth and Planetary Science Letters*, 107: 523-538.

Horgan, H., Bannister, S.C., Naish, T.R., Wilson, G., Pyne, A., Clifford, A., Finnemore, M., 2003. ANDRILL site investigations/seismic surveys, McMurdo and southern McMurdo Ice Shelf, McMurdo Sound, Antarctica: Institute of Geological & Nuclear Sciences science report, v. 2003/05, 47 pp.

Horgan, H., Bannister, S.C., 2004. Explosive source seismic experiments from a sea-ice platform, McMurdo Sound 2003: Institute of Geological & Nuclear Sciences science report, v. 2004/15, 23 pp.

Horgan, H., Naish, T., Bannister, S., Balfour, N., Wilson, G., 2005. Seismic stratigraphy of the Plio-Pleistocene Ross Island flexural moat-fill: a prognosis for ANDRILL Program drilling beneath McMurdo-Ross Ice Shelf. *Global and Planetary Change*, 45: 83-97.

Huerta, A., 2006. Influence of the Transantarctic Mountains on the evolution of the East Antarctic Ice Sheet; insights from landscape analysis. *Geophysical Research Abstracts*, v. 8, 08808.

Huerta, A.D., Harry, D.L., 2007. The transition from diffuse to focused extension: Modeled evolution of the West Antarctic Rift system. *Earth and Planetary Science Letters*, 255: 133–147.

Huybers, P., Wunsch, C., 2005. Obliquity pacing of the late Pleistocene glacial terminations. *Nature*, 434: 491-494.

Huybers, P., 2006. Early Pleistocene Glacial Cycles and the Integrated Summer Insolation Forcing. *Science*, 313: 508-511.

Imbrie, J., Berger, A., Boyle, E.A., Clemens, S.C., Duffy, A., Howard, W.R., Kukla, G., Kutzbach, J., Martinson, D.G., McIntyre, A., Mix, A.C., Molfino, B., Morley, J.J., Peterson, L.C., Pisias, N.G., Prell, W.L., Raymo, M.E., Shackleton, N.J., Toggweiler, J.R., 1993. On the structure and origin of major glaciation cycles: 2. The 100,000-year cycle. *Paleoceanography*, 8: 699-735.

IPCC, 2001. Climate Change 2001: The Scientific Basis. Contribution of Working Group I to the Third Assessment Report of the Intergovernmental Panel on Climate Change. Cambridge University Press, Cambridge, p 879.

IPCC, 2007. Climate Change 2007 The Physical Science Basis. Contribution of Working Group I to the Fourth Assessment Report of the Intergovernmental Panel on Climate Change. Cambridge University Press, Cambridge, 989 pp.

Japsen, P., Bonow, J.M., Green, P.F., Chalmers, J.A., Lidmar-Bergstrom, K., 2006. Elevated, passive continental margins: long-term highs or Neogene uplifts? New evidence from West Greenland. *Earth and Planetary Sciences Letters,* 248: 330-339.

Karner, G.D., Studinger, M., Bell, R.E., 2005. Gravity anomalies of sedimentary basins and their mechanical implications: Application to the Ross Sea basins, West Antarctica. *Earth and Planetary Science Letters*, 235: 577-596.

Kearey, P., Brooks, M., Hill, I., 2002. An Introduction to Geophysical Exploration: Wiley-Blackwell Publishing.

Kellogg. D.E., Kellogg, T.B., 1996. Diatoms in South Pole ice: Implications for eolian contamination of Sirius Group deposits. *Geology*, 24: 115-118.

Kennett, J.P., Houtz, R.E., Andrews, P.B., Edwards, A.R., Gostin, V.A., Hajos, M., Hampton, M.A., Jenkins, D.G., Margolis, S.V., Ovenshine, A.T., Perch-Nielsen, K., 1974. Development of the Circum-Antarctic Current. *Science*, v. 186, 4159: 144-147.

Kennett, J.P., Vella, P., 1975. Late Cenozoic planktonic foraminifera and palaeoceanography at DSDP Site 284 in the cool subtropical south Pacific. In: Kennett, J.P., Houtz, R.E., et al., *Initial Reports of the Deep Sea Drilling Project 29*, U.S. Government Printing Office, 869-782.

Kennett, J.P., 1977. Cenozoic evolution of Antarctic glaciation, the Circum-Antarctic Ocean, and their impact on global paleoceanography. *Journal of Geophysical Research*, 82: 3843-3860.

Kennett, J.P., Hodell, D.A., 1993. Evidence for relative climatic stability of Antarctica during the Early Pliocene: A marine perspective. *Geografiska Annaler*, 75A (4): 205-220.

Kominz, M.A., Pekar, S.F., 2001. Oligocene eustasy from two-dimensional sequence stratigraphic backstripping. *Geological Society of America Bulletin*, 113: 291-304.

Krissek, L.A., Browne, G., Carter, L., Cowan, E., Dunbar, G., McKay, R., Naish, T., Powell, R., Reed, J., Wilch, T., and the ANDRILL-MIS Science Team, 2007. Sedimentology and Stratigraphy of the AND-1B Core, ANDRILL McMurdo Ice Shelf Project, Antarctica. *Terra Antartica*, 14 (2): 185-222.

Kyle, P.R., 1990a. A.III Erebus Volcanic Province; Summary. In: LeMasurier, W.E., Thomson, J.W., Baker, P.E., Kyle, P.R., Rowley, P.D., Smellie, J.L., and Verwoerd, W.J., eds., *Volcanoes of the Antarctic Plate and Southern Oceans*, v.48: Antarctic Research Series: Washington, American Geophysical Union p. 81-88.

Kyle, P.R., 1990b. McMurdo Volcanic Group, western Ross Embayment; Introduction. In: LeMasurier, W.E., Thomson, J.W., Baker, P.E., Kyle, P.R., Rowley, P.D., Smellie, J.L., and Verwoerd, W.J., eds., *Volcanoes of the Antarctic Plate and Southern Oceans*, v.48: Antarctic Research Series: Washington, American Geophysical Union, p. 18-25.

Lamb, H.H., (1985). *Climate History and the Future* (2nd Edition). Routledge.

LeMasurier, W.E., Thomson, J.W., 1990. Volcanoes of the Antarctic plate and Southern Oceans. *Antarctic Research Series*, v.48, Washington D.C., American Geophysical Union.

Levander, A.R., 1989. Finite-difference forward modeling in seismology. In: *Encyclopedia of Solid Earth Geophysics*, D.E. James, editor, Van Nostrand Rheinhold, New York, 410-431.

Lisiecki, L.E., Raymo, M.E., 2007. Plio–Pleistocene climate evolution: trends and transitions in glacial cycle dynamics. *Quaternary Science Reviews*, 26: 56-69.

Liu, C.S., Sandwell, D.T., Curry, J.R., 1982. The negative gravity field over the 85°E ridge. *Journal of Geophysical Research*, 87, (B9): 7673– 7686.

Lizarralde, D., Swift, S., 1999. Smooth inversion of VSP traveltime data. *Geophysics,* 64: 659-661.

Manley, P. L. and S. Brachfeld (2007), Synthetic seismograms and spectral cycles on the Andvord and Schollaert Drifts: Antarctic Peninsula, in Antarctica: A Keystone in a Changing World – Online Proceedings of the 10th ISAES, edited by A. K. Cooper and C. R. Raymond et al., USGS Open-File Report 2007-1047, Short Research Paper 018, 5 p.; doi:10.3133/of2007-1047.srp018.

Marchant, D.R., Swisher, C.C., Lux, D.R., West, D.P., Denton, G.H., 1993. Pliocene paleoclimate and East Antarctic Ice- Sheet history from surficial ash deposits. *Science*, 260: 667–670.

Marchant, D.R., Denton, G.H., Swisher, C.C., Potter, N., 1996. Late Cenozoic Antarctic paleoclimate reconstructed from volcanic ashes in the Dry Valleys region of southern Victoria Land. *Geological Society of America Bulletin*, 108: 181–194.

Maslin, M.A., Li, X.S., Loutre, M.-F., Berger, A., 1998. The contribution of orbital forcing to the progressive intensification of the Northern Hemisphere glaciation: *Quaternary Science Reviews*, 17: 411–426.

Mercer, J.H., 1978. West Antarctic ice sheet and CO_2 greenhouse effect: a threat of disaster. *Nature*, 271: 321-325.

McKay, R., 2008. Late Cenozoic (13-0 Myr) glacimarine sedimentology, facies analysis, and sequence stratigraphy from the Western Ross Embayment, Antarctica: Implications for the variability of the West Antarctic Ice Sheet. *Unpublished PhD thesis*, Victoria University of Wellington: Wellington. 262pp.

McKay, R.M., Dunbar, G.B., Naish, T.R., Barrett, P.J., Carter, L., Harper, M., 2008. Retreat history of the Ross Ice Sheet (Shelf) since the Last Glacial Maximum from deep-basin sediment cores around Ross Island. *Palaeogeography, Palaeoclimatology, Palaeoecology*, 260 (1-2): 245-261.

McQuillin, R., Bacon, M., Barclay, W., 1984. An Introduction to Seismic Interpretation: Reflection Seismics in Petroleum Exploration. Graham and Trotman, London.

Medina-Elizalde, M., Lea, D.W., 2005. The Mid-Pleistocene Transition in the Tropical Pacific. *Science*, 310: 1009-1012.

Melhuish, A., Henrys, S.A., Bannister, S., Davey, F.J., 1995. Seismic profiling adjacent to Ross Island: constraints on late Cenozoic stratigraphy and tectonics. *Terra Antarctica*, 2(2): 127-136.

Michalchuk, B.R., 2006. Synthetic Seismograms and Physical Properties Generated from Sediments in Maxwell Bay, Antarctica - A Study of Climate History. Submitted in partial fulfillment of the requirements for the degree of Bachelor of Arts Department of Geology, Middlebury College, Middlebury Vermont, 69 p.

Mildenhall, D.C., 1989. Terrestrial palynology. In: Barrett, P.J. (Ed.), Antarctic Cenozoic History from the CIROS-1 Drillhole, McMurdo Sound, Antarctica. Dept. Sci. Ind. Res. Bull. Wellington 245: 119-127.

Miller, K.G., Fairbanks, R.G., Mountain, G.S., 1987. Tertiary oxygen isotope synthesis, sea-level history, and continental margin erosion. *Paleoceanography*, 2: 1-19.

Miller, K.G., Wright, J.D. and Fairbanks, R.G., 1991. Unlocking the ice-house: Oligocene-Miocene oxygen isotopes, eustasy and margin erosion: *Journal of Geophysical Research*, *B, Solid Earth and Planets*, **v. 96**, p. 6829–6848.

Miller, M.F., Mabin, M.C.G., 1998. Antarctic Neogene Landscapes - In the Refrigerator or in the Deep Freeze? *GSA Today*, v.8, 4: 1-3.

Moore, J.A., Kyle, P.R., 1990. A. 17 Mount Erebus. In: LeMasurier, W.E., Thomson, J.W. (Eds), Volcanoes of the Antarctica Plate and Southern Oceans. American Geophysical Union, Washington, DC, pp. 103-108.

Morin R., Williams T., Henrys S., Crosby T., Hansaraj D., & the ANDRILL MIS-Science Team, 2007. Downhole Measurements in the AND-1B Borehole, ANDRILL McMurdo Ice Shelf Project, Antarctica. *Terra Antartica*, 14 (2): 167-174.

Mudelsee, M., Schulz, M., 1997. The Mid-Pleistocene climate transition: onset of 100 ka cycle lags ice volume build up by 280 ka. *Earth and Planetary Science Letters*, 151: 117-123.

Naish, T.R., Woolfe, K.J., Barrett, P.J., et al. 2001. Orbitally induced oscillations in the East Antarctic ice sheet at the Oligocene/Miocene boundary. *Nature*, 413: 719-723.

Naish, T.R., Levy, R.H., Powell, R.D., and MIS Science and Operations Team Members, 2006. *Scientific Logistics Implementation Plan for the ANDRILL McMurdo Ice Shelf Project*. ANDRILL Contribution 7. University of Nebraska-Lincoln, Lincoln-NE. 117 pp.

Naish, T.R., R.D. Powell, S. Henrys, G. S. Wilson, L. A. Krissek, F. Niessen, M. Pompilio, R. Scherer, F. Talarico, R.H. Levy, A. Pyne, 2007a. Late Neogene climate history of the Ross Embayment: Initial results from the ANDRILL McMurdo Ice Shelf Project. *Antarctica: A keystone in a Changing World – Online Proceedings of the 10th ISAES*, edited by A. K. Cooper and C. R. Raymond et al., USGS Open-File Report 2007-xxx, yyy, 1-11.

Naish, T., Powell, R., Levy, R., Henrys, S., Krissek, L., Niessen, F., Pompilio, M., Scherer, R., Wilson, G., & the ANDRILL-MIS Science Team, 2007b. Synthesis of the Initial Scientific Results of the MIS Project (AND-1B Core), Victoria Land Basin, Antarctica. *Terra Antartica*, 14(2): 317-333.

Naish, T., Powell, R., Levy, R., & the ANDRILL-MIS Science Team, 2007c. Background to the ANDRILL McMurdo Ice Shelf Project (Antarctica) and Initial Science Volume. *Terra Antartica*, 14(2): 121-130.

Naish, T.R., Powell, R., & the ANDRILL-MIS Science Team, 2009. Obliquity-paced Pliocene West Antarctic ice sheet oscillations. *Nature*, 458: 322-329.

Niessen, F., Magens, D., Gebhardt, A.C., 2007. Physical Properties of the AND-1B Core, ANDRILL, McMurdo Ice Shelf Project, Antarctica. *Terra Antartica*, 14(2): 155-166.

Paillard, D., Parrenin, F. 2004. The Antarctic ice sheet and the triggering of deglaciations. *Earth and Planetary Science Letters*, 227: 263-271.

Pälike, H., Norris, R.D., Herrle, J.O., Wilson, P.A., Coxall, H.K., Lear, C.H., Shackleton, N.J., Tripati, A.K., Wade, B.S., 2006. The Heartbeat of the Oligocene Climate System. *Science*, 314: 1894-1898.

Passchier, S., 2001. Provenance of the Sirius Group and related Upper Cenozoic glacial deposits from the Transantarctic Mountains, Antarctica: relation to landscape evolution and ice-sheet drainage. *Sedimentary Geology*, 144: 263-290.

Pekar, S.F., DeConto, R.M., 2006. High-resolution ice-volume estimates for the early Miocene: Evidence for a dynamic ice sheet in Antarctica. *Palaeogeography, Palaeoclimatology, Palaeoecology,* 231: 101-109.

Pekar, S.F., DeConto, R.M., Harwood, D.M., 2006. Resolving a late Oligocene conundrum: Deep-sea warming and Antarctic glaciation. *Palaeogeography, Palaeoclimatology, Palaeoecology,* 231: 29-40.

Pompilio, M., Dunbar, N., Gebhardt, A, Helling, D., Kuhn, G., Kyle, P., McKay, R., Talarico, F., Tulaczyk, S., Vogel, S., Wilch, T., and the ANDRILL MIS Science Team. 2007. Petrology and Geochemistry of the AND-1B Core, ANDRILL McMurdo Ice Shelf Project, Antarctica. *Terra Antartica* 14 (2): 255-288.

Prebble, J.G., Raine, J.I., Barrett, P.J., Hannah, M.J., 2006. Vegetation and climate from two Oligocene glacioeustatic sedimentary cycles (31 and 24 Ma) cored by the Cape Roberts Project, Victoria Land Basin, Antarctica. *Palaeogeography, Palaeoclimatology, Palaeoecology*, 231: 41-57.

Raine, J.I., 1998. Terrestrial palynomorphs from Cape Roberts Project drillhole CRP-1, Ross Sea, Antarctica. *Terra Antartica*, 5: 539–548.

Raine, J.I., Askin, R.A., 2001. Oligocene and Early Miocene terrestrial palynology of the Cape Roberts Drillhole CRP-2/2A, Victoria Land Basin, Antarctica. *Terra Antartica*, 7: 389– 400.

Ravelo, A.C., Andreasen, D.H., 2000. Enhanced circulation during a warm period. *Geophysical Research Letters*, 27: 1000-1004.

Ravens, J., 1999. Globe Claritas, Seismic processing dictionary. GNS Science Technical Report 99/12, 307 pp.

Raymo, M.E., Ruddiman, W.F., Backman, J., Clement, B.M., Martinson, D.G., 1989. Late Pliocene variation in northern hemisphere ice sheets and North Atlantic deep water circulation. *Paleoceanography*, 4: 413-446.

Raymo, M.E., Lisiecki, L.E., Nisancioglu, K.H., 2006. Plio-Pleistocene Ice Volume, Antarctic Climate, and the Global $\delta^{18}O$ Record. *Science*, 313: 492-495.

Rebesco, M., Camerlenghi, A., Geletti, R., Canals, M., 2006. Margin architecture reveals the transition to the modern Antarctic ice sheet ca. 3 Ma. *Geology*, v.34, 4: 301–304.

Rignot, E., Casassa, G., Gogineni, P., Krabill, W., Rivera, A., Thomas, R., 2004. Accelerated ice discharge from the Antarctic Peninsula following the collapse of Larsen B ice shelf. *Geophysical Research Letters*, v. 31, 18: L18401.

Rignot, E., 2006. Changes in ice dynamics and mass balance of the Antarctic ice sheet. *Philosophical Transactions of the Royal Society A*, 364: 1637–1655.

Roberts, A.P., Wilson, G.S., Harwood, D.M., Verosub, K.L., 2003. Glaciation across the Oligocene–Miocene boundary in Southern McMurdo Sound, Antarctica: new chronology from the CIROS-1 drill hole. *Palaeogeography, Paleoclimatology, Palaeoecology*, 198: 113-130.

Rocchi, S., Armienti, P., D'Orazio, M., Tonarini, S.,Wijbrans, J.R., Di Vincenzo, G., 2002. Cenozoic magmatism in the western Ross Embayment: role of mantle plume versus plate dynamics in the development of the West Antarctic Rift System. *Journal of Geophysical Research,* 107.

Rocchi, S., Storti, F., Di Vincenzo, G., Rosetti, F., 2003. Intraplate strike–slip tectonics as an alternative to mantle plume activity for the Cenozoic rift magmatism in the Ross Sea region, Antarctica. In: Storti, F., Holdsworth, R.E., Salvini, F. (Eds.), Intraplate Strike–Slip Deformation Belts. Geological Society London, Special Publications, vol. 210, pp. 145–158.

Rocchi, S., Armienti, P., Di Vincenzo, G., 2005. No plume, no rift magmatism in the West Antarctic Rift. In: Foulger, G.R., Natland, J.H., Presnall, D.C., Anderson, D.L. (Eds.), Plates, Plumes and Paradigms. Geological Society of America Special Paper, vol. 388, pp. 435–447.

Roksandic, M. M., 1978. Seismic Facies Analysis Concepts: *Geophysical Prospecting* v. 26 (2): 303-485.

Ruppel, C., 1995. Extensional processes in continental lithosphere. *Journal of Geophysical Research*, 100 (B12): 24,187-24,215.

Salvini, F., Brancolini, G., Busetti, M., Storti, F., Mazzarini, F., Coren, F.,1997. Cenozoic geodynamics of the Ross Sea region, Antarctica: crustal extension, intraplate strike-slip faulting, and tectonic inheritance, *Journal of Geophysical Research*, 102(B11): 24,669–24,696.

Sams M. S., Neep J. P., Worthington M. H., King M. S., 1997. The measurement of velocity dispersion and frequency-dependent intrinsic attenuation in sedimentary rocks. *Geophysics* 62:1456-1464.

Shackleton, N. J., Kennett, J. P., 1975. Paleotemperature history of the Cenozoic and the initiation of Antarctic glaciation: oxygen and carbon isotope analyses in DSDP Sites 277, 279 and 281. In Kennett, J.P., Houtz, R.E. et al, *Initial Reports of the Deep Sea Drilling Project*, v.XXIX, Washington (U.S. Government Printing Office), 29: 743-755.

Shackleton, N.J., Blackman, J., Zimmerman, H., Kent, D.V., Hall, M.A., Roberts, D.G., Schnitker, D., Baldauf, J.G., Desprairies, A., Homrighausen, R., Huddlestun, P., Keene, J.B., Kaltenback, A.J., Krumsiek, K.A.O., Morton, A.C., Murray, J.W., Westberg-Smith, J., 1984. Oxygen isotope calibration of the onset of ice-rafting and the history of glaciation in the North Atlantic region: *Nature* (London), 307: 620–623.

Shackleton, N. J., Hall, M.A., Pate, D., 1995. Pliocene stable isotope stratigraphy of Site 846. Proceedings of the Ocean Drilling Program Scientific Results, 138: 337-353.

Shackleton, N.J., 2000. The 100,000-Year Ice-Age Cycle Identified and Found to Lag Temperature, Carbon Dioxide, and Orbital Eccentricity. *Science*, 289: 1897-1902.

Steinberger, B., Sutherland, R., O'Connell, R.J., 2004. Prediction of Emperor-Hawaii seamount locations from a revised model of global plate motion and mantle flow. *Nature*, 430: 167-173.

Stern, T.A., ten Brink, U.S., 1989. Flexural uplift of the Transantarctic Mountains. *Journal of Geophysical Research*, 94: 10315-10330.

Stewart, R.R., 1998. Multimode deconvolution. *CREWES Research Report*, v. 10: 23-1 – 23-7.

Stroeven, A.P., Prentice, M.L., Kleman, J., 1996. On marine microfossil transport and pathways in Antarctica during the late Neogene: Evidence from the Sirius Group at Mount Fleming. *Geology*, 24: 727-730.

Sugden, D.E., Marchant, D.R., Denton, G.H., 1993. The case for a stable East Antarctic Ice Sheet: The Background. *Geografiska Annaler*, 75A (4): 151-154.

Sugden, D., Denton, G., 2004. Cenozoic landscape evolution of the Convoy Range to Mackay Glacier area, Transantarctic Mountains; onshore to offshore synthesis. *Geological Society of America Bulletin*, 116(7-8):840-857.

Thorn, V.C., 2001. Oligocene and Early Miocene phytoliths from CRP-2/2A and CRP-3, Victoria Land Basin, Antarctica. *Terra Antartica*, 8,: 407-422.

Tonarini, S., Rocchi, S., Armienti, P., Innocenti, F., 1997. Constraints on timing of Ross Sea rifting inferred from Cainozoic intrusions from northern Victoria Land, Antarctica. In: *The Antarctic Region: Geological Evolution and Processes*. Ricci, C.A. (Ed.). Terra Antarctica Publication, Siena, pp. 511–521.

Trey, H., Cooper, A.K., Pellis, G., Della Vedova, B., Cochrane, G., Brancolini, G., Makris, J., 1999. Transect across the West Antarctic Rift System in the Ross Sea, Antarctica. *Tectonophysics*, 301: 61-74.

Vaughan, D.G., Arthern, R., 2007. Why Is It Hard to Predict the Future of Ice Sheets? *Science*, 315: 1503-1504.

Webb, P.N., Harwood, D.M., 1991. Late Cenozoic glacial history of the Ross Embayment, Antarctica. *Quaternary Science Reviews*, 10: 215-224.

Whitehead, J.M., Quilty, P.G., Harwood, D.M., McMinn, A., 2001. Ealr Pliocene paleoenvironment of the Sørsdal Formation, Vestfold Hills, based on diatom data. *Marine Micropaleontology*, 41: 125-152.

Whittaker, J., 2005, Cenozoic Structural and Stratigraphic History of McMurdo Sound, Antarctica [MSc thesis]: Wellington, New Zealand, Victoria University of Wellington.

Wilson, G.S., 1995a. The Neogene East Antarctic ice sheet: A dynamic or stable feature? *Quaternary Science Reviews*, 14: 101-123.

Wilson, T.J., 1995b. Cenozoic transtension along the Transantarctic Mountains–West Antarctic Rift boundary, southern Victoria Land, Antarctica. *Tectonics*, 14 (2): 531-545.

Wilson, G.S., Roberts, A.P., Verosub, K.L., Florindo, F., Sagnotti, L., 1998. Magnetobiostratigraphic chronology of the Eocene–Oligocene transition in the CIROS-1 core, Victoria Land margin, Antarctica: Implications for Antarctic glacial history. *Geological Society of America Bulletin*, 110: 35–47.

Wilson, T.J., Lawver, L.A., Henrys, S.A, Mukasa, S., Horgan, H., Weiderspahn, M., Davis, M., Whittaker, J., Lowe, A., Watson, M., 2004. Cruise Report NBP0401 19 January to 18 February 2004 – McMurdo Station to McMurdo Station, Ross Sea, Antarctica, Institute of Geological & Nuclear Sciences Science Report 2004/03, p. 85.

Wilson, G., Damaske, D., Moller, H.-D., Tinto, K., Jordan, T., 2007a. The geological evolution of southern McMurdo Sound – new evidence from a high resolution aeromagnetic survey. *Geophysical Journal International*, 170: 93-100.

Wilson, G., Levy, R., Browne, G., Dunbar, N., Florindo, F., Henrys, S., Graham, I., McIntosh, W., McKay, R., Naish, T., Ohneiser, C., Powell, R., Ross, J., Sagnotti, L., Scherer, R., Sjunneskog, C., Strong, C.P., Taviani, M., Winter, D., and the ANDRILL-MIS Science Team, 2007b. Preliminary Integrated Chronostratigraphy of the AND-1B Core, ANDRILL McMurdo Ice Shelf Project, Antarctica. *Terra Antartica*, 14(2): 297-316.

Wilson, T., Henrys, S., Hannah, M., Jarrard, R., Fielding, C., Barrett, P., Paulsen, T., (unpublished). New Rift History for West Antarctica.

Wrenn, J.H., Webb, P.N., 1982. Physiographic analysis and interpretation of the Ferrar Glacier–Victoria Valley area, Antarctica. In: Craddock, C. (Ed.), *Antarctic Geoscience*, University of Wisconsin Press, Madison, pp. 1091– 1099.

Wright, A.C., Kyle, P.R., 1990a. A.15 Mount Bird. In: LeMasurier, W.E., Thomson, J.W. (Eds.), Volcanoes of the Antarctica Plate and Southern Oceans. American Geophysical Union, Washington, DC, pp. 97– 98.

Wright, A.C., Kyle, P.R., 1990b. A.16 Mount Terror. In: LeMasurier, W.E., Thomson, J.W. (Eds.), Volcanoes of the Antarctica Plate and Southern Oceans. American Geophysical Union, Washington, pp. 99– 102.

Wright, J.D., Miller, K.G. and Fairbanks, R.G., 1992. Early and middle Miocene stable isotopes: implications for deepwater circulation and climate: *Paleoceanography*, **v. 7**, p. 357–389.

Zachos, J.C., Breza, J.R., Wise, S.W., 1992. Early Oligocene ice sheet expansion on Antarctica: stable isotope and sedimentological evidence from Kerguelen Plateau, southern Indian Ocean. *Geology*, 20: 569–573.

Zachos, J.C., Quinn, T. M., Salamy, K.A., 1996. High-resolution (104 years) deep-sea foraminiferal stable isotope records of the Eocene–Oligocene climate transition. *Paleoceanography* 11: 251–266.

Zachos, J.C., Flower, B.P. and Paul, H.A., 1997. Orbitally paced climate oscillations across the Oligocene/Miocene boundary: *Nature* (London), 388: 567–570.

Zachos, J., Pagani, M., Sloan, L., Thomas, E., 2001a. Trends, rhythms, and aberrations in global climate 65 Ma to present. *Science,* 292: 686–693.

Zachos, J., Shackleton, N.J., Revenaugh, J.S., Pälike, H., Flower, B.P., 2001b. Climate response to orbital forcing across the Oligocene–Miocene boundary. *Science,* 292: 274– 278.

APPENDIX A – Seismic Processing Parameters (2005 Data)

MIS-3 Line

 # Mis3Job01.job

2). Read in SEGY data (mis3_100.csgy)
3). Resample data from 1 ms to 2 ms
4). Write to disc file (Mis3.dsc)

 # Mis3Job02.job

2). Read disc file (Mis3.dsc)
3). Apply trace edit using edit file (Mis3.tre)
4). Add geometry (mis3.geom)
5). Apply spherical divergence correction using velocities from file Mis3_brute.nmo
    --> done iteratively, as velocity fields evolved
7). Apply band-pass filter (8-12-100-140 Hz)
    --> values ranging from 0 to 200 Hz was tested, these values were most effective
8). Write to shots file (Mis3.shots)

 # Mis3Job02_view.job

2). Read in shots file (Mis3.shots)
4). View shots (using XVIEW)

 # Mis3Job03.job

2). Read in shots file (Mis3.shots) using DISCGATH module → outputs CDP's
3). Apply static correction using STATIC module to time-shift data up and change trace length from 6000 ms to 5500 ms
    --> this was done to remove the distorting effects from the bottom of the record, that were affecting data higher up in the section
4). Apply surgical mute from mute file (mis3.smu)
5). Reorder CDP's into CDP order, based on geometry (mis3.geom)
6). Apply NMO correction using velocity file (Mis3_brute.nmo)
    --> done iteratively, as velocity fields evolved
7). Write to CDP file (Mis3.cdp)
8). Stack data to produce a stacked section
9). Apply band-pass filter (8-12-100-140 Hz)
10). Apply deconvolution filter using file (Mis3_decon.sde)
    --> this file created based on deconvolution filter testing. Zero cross-over time observed (10 ms) and filter created around this. Varying gap and operator lengths tested, with one being held constant and the other varying, and vice-versa. Chosen length = 200, chosen gap = 12.
11). to 15). Test SCDECON which was unsuccessful. DECONW seemed to work suitably

16). to 18). Write to stacked section using JCS (Mis3.stack, Mis3_decon.stack, Mis3_scdecon.stack)

Mis3Job03_view.job

2). Read in stacked sections from list file (decon_compare3.lis)
3). Apply surgical mute (cutoff3.smu) to remove ice and water above seafloor
5). View each section in separate panels

Mis3Job04.job

2). Read in stack with DECONW applied to it (Mis3_decon.stack)
3). to 5). Migrate data using FDMIG (finite difference migration)
      --> DX (distance between traces) = 24 [half the geophone spacing]
        WINDSIZ kept constant at 20
        THETA kept constant at 0.8
        VELFILE = Mis3_brute_interval.nmo (interval velocities created in isovels)
        SCALAR value taken to be 0.8
6). Write to migrated stacked section (Mis3_deconwmig.stack)

Mis3Job04_view.job

2). Read in stacked sections from list file (mig_compare.lis) for comparison
      --> regular, decon applied, decon and migrated (Mis3.stack, Mis3_decon.stack, Mis3_deconwmig.stack)
3). Apply surgical mute (cutoff3.smu) to remove ice and water above seafloor
4). to 7). Apply BALANCE and AGC (automatic gain control)
8). View all sections in separate panels

Mis3Job05.job

--> The same job flow as Mis3Job04.job, but using JCS to create 7 jobs each testing different SCALAR values in the FDMIG module. Values varied between 0.5 and 1.15. Chosen value = 0.8 as it produced the best section

Mis3Job05_view.job

2). Read in migrated section (Mis3_deconwmig.stack)
3). to 5). 'If loop' testing different values for a band-pass filter, to remove low frequency noise introduced after deconvolution
      --> frequencies (Hz) tested = F1   F2   F3   F4
                                    0-0   10-70 100-180 200-350
6). Chosen band-pass filter = (0-40-110-220 Hz)
7). Apply surgical mute (cutoff3.smu) to remove ice and water above seafloor
8). to 11). Apply BALANCE and AGC (automatic gain control)
12). View FINAL section

MIS-4 Line

Mis4Job01.job

2). Read in SEGY data (mis4_100.csgy) --> shots 102:178 (refer to observers logs)
3). Resample data from 1 ms to 2 ms
6). Write to disc file (Mis4.dsc)

Mis4Job02.job

2). Read in disc file (Mis4.dsc)
3). Apply trace edit from file Mis4.tre
6). Add geometry (mis4_june.geom)
7). Apply spherical divergence correction using velocities from velocity file (Mis4_brute.nmo)
    --> done iteratively, as velocity fields evolved
8). Apply BALANCE → scales individual traces by a slowly varying or constant scalar, so that the average power (or average amplitude) of the output trace is constant for all traces output from this process
9). Apply band-pass filter (8-12-100-140 Hz)
    --> values ranging from 0 to 200 Hz was tested
10). Write to shots file (Mis4.shots)

Mis4Job02_view.job

2). Read in shots file (Mis4.shots)
3). Apply BALANCE
4). View shot data

Mis4Job03.job

2). Read in shots file (Mis4.shots) using DISGATH
3). Apply static correction using STATIC module to time-shift data up and change trace length from 6000 ms to 5500 ms
4). Apply surgical mute using mute file (mis4.smu)
5). Reorder CDP's based on geometry (mis4_june.geom) using CDPSORT
6). Apply NMO correction based on velocity file (Mis4_brute.nmo)
    --> done iteratively, as velocity fields evolved
7). Write to CDP file (Mis4.cdp)
8). Stack data (48 fold)
9). Apply band-pass filter (8-12-100-140 Hz)
10). Apply deconvolution filter using file (Mis4_decon.sde)
    --> file created based on deconvolution filter testing. Zero cross-over time observed (10 ms) and filter created around this. Varying gap and operator lengths tested, with one being held constant and the other varying, and vice-versa. Chosen length = 200, chosen gap = 12.
11). to 15). Tested SCDECON (shot-consistent) but it was unsuccessful. DECONW seemed to work suitably
16). to 18). Write to stacked section (Mis4.stack, Mis4_decon.stack, Mis4_scdecon.stack)

Mis4Job03_view.job

2). Read in stacked sections from list file (decon_compare4.lis)
3). Apply surgical mute (cutoff4.smu) to remove ice and water above seafloor
5). View each section in separate panels

Mis4Job04.job

2). Read in stack with DECONW applied to it (Mis4_decon.stack)
3). to 5). Migrate data using FDMIG (finite difference migration)
    --> DX (distance between traces) = 24 [half the geophone spacing]
      WINDSIZ kept constant at 20
      THETA kept constant at 0.8
      VELFILE = Mis3_brute_interval.nmo (interval velocities created in isovels)
      SCALAR value taken to be 0.8
6). Write to migrated stacked section (Mis4_deconwmig.stack)

Mis4Job04_view.job

2). Read in stacked sections from list file (mig_compare.lis) for comparison
    --> regular, decon applied, decon and migrated (Mis4.stack, Mis4_decon.stack, Mis4_deconwmig.stack)
3). Apply surgical mute (cutoff4.smu) to remove ice and water above seafloor
4). to 7). Apply BALANCE and AGC (automatic gain control)
8). View all sections in separate panels

Mis4Job05.job

--> The same processing flow as Mis4Job04.job, but uses JCS to create 7 jobs each testing different SCALAR values in the FDMIG module. Values varied between 0.5 and 1.15. Chosen value = 0.8 as it produced the best section

Mis4Job05_view.job

2). Read in migrated section (Mis4_deconwmig.stack)
3). to 5). 'If loop' testing different values for a band-pass filter, to remove low frequency noise introduced after deconvolution
    --> frequencies (Hz) tested = F1   F2   F3   F4
                   0-0 10-70 100-180 200-350
6). Chosen band-pass filter = (0-40-110-220 Hz)
7). Apply surgical mute (cutoff4.smu) to remove ice and water above seafloor
8). to 11). Apply BALANCE and AGC (automatic gain control)
12). view FINAL section

MIS-5 Line

Mis5Job01.job

2). Read in SEGY data (mis5_100.csgy)
3). Reset trace headers using SETHEADER
→ SPARE1=SHOTID CHANNEL=FTRACE

4). Reset trace headers using SETHEADER
→ SHOTID=RECORDNUM
5). Reset primary and secondary keys using SETKEY
→ PKEY=SHOTID SKEY=CHANNEL
6). Write to disc file (Mis5.dsc)

Mis5Job02.job

2). Read in disc file (Mis5.dsc) shots 101:279
3). Use CHECKHDR to identify possible problem areas in the trace headers
4). Use CHECKTR to print a message if a trace contains samples which exceed the specified value
5). Resample data from 1 ms to 2 ms
6). Add geometry (mis5_stuart.geom)
7). Apply trace edit from file Mis5_frontmuted.tre (i.e. zeroes traces)
8). Apply spherical divergence correction using velocities from velocity file (recover.nmo)
--> done iteratively, as velocity fields evolved
9). Apply BALANCE
10). Apply band-pass filter (8-12-100-140 Hz)
--> values ranging from 0 to 200 Hz was tested, these values were most effective
11). Write to shots file (mis5.shots)

Mis5Job02_view.job

2). Read in shots file (mis5_june.shots)
3). Apply BALANCE
4). View shots

Mis5Job03.job

2). Read in shots file (mis5_june.shots) using DISGATH
3). Apply static correction to shift data up and changes trace length from 6000 ms to 5500 ms
4). Apply surgical mute from mute file (mis5.smu)
5). Reorder CDP's based on geometry (mis5_stuart.geom) using CDPSORT
6). Apply NMO correction based on velocity file (recover.nmo)
--> done iteratively, as velocity fields evolved
7). Writes to CDP file (mis5.cdp)
8). Stack data (48 fold)
9). Apply band-pass filter (8-12-100-140 Hz)

10). Apply deconvolution filter from file (mis5_decon.sde)

--> file created based on deconvolution filter testing. Zero cross-over time observed (10 ms) and filter created around this. varying gap and operator lengths tested, with one being held constant and the other varying, and vice-versa. Chosen length = 200, chosen gap = 12.

11). to 15). Tested SCDECON (shot-consistent) but proved unsuccessful. DECONW seemed to work suitably

16). to 18). Write to stacked section (mis5_june.stack, mis5_decon_june.stack, mis5_scdecon_june.stack)

Mis5Job03_view.job

2). Read in stacked sections from list file (mig_compare.lis) for comparison

--> regular, decon applied, decon and migrated (Mis5_june.stack, Mis5_decon_june.stack, Mis5_deconwmig_june.stack)

3). Apply surgical mute (cutoff.smu) to remove ice and water above seafloor

5). View stacked section

Mis5Job04.job

2). Read in stack with DECONW applied to it (Mis5_decon_june.stack)

3). to 5). Migrates data using FDMIG (finite difference migration)

--> DX (distance between traces) = 24 [half the geophone spacing]
WINDSIZ kept constant at 20
THETA kept constant at 0.8
VELFILE = Mis5_brute_interval.nmo (interval velocities created in isovels)
SCALAR value taken to be 0.8

6). Write to migrated stacked section (Mis5_deconwmig_june.stack)

Mis5Job04_view.job

2). Read in stacked sections from list file (mig_compare.lis) for comparison

--> regular, decon applied, decon and migrated (Mis5_june.stack, Mis5_decon_june.stack, Mis5_deconwmig_june.stack)

3). Apply band-pass filter (0-50-110-300 Hz)

4). Apply surgical mute (cutoff.smu) to remove ice and water above seafloor

5). to 8). Apply BALANCE and AGC (automatic gain control)

9). View all sections in separate panels

Mis5Job05.job

--> The same processing flow as Mis5Job04.job, but uses JCS to create 7 jobs each testing different SCALAR values in the FDMIG module. Values varied between 0.5 and 1.15. Chosen value = 0.8 as it produced the best section

 # Mis5Job05_view.job

2). Read in migrated section (Mis5_deconwmig.stack)

3). to 8). 'If loop' testing different values for a band-pass filter, to remove low frequency noise introduced after deconvolution

       --> frequencies (Hz) tested = F1   F2   F3   F4

                                0-0   10-70   100-180 200-350

         from file (Mis5_filters.fdf)

9). chosen band-pass filter =

                    0-15-110-200 (time on 0ms, time off 1000ms)

                    0-50-100-120 (time on 1200ms, time off 1400ms)

                    0-50-90-110 (time on 1500ms, time off 5500ms)

         from file (Mis5_BPfilt.filt)

11). Apply surgical mute (cutoff.smu) to remove ice and water above seafloor

12). to 15). Apply BALANCE and AGC (automatic gain control)

16). View FINAL section

APPENDIX B – Seismic Processing (2005 Data)
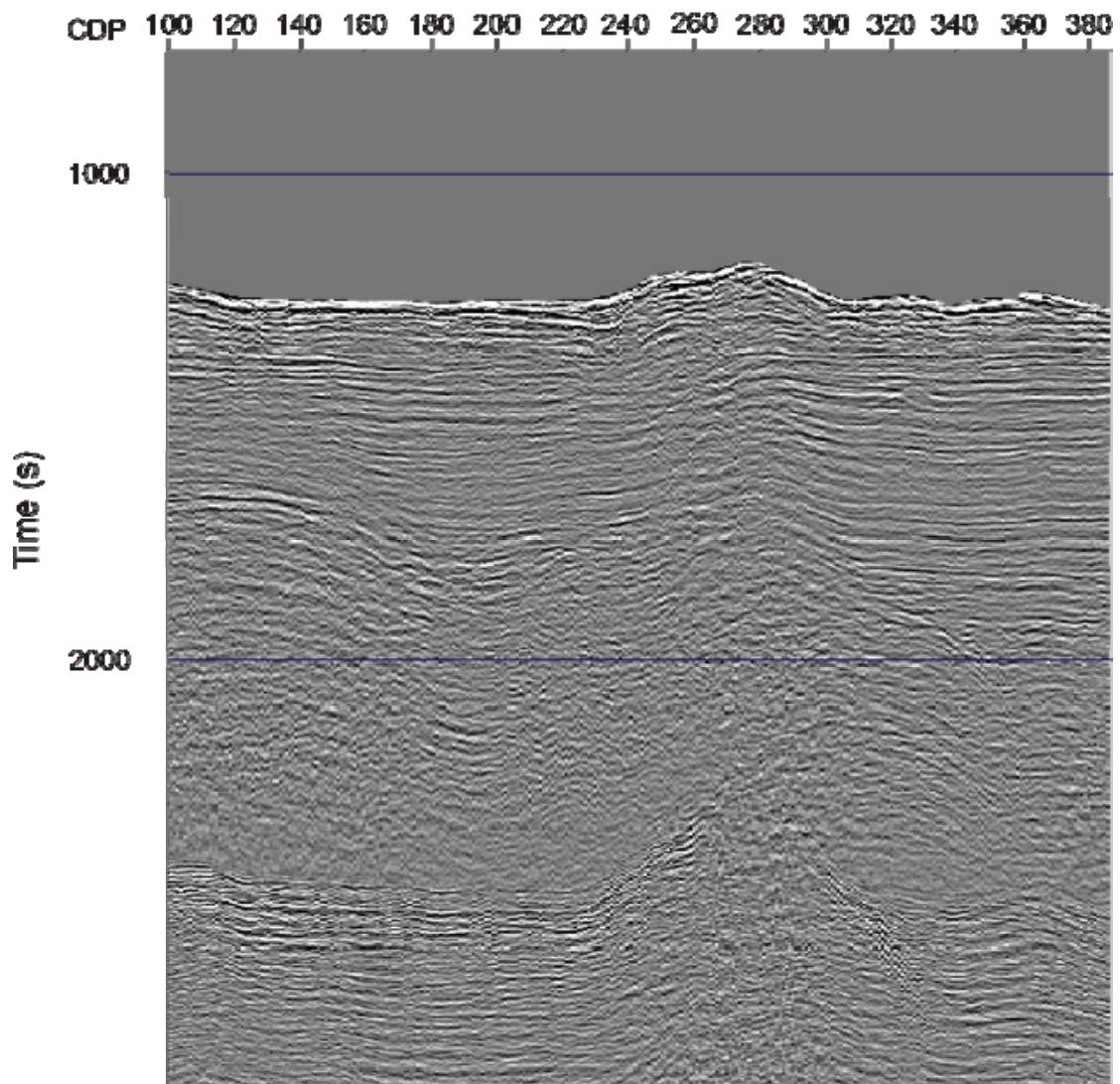
Figure A1. MIS-3 stacked section with spherical divergence, band-pass filtering, NMO correction and deconvolution applied.
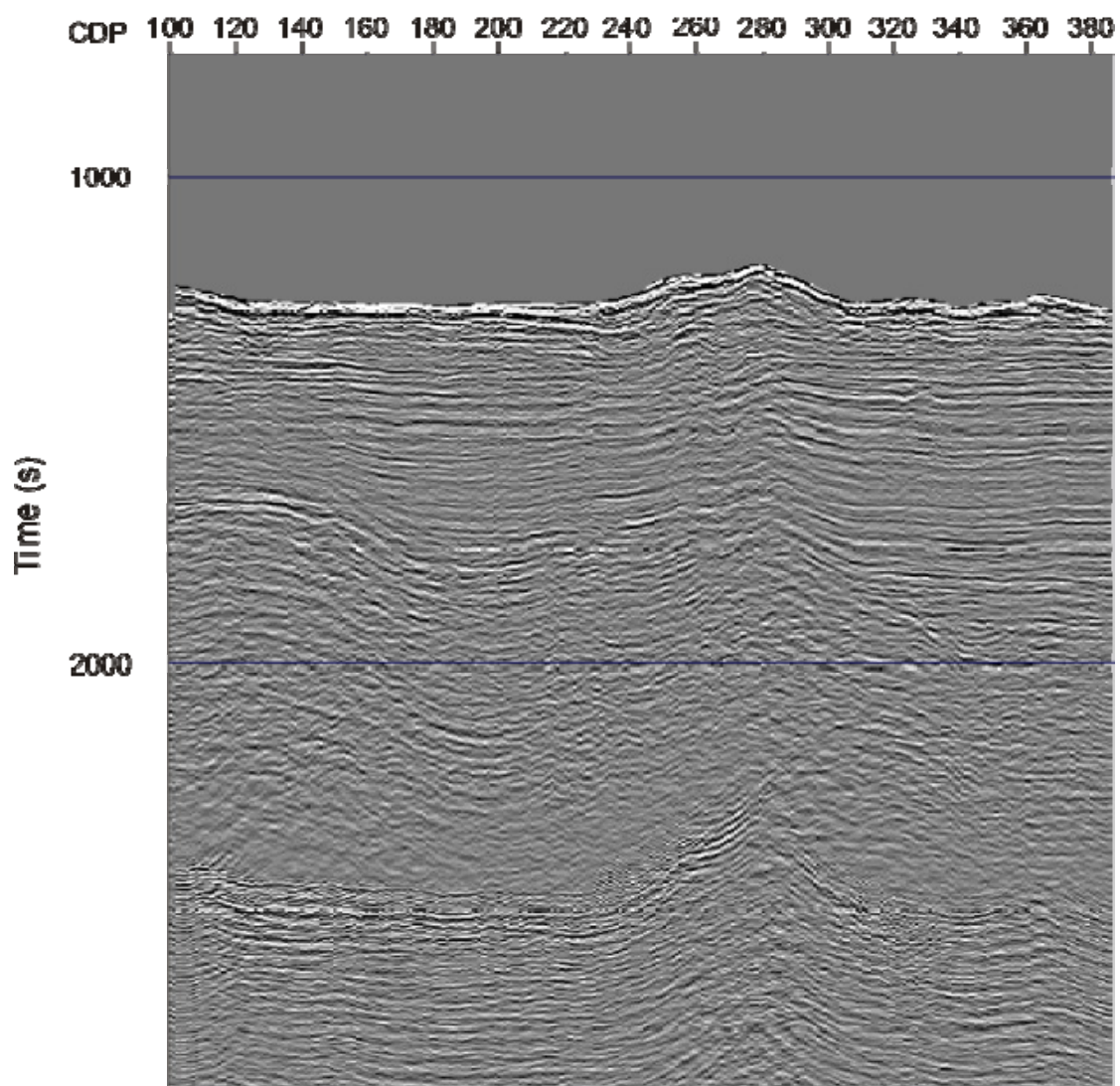
Figure A2. MIS-3 stacked section with spherical divergence, band-pass filtering, NMO correction and migration applied.
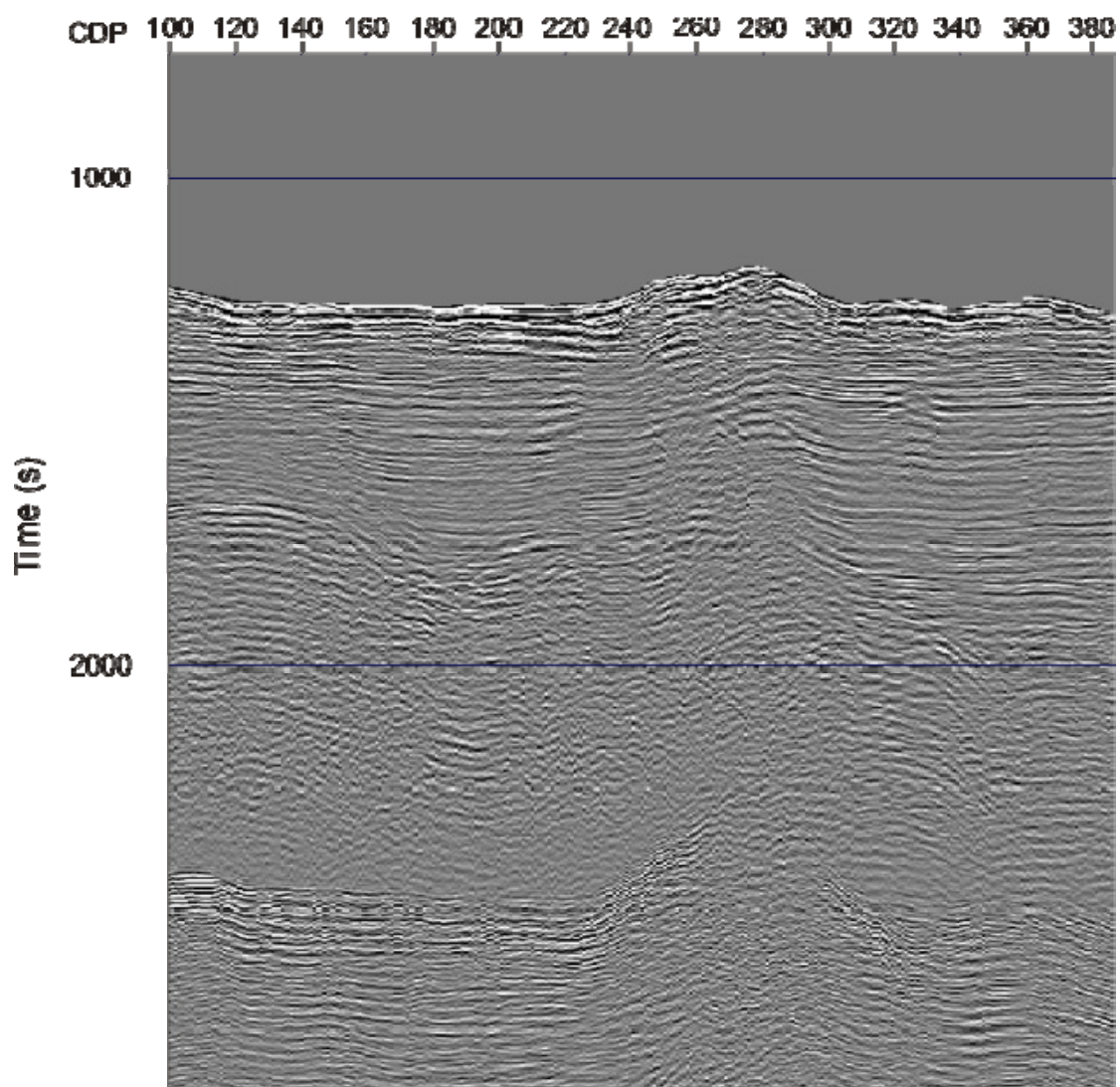
Figure A3. MIS-3 final processed section.
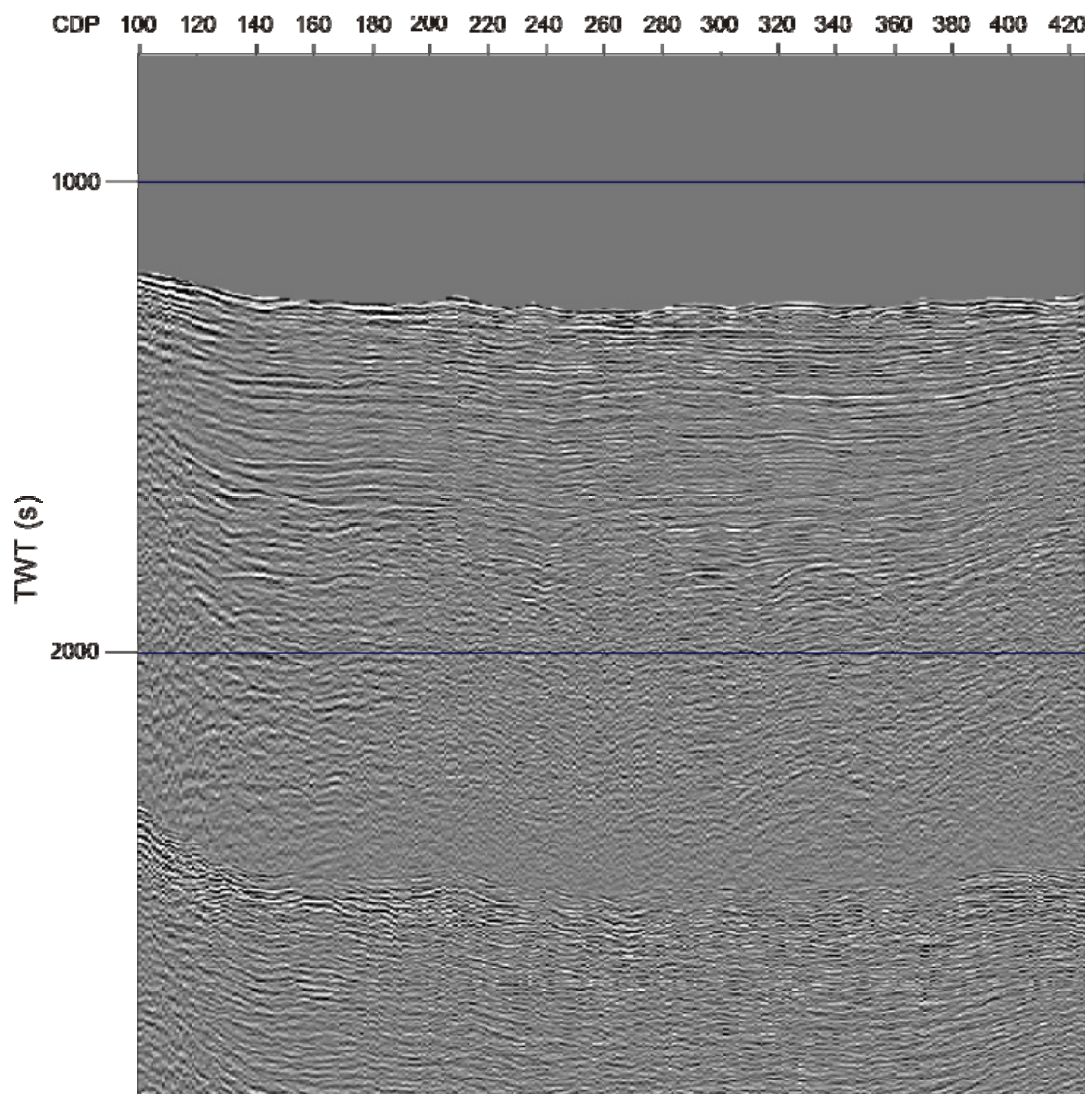
Figure A4. MIS-4 stacked section with spherical divergence, band-pass filtering, NMO correction and deconvolution applied.
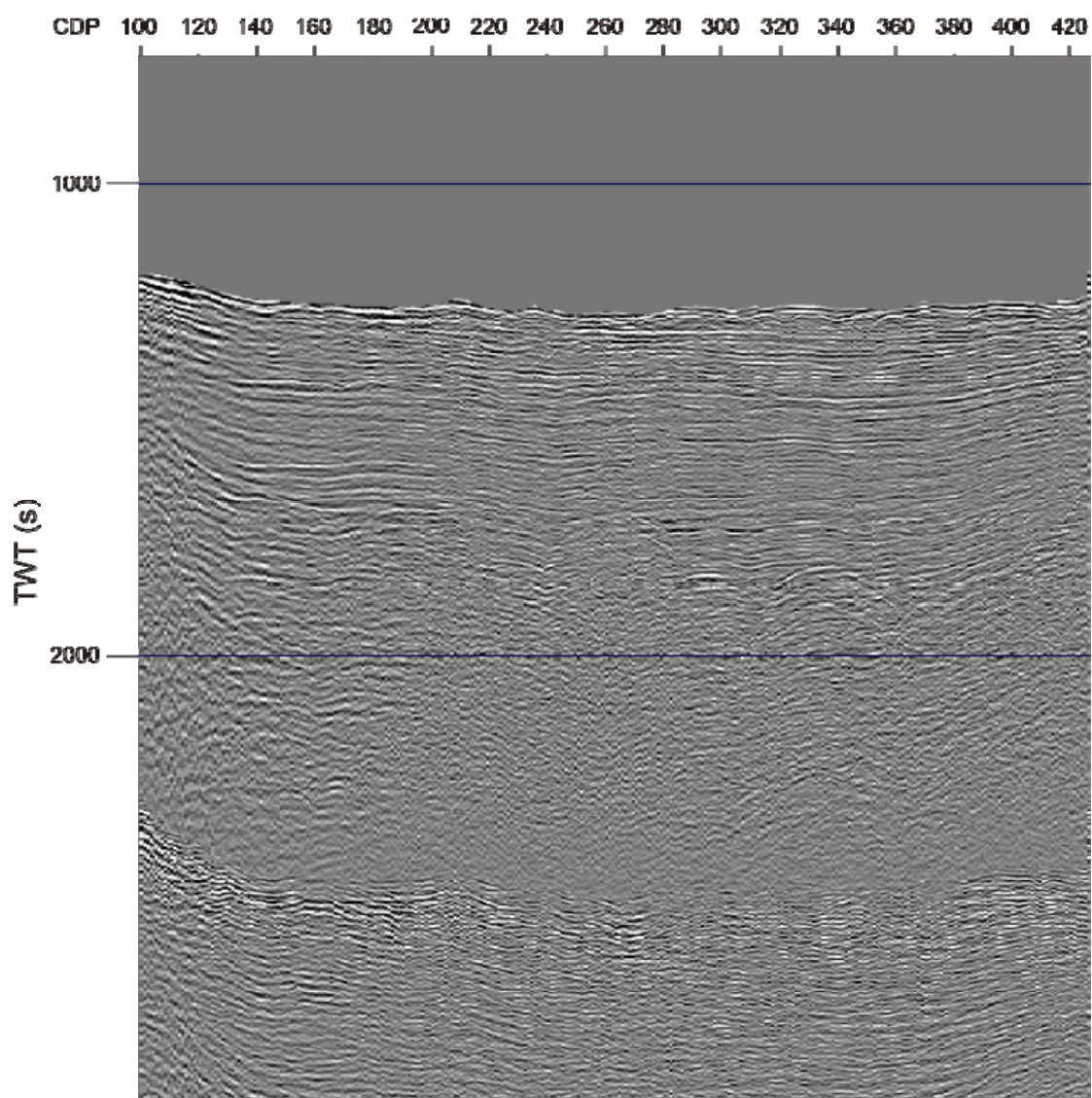
Figure A5. MIS-4 stacked section with spherical divergence, band-pass filtering, NMO correction and migration applied.
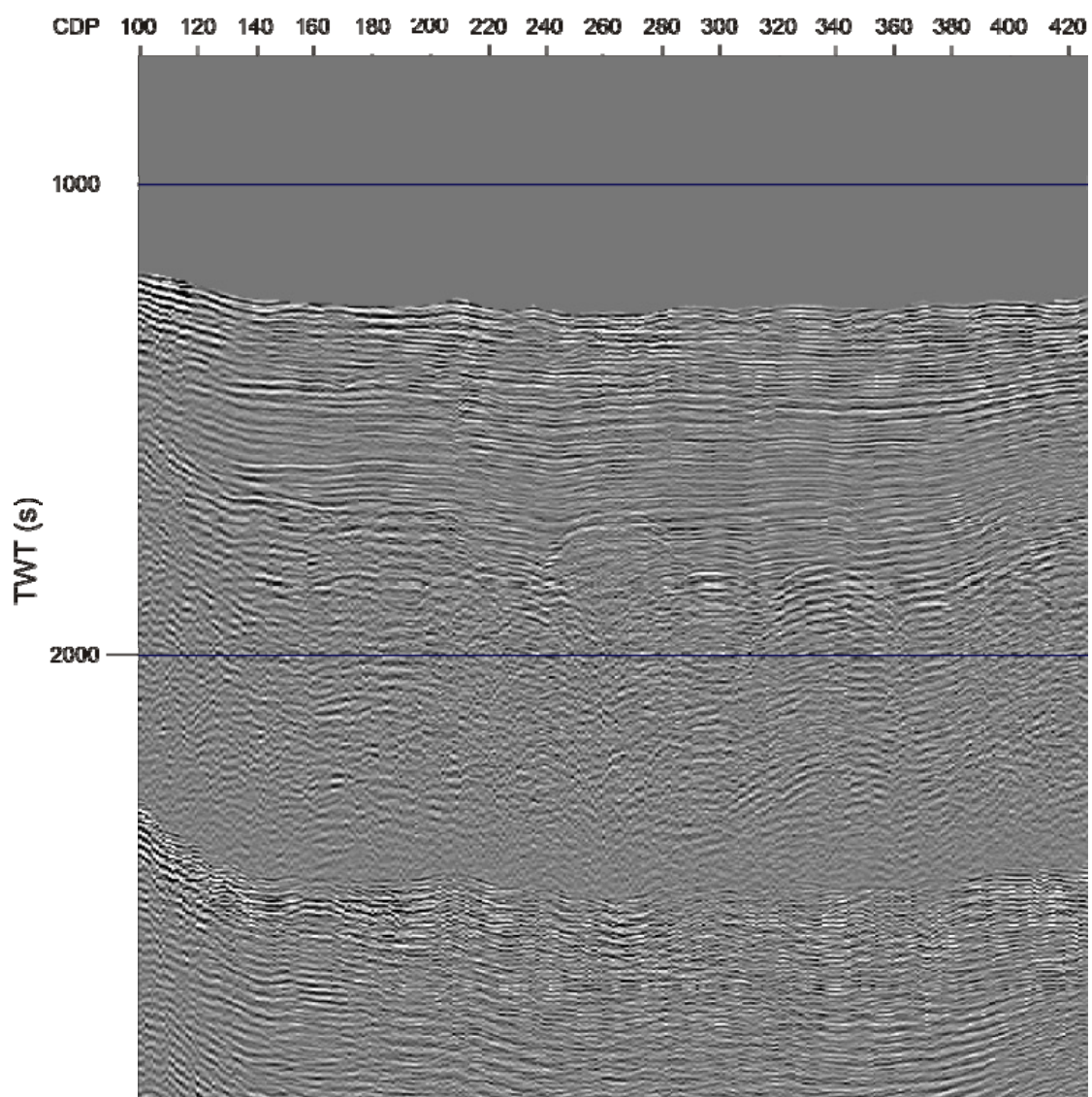
Figure A6. MIS-4 final processed section.
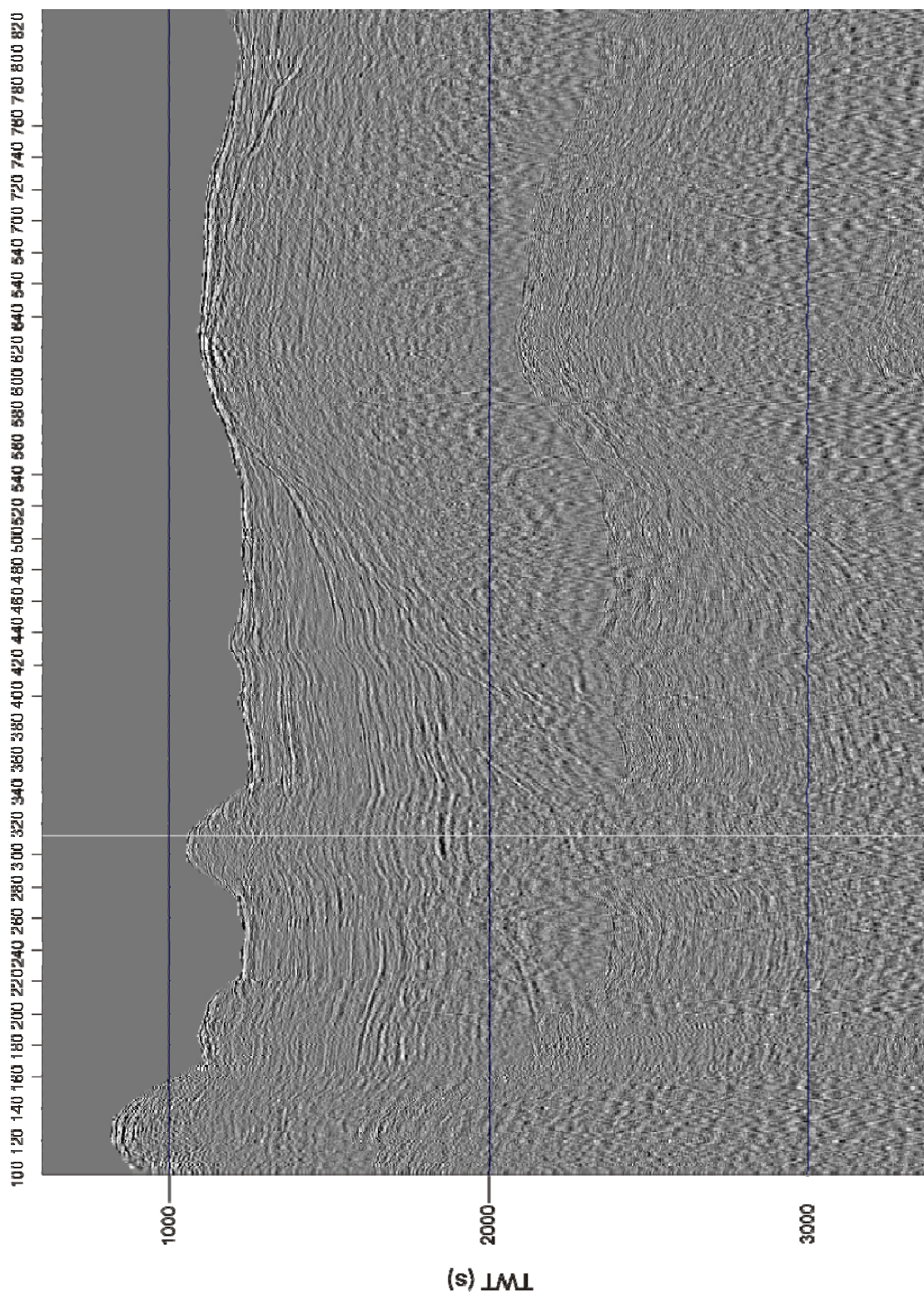
Figure A7. MIS-5 stacked section with spherical divergence, band-pass filtering, NMO correction and deconvolution applied.
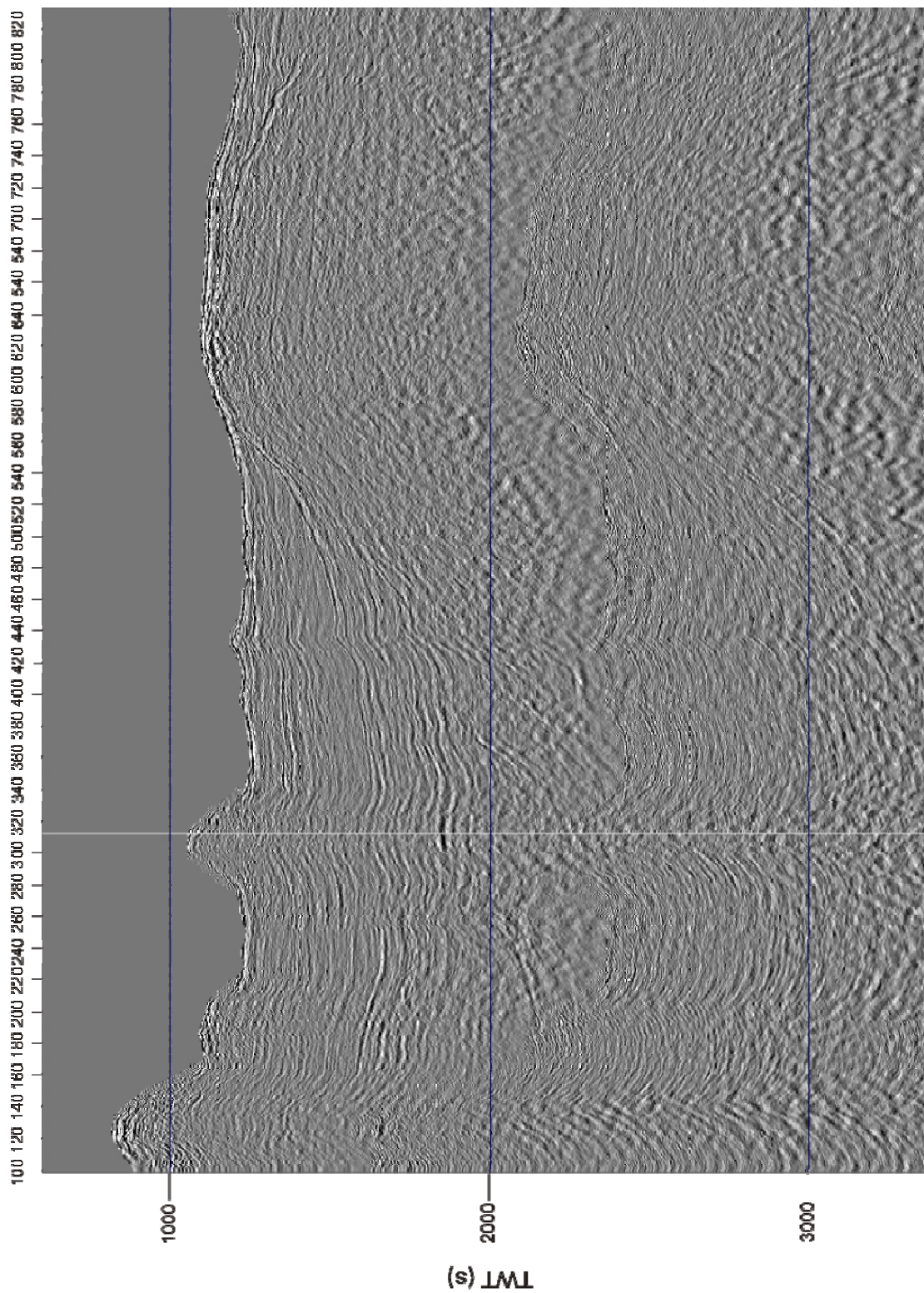
Figure A8. MIS-4 stacked section with spherical divergence, band-pass filtering, NMO correction and migration applied.
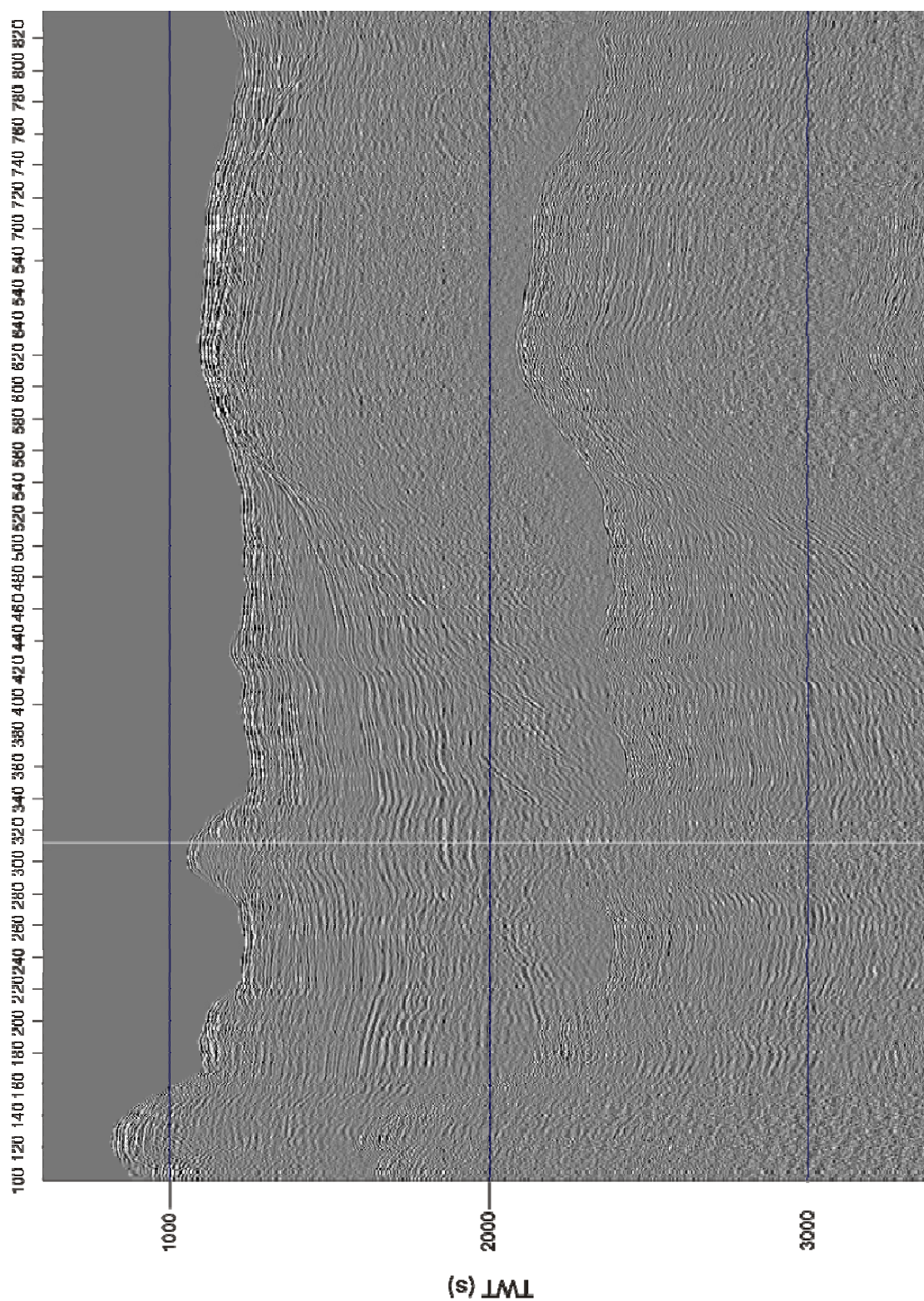
Figure A9. MIS-5 final processed section.
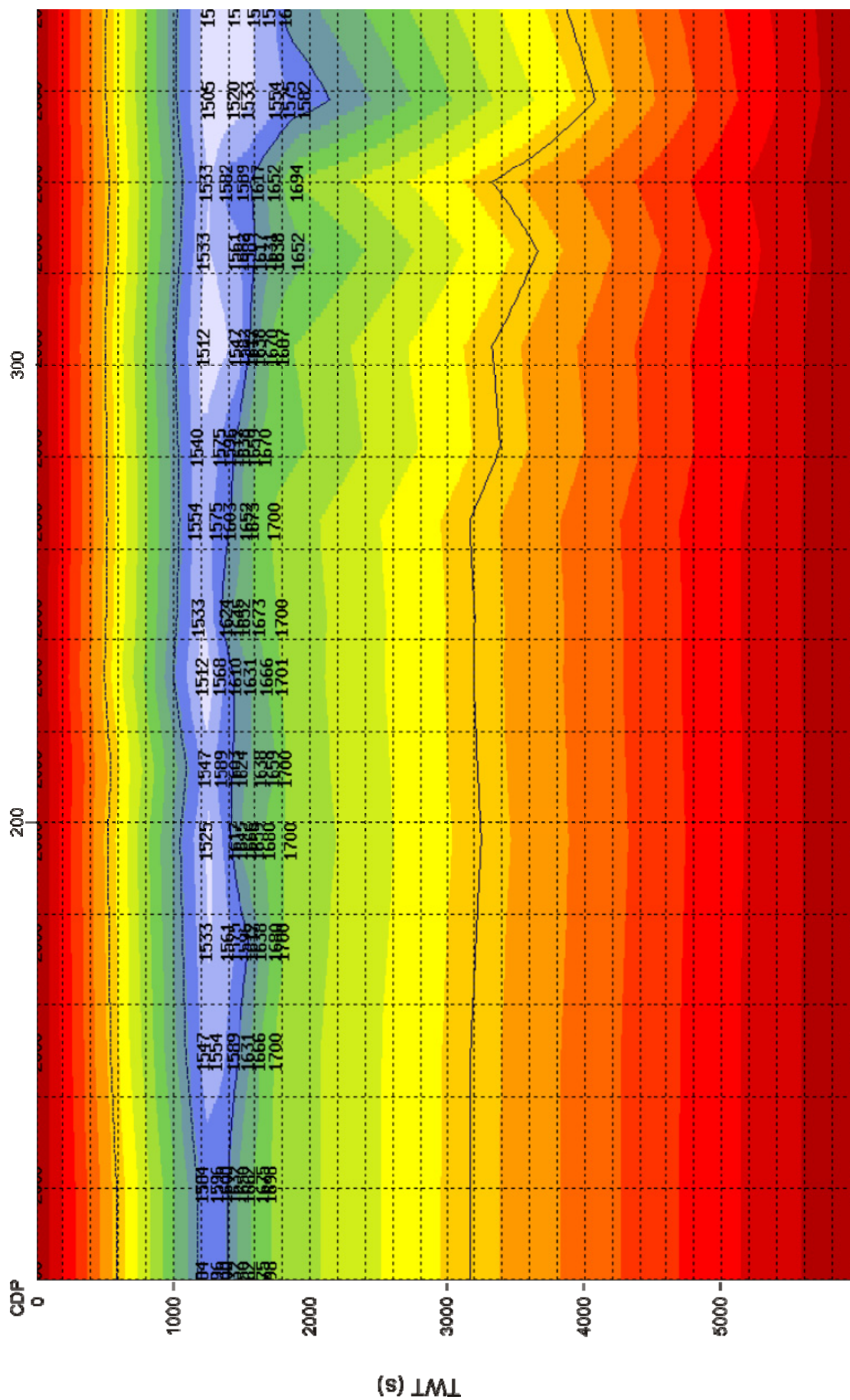
Figure A10. MIS-3 velocity field.
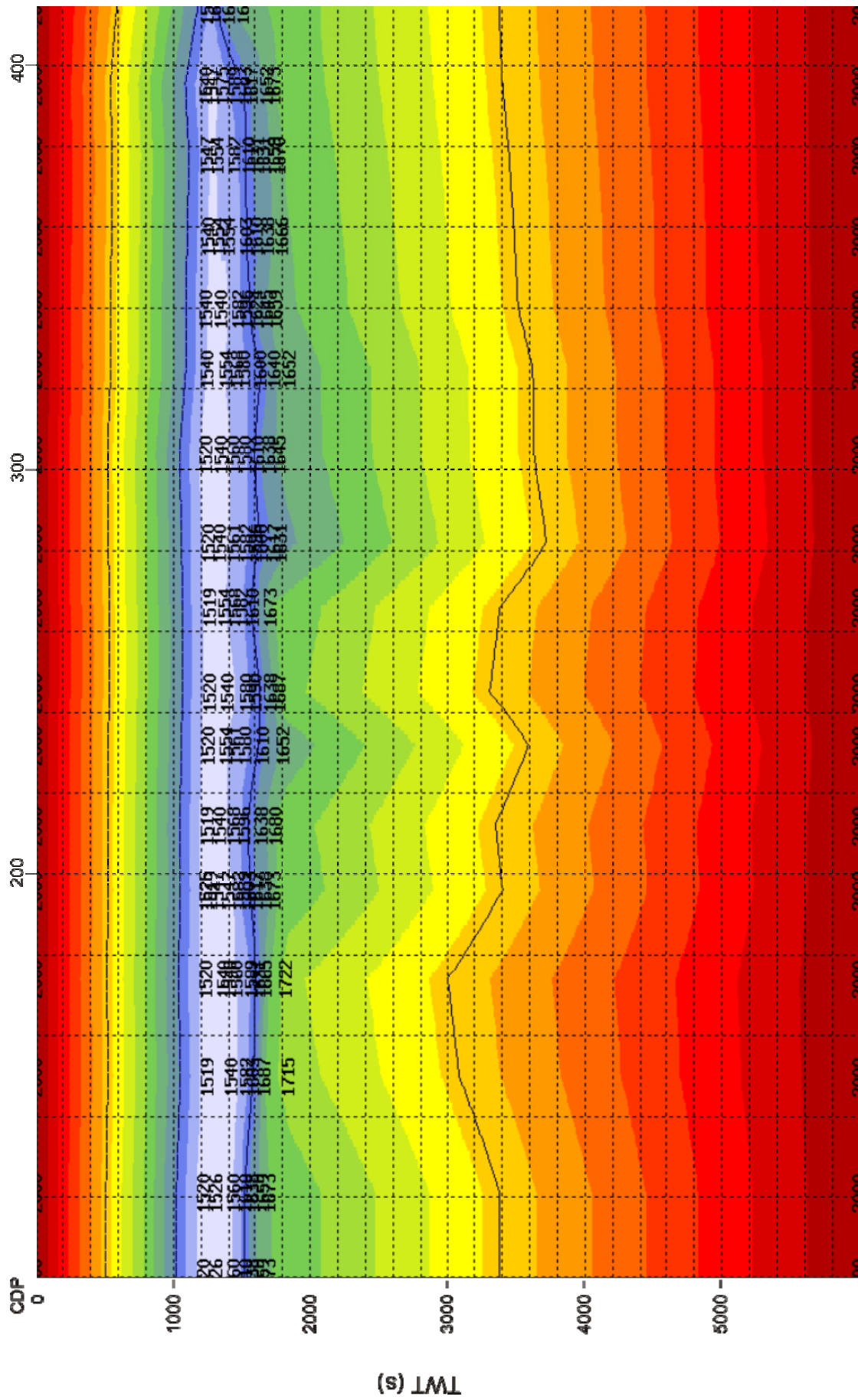
Figure A11. MIS-4 velocity field.
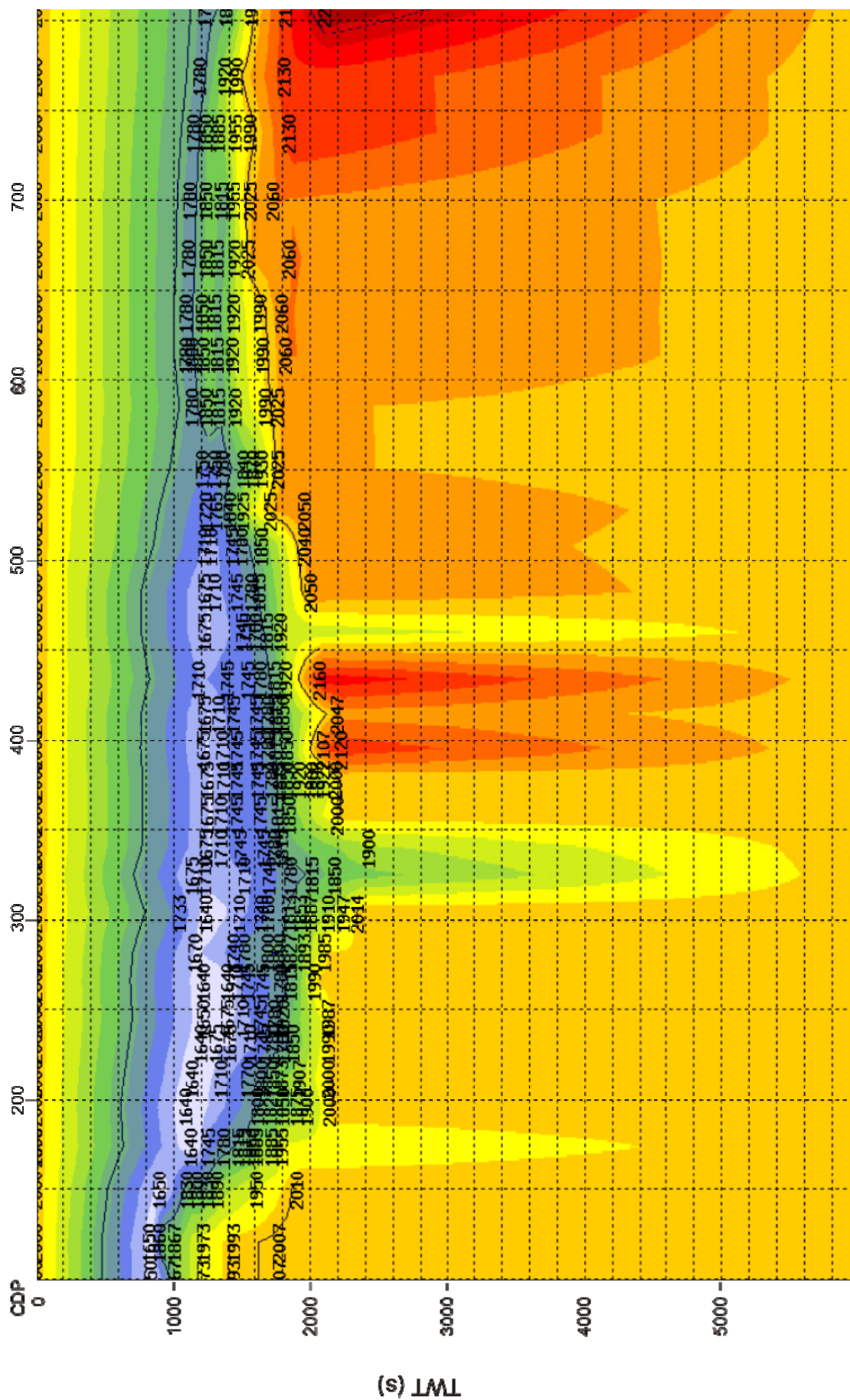
Figure A12. MIS-5 velocity field.

APPENDIX C – VSP (Phase I and II) Seismic Processing Parameters

 # read_AND-1.job

2). Read in SEGY data (AND-1.sgy)
3). View data

 # geom_AND-1.job

2). Read in SEGY data (AND-1.sgy)
3, 4, 5). Remove traces 6 to 24
6). Set last trace to SHOTID
7). Add geometry (MIS1.geom)
8). Write to shot file (AND-1_geom.sht)
9). View data

 # gath_AND-1.job

2). Read in shot file (AND-1_2_geom.sht) using DISCSORT
4). View the data

 # disp_AND-1.job

2). Read in shot file (AND-1_2_geom.sht) using DISCSORT
4). Apply high pass filter (0-200 Hz)
5). Apply BALANCE
6). Reset trace header using SETHEADER --> SHOTID = SPARE1, CHANNEL = SPARE2, FTRACE = SPARE3
7). Reset trace header using SETHEADER --> SHOTID into SHOT_PEG, and FTRACE = 0
8). Renumber secondary key to CHANNEL
9). Set last trace to SHOT_PEG
10). Write to shot file (AND-1_2_offsort.sht) → this allows the entire gather, offset ordered but not into each of the 5 channels, to be brought into SV for first-break picking

 # offset_sort.job

2). Read in shot file (AND-1_2_geom.sht)
6). Reset trace header --> SPARE1 = SHOTID
7). Reset trace header --> SPARE2 = CHANNEL
8). Use GENSORT to sort by FTRACE (primary) and OFFSET (secondary)
9). Reset trace header --> SHOTID = FTRACE
10). Renumber secondary key to CHANNEL
11). Set last trace to SHOTID
15). Write shots file (Mis1.shots)

 # addpick_AND-1.job

Dhiresh Hansaraj   8/09/2009

2). Read in shots file (Mis1.shots)
3). Add first-breaks picks from pic file to SOURCE_STATIC trace header
→ first-breaks were picked using SQC and saved as pic files
4). Write to shots file (Mis1_picks.shots)

static_AND-1.job

2). Read in shots file (Mis1_picks.shots).
3). Apply high-pass filter (20-35 Hz)
4). Apply band-stop filter (48, 49, 51, 52 Hz)
5). Apply static shift, from header SOURCE_STATIC
7). View data

MIS1_extract.job

2). Read in shots file (AND-1_2_offsort.sht)
3 to 5). Apply IFNOT loop with TREMOVE to remove all offsets that are not between 12530 and the end of the file.
→ this extracts only the lower section of the data where quality is higher
6). Set last trace to SHOTID
7). Reset trace header --> SPARE4 = 2
8). Write shots file (AND-1_2_partial.sht)

MIS1_3_merge.job

2). Read in shots file (AND-1_2_partial.sht)
3 to 7). Apply IFNOT loop with TREMOVE to remove all offsets that are not between 1 and 12460 and the end of the file.
→ this extracts only the upper section of the data where quality is higher
8). Set last trace to SHOTID
9). Write shots file (MIS1_3_merge.sht)

 # FKfilt_AND-1.job

2). Read in shots file (Mis_mergepicks.shots)
4). Apply static shift UP, using values in SOURCE_STATIC trace header
5 to 9). Apply ZEROMUTE before applying FKMUTE using mute file (synth_fkmute.mut). Polygon mute was created using FKspectrum zoom within XVIEW.
10). Apply static shift DOWN (after FK muting), using values in SOURCE_STATIC trace header
12). View the data

 # Final_VSP.job

2). Read in shots file (Mis1_join_3_picks.shots)
3). Apply high-pass filter using FDFILT (25 Hz – 75 Hz)
4). Apply static shift UP, using values in SOURCE_STATIC trace header
5 to 7). Apply ZEROMUTE before applying FKMUTE using mute file (tmp2.mut). Polygon mute was created using FKspectrum zoom within XVIEW.
9). Apply static shift DOWN (after FK muting), using values in SOURCE_STATIC trace header
10). Apply static shift DOWN (after FK muting), using values in SOURCE_STATIC trace header
12). Write shots file (Final_VSP_flat.shots)

APPENDIX D – Survey Data (2005)

MIS-3 Line

Flag Number	N	E	Height (masl)	Latitude [S]	Longitude [E]	WGS84 elevation (m)
misiii0077	1355008.374	548114.881	19.137	-77.87257710	167.0519887	-36.217
misiii0078	1354961.289	548103.383	19.051	-77.87300234	167.0515690	-36.303
misiii0079	1354915.240	548092.308	19.127	-77.87341819	167.0511658	-36.227
misiii0080	1354868.271	548080.995	18.925	-77.87384233	167.0507537	-36.429
misiii0081	1354822.111	548069.448	18.889	-77.87425931	167.0503305	-36.464
misiii0082	1354774.993	548058.110	18.920	-77.87468481	167.0499176	-36.434
misiii0083	1354728.357	548046.677	18.848	-77.87510602	167.0494998	-36.506
misiii0084	1354681.173	548035.198	18.724	-77.87553214	167.0490809	-36.630
misiii0085	1354634.935	548023.967	18.707	-77.87594972	167.0486711	-36.647
misiii0086	1354587.822	548012.595	18.681	-77.87637518	167.0482566	-36.673
misiii0087	1354541.985	548001.768	18.552	-77.87678904	167.0478634	-36.802
misiii0088	1354495.076	547990.298	18.535	-77.87721270	167.0474444	-36.819
misiii0089	1354448.874	547979.498	18.441	-77.87762981	167.0470528	-36.913
misiii0090	1354401.787	547968.163	18.460	-77.87805502	167.0466398	-36.894
misiii0091	1354355.461	547957.245	18.338	-77.87847328	167.0462433	-37.016
misiii0092	1354308.236	547946.214	18.476	-77.87889964	167.0458433	-36.878
misiii0093	1354261.916	547935.182	18.248	-77.87931788	167.0454420	-37.106
misiii0094	1354214.714	547924.136	18.300	-77.87974402	167.0450413	-37.054
misiii0095	1354168.032	547913.187	18.229	-77.88016548	167.0446439	-37.125
misiii0096	1354120.794	547902.059	18.115	-77.88059198	167.0442397	-37.239
misiii0097	1354074.052	547890.984	18.029	-77.88101402	167.0438370	-37.325
misiii0098	1354026.680	547879.919	18.095	-77.88144169	167.0434356	-37.259
misiii0099	1353979.816	547868.897	17.972	-77.88186479	167.0430353	-37.382
misiii0100	1353932.548	547857.634	17.874	-77.88229160	167.0426253	-37.480
misiii0100.5	1353908.970	547851.970	17.661	-77.88250451	167.0424188	-37.693
misiii0101	1353886.007	547846.834	17.827	-77.88271174	167.0422339	-37.527
misiii0102	1353838.785	547835.698	17.728	-77.88313809	167.0418292	-37.626
misiii0102.5	1353815.345	547830.153	17.432	-77.88334973	167.0416276	-37.922
misiii0103	1353792.476	547824.641	17.593	-77.88355624	167.0414265	-37.761
misiii0104	1353745.054	547813.513	17.631	-77.88398438	167.0410223	-37.723
misiii0104.5	1353721.439	547808.239	17.378	-77.88419749	167.0408325	-37.976
misiii0105	1353698.642	547802.492	17.553	-77.88440343	167.0406212	-37.801
misiii0106	1353651.385	547791.344	17.461	-77.88483009	167.0402159	-37.893
misiii0106.5	1353627.595	547786.298	17.174	-77.88504471	167.0400360	-38.180
misiii0107	1353604.781	547780.655	17.369	-77.88525077	167.0398292	-37.985
misiii0108	1353557.398	547769.532	17.346	-77.88567856	167.0394251	-38.008
misiii0108.5	1353533.711	547763.753	17.088	-77.88589247	167.0392138	-38.266
misiii0109	1353511.257	547758.149	17.210	-77.88609530	167.0390080	-38.144
misiii0110	1353463.800	547746.886	17.223	-77.88652378	167.0385980	-38.131
misiii0110.5	1353440.105	547741.056	17.032	-77.88673779	167.0383845	-38.322
misiii0111	1353417.211	547735.914	17.108	-77.88694441	167.0381991	-38.246
misiii0112	1353370.097	547724.798	17.109	-77.88736977	167.0377948	-38.245
misiii0112.5	1353346.151	547719.337	16.993	-77.88758591	167.0375974	-38.361
misiii0113	1353323.298	547713.795	17.048	-77.88779229	167.0373948	-38.306
misiii0114	1353275.992	547702.699	16.986	-77.88821937	167.0369916	-38.368
misiii0114.5	1353252.381	547697.163	16.716	-77.88843254	167.0367904	-38.638

Dhiresh Hansaraj   8/09/2009

Flag Number	N	E	Height (masl)	Latitude [S]	Longitude [E]	WGS84 elevation (m)
misiii0115	1353229.536	547691.692	16.881	-77.88863882	167.0365909	-38.473
misiii0116	1353182.361	547680.293	16.851	-77.88906482	167.0361744	-38.503
misiii0116.5	1353158.536	547674.969	16.672	-77.88927983	167.0359826	-38.682
misiii0117	1353135.659	547669.377	16.743	-77.88948643	167.0357779	-38.611
misiii0118	1353088.327	547658.359	16.750	-77.88991372	167.0353779	-38.603
misiii0118.5	1353064.706	547652.604	16.575	-77.89012704	167.0351674	-38.779
misiii0119	1353041.779	547647.268	16.677	-77.89033401	167.0349737	-38.677
misiii0120	1352994.559	547636.074	16.649	-77.89076035	167.0345660	-38.705
misiii0120.5	1352970.856	547630.553	16.526	-77.89097433	167.0343655	-38.828
misiii0121	1352947.687	547624.874	16.549	-77.89118357	167.0341575	-38.805
misiii0122	1352900.363	547613.641	16.505	-77.89161085	167.0337482	-38.849
misiii0122.5	1352876.944	547607.548	16.373	-77.89182246	167.0335229	-38.981
misiii0123	1352853.574	547602.484	16.458	-77.89203332	167.0333413	-38.896
misiii0124	1352806.138	547591.493	16.392	-77.89246153	167.0329425	-38.962
misiii0124.5	1352782.267	547585.662	16.299	-77.89267711	167.0327290	-39.055
misiii0125	1352759.610	547580.071	16.352	-77.89288173	167.0325239	-39.002
misiii0126	1352712.570	547568.415	16.297	-77.89330660	167.0320960	-39.057
misiii0126.5	1352688.562	547563.386	16.170	-77.89352316	167.0319169	-39.184
misiii0127	1352666.037	547558.144	16.281	-77.89372650	167.0317265	-39.073
misiii0128	1352618.745	547546.778	16.132	-77.89415353	167.0313114	-39.222
misiii0128.5	1352595.049	547541.986	15.942	-77.89436722	167.0311419	-39.412
misiii0129	1352571.846	547536.646	16.038	-77.89457666	167.0309483	-39.316
misiii0130	1352524.309	547525.746	16.015	-77.89500574	167.0305533	-39.339
misiii0130.5	1352500.662	547520.195	15.934	-77.89521922	167.0303513	-39.420
misiii0131	1352477.951	547514.798	16.048	-77.89542428	167.0301545	-39.306
misiii0132	1352430.612	547503.713	15.915	-77.89585164	167.0297513	-39.439
misiii0132.5	1352406.835	547498.578	15.839	-77.89606616	167.0295673	-39.515
misiii0133	1352383.675	547493.119	15.828	-77.89627525	167.0293684	-39.525
misiii0134	1352336.260	547482.510	15.741	-77.89670315	167.0289856	-39.613
misiii0134.5	1352312.335	547477.215	15.705	-77.89691904	167.0287949	-39.648
misiii0135	1352289.761	547471.972	15.804	-77.89712281	167.0286044	-39.550
misiii0136	1352242.469	547461.253	15.733	-77.89754964	167.0282167	-39.621
misiii0136.5	1352218.574	547456.212	15.526	-77.89776519	167.0280368	-39.828
misiii0137	1352195.553	547450.703	15.612	-77.89797305	167.0278355	-39.742
misiii0138	1352148.048	547439.735	15.521	-77.89840186	167.0274374	-39.833
misiii0138.5	1352124.406	547434.429	15.434	-77.89861522	167.0272458	-39.920
misiii0139	1352101.057	547429.338	15.486	-77.89882589	167.0270629	-39.868
misiii0140	1352053.494	547418.760	15.472	-77.89925509	167.0266814	-39.882
misiii0140.5	1352029.713	547413.576	15.364	-77.89946966	167.0264952	-39.990
misiii0141	1352006.598	547408.401	15.438	-77.89967826	167.0263083	-39.916
misiii0142	1351959.079	547397.622	15.322	-77.90010714	167.0259182	-40.032
misiii0142.5	1351935.108	547392.693	15.222	-77.90032333	167.0257431	-40.132
misiii0143	1351912.204	547387.452	15.255	-77.90053006	167.0255531	-40.099
misiii0144	1351864.746	547377.154	15.272	-77.90095824	167.0251833	-40.082
misiii0144.5	1351840.926	547372.039	15.206	-77.90117313	167.0250000	-40.148
misiii0145	1351817.958	547366.976	15.279	-77.90138038	167.0248177	-40.075
misiii0146	1351770.517	547356.237	15.228	-77.90180854	167.0244290	-40.126
misiii0146.5	1351746.634	547351.527	15.142	-77.90202387	167.0242631	-40.212
misiii0147	1351724.479	547346.405	15.144	-77.90222386	167.0240770	-40.210
misiii0148	1351677.851	547336.130	15.207	-77.90264459	167.0237070	-40.147

Dhiresh Hansaraj   8/09/2009

Flag Number	N	E	Height (masl)	Latitude [S]	Longitude [E]	WGS84 elevation (m)
misiii0148.5	1351654.406	547331.120	15.099	-77.90285609	167.0235275	-40.255
misiii0149	1351631.463	547326.495	15.242	-77.90306298	167.0233638	-40.112
misiii0150	1351584.702	547316.751	15.081	-77.90348474	167.0230166	-40.273
misiii0150.5	1351561.344	547311.472	14.872	-77.90369555	167.0228255	-40.482
misiii0151	1351538.847	547306.750	14.913	-77.90389847	167.0226570	-40.441
misiii0152	1351492.127	547296.516	14.871	-77.90432002	167.0222886	-40.483
misiii0152.5	1351468.678	547290.837	14.626	-77.90453177	167.0220806	-40.728
misiii0153	1351445.693	547286.229	14.851	-77.90473902	167.0219176	-40.503
misiii0154	1351398.843	547276.174	14.823	-77.90516168	167.0215571	-40.531
misiii0154.5	1351375.500	547270.516	14.542	-77.90537246	167.0213498	-40.812
misiii0155	1351352.675	547266.009	14.688	-77.90557826	167.0211909	-40.666
misiii0156	1351305.991	547255.547	14.697	-77.90599955	167.0208127	-40.657
misiii0156.5	1351282.343	547250.389	14.414	-77.90621291	167.0206271	-40.940
misiii0157	1351259.377	547245.918	14.674	-77.90641995	167.0204699	-40.680
misiii0158	1351212.280	547235.464	14.622	-77.90684494	167.0200927	-40.732
misiii0158.5	1351188.552	547230.414	14.232	-77.90705899	167.0199118	-41.122
misiii0159	1351165.659	547225.586	14.493	-77.90726549	167.0197392	-40.860
misiii0160	1351118.736	547215.287	14.440	-77.90768887	167.0193683	-40.914
misiii0160.5	1351094.867	547210.274	14.266	-77.90790417	167.0191892	-41.088
misiii0161	1351072.255	547205.314	14.409	-77.90810819	167.0190106	-40.945
misiii0162	1351025.158	547195.348	14.382	-77.90853302	167.0186540	-40.972
misiii0162.5	1351001.629	547190.202	14.086	-77.90874531	167.0184687	-41.267
misiii0163	1350978.494	547185.269	14.374	-77.90895401	167.0182919	-40.980
misiii0164	1350931.257	547174.993	14.396	-77.90938020	167.0179223	-40.958
misiii0164.5	1350907.509	547169.495	14.121	-77.90959456	167.0177223	-41.233
misiii0165	1350884.114	547164.580	14.389	-77.90980558	167.0175467	-40.965
misiii0166	1350837.111	547154.300	14.328	-77.91022967	167.0171765	-41.026
misiii0166.5	1350813.356	547148.906	14.075	-77.91044406	167.0169809	-41.279
misiii0167	1350790.170	547143.840	14.258	-77.91065325	167.0167984	-41.096
misiii0168	1350742.661	547133.451	14.109	-77.91108191	167.0164243	-41.245
misiii0168.5	1350718.802	547127.586	13.845	-77.91129737	167.0162087	-41.509
misiii0169	1350696.131	547123.138	14.211	-77.91150177	167.0160519	-41.143
misiii0170	1350648.800	547112.843	14.141	-77.91192880	167.0156814	-41.213
misiii0170.5	1350625.075	547107.359	13.983	-77.91214295	167.0154819	-41.371
misiii0171	1350601.932	547102.871	14.139	-77.91235158	167.0153241	-41.215
misiii0172	1350554.651	547092.440	14.067	-77.91277820	167.0149477	-41.287
misiii0172.5	1350530.848	547086.972	13.797	-77.91299305	167.0147489	-41.557
misiii0173	1350507.905	547082.410	13.992	-77.91319990	167.0145876	-41.362
misiii0174	1350460.766	547072.062	14.052	-77.91362523	167.0142145	-41.302
misiii0174.5	1350436.734	547066.698	13.885	-77.91384209	167.0140205	-41.469
misiii0175	1350414.308	547062.149	14.155	-77.91404432	167.0138589	-41.199
misiii0176	1350367.005	547051.882	13.919	-77.91447109	167.0134895	-41.435
misiii0176.5	1350343.049	547046.658	13.658	-77.91468723	167.0133013	-41.696
misiii0177	1350320.726	547041.773	13.994	-77.91488863	167.0131253	-41.360
misiii0178	1350273.230	547031.778	13.910	-77.91531704	167.0127676	-41.444
misiii0178.5	1350249.774	547026.635	13.675	-77.91552867	167.0125822	-41.678
misiii0179	1350226.484	547021.774	13.860	-77.91573874	167.0124085	-41.494
misiii0180	1350178.727	547011.707	13.885	-77.91616951	167.0120482	-41.469
misiii0180.5	1350154.894	547006.490	13.632	-77.91638454	167.0118601	-41.722
misiii0181	1350132.296	547001.567	13.830	-77.91658842	167.0116828	-41.524

Dhiresh Hansaraj   8/09/2009

Flag Number	N	E	Height (masl)	Latitude [S]	Longitude [E]	WGS84 elevation (m)
misiii0182	1350085.047	546991.464	13.791	-77.91701464	167.0113201	-41.563
misiii0182.5	1350061.257	546986.410	13.480	-77.91722925	167.0111389	-41.874
misiii0183	1350038.593	546981.486	13.631	-77.91743372	167.0109616	-41.723
misiii0184	1349991.327	546971.403	13.629	-77.91786009	167.0105997	-41.725
misiii0184.5	1349966.975	546966.461	13.403	-77.91807969	167.0104241	-41.951
misiii0185	1349944.602	546961.605	13.691	-77.91828153	167.0102493	-41.663
misiii0186	1349897.512	546951.500	13.652	-77.91870634	167.0098861	-41.702
misiii0186.5	1349873.904	546945.811	13.409	-77.91891950	167.0096775	-41.945
misiii0187	1349850.813	546941.660	13.599	-77.91912756	167.0095338	-41.755
misiii0188	1349803.667	546931.479	13.524	-77.91955288	167.0091675	-41.829
misiii0188.5	1349780.144	546926.285	13.406	-77.91976513	167.0089798	-41.948
misiii0189	1349756.720	546921.423	13.512	-77.91997639	167.0088062	-41.842
misiii0190	1349709.608	546911.283	13.615	-77.92040140	167.0084415	-41.739
misiii0190.5	1349686.143	546906.541	13.477	-77.92061299	167.0082731	-41.877
misiii0191	1349663.596	546901.362	13.574	-77.92081649	167.0080846	-41.780
misiii0192	1349616.270	546891.260	13.600	-77.92124340	167.0077219	-41.754
misiii0192.5	1349592.621	546886.174	13.462	-77.92145675	167.0075389	-41.891
misiii0193	1349569.669	546881.261	13.441	-77.92166379	167.0073624	-41.913
misiii0194	1349522.452	546871.160	13.417	-77.92208972	167.0069995	-41.937
misiii0194.5	1349499.329	546866.265	13.376	-77.92229830	167.0068239	-41.978
misiii0195	1349475.899	546861.202	13.394	-77.92250968	167.0066417	-41.960
misiii0196	1349428.635	546851.189	13.429	-77.92293600	167.0062825	-41.925
misiii0196.5	1349405.127	546846.173	13.335	-77.92314806	167.0061023	-42.019
misiii0197	1349382.301	546841.557	13.390	-77.92335389	167.0059383	-41.964
misiii0198	1349335.254	546831.352	13.328	-77.92377833	167.0055705	-42.026
misiii0198.5	1349311.897	546826.399	13.349	-77.92398901	167.0053928	-42.005
misiii0199	1349288.962	546821.346	13.447	-77.92419595	167.0052102	-41.907
misiii0200	1349241.988	546810.902	13.435	-77.92461981	167.0048321	-41.919
misiii0200.5	1349218.489	546806.402	13.339	-77.92483163	167.0046739	-42.015
misiii0201	1349195.097	546801.259	13.303	-77.92504268	167.0044881	-42.051
misiii0202	1349147.811	546791.243	13.234	-77.92546921	167.0041287	-42.119
misiii0202.5	1349124.480	546786.470	13.219	-77.92567960	167.0039585	-42.135
misiii0203	1349101.086	546781.059	13.383	-77.92589076	167.0037612	-41.971
misiii0204	1349053.681	546770.874	13.297	-77.92631840	167.0033947	-42.057
misiii0204.5	1349030.310	546766.095	13.273	-77.92652915	167.0032244	-42.081
misiii0205	1349007.235	546760.930	13.360	-77.92673737	167.0030371	-41.994
misiii0206	1348959.959	546750.750	13.240	-77.92716386	167.0026706	-42.114
misiii0206.5	1348936.592	546746.310	13.160	-77.92737447	167.0025147	-42.194
misiii0207	1348913.131	546740.683	13.316	-77.92758629	167.0023082	-42.038
misiii0208	1348865.709	546730.728	13.372	-77.92801402	167.0019514	-41.982
misiii0208.5	1348842.466	546726.545	13.048	-77.92822344	167.0018064	-42.306
misiii0209	1348819.270	546721.039	13.293	-77.92843285	167.0016046	-42.061
misiii0210	1348771.866	546711.135	13.249	-77.92886039	167.0012500	-42.105
misiii0210.5	1348748.651	546706.632	13.202	-77.92906967	167.0010912	-42.152
misiii0211	1348725.174	546701.041	13.290	-77.92928161	167.0008862	-42.063
misiii0212	1348677.814	546691.256	13.359	-77.92970873	167.0005365	-41.995
misiii0212.5	1348654.784	546686.475	13.157	-77.92991643	167.0003655	-42.197
misiii0213	1348630.992	546681.158	13.199	-77.93013112	167.0001726	-42.155
misiii0214	1348583.546	546670.979	13.175	-77.93055912	166.9998062	-42.179
misiii0214.5	1348560.164	546665.921	13.086	-77.93077006	166.9996239	-42.268

Flag Number	N	E	Height (masl)	Latitude [S]	Longitude [E]	WGS84 elevation (m)
misiii0215	1348536.957	546661.107	13.122	-77.93097935	166.9994517	-42.232
misiii0216	1348489.593	546650.812	13.092	-77.93140665	166.9990801	-42.262
misiii0216.5	1348466.552	546645.881	13.094	-77.93161450	166.9989026	-42.260
misiii0217	1348442.626	546641.127	13.107	-77.93183021	166.9987340	-42.247
misiii0218	1348394.882	546630.545	13.210	-77.93226101	166.9983506	-42.144
misiii0218.5	1348371.694	546625.780	13.231	-77.93247011	166.9981805	-42.123
misiii0219	1348347.851	546620.622	13.135	-77.93268521	166.9979944	-42.219
misiii0220	1348300.126	546610.936	12.981	-77.93311555	166.9976494	-42.373
misiii0220.5	1348275.793	546606.042	12.947	-77.93333495	166.9974753	-42.406
misiii0221	1348252.992	546601.015	13.055	-77.93354067	166.9972933	-42.299
misiii0222	1348205.373	546590.996	12.836	-77.93397017	166.9969338	-42.518
misiii0223	1348158.317	546581.134	12.898	-77.93439458	166.9965801	-42.456
misiii0224	1348110.749	546571.139	12.955	-77.93482362	166.9962215	-42.399
misiii0225	1348063.842	546561.259	13.072	-77.93524670	166.9958668	-42.282
misiii0226	1348016.313	546551.437	13.013	-77.93567532	166.9955155	-42.341
misiii0227	1347969.834	546541.847	13.113	-77.93609448	166.9951725	-42.241
misiii0228	1347922.489	546531.893	12.922	-77.93652149	166.9948152	-42.432
misiii0229	1347875.880	546522.205	12.884	-77.93694185	166.9944682	-42.470
misiii0230	1347828.251	546512.511	12.893	-77.93737134	166.9941224	-42.461
misiii0231	1347781.697	546502.720	12.946	-77.93779122	166.9937709	-42.408
misiii0232	1347734.154	546492.739	12.745	-77.93822002	166.9934126	-42.609
misiii0233	1347686.812	546483.052	12.750	-77.93864693	166.9930666	-42.604
misiii0234	1347639.283	546473.108	12.887	-77.93907559	166.9927099	-42.467
misiii0235	1347591.837	546463.348	12.861	-77.93950345	166.9923608	-42.493
misiii0236	1347544.119	546453.586	12.728	-77.93993375	166.9920121	-42.625
misiii0237	1347497.154	546444.044	12.735	-77.94035725	166.9916717	-42.619
misiii0238	1347449.546	546434.119	12.715	-77.94078661	166.9913158	-42.639
misiii0239	1347401.808	546424.175	12.740	-77.94121714	166.9909592	-42.614
misiii0240	1347354.150	546413.994	12.654	-77.94164703	166.9905923	-42.699
misiii0241	1347306.961	546403.799	12.696	-77.94207272	166.9902242	-42.658
misiii0242	1347259.539	546393.612	12.740	-77.94250050	166.9898567	-42.614
misiii0243	1347212.422	546383.511	12.787	-77.94292551	166.9894923	-42.567
misiii0244	1347165.157	546373.210	12.840	-77.94335192	166.9891196	-42.514

Dhiresh Hansaraj   8/09/2009

MIS-4 Line

Flag Number	N	E	Height (masl)	Latitude [S]	Longitude [E]	WGS84 elevation (m)
misiv0077	1353963.086	544792.849	8.87	-77.88294454	166.911871	-46.484
misiv0078	1353932.394	544829.739	8.945	-77.88320862	166.9134873	-46.409
misiv0079	1353901.866	544866.801	9.161	-77.88347117	166.9151106	-46.193
misiv0080	1353871.155	544903.944	9.139	-77.88373533	166.9167377	-46.215
misiv0081	1353840.732	544939.962	9.318	-77.88399723	166.9183166	-46.036
misiv0082	1353809.731	544976.85	9.315	-77.88426404	166.9199334	-46.039
misiv0083	1353779.137	545013.18	9.462	-77.88452736	166.9215259	-45.892
misiv0084	1353748.08	545050.175	9.696	-77.88479463	166.9231475	-45.658
misiv0085	1353717.54	545086.281	9.649	-77.88505751	166.9247305	-45.705
misiv0086	1353686.535	545123.112	9.731	-77.88532434	166.9263451	-45.623
misiv0087	1353656.25	545159.063	9.705	-77.88558497	166.9279213	-45.649
misiv0088	1353625.337	545195.864	9.816	-77.88585096	166.9295347	-45.538
misiv0089	1353594.473	545232.345	9.885	-77.88611659	166.9311345	-45.469
misiv0090	1353563.31	545268.925	9.957	-77.88638488	166.9327389	-45.397
misiv0091	1353531.854	545305.771	10.043	-77.88665569	166.9343552	-45.311
misiv0092	1353500.537	545342.92	10.119	-77.88692516	166.9359843	-45.235
misiv0093	1353469.817	545379.469	10.205	-77.88718946	166.937587	-45.149
misiv0094	1353438.543	545415.641	10.237	-77.88745881	166.9391745	-45.117
misiv0095	1353408.701	545451.362	10.264	-77.88771547	166.9407408	-45.09
misiv0096	1353377.556	545487.842	10.401	-77.88798356	166.9423413	-44.953
misiv0097	1353346.621	545523.755	10.489	-77.88824993	166.9439175	-44.865
misiv0098	1353315.44	545560.351	10.546	-77.88851829	166.9455232	-44.808
misiv0099	1353284.946	545596.152	10.741	-77.88878072	166.9470941	-44.613
misiv0100	1353253.549	545632.599	10.752	-77.88905105	166.9486939	-44.602
misiv0100.5	1353238.519	545650.638	10.735	-77.88918027	166.949485	-44.618
misiv0101	1353223.326	545668.308	10.805	-77.88931107	166.9502606	-44.549
misiv0102	1353192.095	545704.654	10.808	-77.88957992	166.9518561	-44.546
misiv0102.5	1353176.641	545722.204	10.882	-77.88971308	166.952627	-44.472
misiv0103	1353161.141	545739.911	10.97	-77.8898466	166.9534046	-44.384
misiv0104	1353129.881	545776.175	10.959	-77.89011571	166.9549967	-44.395
misiv0104.5	1353114.681	545793.838	11.044	-77.89024655	166.9557721	-44.31
misiv0105	1353099.166	545811.566	10.964	-77.8903802	166.9565508	-44.39
misiv0106	1353068.167	545847.701	11.08	-77.890647	166.9581372	-44.274
misiv0106.5	1353052.789	545865.705	11.201	-77.89077932	166.9589275	-44.153
misiv0107	1353037.549	545883.489	11.297	-77.89091048	166.9597082	-44.057
misiv0108	1353006.315	545919.855	11.185	-77.89117929	166.9613049	-44.169
misiv0108.5	1352990.817	545937.891	11.296	-77.89131267	166.9620968	-44.058
misiv0109	1352975.565	545955.905	11.31	-77.89144386	166.9628875	-44.044
misiv0110	1352944.39	545992.261	11.276	-77.89171212	166.9644837	-44.077
misiv0110.5	1352929.499	546009.664	11.481	-77.89184025	166.9652478	-43.872
misiv0111	1352914.259	546027.121	11.513	-77.89197148	166.9660148	-43.841
misiv0112	1352883.356	546063.438	11.547	-77.89223731	166.9676091	-43.807
misiv0112.5	1352867.883	546081.868	11.65	-77.89237033	166.968418	-43.704
misiv0113	1352852.108	546099.321	11.628	-77.89250636	166.9691856	-43.726
misiv0114	1352821	546135.701	11.615	-77.89277398	166.9707831	-43.739
misiv0114.5	1352805.86	546153.772	11.657	-77.89290412	166.9715762	-43.697
misiv0115	1352790.136	546171.597	11.754	-77.89303956	166.9723596	-43.6
misiv0116	1352759.056	546207.74	11.959	-77.89330699	166.9739471	-43.395

Dhiresh Hansaraj   8/09/2009

Flag Number	N	E	Height (masl)	Latitude [S]	Longitude [E]	WGS84 elevation (m)
misiv0116.5	1352743.668	546226.13	11.869	-77.89343925	166.9747542	-43.485
misiv0117	1352728.243	546243.714	11.845	-77.89357207	166.9755271	-43.509
misiv0118	1352696.962	546279.805	11.977	-77.89384129	166.9771128	-43.377
misiv0118.5	1352681.904	546298.039	12.092	-77.89397064	166.9779128	-43.262
misiv0119	1352666.384	546315.65	12.065	-77.8941043	166.978687	-43.289
misiv0120	1352635.446	546351.848	12.095	-77.8943704	166.9802769	-43.259
misiv0120.5	1352620.351	546369.632	12.126	-77.8945002	166.9810579	-43.228
misiv0121	1352604.775	546387.724	12.073	-77.8946342	166.9818527	-43.281
misiv0122	1352573.056	546423.883	12.355	-77.89490729	166.9834422	-42.999
misiv0122.5	1352557.1	546441.887	12.392	-77.89504473	166.9842339	-42.962
misiv0123	1352541.804	546459.421	12.251	-77.89517638	166.9850046	-43.102
misiv0124	1352510.28	546495.983	12.434	-77.89544759	166.9866112	-42.92
misiv0124.5	1352497.194	546515.191	12.452	-77.89555895	166.9874502	-42.902
misiv0125	1352480.88	546529.343	12.506	-77.89570075	166.988078	-42.848
misiv0126	1352449.073	546565.571	12.615	-77.89597456	166.9896709	-42.739
misiv0126.5	1352434.099	546584.187	12.892	-77.896103	166.9904874	-42.462
misiv0127	1352418.2	546601.184	12.711	-77.8962402	166.9912362	-42.643
misiv0128	1352387.067	546638.071	12.77	-77.89650778	166.9928563	-42.584
misiv0128.5	1352371.235	546656.591	12.965	-77.89664391	166.9936701	-42.389
misiv0129	1352356.609	546673.739	12.941	-77.89676966	166.9944235	-42.413
misiv0130	1352325.404	546710.921	13.179	-77.89703777	166.9960565	-42.175
misiv0130.5	1352309.805	546729.503	13.276	-77.89717179	166.9968727	-42.078
misiv0131	1352294.79	546746.862	13.243	-77.89730095	166.9976357	-42.111
misiv0132	1352263.472	546783.653	13.304	-77.89757017	166.9992523	-42.05
misiv0132.5	1352247.897	546802.296	13.43	-77.89770395	167.0000711	-41.924
misiv0133	1352232.565	546820.392	13.432	-77.89783572	167.0008662	-41.922
misiv0134	1352200.971	546857.196	13.488	-77.89810739	167.0024839	-41.866
misiv0134.5	1352185.836	546875.734	13.501	-77.89823724	167.0032976	-41.853
misiv0135	1352170.487	546893.068	13.658	-77.89836938	167.0040602	-41.696
misiv0136	1352139.065	546929.838	13.664	-77.89863951	167.0056764	-41.69
misiv0136.5	1352123.429	546948.493	13.673	-77.89877381	167.0064959	-41.681
misiv0137	1352108.498	546965.838	13.649	-77.8989022	167.0072585	-41.704
misiv0138	1352076.935	547002.548	13.867	-77.89917358	167.0088724	-41.487
misiv0138.5	1352061.077	547020.981	13.893	-77.89930992	167.0096828	-41.461
misiv0139	1352046.325	547038.62	13.889	-77.89943661	167.0104577	-41.465
misiv0140	1352014.851	547075.458	13.98	-77.89970714	167.0120771	-41.374
misiv0140.5	1351999.274	547093.884	14.103	-77.89984097	167.0128869	-41.251
misiv0141	1351983.906	547111.594	14.084	-77.89997313	167.0136658	-41.269
misiv0142	1351952.309	547148.33	14.225	-77.90024478	167.0152812	-41.129
misiv0142.5	1351936.611	547166.567	14.318	-77.90037974	167.0160832	-41.036
misiv0143	1351921.737	547184.055	14.322	-77.90050754	167.0168519	-41.032
misiv0144	1351890.042	547220.807	14.519	-77.90078004	167.0184683	-40.835
misiv0144.5	1351874.166	547238.958	14.613	-77.90091661	167.0192669	-40.741
misiv0145	1351859.24	547256.432	14.682	-77.90104487	167.0200352	-40.672
misiv0146	1351827.468	547292.965	14.76	-77.90131811	167.0216425	-40.594
misiv0146.5	1351811.997	547311.542	14.855	-77.9014509	167.0224587	-40.499
misiv0147	1351796.324	547328.852	14.97	-77.90158591	167.0232212	-40.384
misiv0148	1351764.494	547365.279	15.127	-77.90185968	167.0248242	-40.227
misiv0148.5	1351749.417	547383.855	15.281	-77.90198894	167.0256399	-40.073
misiv0149	1351734.35	547401.667	15.224	-77.90211835	167.026423	-40.13

Dhiresh Hansaraj   8/09/2009

Flag Number	N	E	Height (masl)	Latitude [S]	Longitude [E]	WGS84 elevation (m)
misiv0150	1351703.534	547437.71	15.217	-77.90238314	167.0280082	-40.137
misiv0150.5	1351688.113	547455.414	15.354	-77.90251574	167.0287873	-40
misiv0151	1351673.259	547473.439	15.215	-77.90264317	167.0295792	-40.139
misiv0152	1351642.443	547509.436	15.178	-77.90290795	167.0311626	-40.176
misiv0152.5	1351627.173	547526.999	15.341	-77.90303925	167.0319354	-40.013
misiv0153	1351612.069	547544.775	15.254	-77.90316897	167.0327172	-40.1
misiv0154	1351581.162	547581.075	15.315	-77.90343446	167.0343137	-40.039
misiv0154.5	1351565.707	547598.91	15.343	-77.90356731	167.0350986	-40.011
misiv0155	1351550.728	547616.657	15.33	-77.90369592	167.035879	-40.024
misiv0156	1351520.058	547652.965	15.391	-77.90395927	167.0374757	-39.963
misiv0156.5	1351504.851	547670.917	15.412	-77.90408986	167.0382652	-39.942
misiv0157	1351489.601	547688.608	15.452	-77.90422091	167.0390437	-39.902
misiv0158	1351458.506	547724.663	15.551	-77.90448812	167.0406303	-39.803
misiv0158.5	1351443.422	547742.461	15.543	-77.90461764	167.0414132	-39.811
misiv0159	1351427.845	547760.461	15.538	-77.90475151	167.0422054	-39.816
misiv0160	1351396.891	547797.279	15.538	-77.9050172	167.0438246	-39.816
misiv0160.5	1351381.355	547815.295	15.615	-77.9051507	167.0446175	-39.739
misiv0161	1351365.921	547832.906	15.604	-77.90528341	167.0453929	-39.75
misiv0162	1351335.042	547869.579	15.691	-77.90554845	167.0470059	-39.663
misiv0162.5	1351319.882	547887.407	15.769	-77.90567863	167.0477903	-39.585
misiv0163	1351304.075	547905.415	15.659	-77.90581454	167.0485834	-39.695
misiv0164	1351272.681	547941.939	15.779	-77.90608423	167.0501909	-39.575
misiv0164.5	1351257.551	547959.888	15.875	-77.90621409	167.0509805	-39.479
misiv0165	1351241.983	547977.759	15.97	-77.90634789	167.0517674	-39.384
misiv0166	1351211.117	548014.261	15.924	-77.90661284	167.0533733	-39.43
misiv0166.5	1351195.616	548032.615	15.909	-77.90674589	167.0541809	-39.445
misiv0167	1351180.376	548050.277	16.013	-77.90687682	167.0549584	-39.341
misiv0168	1351149.476	548086.8	15.967	-77.90714204	167.0565655	-39.387
misiv0168.5	1351134.329	548104.916	15.84	-77.90727198	167.0573624	-39.514
misiv0169	1351118.86	548122.523	16.049	-77.90740497	167.0581379	-39.305
misiv0170	1351087.683	548158.936	16.109	-77.90767269	167.0597408	-39.245
misiv0170.5	1351072.24	548176.919	15.996	-77.90780532	167.0605326	-39.358
misiv0171	1351056.947	548194.764	16.133	-77.90793664	167.0613182	-39.221
misiv0172	1351025.844	548231.157	16.178	-77.90820369	167.0629202	-39.176
misiv0172.5	1351010.57	548249.456	16.185	-77.9083347	167.0637252	-39.169
misiv0173	1350995.252	548267.11	16.25	-77.90846629	167.0645027	-39.104
misiv0174	1350963.961	548303.667	16.267	-77.90873495	167.0661123	-39.086
misiv0174.5	1350949.063	548321.479	16.119	-77.90886273	167.066896	-39.235
misiv0175	1350933.588	548339.158	16.288	-77.90899572	167.0676749	-39.066
misiv0176	1350902.351	548375.554	16.455	-77.90926394	167.0692775	-38.899
misiv0176.5	1350887.409	548393.793	16.258	-77.90939197	167.0700796	-39.095
misiv0177	1350871.639	548411.519	16.335	-77.90952758	167.0708611	-39.019
misiv0178	1350840.424	548448.075	16.439	-77.90979552	167.0724707	-38.915
misiv0178.5	1350825.033	548466.11	16.364	-77.90992763	167.0732648	-38.99
misiv0179	1350808.896	548485.137	16.579	-77.9100661	167.0741025	-38.775
misiv0180	1350778.563	548520.981	16.558	-77.91032635	167.0756805	-38.796
misiv0180.5	1350764.462	548536.936	16.5	-77.91044756	167.0763838	-38.854
misiv0181	1350748.211	548555.013	16.561	-77.91058735	167.0771811	-38.793
misiv0182	1350716.615	548591.711	16.562	-77.91085862	167.0787976	-38.792
misiv0182.5	1350701.465	548610.123	16.512	-77.91098844	167.0796076	-38.842

Dhiresh Hansaraj   8/09/2009

Flag Number	N	E	Height (masl)	Latitude [S]	Longitude [E]	WGS84 elevation (m)
misiv0183	1350685.747	548628.375	16.657	-77.91112338	167.0804117	-38.697
misiv0184	1350654.531	548665.325	16.645	-77.91139115	167.0820385	-38.709
misiv0184.5	1350639.417	548683.338	16.545	-77.91152076	167.0828315	-38.809
misiv0185	1350623.463	548701.776	16.706	-77.91165775	167.0836439	-38.648
misiv0186	1350592.31	548738.493	16.822	-77.91192502	167.0852609	-38.532
misiv0186.5	1350577.263	548756.716	16.692	-77.91205395	167.0860628	-38.662
misiv0187	1350561.832	548774.573	16.739	-77.91218643	167.0868497	-38.615
misiv0188	1350530.682	548811.063	16.831	-77.91245372	167.088457	-38.522
misiv0188.5	1350515.587	548828.978	16.732	-77.91258317	167.0892459	-38.622
misiv0189	1350499.871	548847.092	16.994	-77.91271812	167.0900443	-38.36
misiv0190	1350468.73	548883.893	16.842	-77.91298521	167.0916651	-38.512
misiv0190.5	1350453.361	548902.282	16.805	-77.91311696	167.0924747	-38.549
misiv0191	1350437.939	548920.153	16.98	-77.91324934	167.0932623	-38.374
misiv0192	1350406.648	548956.737	16.934	-77.91351782	167.0948742	-38.42
misiv0192.5	1350391.446	548975.087	16.952	-77.91364807	167.095682	-38.402
misiv0193	1350375.935	548992.699	16.95	-77.91378133	167.0964587	-38.404
misiv0194	1350344.761	549029.34	17.085	-77.91404873	167.098073	-38.269
misiv0194.5	1350329.515	549047.754	17.031	-77.91417935	167.0988837	-38.323
misiv0195	1350314.233	549065.357	17.003	-77.91431054	167.0996597	-38.351
misiv0196	1350283.143	549102.012	17.145	-77.91457716	167.1012746	-38.208
misiv0196.5	1350267.889	549120.508	17.131	-77.91470782	167.1020889	-38.223
misiv0197	1350252.172	549138.362	17.241	-77.91484282	167.1028764	-38.113
misiv0198	1350221.138	549175.099	17.124	-77.9151089	167.1044948	-38.23
misiv0198.5	1350206.095	549193.296	17.112	-77.91523775	167.1052961	-38.242
misiv0199	1350190.683	549211.545	17.252	-77.91536988	167.1061	-38.102
misiv0200	1350159.301	549247.864	17.231	-77.9156392	167.1077013	-38.123
misiv0200.5	1350144.253	549266.069	17.287	-77.91576807	167.108503	-38.067
misiv0201	1350129.061	549284.12	17.301	-77.9158983	167.1092982	-38.053
misiv0202	1350097.909	549320.795	17.334	-77.91616541	167.1109145	-38.02
misiv0202.5	1350082.877	549338.632	17.337	-77.91629426	167.1117004	-38.017
misiv0203	1350067.094	549356.647	17.425	-77.91642978	167.1124951	-37.929
misiv0204	1350036.015	549393.249	17.521	-77.91669625	167.1141083	-37.833
misiv0204.5	1350020.837	549411.436	17.385	-77.91682628	167.1149095	-37.969
misiv0205	1350005.256	549429.602	17.434	-77.91695993	167.1157104	-37.92
misiv0206	1349974.092	549466.244	17.478	-77.91722713	167.1173256	-37.876
misiv0206.5	1349958.7	549484.477	17.438	-77.91735906	167.1181292	-37.916
misiv0207	1349943.351	549502.493	17.628	-77.91749066	167.1189233	-37.726
misiv0208	1349912.27	549539.201	17.613	-77.91775708	167.1205414	-37.741
misiv0208.5	1349897.031	549557.416	17.509	-77.91788763	167.121344	-37.845
misiv0209	1349881.232	549575.493	17.711	-77.91802324	167.1221416	-37.643
misiv0210	1349850.038	549612.248	17.713	-77.91829064	167.1237619	-37.64
misiv0210.5	1349835.154	549630.573	17.597	-77.91841796	167.1245687	-37.757
misiv0211	1349819.315	549648.549	17.857	-77.91855395	167.1253622	-37.497
misiv0212	1349788.201	549685.376	17.641	-77.91882059	167.1269856	-37.713
misiv0212.5	1349772.961	549703.734	17.67	-77.91895109	167.1277944	-37.684
misiv0213	1349757.382	549721.865	17.735	-77.91908469	167.1285941	-37.619
misiv0214	1349726.089	549758.626	17.854	-77.91935294	167.1302151	-37.499
misiv0214.5	1349710.834	549776.912	17.68	-77.91948358	167.131021	-37.674
misiv0215	1349695.196	549795.015	17.969	-77.9196177	167.1318197	-37.385
misiv0216	1349663.831	549831.866	17.927	-77.91988655	167.1334448	-37.427

Dhiresh Hansaraj   8/09/2009

Flag Number	N	E	Height (masl)	Latitude [S]	Longitude [E]	WGS84 elevation (m)
misiv0216.5	1349648.398	549850.031	17.819	-77.92001881	167.1342459	-37.535
misiv0217	1349632.857	549868.204	17.927	-77.92015204	167.1350475	-37.427
misiv0218	1349601.39	549905.347	18.082	-77.92042169	167.1366854	-37.272
misiv0218.5	1349586.064	549923.559	17.859	-77.92055297	167.1374883	-37.495
misiv0219	1349570.423	549941.851	17.949	-77.92068705	167.1382952	-37.405
misiv0220	1349539.061	549978.78	17.935	-77.92095579	167.139924	-37.419
misiv0220.5	1349523.885	549996.824	17.818	-77.92108578	167.1407196	-37.536
misiv0221	1349508.194	550015.158	17.925	-77.92122029	167.1415284	-37.429
misiv0222	1349476.758	550051.948	18.125	-77.92148973	167.1431515	-37.228
misiv0222.5	1349461.7	550070.196	18.004	-77.92161858	167.1439557	-37.35
misiv0223	1349446	550088.445	18.203	-77.92175318	167.144761	-37.151
misiv0224	1349414.545	550125.213	18.265	-77.92202278	167.1463833	-37.089
misiv0224.5	1349399.268	550143.801	18.15	-77.92215347	167.1472025	-37.204
misiv0225	1349384.163	550161.316	18.403	-77.92228298	167.1479755	-36.951
misiv0226	1349352.891	550198.193	18.335	-77.92255088	167.1496023	-37.019
misiv0226.5	1349337.67	550216.453	18.289	-77.92268117	167.1504074	-37.065
misiv0227	1349322.35	550234.465	18.594	-77.92281228	167.151202	-36.825
misiv0228	1349290.804	550271.213	18.318	-77.92308281	167.152824	-37.036
misiv0228.5	1349275.668	550289.614	18.185	-77.92321229	167.1536351	-37.169
misiv0229	1349259.914	550307.753	18.426	-77.92334738	167.1544359	-36.928
misiv0230	1349228.537	550344.422	18.374	-77.92361626	167.1560543	-36.98
misiv0230.5	1349213.576	550362.476	18.177	-77.92374427	167.1568503	-37.177
misiv0231	1349197.793	550380.74	18.528	-77.92387957	167.1576567	-36.826
misiv0232	1349166.4	550417.379	18.534	-77.92414858	167.1592739	-36.82
misiv0232.5	1349151.307	550435.677	18.296	-77.92427769	167.1600807	-37.058
misiv0233	1349135.573	550453.672	18.564	-77.92441263	167.1608755	-36.789
misiv0234	1349104.33	550490.353	18.562	-77.92468027	167.1624944	-36.792
misiv0234.5	1349089.524	550508.654	18.391	-77.92480679	167.1633009	-36.963
misiv0235	1349073.898	550526.496	18.694	-77.9249408	167.1640891	-36.66
misiv0236	1349042.497	550563.235	18.728	-77.92520982	167.1657109	-36.626
misiv0236.5	1349027.369	550581.602	18.521	-77.9253392	167.1665208	-36.833
misiv0237	1349011.89	550599.599	18.619	-77.92547184	167.1673155	-36.735
misiv0238	1348980.669	550636.334	18.705	-77.92573922	167.1689369	-36.649
misiv0238.5	1348965.179	550654.475	18.558	-77.9258719	167.1697378	-36.796
misiv0239	1348949.771	550672.688	18.866	-77.92600383	167.1705417	-36.488
misiv0240	1348918.496	550709.616	18.843	-77.92627161	167.1721717	-36.51
misiv0240.5	1348903.028	550727.631	18.636	-77.92640413	167.1729672	-36.718
misiv0241	1348887.198	550746.023	18.816	-77.92653976	167.1737794	-36.538
misiv0242	1348855.836	550783.181	18.806	-77.92680823	167.1754195	-36.548
misiv0243	1348825.073	550819.678	18.904	-77.92707155	167.1770304	-36.45
misiv0244	1348793.805	550856.497	19	-77.92733927	167.178656	-36.354
misiv0245	1348763.115	550892.616	18.872	-77.92760204	167.1802508	-36.482
misiv0246	1348731.83	550929.51	18.942	-77.92786986	167.1818797	-36.412
misiv0247	1348700.696	550966.368	18.97	-77.92813634	167.183507	-36.384
misiv0248	1348669.489	551003.228	18.984	-77.92840346	167.1851345	-36.37
misiv0249	1348638.515	551039.86	19.033	-77.92866856	167.1867519	-36.321
misiv0250	1348607.072	551077.025	19.034	-77.92893767	167.188393	-36.32
misiv0251	1348576.263	551113.642	19.265	-77.92920129	167.1900097	-36.089
misiv0252	1348544.825	551150.731	19.269	-77.92947036	167.1916477	-36.085
misiv0253	1348513.981	551187.403	19.077	-77.92973425	167.1932669	-36.277

Dhiresh Hansaraj   8/09/2009

Flag Number	N	E	Height (masl)	Latitude [S]	Longitude [E]	WGS84 elevation (m)
misiv0254	1348482.463	551224.171	19.233	-77.93000412	167.1948914	-36.121
misiv0255	1348451.547	551260.687	19.325	-77.93026869	167.1965042	-36.029
misiv0256	1348420.035	551297.834	19.286	-77.93053837	167.1981451	-36.068
misiv0257	1348388.766	551334.356	19.309	-77.93080608	167.1997589	-36.045
misiv0258	1348357.361	551371.439	19.325	-77.9310748	167.2013969	-36.029
misiv0259	1348326.116	551408.072	19.333	-77.93134224	167.2030156	-36.021
misiv0260	1348294.672	551445.157	19.396	-77.93161129	167.204654	-35.957
misiv0261	1348263.764	551481.292	19.52	-77.93187585	167.2062509	-35.834
misiv0262	1348232.469	551518.399	19.503	-77.93214355	167.2078901	-35.851
misiv0263	1348201.246	551555.324	19.434	-77.93241065	167.2095215	-35.92
misiv0264	1348169.677	551592.49	19.547	-77.93268076	167.2111638	-35.807

Dhiresh Hansaraj   8/09/2009

MIS-5 Line

Flag Number	N	E	Height (masl)	Latitude [S]	Longitude [E]	WGS84 elevation (m)
misv0077	1360303.02	546711.391	19.432	-77.82559574	166.9845373	-35.922
misv0078	1360302.135	546759.91	19.538	-77.82558894	166.9865983	-35.816
misv0079	1360300.712	546806.015	19.568	-77.82558768	166.9885576	-35.786
misv0080	1360299.28	546853.82	19.71	-77.82558597	166.9905891	-35.644
misv0081	1360297.683	546900.567	19.896	-77.82558604	166.9925759	-35.458
misv0082	1360295.992	546948.194	19.938	-77.82558667	166.9946002	-35.416
misv0083	1360294.118	546994.886	20.013	-77.82558921	166.9965851	-35.341
misv0084	1360292.378	547042.894	20.1	-77.82559014	166.9986256	-35.254
misv0085	1360290.639	547090.449	20.386	-77.82559117	167.0006469	-34.968
misv0086	1360289.153	547138.77	20.356	-77.8255897	167.0027004	-34.998
misv0087	1360287.262	547186.6	20.412	-77.82559198	167.0047336	-34.941
misv0088	1360285.654	547234.739	20.529	-77.82559163	167.0067795	-34.825
misv0089	1360283.837	547282.674	20.543	-77.82559319	167.0088171	-34.811
misv0090	1360282.157	547330.958	20.683	-77.8255934	167.0108692	-34.671
misv0091	1360280.478	547378.99	20.744	-77.82559366	167.0129107	-34.61
misv0092	1360278.674	547427.405	20.759	-77.82559491	167.0149686	-34.595
misv0093	1360276.818	547475.152	21.05	-77.82559682	167.0169983	-34.304
misv0094	1360275.173	547523.533	20.971	-77.82559663	167.0190545	-34.383
misv0095	1360273.368	547571.702	21.115	-77.82559793	167.021102	-34.239
misv0096	1360271.324	547619.994	21.235	-77.8256013	167.0231551	-34.119
misv0097	1360269.756	547668.153	21.207	-77.82560045	167.0252018	-34.146
misv0098	1360268.079	547716.539	21.38	-77.82560047	167.0272583	-33.974
misv0099	1360266.376	547764.463	21.505	-77.82560087	167.0292952	-33.848
misv0100	1360264.538	547812.868	21.53	-77.82560231	167.0313527	-33.824
misv0100.5	1360263.884	547837.175	21.722	-77.82560062	167.0323855	-33.632
misv0101	1360262.866	547860.416	21.701	-77.82560251	167.0333737	-33.653
misv0102	1360261.133	547908.774	21.768	-77.82560299	167.0354291	-33.585
misv0102.5	1360260.421	547933.041	21.867	-77.82560182	167.0364603	-33.487
misv0103	1360259.7	547956.412	21.916	-77.82560099	167.0374534	-33.438
misv0104	1360257.852	548004.841	21.978	-77.82560246	167.039512	-33.375
misv0104.5	1360257.248	548028.89	21.987	-77.82560036	167.0405338	-33.367
misv0105	1360256.338	548052.601	21.957	-77.82560112	167.0415417	-33.397
misv0106	1360254.444	548101.294	22.087	-77.82560288	167.0436116	-33.267
misv0106.5	1360253.702	548125.411	22.151	-77.82560198	167.0446365	-33.203
misv0107	1360252.752	548149.48	22.253	-77.82560297	167.0456596	-33.101
misv0108	1360250.913	548198.127	22.273	-77.82560422	167.0477274	-33.081
misv0108.5	1360250.497	548221.904	22.44	-77.82560051	167.0487374	-32.914
misv0109	1360249.424	548246.008	22.385	-77.82560257	167.0497622	-32.969
misv0110	1360247.576	548294.431	22.579	-77.82560394	167.0518205	-32.775
misv0110.5	1360246.938	548318.163	22.557	-77.8256022	167.0528289	-32.796
misv0111	1360246.257	548342.168	22.661	-77.82560077	167.0538489	-32.693
misv0112	1360244.681	548390.781	22.667	-77.82559961	167.0559149	-32.687
misv0112.5	1360243.688	548414.886	22.713	-77.82560093	167.0569397	-32.641
misv0113	1360242.872	548438.613	22.833	-77.82560077	167.0579481	-32.521
misv0114	1360241.298	548487.362	22.923	-77.82559953	167.0600199	-32.431
misv0114.5	1360240.466	548511.559	22.838	-77.82559936	167.0610483	-32.516
misv0115	1360239.55	548535.425	22.988	-77.82560004	167.0620627	-32.366
misv0116	1360237.936	548584.073	22.984	-77.82559915	167.0641303	-32.37

Dhiresh Hansaraj 8/09/2009

Flag Number	N	E	Height (masl)	Latitude [S]	Longitude [E]	WGS84 elevation (m)
misv0116.5	1360237.307	548608.487	23.029	-77.82559708	167.0651676	-32.325
misv0117	1360236.192	548632.153	23.042	-77.8255996	167.0661739	-32.312
misv0118	1360234.515	548680.957	23.179	-77.82559919	167.0682482	-32.175
misv0118.5	1360233.713	548705.328	23.118	-77.82559867	167.0692839	-32.236
misv0119	1360232.777	548729.021	23.246	-77.82559955	167.0702911	-32.108
misv0120	1360230.978	548777.623	23.349	-77.82560027	167.0723569	-32.005
misv0120.5	1360230.382	548801.6	23.478	-77.82559801	167.0733756	-31.875
misv0121	1360229.394	548825.593	23.428	-77.82559926	167.0743956	-31.926
misv0122	1360227.604	548874.171	23.488	-77.82559988	167.0764604	-31.866
misv0122.5	1360226.963	548898.203	23.512	-77.82559799	167.0774816	-31.842
misv0123	1360225.826	548922.057	23.534	-77.82560059	167.0784959	-31.82
misv0124	1360224.079	548970.704	23.703	-77.82560078	167.0805635	-31.651
misv0124.5	1360223.398	548994.677	23.55	-77.82559925	167.0815822	-31.804
misv0125	1360222.411	549018.671	23.657	-77.82560045	167.0826023	-31.697
misv0126	1360220.725	549067.342	23.78	-77.82560005	167.0846708	-31.574
misv0126.5	1360220.132	549091.283	23.748	-77.82559773	167.085688	-31.606
misv0127	1360218.942	549115.666	23.839	-77.82560061	167.0867249	-31.515
misv0128	1360217.221	549164.375	23.803	-77.82560048	167.0887951	-31.551
misv0128.5	1360216.878	549188.497	23.857	-77.82559585	167.0898196	-31.497
misv0129	1360215.67	549212.845	23.922	-77.82559888	167.090855	-31.432
misv0130	1360214.014	549261.659	23.986	-77.82559811	167.0929296	-31.368
misv0130.5	1360213.554	549285.959	24.132	-77.82559445	167.0939619	-31.222
misv0131	1360212.335	549309.973	24.117	-77.82559768	167.0949831	-31.237
misv0132	1360210.738	549358.699	24.291	-77.82559637	167.0970539	-31.062
misv0132.5	1360210.434	549383.108	24.203	-77.82559127	167.0980905	-31.151
misv0133	1360209.237	549406.713	24.311	-77.82559441	167.0990943	-31.043
misv0134	1360207.513	549455.364	24.322	-77.82559424	167.1011621	-31.032
misv0134.5	1360207.026	549479.448	24.365	-77.82559086	167.1021853	-30.989
misv0135	1360205.929	549503.818	24.448	-77.82559285	167.1032214	-30.906
misv0136	1360204.236	549552.48	24.461	-77.82559236	167.1052896	-30.893
misv0136.5	1360203.98	549576.777	24.615	-77.82558684	167.1063214	-30.739
misv0137	1360202.6	549600.779	24.694	-77.82559147	167.1073424	-30.66
misv0138	1360200.977	549649.494	24.721	-77.8255903	167.1094128	-30.633
misv0138.5	1360200.617	549673.73	24.748	-77.8255857	167.1104421	-30.606
misv0139	1360199.324	549697.703	24.816	-77.82558955	167.1114617	-30.538
misv0140	1360197.587	549746.509	24.823	-77.82558935	167.1135361	-30.531
misv0140.5	1360197.135	549770.978	24.979	-77.82558548	167.1145755	-30.375
misv0141	1360196.336	549793.348	25.004	-77.82558541	167.1155263	-30.35
misv0142	1360194.741	549841.759	25.151	-77.82558403	167.1175837	-30.203
misv0142.5	1360193.578	549865.794	25.246	-77.82558666	167.1186058	-30.108
misv0143	1360192.829	549889.758	25.192	-77.82558561	167.1196241	-30.162
misv0144	1360191.195	549938.5	25.314	-77.82558444	167.1216957	-30.039
misv0144.5	1360190.409	549962.625	25.398	-77.82558366	167.122721	-29.956
misv0145	1360189.331	549986.572	25.444	-77.82558554	167.1237391	-29.91
misv0146	1360187.862	550035.323	25.584	-77.82558286	167.1258108	-29.77
misv0146.5	1360186.997	550060.213	25.633	-77.82558252	167.1268686	-29.721
misv0147	1360186.267	550083.339	25.681	-77.82558154	167.1278515	-29.673
misv0148	1360184.311	550131.912	25.871	-77.82558324	167.1299163	-29.483
misv0148.5	1360183.631	550156.113	25.779	-77.82558146	167.1309446	-29.575
misv0149	1360182.553	550179.854	25.87	-77.82558337	167.1319541	-29.484

Dhiresh Hansaraj   8/09/2009

Flag Number	N	E	Height (masl)	Latitude [S]	Longitude [E]	WGS84 elevation (m)
misv0150	1360180.732	550228.57	26.036	-77.82558379	167.1340248	-29.318
misv0150.5	1360179.928	550253.125	26.037	-77.82558298	167.1350683	-29.317
misv0151	1360178.929	550276.739	26.083	-77.82558422	167.1360722	-29.271
misv0152	1360176.961	550325.521	26.147	-77.82558591	167.138146	-29.207
misv0152.5	1360176.282	550350.341	26.278	-77.82558388	167.1392006	-29.076
misv0153	1360175.204	550373.587	26.253	-77.82558593	167.140189	-29.1
misv0154	1360173.477	550422.393	26.323	-77.82558542	167.1422634	-29.031
misv0154.5	1360172.431	550446.378	26.331	-77.82558693	167.1432832	-29.023
misv0155	1360171.502	550470.774	26.495	-77.82558726	167.1443202	-28.859
misv0156	1360169.638	550519.573	26.562	-77.82558795	167.1463945	-28.792
misv0156.5	1360169.181	550543.952	26.567	-77.82558404	167.14743	-28.786
misv0157	1360168.265	550568.003	26.611	-77.82558435	167.1484524	-28.743
misv0158	1360166.673	550617.001	26.704	-77.8255825	167.1505347	-28.65
misv0158.5	1360166.147	550641.417	26.698	-77.82557919	167.1515719	-28.656
misv0159	1360164.95	550664.995	26.711	-77.82558215	167.1525746	-28.643
misv0160	1360163.373	550713.878	26.93	-77.82558018	167.154652	-28.424
misv0160.5	1360162.166	550738.532	26.917	-77.82558286	167.1557004	-28.436
misv0161	1360161.059	550762.454	26.95	-77.8255849	167.1567176	-28.404
misv0162	1360159.34	550811.376	27.058	-77.82558415	167.1587969	-28.296
misv0162.5	1360158.625	550835.703	26.998	-77.82558253	167.1598306	-28.356
misv0163	1360157.5	550859.627	27.052	-77.8255847	167.1608479	-28.302
misv0164	1360155.615	550908.546	27.071	-77.82558542	167.1629274	-28.282
misv0164.5	1360155.016	550933.069	27.155	-77.82558267	167.1639692	-28.199
misv0165	1360154.015	550956.565	27.146	-77.82558386	167.1649681	-28.208
misv0166	1360152.055	551005.537	27.251	-77.8255852	167.16705	-28.102
misv0166.5	1360151.588	551029.66	27.31	-77.82558139	167.1680746	-28.043
misv0167	1360150.397	551053.72	27.265	-77.82558408	167.1690978	-28.089
misv0168	1360148.55	551102.496	27.283	-77.82558444	167.1711711	-28.071
misv0168.5	1360147.719	551126.623	27.295	-77.82558388	167.1721965	-28.059
misv0169	1360146.642	551150.829	27.312	-77.82558548	167.1732257	-28.042
misv0170	1360144.854	551199.914	27.483	-77.82558518	167.175312	-27.871
misv0170.5	1360143.859	551224.282	27.51	-77.82558599	167.1763479	-27.843
misv0171	1360143.027	551247.956	27.428	-77.82558556	167.1773541	-27.926
misv0172	1360141.121	551297.219	27.539	-77.82558623	167.1794482	-27.815
misv0172.5	1360140.188	551321.526	27.524	-77.82558648	167.1804815	-27.83
misv0173	1360139.31	551345.335	27.47	-77.82558641	167.1814935	-27.884
misv0174	1360137.472	551394.499	27.674	-77.82558646	167.1835832	-27.68
misv0174.5	1360136.433	551418.743	27.581	-77.82558767	167.1846139	-27.773
misv0175	1360135.406	551442.616	27.757	-77.82558889	167.1856289	-27.597
misv0176	1360133.623	551491.671	27.707	-77.82558847	167.1877139	-27.647
misv0176.5	1360133.267	551515.904	27.686	-77.82558355	167.1887431	-27.668
misv0177	1360131.837	551539.576	27.763	-77.82558843	167.1897502	-27.591
misv0178	1360129.877	551588.646	27.871	-77.82558955	167.1918361	-27.483
misv0178.5	1360129.248	551613.023	27.827	-77.82558701	167.1928719	-27.527
misv0179	1360128.158	551637.045	27.884	-77.82558872	167.1938932	-27.47
misv0180	1360126.274	551686.23	27.888	-77.82558909	167.195984	-27.466
misv0180.5	1360125.695	551710.897	27.937	-77.825586	167.1970319	-27.417
misv0181	1360124.734	551734.566	28.03	-77.82558665	167.1980381	-27.324
misv0182	1360122.655	551783.686	28.042	-77.82558875	167.2001264	-27.312
misv0182.5	1360122.458	551808.099	28.04	-77.82558231	167.201163	-27.314

Flag Number	N	E	Height (masl)	Latitude [S]	Longitude [E]	WGS84 elevation (m)
misv0183	1360121.287	551831.785	28.012	-77.82558482	167.2021702	-27.342
misv0184	1360119.491	551880.78	28.083	-77.82558441	167.2042527	-27.271
misv0184.5	1360118.91	551905.317	28.121	-77.82558134	167.2052951	-27.233
misv0185	1360118.015	551929.105	28.166	-77.82558133	167.2063063	-27.188
misv0186	1360116.266	551978.244	28.054	-77.82558042	167.2083949	-27.3
misv0186.5	1360115.499	552002.681	28.236	-77.82557904	167.2094333	-27.117
misv0187	1360114.503	552026.983	28.278	-77.82557974	167.2104665	-27.076
misv0188	1360112.713	552076.032	28.316	-77.8255792	167.2125512	-27.038
misv0188.5	1360112.03	552100.584	28.398	-77.82557701	167.2135944	-26.956
misv0189	1360110.795	552124.525	28.302	-77.82557996	167.2146126	-27.051
misv0190	1360109.169	552173.679	28.403	-77.82557788	167.2167016	-26.951
misv0190.5	1360108.275	552198.296	28.436	-77.82557754	167.2177479	-26.918
misv0191	1360106.989	552222.589	28.505	-77.82558082	167.2187812	-26.849
misv0192	1360105.427	552271.932	28.567	-77.82557806	167.2208781	-26.787
misv0192.5	1360104.736	552296.364	28.636	-77.82557595	167.2219162	-26.718
misv0193	1360103.782	552319.808	28.638	-77.82557653	167.2229128	-26.716
misv0194	1360101.983	552368.914	28.712	-77.82557595	167.2250001	-26.642
misv0194.5	1360101.377	552394.025	28.687	-77.82557283	167.2260669	-26.667
misv0195	1360100.303	552417.41	28.591	-77.82557449	167.2270613	-26.763
misv0196	1360098.411	552466.586	28.798	-77.82557468	167.2291516	-26.556
misv0196.5	1360098.25	552491.053	28.762	-77.82556779	167.2301904	-26.592
misv0197	1360096.633	552514.97	28.819	-77.82557412	167.2312082	-26.535
misv0198	1360094.899	552564.134	28.84	-77.82557287	167.2332977	-26.513
misv0198.5	1360094.198	552588.526	28.847	-77.82557082	167.2343342	-26.507
misv0199	1360093.084	552612.445	28.896	-77.82557262	167.2353513	-26.458
misv0200	1360091.27	552661.757	28.925	-77.82557201	167.2374472	-26.429
misv0200.5	1360090.448	552686.152	28.943	-77.82557103	167.238484	-26.411
misv0201	1360089.354	552710.427	28.947	-77.82557251	167.2395161	-26.407
misv0202	1360087.681	552759.556	28.937	-77.82557067	167.2416042	-26.417
misv0202.5	1360087.311	552784.149	28.953	-77.82556556	167.2426486	-26.401
misv0203	1360086.151	552808.051	29.163	-77.82556774	167.243665	-26.191
misv0204	1360084.073	552857.191	29.146	-77.8255695	167.2457541	-26.207
misv0204.5	1360083.446	552881.895	29.193	-77.82556663	167.2468037	-26.161
misv0205	1360082.398	552905.62	29.175	-77.82556786	167.2478124	-26.179
misv0206	1360080.417	552955.035	29.11	-77.82556861	167.2499131	-26.243
misv0206.5	1360079.492	552979.463	29.296	-77.8255685	167.2509514	-26.058
misv0207	1360078.628	553003.328	29.275	-77.82556802	167.2519658	-26.079
misv0208	1360076.913	553052.557	29.294	-77.82556642	167.2540581	-26.059
misv0208.5	1360076.306	553076.911	29.393	-77.82556346	167.2550928	-25.961
misv0209	1360075.112	553100.474	29.416	-77.82556603	167.2560949	-25.938
misv0210	1360073.122	553149.733	29.474	-77.82556686	167.2581889	-25.88
misv0210.5	1360072.794	553173.978	29.427	-77.82556143	167.2592185	-25.927
misv0211	1360071.376	553198.195	29.49	-77.82556576	167.2602487	-25.864
misv0212	1360069.571	553247.405	29.53	-77.82556491	167.2623403	-25.824
misv0212.5	1360068.724	553272.026	29.536	-77.82556398	167.2633867	-25.818
misv0213	1360067.834	553295.844	29.708	-77.8255637	167.2643992	-25.645
misv0214	1360066.102	553344.963	29.619	-77.82556221	167.2664868	-25.735
misv0214.5	1360065.143	553369.311	29.711	-77.82556236	167.2675218	-25.643
misv0215	1360064.191	553393.693	29.584	-77.82556243	167.2685583	-25.77
misv0216	1360062.518	553442.901	29.696	-77.82556034	167.2706496	-25.658

Dhiresh Hansaraj   8/09/2009

Flag Number	N	E	Height (masl)	Latitude [S]	Longitude [E]	WGS84 elevation (m)
misv0216.5	1360061.794	553467.573	29.994	-77.82555826	167.271698	-25.36
misv0217	1360060.656	553491.37	29.883	-77.82556018	167.2727099	-25.471
misv0218	1360058.854	553540.519	29.788	-77.82555924	167.274799	-25.566
misv0218.5	1360058.363	553564.866	29.799	-77.82555517	167.2758332	-25.554
misv0219	1360057.117	553588.922	29.881	-77.82555795	167.2768563	-25.473
misv0220	1360055.378	553638.231	29.953	-77.82555636	167.278952	-25.401
misv0220.5	1360054.58	553662.91	29.866	-77.8255549	167.2800008	-25.488
misv0221	1360053.724	553686.626	30.05	-77.82555431	167.2810088	-25.303
misv0222	1360051.802	553735.891	30.029	-77.82555433	167.283103	-25.325
misv0222.5	1360051.168	553760.547	30.108	-77.82555141	167.2841505	-25.246
misv0223	1360050.08	553784.314	30.136	-77.82555284	167.2851611	-25.218
misv0224	1360048.269	553833.43	30.27	-77.8255519	167.2872487	-25.084
misv0224.5	1360047.356	553857.965	30.2	-77.82555149	167.2882916	-25.154
misv0225	1360046.333	553882.373	30.159	-77.82555212	167.2893292	-25.194
misv0226	1360044.575	553931.63	30.217	-77.82555061	167.2914228	-25.137
misv0226.5	1360044.069	553956.047	30.373	-77.82554659	167.29246	-24.981
misv0227	1360042.867	553979.937	30.327	-77.82554898	167.293476	-25.027
misv0228	1360040.932	554029.104	30.468	-77.82554906	167.295566	-24.886
misv0228.5	1360040.239	554053.413	30.433	-77.82554674	167.2965989	-24.921
misv0229	1360039.089	554077.558	30.44	-77.82554856	167.2976256	-24.914
misv0230	1360037.555	554126.876	30.444	-77.82554496	167.2997214	-24.91
misv0230.5	1360036.847	554151.447	30.564	-77.82554266	167.3007655	-24.79
misv0231	1360035.77	554175.292	30.585	-77.82554392	167.3017793	-24.769
misv0232	1360033.99	554224.556	30.462	-77.82554252	167.3038732	-24.892
misv0232.5	1360033.011	554248.545	30.607	-77.82554283	167.304893	-24.747
misv0233	1360032.244	554272.738	30.653	-77.82554118	167.3059211	-24.701
misv0234	1360030.492	554322.056	30.649	-77.82553948	167.3080173	-24.705
misv0234.5	1360030.107	554346.275	30.634	-77.82553438	167.3090458	-24.719
misv0235	1360028.92	554370.997	30.704	-77.82553628	167.3100971	-24.649
misv0236	1360027.26	554420.142	30.693	-77.82553379	167.3121857	-24.661
misv0236.5	1360026.195	554444.326	30.907	-77.82553477	167.313214	-24.447
misv0237	1360025.423	554468.355	30.82	-77.82553318	167.3142351	-24.534
misv0238	1360023.455	554517.699	30.933	-77.82553334	167.3163327	-24.421
misv0238.5	1360022.618	554542.187	30.969	-77.82553217	167.3173734	-24.385
misv0239	1360021.856	554566.183	30.944	-77.82553049	167.3183932	-24.41
misv0240	1360020.051	554615.314	30.74	-77.82552923	167.3204814	-24.614
misv0240.5	1360019.181	554639.776	30.863	-77.82552834	167.3215211	-24.491
misv0241	1360018.424	554663.742	30.929	-77.82552662	167.3225396	-24.425
misv0242	1360016.469	554712.035	31.049	-77.82552697	167.3245926	-24.305
misv0242.5	1360015.991	554736.106	31.024	-77.8255227	167.325615	-24.33
misv0243	1360015.098	554759.183	31.05	-77.8255225	167.3265959	-24.304
misv0244	1360013.385	554807.36	31.143	-77.82552069	167.3286436	-24.211
misv0244.5	1360012.689	554831.536	31.11	-77.82551831	167.3296708	-24.244
misv0245	1360011.578	554855.19	31.149	-77.82551984	167.3306767	-24.205
misv0246	1360009.813	554903.54	31.326	-77.82551841	167.3327317	-24.028
misv0246.5	1360009.232	554927.686	31.182	-77.825515	167.3337575	-24.171
misv0247	1360007.839	554951.411	31.389	-77.82551901	167.3347668	-23.965
misv0248	1360006.159	555000.001	31.278	-77.82551671	167.3368319	-24.076
misv0248.5	1360005.671	555024.119	31.234	-77.82551246	167.3378563	-24.12
misv0249	1360004.496	555047.532	31.319	-77.82551461	167.338852	-24.035

Dhiresh Hansaraj   8/09/2009

Flag Number	N	E	Height (masl)	Latitude [S]	Longitude [E]	WGS84 elevation (m)
misv0250	1360002.787	555095.872	31.445	-77.82551263	167.3409066	-23.909
misv0250.5	1360002.234	555120.215	31.303	-77.82550887	167.3419407	-24.051
misv0251	1360001.086	555143.908	31.51	-77.82551067	167.3429482	-23.844
misv0252	1359999.455	555192.539	31.459	-77.82550784	167.3450149	-23.895
misv0252.5	1359999.209	555217.14	31.479	-77.82550123	167.3460595	-23.875
misv0253	1359997.743	555240.672	31.55	-77.82550591	167.3470607	-23.804
misv0254	1359996.198	555289.565	31.667	-77.8255022	167.3491384	-23.687
misv0254.5	1359995.672	555313.837	31.925	-77.82549819	167.3501695	-23.429
misv0255	1359994.239	555337.67	31.727	-77.82550246	167.3511834	-23.627
misv0256	1359992.557	555386.642	31.566	-77.82549991	167.3532648	-23.788
misv0256.5	1359992.279	555410.998	31.71	-77.82549365	167.3542989	-23.643
misv0257	1359990.755	555435.108	31.646	-77.82549861	167.3553248	-23.707
misv0258	1359989.228	555483.978	31.796	-77.82549468	167.3574015	-23.558
misv0258.5	1359988.846	555508.521	31.828	-77.82548926	167.3584438	-23.525
misv0259	1359987.739	555532.288	31.816	-77.8254906	167.3594544	-23.538
misv0260	1359986.366	555581.027	31.812	-77.8254853	167.3615253	-23.542
misv0260.5	1359985.909	555605.238	31.792	-77.82548066	167.3625536	-23.562
misv0261	1359984.594	555629.404	31.774	-77.8254837	167.3635815	-23.58
misv0262	1359983.341	555678.209	31.935	-77.82547729	167.365655	-23.418
misv0262.5	1359982.75	555702.936	31.847	-77.82547363	167.3667055	-23.507
misv0263	1359981.769	555726.369	31.935	-77.82547394	167.3677017	-23.418
misv0264	1359979.862	555775.201	31.954	-77.82547334	167.3697774	-23.4
misv0264.5	1359979.068	555799.585	32.063	-77.82547161	167.3708136	-23.291
misv0265	1359977.956	555823.486	31.972	-77.8254729	167.3718299	-23.382
misv0266	1359976.47	555872.41	32.02	-77.82546847	167.3739088	-23.334
misv0266.5	1359975.689	555896.819	32.003	-77.8254666	167.3749461	-23.351
misv0267	1359974.773	555920.652	32.058	-77.82546615	167.3759592	-23.296
misv0268	1359973.157	555969.574	32.192	-77.82546285	167.3780383	-23.162
misv0268.5	1359972.671	555993.944	32.185	-77.82545834	167.3790734	-23.168
misv0269	1359971.367	556018.032	32.212	-77.82546125	167.3800979	-23.142
misv0270	1359969.863	556066.999	32.203	-77.82545689	167.3821787	-23.151
misv0270.5	1359969.188	556091.34	32.193	-77.82545408	167.3832129	-23.161
misv0271	1359968.178	556115.327	32.384	-77.82545438	167.3842327	-22.969
misv0272	1359966.386	556164.365	32.52	-77.82545255	167.386317	-22.834
misv0272.5	1359966.133	556188.662	32.526	-77.82544595	167.3873486	-22.828
misv0273	1359964.978	556212.637	32.537	-77.82544754	167.3883681	-22.817
misv0274	1359963.276	556261.626	32.741	-77.82544489	167.3904501	-22.613
misv0274.5	1359963.219	556285.98	32.648	-77.8254365	167.3914838	-22.706
misv0275	1359961.703	556309.913	32.712	-77.82544132	167.3925022	-22.642
misv0276	1359961.279	556359.086	32.843	-77.8254335	167.394584	-22.51
misv0276.5	1359959.779	556383.186	32.746	-77.82543174	167.3956152	-22.608
misv0277	1359959.548	556407.013	32.802	-77.82542508	167.3966268	-22.551
misv0278	1359957.941	556456.131	32.799	-77.82542147	167.3987142	-22.555
misv0278.5	1359956.393	556480.827	32.712	-77.82542628	167.399765	-22.642
misv0279	1359956.241	556504.645	32.779	-77.8254189	167.400776	-22.574
misv0280	1359954.587	556553.825	32.844	-77.82541565	167.4028661	-22.51
misv0280.5	1359953.101	556578.651	32.969	-77.82541983	167.4039223	-22.385
misv0281	1359953.079	556602.261	32.745	-77.82541136	167.4049244	-22.609
misv0282	1359951.575	556651.271	32.835	-77.8254068	167.4070069	-22.519
misv0282.5	1359949.881	556675.667	32.948	-77.82541299	167.4080453	-22.406

Dhiresh Hansaraj   8/09/2009

Flag Number	N	E	Height (masl)	Latitude [S]	Longitude [E]	WGS84 elevation (m)
misv0283	1359950.047	556699.114	33.018	-77.82540288	167.4090401	-22.336
misv0284	1359948.246	556748.171	33.481	-77.82540092	167.4111252	-21.873
misv0284.5	1359946.676	556772.798	33.521	-77.82540591	167.412173	-21.833
misv0285	1359946.815	556796.709	33.381	-77.82539584	167.4131876	-21.972
misv0286	1359945.19	556845.798	33.427	-77.82539228	167.4152737	-21.927
misv0286.5	1359943.929	556870.694	33.313	-77.82539438	167.4163325	-22.041
misv0287	1359943.634	556894.116	33.338	-77.82538837	167.417327	-22.016
misv0288	1359941.95	556943.131	33.256	-77.82538533	167.4194101	-22.098
misv0288.5	1359940.536	556967.681	33.516	-77.8253889	167.4204545	-21.838
misv0289	1359940.379	556991.321	33.403	-77.82538157	167.421458	-21.95
misv0290	1359938.809	557040.335	33.38	-77.82537748	167.4235408	-21.974
misv0290.5	1359937.388	557064.842	33.356	-77.82538112	167.4245834	-21.998
misv0291	1359937.145	557088.984	33.341	-77.82537434	167.4256084	-22.013
misv0292	1359935.482	557138.095	33.315	-77.82537102	167.4276955	-22.038
misv0292.5	1359934.063	557162.787	33.42	-77.82537457	167.4287459	-21.934
misv0293	1359933.867	557186.409	33.331	-77.82536754	167.4297488	-22.023
misv0294	1359932.48	557235.38	33.383	-77.82536177	167.4318295	-21.971
misv0294.5	1359930.621	557259.659	33.419	-77.82536939	167.4328631	-21.935
misv0295	1359930.892	557283.619	33.457	-77.82535805	167.4338795	-21.897
misv0296	1359929.226	557332.546	33.387	-77.82535476	167.4359588	-21.966
misv0296.5	1359927.966	557357.041	33.402	-77.82535692	167.4370005	-21.952
misv0297	1359927.841	557380.621	33.438	-77.82534925	167.4380015	-21.916
misv0298	1359926.214	557429.651	33.464	-77.82534554	167.4400851	-21.89
misv0298.5	1359924.703	557454.059	33.531	-77.82534997	167.4411236	-21.823
misv0299	1359924.448	557477.899	33.491	-77.82534335	167.4421358	-21.862
misv0300	1359922.939	557527.024	33.616	-77.82533852	167.4442232	-21.738
misv0300.5	1359921.19	557551.674	33.652	-77.82534497	167.4452724	-21.702
misv0301	1359921.411	557575.134	33.533	-77.82533422	167.4462676	-21.821
misv0302	1359919.806	557624.148	33.649	-77.82533026	167.4483505	-21.705
misv0302.5	1359918.396	557648.534	33.587	-77.82533375	167.4493879	-21.767
misv0303	1359918.345	557672.558	33.754	-77.82532522	167.4504075	-21.6
misv0304	1359916.885	557721.591	33.528	-77.82531992	167.452491	-21.825
misv0304.5	1359915.38	557746.259	33.695	-77.82532414	167.4535405	-21.659
misv0305	1359915.45	557770.09	33.731	-77.82531458	167.4545517	-21.623
misv0306	1359914.104	557819.211	33.812	-77.82530819	167.4566387	-21.542
misv0306.5	1359912.848	557843.579	33.714	-77.82531028	167.4576751	-21.64
misv0307	1359912.649	557867.918	33.858	-77.82530292	167.4587083	-21.496
misv0308	1359911.285	557917.162	33.743	-77.82529662	167.4608005	-21.611
misv0308.5	1359910.36	557941.57	33.926	-77.82529572	167.461838	-21.428
misv0309	1359909.859	557965.352	33.882	-77.82529126	167.4628481	-21.472
misv0310	1359908.142	558014.458	33.956	-77.82528814	167.4649351	-21.398
misv0310.5	1359907.143	558038.752	33.841	-77.82528792	167.4659679	-21.513
misv0311	1359906.749	558062.98	33.905	-77.82528232	167.4669968	-21.449
misv0312	1359905.499	558112.102	33.972	-77.82527498	167.4690836	-21.382
misv0312.5	1359904.126	558136.528	34.103	-77.82527806	167.4701226	-21.251
misv0313	1359903.746	558160.6	34.195	-77.82527237	167.4711448	-21.159
misv0314	1359902.06	558209.803	34.185	-77.82526888	167.4732359	-21.169
misv0314.5	1359900.595	558234.295	34.128	-77.82527273	167.4742779	-21.226
misv0315	1359900.315	558258.009	34.057	-77.82526627	167.4752847	-21.296
misv0316	1359898.526	558307.142	34.229	-77.82526369	167.477373	-21.125

Dhiresh Hansaraj   8/09/2009

Flag Number	N	E	Height (masl)	Latitude [S]	Longitude [E]	WGS84 elevation (m)
misv0316.5	1359897.397	558331.587	34.224	-77.82526453	167.4784124	-21.13
misv0317	1359897.092	558355.372	34.259	-77.82525825	167.4794223	-21.095
misv0318	1359895.423	558404.456	34.315	-77.82525459	167.4815082	-21.038
misv0318.5	1359894.304	558428.693	34.271	-77.82525541	167.4825388	-21.082
misv0319	1359893.833	558453.052	34.396	-77.82525039	167.4835734	-20.958
misv0320	1359892.051	558501.981	34.304	-77.82524776	167.4856529	-21.05
misv0320.5	1359890.899	558526.434	34.445	-77.82524878	167.4866927	-20.909
misv0321	1359890.42	558550.093	34.615	-77.82524408	167.4876976	-20.739
misv0322	1359888.894	558599.194	34.464	-77.82523907	167.489784	-20.89
misv0322.5	1359887.55	558623.434	34.405	-77.82524187	167.4908151	-20.949
misv0323	1359887.388	558647.841	34.595	-77.82523403	167.4918511	-20.759
misv0324	1359885.771	558697.033	34.487	-77.82522976	167.4939416	-20.867
misv0324.5	1359884.232	558721.721	34.803	-77.82523413	167.494992	-20.551
misv0325	1359884.099	558745.784	34.481	-77.82522614	167.4960134	-20.872
misv0326	1359882.432	558795.001	34.784	-77.82522229	167.498105	-20.57
misv0326.5	1359881.002	558819.431	34.621	-77.82522576	167.4991443	-20.732
misv0327	1359880.603	558843.452	34.642	-77.82522015	167.5001644	-20.712
misv0328	1359878.988	558892.622	34.658	-77.82521581	167.5022538	-20.695
misv0328.5	1359877.407	558917.069	34.605	-77.82522061	167.5032942	-20.749
misv0329	1359877.261	558940.979	34.67	-77.82521277	167.5043091	-20.684
misv0330	1359875.673	558990.263	34.636	-77.82520812	167.5064034	-20.718
misv0330.5	1359874.164	559014.391	34.544	-77.82521238	167.50743	-20.809
misv0331	1359874.109	559038.474	34.78	-77.82520364	167.508452	-20.573
misv0332	1359871.497	559087.645	34.64	-77.82520817	167.5105434	-20.714
misv0332.5	1359870.848	559112.01	34.671	-77.82520463	167.5115785	-20.683
misv0333	1359869.473	559136.415	34.689	-77.82520757	167.5126167	-20.665
misv0334	1359867.905	559185.765	34.593	-77.82520265	167.5147137	-20.761
misv0334.5	1359867.117	559210.095	34.661	-77.82520035	167.5157476	-20.693
misv0335	1359866.356	559234.304	34.596	-77.82519786	167.5167763	-20.758
misv0336	1359864.613	559283.553	34.584	-77.82519451	167.5188694	-20.769
misv0336.5	1359863.611	559307.793	34.657	-77.82519415	167.5198998	-20.697
misv0337	1359862.998	559331.884	34.555	-77.82519035	167.5209233	-20.799
misv0338	1359861.17	559381.062	34.597	-77.82518776	167.5230135	-20.757
misv0338.5	1359860.395	559405.374	34.604	-77.82518532	167.5240466	-20.749
misv0339	1359859.487	559429.661	34.601	-77.82518408	167.5250788	-20.753
misv0340	1359857.812	559478.833	34.495	-77.82518009	167.5271685	-20.859
misv0340.5	1359857.157	559503.092	34.511	-77.82517659	167.5281991	-20.843
misv0341	1359856.278	559527.33	34.618	-77.82517509	167.5292293	-20.736
misv0342	1359854.579	559576.428	34.555	-77.82517131	167.5313159	-20.798
misv0342.5	1359853.785	559600.878	34.501	-77.82516895	167.5323549	-20.853
misv0343	1359852.774	559624.762	34.53	-77.82516877	167.5333702	-20.824
misv0344	1359851.091	559673.906	34.48	-77.82516479	167.5354587	-20.874
misv0344.5	1359850.414	559698.12	34.5	-77.82516147	167.5364875	-20.854
misv0345	1359849.442	559722.484	34.505	-77.82516072	167.5375232	-20.848
misv0346	1359847.979	559771.739	34.643	-77.82515472	167.5396159	-20.711
misv0346.5	1359847.116	559796.129	34.578	-77.82515297	167.5406525	-20.775
misv0347	1359846.366	559820.219	34.347	-77.82515033	167.5416761	-21.006
misv0348	1359844.68	559869.529	34.399	-77.82514626	167.5437717	-20.954
misv0348.5	1359844.187	559893.862	34.338	-77.82514121	167.5448051	-21.016
misv0349	1359842.943	559918.155	34.373	-77.82514289	167.5458383	-20.981

Dhiresh Hansaraj   8/09/2009

Flag Number	N	E	Height (masl)	Latitude [S]	Longitude [E]	WGS84 elevation (m)
misv0350	1359841.405	559967.421	34.392	-77.82513749	167.5479317	-20.961
misv0350.5	1359840.586	559992.128	34.463	-77.8251352	167.5489816	-20.891
misv0351	1359839.693	560015.965	34.31	-77.8251339	167.5499948	-21.044
misv0352	1359838.048	560065.233	34.349	-77.82512942	167.5520885	-21.005
misv0352.5	1359837.324	560089.722	34.302	-77.82512635	167.5531289	-21.051
misv0353	1359836.427	560113.733	34.382	-77.82512501	167.5541495	-20.972
misv0354	1359834.831	560162.815	34.266	-77.82512013	167.5562352	-21.088
misv0354.5	1359833.886	560187.23	34.295	-77.82511905	167.5572729	-21.058
misv0355	1359833.072	560211.613	34.382	-77.8251168	167.5583091	-20.971
misv0356	1359831.424	560260.872	34.367	-77.82511229	167.5604024	-20.987
misv0356.5	1359830.759	560285.467	34.376	-77.82510861	167.5614473	-20.978
misv0357	1359829.886	560309.532	34.245	-77.82510701	167.5624701	-21.108
misv0358	1359828.167	560358.8	34.295	-77.8251031	167.5645639	-21.059
misv0358.5	1359827.311	560383.556	34.524	-77.82510105	167.565616	-20.83
misv0359	1359826.691	560407.496	34.512	-77.82509721	167.566633	-20.841
misv0360	1359824.811	560456.728	34.589	-77.82509473	167.5687255	-20.765
misv0360.5	1359824.218	560480.857	34.539	-77.82509056	167.5697505	-20.814
misv0361	1359823.283	560504.813	34.722	-77.82508952	167.5707688	-20.632
misv0362	1359821.539	560553.919	34.562	-77.82508583	167.5728557	-20.791
misv0362.5	1359820.959	560578.368	34.873	-77.82508141	167.5738943	-20.481
misv0363	1359820.058	560602.555	34.76	-77.82507996	167.5749223	-20.593
misv0364	1359818.353	560651.65	34.824	-77.82507589	167.5770087	-20.53
misv0364.5	1359817.593	560675.902	34.752	-77.82507315	167.5780392	-20.601
misv0365	1359816.776	560699.812	34.818	-77.82507104	167.5790553	-20.536
misv0366	1359814.929	560749.07	34.734	-77.82506814	167.5811489	-20.62
misv0366.5	1359814.555	560773.394	34.733	-77.82506189	167.5821817	-20.62
misv0367	1359813.539	560797.198	34.87	-77.8250616	167.5831937	-20.484
misv0368	1359812.068	560846.43	34.865	-77.82505532	167.5852855	-20.488
misv0368.5	1359811.41	560870.6	34.863	-77.82505166	167.5863124	-20.491
misv0369	1359810.604	560894.702	34.871	-77.82504934	167.5873366	-20.483
misv0370	1359809.062	560943.953	34.893	-77.82504367	167.5894293	-20.46
misv0370.5	1359808.464	560968.045	34.816	-77.82503948	167.5904527	-20.538
misv0371	1359807.476	560992.341	34.945	-77.82503871	167.5914855	-20.409
misv0372	1359806.154	561041.561	34.821	-77.82503104	167.5935765	-20.532
misv0372.5	1359805.083	561065.871	35.118	-77.82503099	167.59461	-20.235
misv0373	1359804.289	561090.18	34.812	-77.82502845	167.595643	-20.542
misv0374	1359802.859	561139.269	34.864	-77.82502178	167.5977286	-20.49
misv0374.5	1359802.382	561163.53	34.848	-77.82501641	167.598759	-20.506
misv0375	1359801.368	561187.522	34.905	-77.82501596	167.5997789	-20.449
misv0376	1359799.796	561236.941	34.929	-77.82501039	167.6018788	-20.424
misv0376.5	1359798.98	561261.419	34.976	-77.82500796	167.602919	-20.378
misv0377	1359798.12	561285.633	34.885	-77.82500602	167.6039481	-20.469
misv0378	1359796.584	561334.97	34.99	-77.82500014	167.6060444	-20.364
misv0378.5	1359795.96	561359.295	34.997	-77.82499603	167.6070778	-20.357
misv0379	1359795.091	561383.757	35.055	-77.82499406	167.6081174	-20.299
misv0380	1359793.276	561433.118	34.958	-77.82499062	167.6102153	-20.396
misv0380.5	1359792.65	561457.713	34.885	-77.82498642	167.6112601	-20.468
misv0381	1359791.843	561481.564	35.02	-77.82498412	167.6122736	-20.334
misv0382	1359790.384	561530.823	34.932	-77.82497751	167.6143665	-20.422
misv0382.5	1359789.481	561555.257	35.004	-77.82497583	167.615405	-20.349

Dhiresh Hansaraj   8/09/2009

Flag Number	N	E	Height (masl)	Latitude [S]	Longitude [E]	WGS84 elevation (m)
misv0383	1359788.444	561579.738	34.947	-77.82497532	167.6164457	-20.406
misv0384	1359787.013	561628.947	34.945	-77.82496845	167.6185364	-20.408
misv0384.5	1359785.849	561653.614	34.854	-77.82496899	167.6195853	-20.5
misv0385	1359785.203	561677.769	34.925	-77.8249651	167.6206114	-20.429
misv0386	1359783.763	561727.318	34.939	-77.82495814	167.6227166	-20.414
misv0386.5	1359783.053	561751.9	35.023	-77.82495464	167.623761	-20.331
misv0387	1359782.056	561775.973	34.924	-77.82495391	167.6247843	-20.43
misv0388	1359780.49	561825.301	34.947	-77.82494813	167.6268803	-20.406
misv0388.5	1359779.784	561849.666	34.927	-77.82494467	167.6279155	-20.427
misv0389	1359778.849	561874.077	34.933	-77.82494323	167.628953	-20.42
misv0390	1359777.366	561923.425	34.898	-77.82493668	167.6310497	-20.455
misv0390.5	1359776.495	561947.968	34.97	-77.8249346	167.6320928	-20.384
misv0391	1359775.42	561972.15	34.802	-77.82493449	167.6331209	-20.552
misv0392	1359774.034	562021.533	35.008	-77.82492703	167.6352188	-20.346
misv0392.5	1359773.333	562045.841	34.887	-77.82492351	167.6362516	-20.467
misv0393	1359772.279	562069.783	34.936	-77.82492329	167.6372695	-20.418
misv0394	1359770.392	562119.271	34.974	-77.82492023	167.6393729	-20.38
misv0394.5	1359770.002	562143.859	34.899	-77.8249138	167.6404169	-20.455
misv0395	1359769.042	562167.94	34.763	-77.82491267	167.6414405	-20.59
misv0396	1359767.375	562217.295	34.867	-77.82490766	167.6435378	-20.487
misv0396.5	1359766.615	562241.918	34.879	-77.82490452	167.644584	-20.474
misv0397	1359765.368	562266.117	34.912	-77.8249059	167.6456132	-20.441
misv0398	1359764.024	562315.468	34.942	-77.82489797	167.6477097	-20.411
misv0398.5	1359763.523	562340.034	34.904	-77.82489251	167.648753	-20.45
misv0399	1359762.468	562363.84	34.873	-77.82489231	167.6497651	-20.481
misv0400	1359760.654	562413.213	34.915	-77.82488856	167.6518635	-20.439
misv0400.5	1359759.934	562437.837	34.878	-77.82488502	167.6529097	-20.476
misv0401	1359759.024	562462.004	34.92	-77.82488336	167.6539368	-20.434
misv0402	1359757.101	562511.344	34.885	-77.82488056	167.656034	-20.469
misv0402.5	1359756.329	562535.932	34.855	-77.82487748	167.6570788	-20.498
misv0403	1359755.383	562560.169	34.939	-77.82487611	167.6581089	-20.415
misv0404	1359753.724	562609.558	34.993	-77.82487089	167.6602077	-20.36
misv0404.5	1359753.117	562634.181	34.961	-77.82486631	167.6612536	-20.392
misv0405	1359752.001	562658.5	34.855	-77.82486641	167.6622876	-20.499
misv0406	1359750.285	562708.018	34.896	-77.82486161	167.6643919	-20.458
misv0406.5	1359749.678	562732.594	34.842	-77.82485703	167.6654358	-20.512
misv0407	1359748.812	562756.78	34.933	-77.82485493	167.6664637	-20.421
misv0408	1359747.176	562806.128	34.869	-77.82484946	167.6685606	-20.485
misv0408.5	1359746.753	562830.384	34.959	-77.82484335	167.6695906	-20.394
misv0409	1359745.764	562854.57	34.827	-77.82484234	167.6706187	-20.527
misv0410	1359744.321	562903.921	34.922	-77.82483511	167.6727154	-20.432
misv0410.5	1359743.739	562928.587	34.777	-77.82483024	167.6737631	-20.577
misv0411	1359742.763	562952.857	34.764	-77.82482905	167.6747947	-20.59
misv0412	1359741.194	563002.423	34.798	-77.82482283	167.6769008	-20.556
misv0412.5	1359740.761	563027.04	34.769	-77.82481663	167.6779461	-20.584
misv0413	1359739.745	563051.457	34.777	-77.82481573	167.678984	-20.576
misv0414	1359737.649	563100.821	34.843	-77.82481427	167.6810825	-20.51
misv0414.5	1359737.686	563125.554	34.912	-77.8248038	167.6821319	-20.442
misv0415	1359736.153	563150.183	34.761	-77.82480744	167.6831798	-20.592
misv0416	1359734.568	563199.706	34.845	-77.82480131	167.6852841	-20.509

Dhiresh Hansaraj   8/09/2009

Flag Number	N	E	Height (masl)	Latitude [S]	Longitude [E]	WGS84 elevation (m)
misv0416.5	1359734.291	563224.203	34.752	-77.82479373	167.686324	-20.602
misv0417	1359733.284	563248.282	34.922	-77.82479285	167.6873476	-20.431
misv0418	1359731.612	563297.912	34.872	-77.82478743	167.6894565	-20.482
misv0418.5	1359731.009	563322.378	34.81	-77.82478277	167.6904957	-20.543
misv0419	1359729.66	563346.426	34.802	-77.82478495	167.6915187	-20.552
misv0420	1359727.838	563395.752	34.789	-77.82478097	167.693615	-20.564
misv0420.5	1359726.753	563420.653	34.714	-77.82478043	167.6946736	-20.64
misv0421	1359725.871	563444.818	34.827	-77.82477837	167.6957006	-20.527
misv0422	1359724.059	563494.32	34.865	-77.82477419	167.6978044	-20.489
misv0422.5	1359723.2	563518.835	34.737	-77.82477176	167.6988462	-20.617
misv0423	1359721.911	563542.936	34.701	-77.82477337	167.6998713	-20.653
misv0424	1359720.559	563592.435	34.728	-77.82476504	167.7019741	-20.625
misv0424.5	1359719.971	563617.229	34.753	-77.82476006	167.7030272	-20.601
misv0425	1359718.625	563641.296	34.739	-77.82476216	167.7040509	-20.614
misv0426	1359716.644	563690.924	34.811	-77.82475937	167.7061604	-20.542
misv0426.5	1359715.672	563715.599	34.844	-77.82475787	167.7072092	-20.509
misv0427	1359714.884	563739.596	34.783	-77.82475499	167.7082288	-20.571
misv0428	1359712.516	563789.089	34.702	-77.8247557	167.7103334	-20.652
misv0428.5	1359712.143	563813.523	34.812	-77.82474891	167.7113707	-20.541
misv0429	1359711.176	563837.49	34.716	-77.82474764	167.7123895	-20.637
misv0430	1359709.305	563886.963	34.683	-77.82474387	167.7144922	-20.671
misv0430.5	1359708.791	563911.498	34.776	-77.82473829	167.7155341	-20.577
misv0431	1359707.801	563935.592	34.685	-77.82473715	167.7165584	-20.669
misv0432	1359705.944	563985.048	34.564	-77.82473323	167.7186603	-20.79
misv0432.5	1359705.046	564009.709	34.584	-77.82473102	167.7197083	-20.769
misv0433	1359704.221	564033.754	34.519	-77.82472841	167.7207301	-20.835
misv0434	1359702.291	564083.239	34.568	-77.8247251	167.7228334	-20.786
misv0434.5	1359701.763	564107.854	34.647	-77.82471959	167.7238788	-20.706
misv0435	1359700.559	564132.142	34.602	-77.82472025	167.7249116	-20.751
misv0436	1359699.171	564181.841	34.701	-77.82471197	167.7270229	-20.653
misv0436.5	1359698.546	564206.46	34.558	-77.82470731	167.7280686	-20.796
misv0437	1359697.637	564230.156	34.505	-77.82470556	167.7290758	-20.848
misv0438	1359695.901	564279.779	34.529	-77.82470039	167.7311845	-20.825
misv0438.5	1359695.347	564304.737	34.593	-77.82469493	167.7322445	-20.761
misv0439	1359694.336	564329.141	34.522	-77.82469379	167.7332819	-20.832
misv0440	1359692.643	564378.763	34.593	-77.82468821	167.7353905	-20.761
misv0440.5	1359691.924	564403.276	34.654	-77.8246844	167.7364319	-20.7
misv0441	1359690.957	564427.457	34.584	-77.82468293	167.7374597	-20.77
misv0442	1359689.407	564477.076	34.509	-77.82467605	167.739568	-20.845
misv0443	1359687.724	564525.587	34.571	-77.82467079	167.7416294	-20.782
misv0444	1359686.114	564575.232	34.406	-77.82466439	167.7437389	-20.948
misv0445	1359684.332	564623.945	34.351	-77.82465991	167.7458091	-21.002
misv0446	1359682.686	564673.504	34.429	-77.82465384	167.7479149	-20.925
misv0447	1359681.198	564722.492	34.391	-77.82464658	167.7499962	-20.962
misv0448	1359679.59	564772.089	34.397	-77.82464012	167.7521036	-20.957
misv0449	1359677.946	564821.163	34.301	-77.82463418	167.7541889	-21.052
misv0450	1359676.058	564870.692	34.296	-77.82463023	167.7562939	-21.058
misv0451	1359674.22	564919.009	34.312	-77.82462632	167.7583475	-21.042
misv0452	1359672.531	564968.485	34.323	-77.82462057	167.7604498	-21.03
misv0453	1359670.732	565016.717	34.401	-77.82461632	167.7624997	-20.953

Dhiresh Hansaraj 8/09/2009

Flag Number	N	E	Height (masl)	Latitude [S]	Longitude [E]	WGS84 elevation (m)
misv0454	1359668.792	565066.275	34.466	-77.82461276	167.7646061	-20.887
misv0455	1359667.111	565114.675	34.425	-77.82460735	167.7666628	-20.928
misv0456	1359665.258	565164.196	34.447	-77.82460299	167.7687674	-20.907
misv0457	1359663.416	565212.747	34.349	-77.82459892	167.7708309	-21.004
misv0458	1359661.672	565262.35	34.411	-77.82459352	167.7729388	-20.943
misv0459	1359659.829	565311.237	34.352	-77.82458929	167.7750164	-21.002
misv0460	1359658.249	565360.746	34.388	-77.82458243	167.77712	-20.965
misv0461	1359656.577	565410.007	34.228	-77.82457648	167.7792133	-21.126
misv0462	1359654.843	565459.621	34.217	-77.82457092	167.7813216	-21.136
misv0463	1359653.178	565508.162	34.099	-77.82456518	167.7833842	-21.254
misv0464	1359651.219	565557.741	34.067	-77.82456162	167.7854915	-21.286

APPENDIX E – Survey Data (2006/2007)

Peg #	LAT	LONG	E_UTM58S	N_UTM58S
Andrill	-77.8888	167.0891	548920.244	1353168.232
S100	-77.8981	167.1026	549199.009	1352119.686
S101	-77.8978	167.1022	549190.854	1352153.481
S102	-77.8976	167.1018	549182.298	1352176.123
S103	-77.8973	167.1014	549174.143	1352209.918
S104	-77.8971	167.101	549165.586	1352232.560
S105	-77.8968	167.1006	549157.430	1352266.355
S106	-77.8966	167.1002	549148.873	1352288.997
S107	-77.8963	167.0997	549138.376	1352322.875
S108	-77.8961	167.0993	549129.818	1352345.517
S109	-77.8958	167.0989	549121.660	1352379.312
S110	-77.8956	167.0985	549113.102	1352401.953
S111	-77.8953	167.0981	549104.942	1352435.748
S112	-77.895	167.0977	549096.783	1352469.543
S113	-77.8948	167.0973	549088.223	1352492.184
S114	-77.8945	167.0969	549080.063	1352525.979
S115	-77.8943	167.0965	549071.502	1352548.620
S116	-77.894	167.096	549061.001	1352582.498
S117	-77.8938	167.0956	549052.440	1352605.139
S118	-77.8935	167.0952	549044.278	1352638.934
S119	-77.8933	167.0948	549035.717	1352661.575
S120	-77.893	167.0944	549027.554	1352695.369
S121	-77.8928	167.094	549018.991	1352718.010
S122	-77.8925	167.0936	549010.827	1352751.804
S123	-77.8922	167.0932	549002.663	1352785.598
S124	-77.892	167.0927	548991.759	1352808.322
S125	-77.8917	167.0923	548983.594	1352842.116
S126	-77.8915	167.0919	548975.030	1352864.757
S127	-77.8912	167.0915	548966.864	1352898.551
S128	-77.891	167.0911	548958.299	1352921.191
S129	-77.8907	167.0907	548950.132	1352954.985
S130	-77.8905	167.0903	548941.567	1352977.626
S131	-77.8902	167.0899	548933.399	1353011.419
N200	-77.8806	167.074	548599.173	1354095.363
N201	-77.8808	167.0744	548607.752	1354072.724
N202	-77.8811	167.0748	548615.936	1354038.933
N203	-77.8814	167.0752	548624.119	1354005.141
N204	-77.8816	167.0757	548635.040	1353982.420
N205	-77.8819	167.0761	548643.223	1353948.628
N206	-77.8821	167.0765	548651.800	1353925.989
N207	-77.8824	167.0769	548659.982	1353892.197
N208	-77.8826	167.0773	548668.559	1353869.558
N209	-77.8829	167.0777	548676.740	1353835.766
N210	-77.8831	167.0781	548685.316	1353813.127
N211	-77.8834	167.0785	548693.496	1353779.335
N212	-77.8836	167.079	548704.413	1353756.613
N213	-77.8839	167.0794	548712.592	1353722.821
N214	-77.8841	167.0798	548721.167	1353700.182
N215	-77.8844	167.0802	548729.345	1353666.390

N216	-77.8847	167.0807	548739.865	1353632.514
N217	-77.8849	167.0811	548748.438	1353609.875
N218	-77.8852	167.0815	548756.615	1353576.082
N219	-77.8854	167.0819	548765.188	1353553.443
N220	-77.8857	167.0823	548773.364	1353519.650
N221	-77.8859	167.0827	548781.937	1353497.011
N222	-77.8862	167.0831	548790.112	1353463.218
N223	-77.8864	167.0836	548801.025	1353440.495
N224	-77.8867	167.084	548809.199	1353406.702
N225	-77.8869	167.0844	548817.770	1353384.063
N226	-77.8872	167.0848	548825.943	1353350.270
N227	-77.8874	167.0852	548834.513	1353327.630
N228	-77.8877	167.0857	548845.027	1353293.754
N229	-77.888	167.0861	548853.199	1353259.961
N230	-77.8882	167.0865	548861.768	1353237.321
N231	-77.8885	167.0869	548869.940	1353203.527

APPENDIX F – CD (Figures 22 to 28)